



**HARD COLLISIONS IN RUBIDIUM USING
SUB-DOPPLER SPECTROSCOPY**

THESIS

Douglas E. Thornton, Second Lieutenant, USAF
AFIT/GEO/ENP/10-M02

**DEPARTMENT OF THE AIR FORCE
AIR UNIVERSITY**

AIR FORCE INSTITUTE OF TECHNOLOGY

Wright-Patterson Air Force Base, Ohio

APPROVED FOR PUBLIC RELEASE; DISTRIBUTION UNLIMITED.

The views expressed in this thesis are those of the author and do not reflect the official policy or position of the United States Air Force, Department of Defense, or the United States Government.

AFIT/GEO/ENP/10-M02

HARD COLLISIONS IN RUBIDIUM USING SUB-DOPPLER SPECTROSCOPY

THESIS

Presented to the Faculty
Department of Electrical and Computer Engineering
Graduate School of Engineering and Management
Air Force Institute of Technology
Air University
Air Education and Training Command
in Partial Fulfillment of the Requirements for the
Degree of Master of Science in Electrical Engineering

Douglas E. Thornton, BSEE
Second Lieutenant, USAF

March 2010

APPROVED FOR PUBLIC RELEASE; DISTRIBUTION UNLIMITED.

AFIT/GEO/ENP/10-M02

HARD COLLISIONS IN RUBIDIUM USING SUB-DOPPLER SPECTROSCOPY

Douglas E. Thornton, BSEE
Second Lieutenant, USAF

Approved:

Glen P. Perram, PhD (Chairman)

Date

Kevin C. Grosss, PhD (Member)

Date

Maj Grady T. Phillips (Member)

Date

Abstract

Homogeneity of the pump and lasing transitions in the Diode Pumped Alkali Laser (DPAL) depend upon the rates for relaxation of velocity groups relative to the optical excitation rates. The effects of cavity mode interactions and hole-burning on the optical excitation rates and gain will be accentuated at the lower pressures enabled by narrow banded diode pump sources. Collisions that interrupt the phase of the emitted electromagnetic wave lead to pressure broadening, whereas collisions that alter the relative velocity of the collision pair reduce hole-burning effects. To better understand laser kinetics of an alkali gain medium, hard collisions, or velocity-changing collisions, is studied and a velocity-changing collision rate has been calculated for rubidium-argon using sub-Doppler spectroscopy. In this technique, a laser beam is split into a higher intensity pump beam ($I \gg I_{sat}$) and a lower intensity probe beam ($I \ll I_{sat}$). The beams are sent counter-propagating through the alkali vapor. The pump beam is amplitude modulated and the probe beam transmission is monitored at the pump beam modulation frequency. Only atoms that interact with both beams generate a signal. This occurs for the zero-velocity group, cross-over resonances, and atoms that suffer a hard collision between absorbing a same Doppler shifted photon from each beam. The spectra results in narrow peaks from the zero-velocity group and cross-over resonances superimposed on a broad Doppler pedestal via collisions. Spectra is gathered at various argon concentrations and pump beam chopping frequency for $^{87}\text{Rb } ^2S_{1/2}F' = 2 \rightarrow ^2P_{3/2}F'' = 1, 2, 3$ hyperfine transitions. Six velocity-groups are observed with approximate line widths of 23 MHz, about four times the natural line width. The spectra is fitted with a well documented, approximate line shape and a collisional fit parameter is extracted. Due to improprieties of the fits, another crude

line shape is also fitted and the ratio of the pedestal area to the narrow resonance area is taken as the collisional fit parameter. Since the collisional fit parameter is inversely dependent to the pump beam chopping frequency, the time scale at which these collisions are allowed to occur is interpolated. The collisional fit parameter and interpolated time scale are used to calculate a velocity-changing collision rate. Both line shapes deliver similar results, thus proving the documented line shape fit inaccuracies negligible. The documented line shape yields a rate $1020.7 \pm 26.3 s^{-1} mTorr^{-1}$ and the second line shape yields a rate of $758.81 \pm 13.90 s^{-1} mTorr^{-1}$, which is a 17% and 13% difference respectively to the chemical kinetic rate of $872.78 \pm 13.73 s^{-1} mTorr^{-1}$. Even though this method does not give better precision, possible curvature of the rate conveys insight of secondary effects.

Acknowledgements

I have many people to thank without whom I would not have been able to accomplish this work. I am most grateful to Dr. Perram, who gave me the opportunity to pursue research in spectroscopy with an electrical engineering background. His patience and guidance throughout have been greatly appreciated. Next, I owe the experiment to Maj Grady Phillips, who collected data from his own experiment for me to analyze to better understand the experimental apparatus before my own experimentation. Without his preceding work, I would have never thought it would be possible to collect data of my own. I owe much gratitude to Dr. Gross for his teachings in the fundamentals that led me to understand this work. My experimental success I owe to Greg Pitz, who helped me understand the lab and was a helpful ear when I had problems. To Mike Ranft and Greg Smith, who helped me get equipment and solve equipment problems I owe a thank you. I appreciate the superior customer service of the Matisse laser technicians who came out on three different occasions to fix and help me understand my laser promptly after I was unsuccessful at fixing it myself. I extend a special thanks to my fellow GEO's and DPAL group members who were supportive in my research and academic endeavors. Lastly, I owe a very personal appreciation to my fiancée, friends, and family who were very patient with me over the past 18 months.

Douglas E. Thornton

Table of Contents

	Page
Abstract	iv
Acknowledgements	vi
List of Figures	ix
List of Tables	xiv
I. Introduction	1
II. Background	3
2.1 Diode Pumped Alkali Laser	3
2.2 Rubidium	6
2.3 Saturation Spectroscopy	7
2.4 Previous Work	12
2.5 Expectations	16
III. Experiment	18
IV. Analysis	21
4.1 Frequency Axis Calibration	21
4.2 Empirical Study	26
4.3 Initial Fits	32
4.4 Line Shape Problem	38
4.5 A Second Fit	41
4.6 Initial Hard Collision Rate Calculation	43
4.7 The Time Scale of Collisions	49
4.8 Final Hard Collision Rate Calculation	53
V. Conclusion	56
5.1 Discussion of Findings	56
5.2 Recommendations for Future Work	56

	Page
A. Rubidium Constants	58
1.1 Rubidium Hyperfine Structure	58
1.2 Rubidium Spectroscopic Constants	60
1.3 Line Shapes	61
B. Data Plots	64
2.1 Data at Single Argon Pressure	64
2.2 Data at Single Chopping Frequency	70
2.3 All Data Fits	76
2.4 Fit Parameter Results	112
Bibliography	125
Vita	129

List of Figures

Figure		Page
1.	Three Level DPAL Diagram of Rubidium	4
2.	Comparison between Galatry and Voigt line shapes	5
3.	Hole Burning in Gain Profile	6
4.	Lorentzian Profile of Rubidium	7
5.	Diagram of the zero velocity group	8
6.	Overlap of two Doppler Profiles resulting in Cross-Over Resonances	10
7.	Cross-Over Resonance Diagram	10
8.	Velocity-Changing Collisions Diagram	11
9.	Experimental Apparatus	18
10.	Fabry-Perot transmission fit	22
11.	Sample Data Set	22
12.	Reference Cell Absorbance Fit Plot	23
13.	Frequency axis calibration	25
14.	Orientation Spectrum	25
15.	Empirical data plots of varied pump power	27
16.	Lorentzian line width and fit parameter, C , versus pump power	28
17.	Empirical data plots of varied probe power	29
18.	Lorentzian line width and fit parameter, C , versus probe power	31
19.	Data plots at a chopping frequency of 2200 Hz and an argon pressure of 30 mTorr	33
20.	Probe Beam Transmission Fit	35

Figure		Page
21.	Comparison with a partial data fit	37
22.	Hyperfine Pumping Diagram	39
23.	Comparison of two different fits at zero pressure	44
24.	Comparison of two different fits at 30 mTorr of Argon	45
25.	Initial collisional rate, Γ_{vcc} , versus argon pressure of both fits	48
26.	Inverse of the collisional fit parameter, C , versus chopping frequency at different pressures	50
27.	Inverse of the collisional fit parameter, C , versus chopping frequency at different pressures	51
28.	Final collisional rate, Γ_{vcc} , versus argon pressure of both fits	55
29.	^{85}Rb Hyperfine Structure of the D_2 Line	58
30.	^{87}Rb Hyperfine Structure of the D_2 Line	59
31.	Data at an argon pressure of 0 mTorr	64
32.	Data at an argon pressure of 30 mTorr	65
33.	Data at an argon pressure of 50 mTorr	66
34.	Data at an argon pressure of 70 mTorr	67
35.	Data at an argon pressure of 90 mTorr	68
36.	Data at an argon pressure of 110 mTorr	69
37.	Data at a pump beam chopping frequency of 700 Hz	70
38.	Data at a pump beam chopping frequency of 1100 Hz	71
39.	Data at a pump beam chopping frequency of 1700 Hz	72
40.	Data at a pump beam chopping frequency of 2200 Hz	73

Figure		Page
43.	Data fits of both line shapes at 0 mTorr of Argon and 700 Hz chopping frequency	76
44.	Data fits of both line shapes at 0 mTorr of Argon and 1100 Hz chopping frequency	77
45.	Data fits of both line shapes at 0 mTorr of Argon and 1700 Hz chopping frequency	78
46.	Data fits of both line shapes at 0 mTorr of Argon and 2200 Hz chopping frequency	79
47.	Data fits of both line shapes at 0 mTorr of Argon and 2800 Hz chopping frequency	80
48.	Data fits of both line shapes at 0 mTorr of Argon and 3200 Hz chopping frequency	81
49.	Data fits of both line shapes at 30 mTorr of Argon and 700 Hz chopping frequency	82
50.	Data fits of both line shapes at 30 mTorr of Argon and 1100 Hz chopping frequency	83
51.	Data fits of both line shapes at 30 mTorr of Argon and 1700 Hz chopping frequency	84
52.	Data fits of both line shapes at 30 mTorr of Argon and 2200 Hz chopping frequency	85
53.	Data fits of both line shapes at 30 mTorr of Argon and 2800 Hz chopping frequency	86
54.	Data fits of both line shapes at 30 mTorr of Argon and 3200 Hz chopping frequency	87
55.	Data fits of both line shapes at 50 mTorr of Argon and 700 Hz chopping frequency	88
56.	Data fits of both line shapes at 50 mTorr of Argon and 1100 Hz chopping frequency	89
57.	Data fits of both line shapes at 50 mTorr of Argon and 1700 Hz chopping frequency	90

Figure	Page
59. Data fits of both line shapes at 50 mTorr of Argon and 2800 Hz chopping frequency	92
60. Data fits of both line shapes at 50 mTorr of Argon and 3200 Hz chopping frequency	93
61. Data fits of both line shapes at 70 mTorr of Argon and 700 Hz chopping frequency	94
62. Data fits of both line shapes at 70 mTorr of Argon and 1100 Hz chopping frequency	95
63. Data fits of both line shapes at 70 mTorr of Argon and 1700 Hz chopping frequency	96
64. Data fits of both line shapes at 70 mTorr of Argon and 2200 Hz chopping frequency	97
65. Data fits of both line shapes at 70 mTorr of Argon and 2800 Hz chopping frequency	98
66. Data fits of both line shapes at 70 mTorr of Argon and 3200 Hz chopping frequency	99
67. Data fits of both line shapes at 90 mTorr of Argon and 700 Hz chopping frequency	100
68. Data fits of both line shapes at 90 mTorr of Argon and 1100 Hz chopping frequency	101
69. Data fits of both line shapes at 90 mTorr of Argon and 1700 Hz chopping frequency	102
70. Data fits of both line shapes at 90 mTorr of Argon and 2200 Hz chopping frequency	103
71. Data fits of both line shapes at 90 mTorr of Argon and 2800 Hz chopping frequency	104
72. Data fits of both line shapes at 90 mTorr of Argon and 3200 Hz chopping frequency	105
73. Data fits of both line shapes at 110 mTorr of Argon and 700 Hz chopping frequency	106

Figure		Page
75.	Data fits of both line shapes at 110 mTorr of Argon and 1700 Hz chopping frequency	108
76.	Data fits of both line shapes at 110 mTorr of Argon and 2200 Hz chopping frequency	109
77.	Data fits of both line shapes at 110 mTorr of Argon and 2800 Hz chopping frequency	110
78.	Data fits of both line shapes at 110 mTorr of Argon and 3200 Hz chopping frequency	111

List of Tables

Table		Page
1.	Initial rate plot data points	47
2.	The time scale parameter τ for each fit in Fig.26 and 27	50
3.	Final rate plot data points	54
4.	Rubidium D_2 Transition Optical Properties	60
5.	Rubidium 85 D Transition Hyperfine Structure Constants	60
6.	^{87}Rb D_2 Transition Hyperfine Structure Constants	60
7.	^{85}Rb D_2 Line Strengths	60
8.	^{87}Rb D_2 Line Strengths	61
9.	First line shape (Eq.(11)) fit results of C , γ , and $\Delta\nu_D$	113
10.	First line shape (Eq.(11)) fit results of the hyperfine transition amplitudes	114
11.	First line shape(Eq. (11)) fit results of the cross-over resonance amplitudes	115
12.	First line shape (Eq.(11)) fit results of the hyperfine transition center line positions	116
13.	First line shape (Eq.(11)) fit results of the cross-over resonance center line positions	117
14.	First line shape (Eq.(11)) fit results of the linear baseline noise	118
15.	Second line shape (Eq.(12)) fit results of A_D , ν_D , and $\Delta\nu_D$	119
16.	Second line shape (Eq.(12)) fit results of the hyperfine transition amplitudes	120
17.	Second line shape (Eq.(12)) fit results of the cross-over resonance amplitudes	121

Table		Page
18.	Second line shape (Eq.(12)) fit results of the hyperfine transition center line positions	122
19.	Second line shape (Eq.(12)) fit results of the cross-over resonance center line positions	123
20.	Second line shape (Eq.(12)) fit results of the γ and linear baseline noise	124

I. Introduction

Currently, the US Air Force's airborne laser (ABL) program uses a chemical oxygen iodine laser (COIL) on a Boeing 747 as another weapon in the United States repertoire for missile defense. The laser uses a singlet oxygen ($O_2(^1\Delta)$) generator to collisionally excite iodine through a supersonic nozzle. The excited iodine then lases at 1.315 microns and the chemicals are evacuated. COIL has been scaled to a level of mission effectiveness with efficiencies of less than 30%. However, the laser has a magazine depth limited the amount chemicals that can be stored on the plane.

Over the past couple of decades, laser diodes have become a well-developed, reliable technology driven by the increasing use in fiber-optic communication, disc drives, and laser pointers. However, laser diodes typically have poor beam quality and cannot be synchronized in large numbers. To correct this, the diode can be used to pump an alkali to create a coherent, good-quality beam. This is the idea behind a diode pumped alkali laser (DPAL). DPALs have gained interest as a high energy weapon to replace COIL. The alkalis have quantum efficiencies greater than 95% and have a foreseen wallplug efficiency of greater than 50% [6]. Also, the alkalis lase at shorter wavelengths, yielding a smaller diffraction limited spot size and greater brightness. The DPAL would have a magazine depth limited only to the amount of electricity that could be generated on the plane.

Because of the recent interest in DPALs as a high energy weapon, the alkalis have gained renewed attention. Since typical diodes have a much larger bandwidth (> 30 GHz) than the alkali pump transition (< 10 GHz), the alkali must be pressure

broadened via "soft", or phase changing, collisions with a buffer gas to spectrally match the diode. Consequently, the inert gas also displaces lasing population due to "hard", or velocity-changing, collisions. These are losses that degrade the efficiency of the system.

To study these losses, saturation spectroscopy can be employed to observe a sub-Doppler spectrum on top of a broad "Doppler pedestal" caused by velocity-changing collisions. The number of velocity changing collisions is proportional to the area of the Lorentzian line shape to the area of the broad Doppler pedestal. This work calculates a velocity-changing collision rate for rubidium-argon using sub-Doppler, saturation spectroscopy.

II. Background

2.1 Diode Pumped Alkali Laser

A DPAL is a 3-level hybrid-gas laser system: the diode pumps the alkali atoms from the $^2S_{1/2}$ to the $^2P_{3/2}$ state at the D_2 transition, the alkali is spin-orbit relaxed via collisions to the $^2P_{1/2}$ state, and lases at the D_1 transition to the $^2S_{1/2}$, as illustrated below in Fig.1. The figure shows the transition frequencies of rubidium. Other considered alkalis include potassium and cesium which have pump wavelengths along with rubidium that coincide with the compact disc drive AlGaAs laser diodes [6].

To ensure maximum efficiency of the system, the alkali line shape must be broadened to spectrally match the diode line shape. Since typical diodes have a band width of about 30 GHz, a buffer gas can be added to the alkali vapor to induce "soft" ,or phase changing, collisions occur which homogeneously broadens the alkali absorption by about 20 MHz/Torr [33; 34]. These are not collisions in the sense of elastic collisions between two billiard balls. Phase changing collisions occur when the buffer gas travels close enough to the alkali that it significantly perturbs the energy levels of the alkali causing random shifts in phase of the absorbed or emitted photon. Alternatively, the buffer gas will also cause "hard" or velocity-changing collisions which narrows the inhomogeneous profile and redistributes the lasing population. These are collisions in the sense of an elastic collision between two billiard balls.

Atoms follow a maxwellian velocity distribution which results in the Doppler profile that describes the distribution of frequencies an atom absorbs or emits at a specific transition. However, when the atom suffers collisions during the absorption or emission of a photon, an averaging over multiple Doppler shifts occurs and results in an inhomogeneous line width that is narrower than the Doppler line width. The narrowing of the inhomogeneous profile is also referred to as collisional narrowing or Dicke

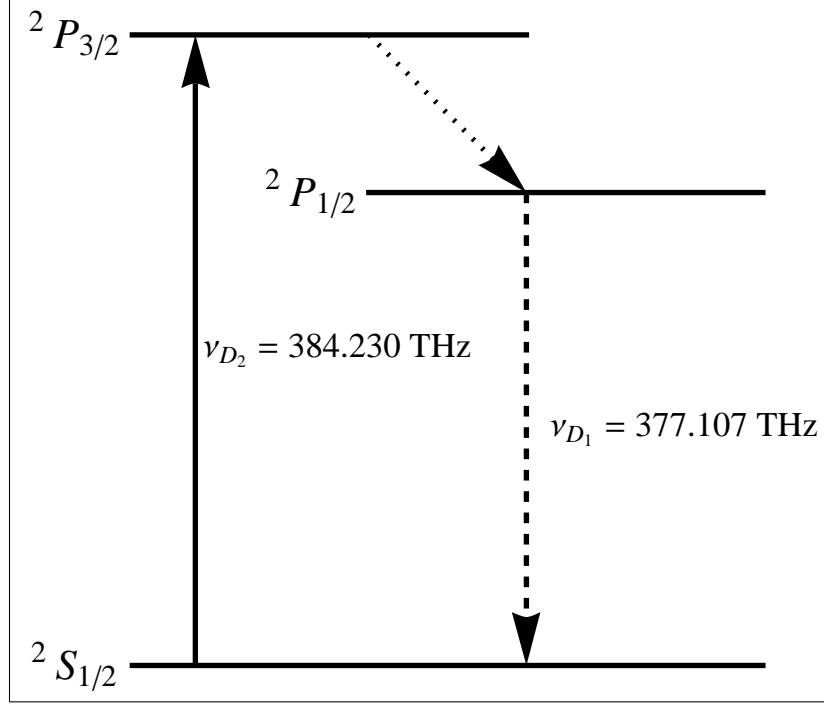


Figure 1. Three level diagram of the DPAL lasing scheme. The solid line is the pump transition, the dotted line is the non-radiative relaxation transition, and the dashed line is the lasing transition.

narrowing, named after Robert H. Dicke who first predicted the phenomenon in 1946 [18]. The resultant line shape is known as the Galatry profile. The Galatry profile is similar the Voigt line shape in that it contains the convolution of the Lorentzian and Doppler profile, but it also includes a collisional narrowing parameter. The difference between the Voigt and Galatry line shapes can be seen in Fig.2. Both line shapes have the same area, however the Galatry line shape has a noticeable lesser line width than a predominately inhomogeneously broadened Voigt line shape. In the bottom panel of Fig.2, the difference between each profile is presented to illustrate the distinct pattern often observed when a Voigt line shape is fitted to data that is better described by the Galatry line shape. This has been observed in cesium absorption spectra at low buffer gas pressures ($< 100 \text{ Torr}$) [32].

In a laser cavity, the possible output optical frequencies are every $\frac{c}{2\ell}$, where c is the speed of light and ℓ is the cavity length, which are called the cavity modes.

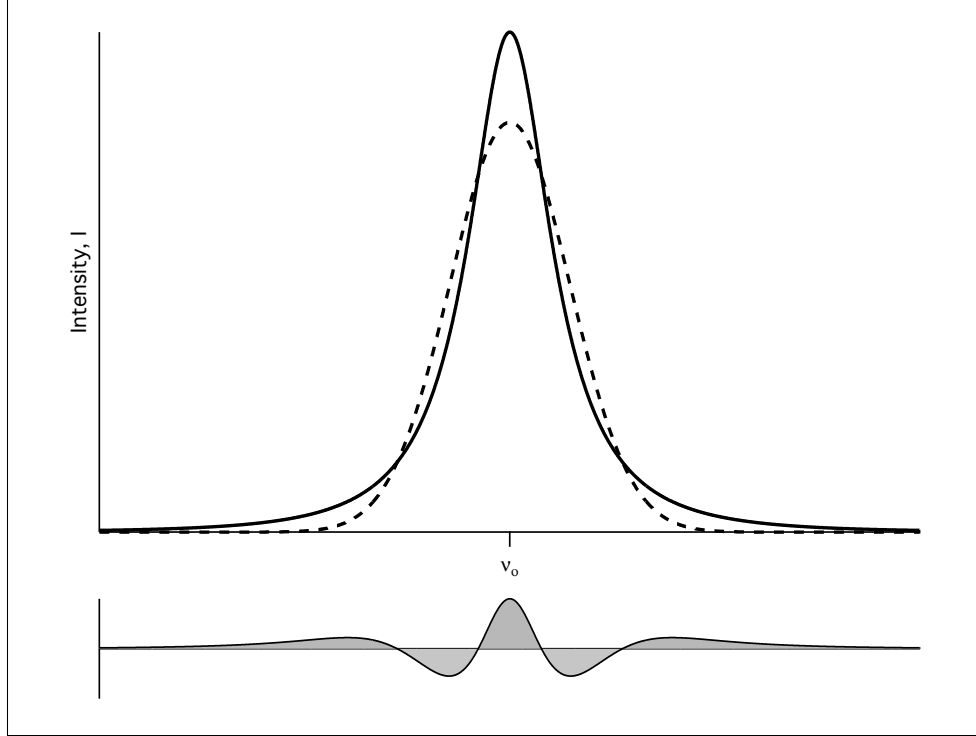


Figure 2. A comparison between Galatry (- - -) and Voigt (—) line shapes. Below the line shapes is the residual from a Voigt line shape fitted to collisionally narrowed data.

These cavity modes must coincide with the gain media profile, which in the case of a DPAL is the alkali vapor D_1 line. When lasing occurs, spectral holes are burnt in the gain profile at each resonator mode with a homogeneous line width as seen in Fig.3. These spectral holes are also referred to Bennett holes, named after William R. Bennet who first observed this phenomenon [7]. The depth of the holes are equal to the losses in the system, the line width is equal to the homogeneous width of the transition, and the area represents the lasing population. Hard collisions remove lasing population and redistributes the lasing population in the gain profile, thus increasing losses. At current buffer gas pressures for a spectrally efficient DPAL(10 - 20 atm), the hard collision effects are negligible. However, with the advent of narrow-banded diode lasers, lower pressures of the buffer gas will be used and the losses due to hard collisions will be more prevalent.

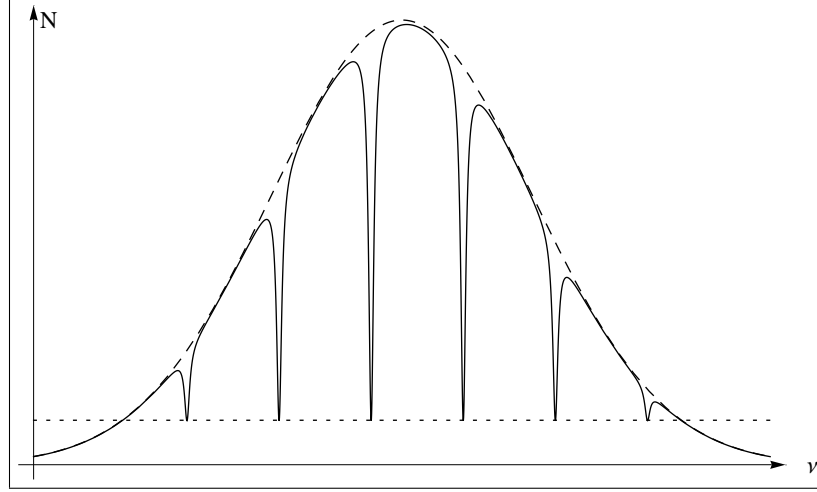


Figure 3. Diagram of hole burning in gain profile. N is the population in the lasing level and ν is frequency. Dashed line: Doppler broaden gain profile without lasing. Solid Line: Gain profile with holes burnt at each resonant mode, equally spaced. The dotted line is the losses that must be overcome.

2.2 Rubidium

Rubidium is one of the possible alkalis used as the gain medium in a DPAL. The pump transition, where the alkali must be spectrally matched to the diode, is the D_2 line which is the $5^2P_{3/2} \rightarrow 5^2P_{1/2}$ transition ($\lambda = 780.241$ nm or $\nu = 384.230$ THz)cite. rubidium has two isotopes, 85 and 87 amu, each having two ground hyperfine states and four excited hyperfine states. The hyperfine splitting of the D_2 line of rubidium is presented in Appendix A. Following the allowed dipole moment transition rule, $\Delta F = 0, \pm 1$, there are six hyperfine lines for each isotope. A rudimentary sub-Doppler spectrum gives a Lorentzian profile of the twelve hyperfine lines. Since the hyperfine splitting in the $5^2P_{3/2}$ level is less than the $5^2S_{1/2}$ level, four groups of three hyperfine lines and three cross-over lines is seen. A theoretical Lorentzian spectrum using the normalized area Lorentzian profile, Eq.(24), is shown in Fig.4 using the hyperfine structure and spectroscopic constants found in Appendix A.

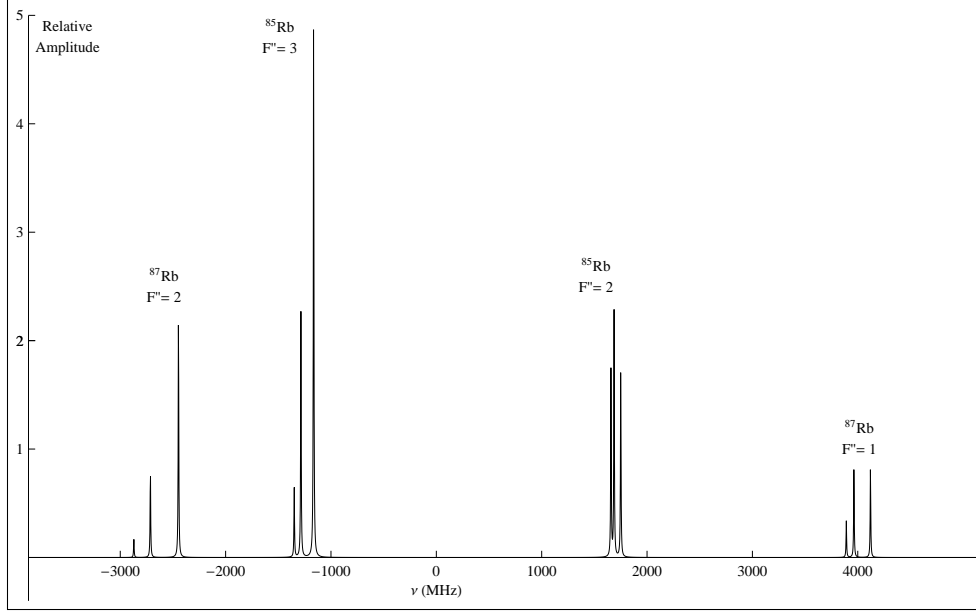


Figure 4. Lorentzian profile of Rb D_2 line. The spectrum follows the Lorentzian line shape at a line width equal to the natural line width, 6 MHz.

2.3 Saturation Spectroscopy

A tunable laser source is split into a pump and probe laser beam, counter-propagated through in an atomic (or molecular) vapor, intersecting in the atomic vapor cell. The intensity of the pump beam is much greater than I_{sat} to completely saturate the investigated transition while the probe beam intensity is much less than I_{sat} to interrogate the saturated system. The saturation intensity, I_{sat} is the optical intensity at which the atomic absorption transition reaches steady state as defined as

$$I_{sat} = \frac{h\nu}{\sigma\tau} \quad (1)$$

where h is Planck's constant, ν is the optical frequency, σ is the absorption cross-section of the atomic transition, and τ is the radiative lifetime of the atomic transition. For clarification, the saturation intensity in this experiment is the laser intensity at which the ground state de-population has reached steady-state, not the excited state

population. The pump beam is amplitude modulated and a lock-in amplifier monitors the probe beam absorption signal at the chopping frequency of the pump beam as the laser scans over the desired transitions. This is often referred as "Lamb dip" spectroscopy [17], since the resulting signal is the Lamb dip profile of the holes burned in the saturated transition.

Photon absorption by an atom occurs when the photon frequency, ω , is equal to transition frequency, ω_o , plus the Doppler shift in the direction of the laser beam,

$$\omega \cong \omega_o + kv_z \quad (2)$$

where k is the magnitude of the wave vector of the photon and v_z is the velocity of the atom in the direction of the photon. A signal can only be generated when an atom absorbs a photon from both beams. This occurs in three different events. The first event is the zero velocity group ($v_z = 0$), which only happens when $\omega = \omega_o$, shown in Fig.5. This is the groups of atoms traveling perpendicular to both beam so that the incident photons from both beams are not Doppler shifted. This results in the atom absorbing photons at the transition frequency \pm the natural half width and a very narrow resonance is observed. Because of this, saturation spectroscopy is also known as sub-Doppler spectroscopy because the Doppler profile is removed and the resolution will be limited by the homogeneous line width.

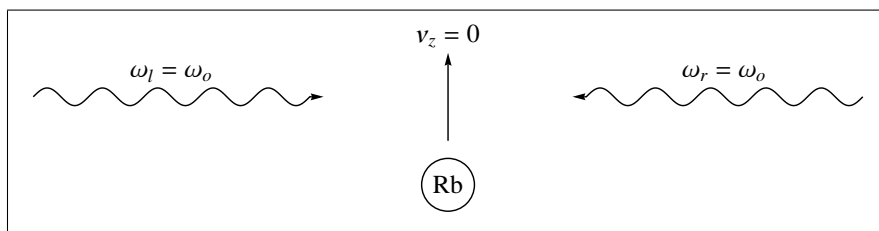


Figure 5. Diagram of the zero velocity group of atoms interacting with counter-propagating photons; ω_l is the photon moving from the left, ω_r is the photon moving from right.

The second event occurs when the Doppler profiles of two transitions significantly overlap as shown in Fig.6. When an atom is traveling at a velocity, v_z , such that it is red shifted the same amount towards one beam as it is blue shifted towards the other beam, the atom can absorb a red or blue shifted photon from one beam, excite to state a or b, $\omega = \omega_{a,b} + kv_z$, and then can absorb a blue or red shifted photon from the other beam and excite to the other state, b or a, $\omega = \omega_{b,a} + kv_z$. These events are called cross-over resonances which occur at a frequency half-way between the two transitions. This is illustrated in Fig.7. This also results in an observed narrow resonance.

The third and last event that occurs is when an atom traveling at v_z , absorbs a red or blue shifted photon, $\omega = \omega_o + kv_z$, suffers a collision which changes its velocity to $-v_z$, and then absorbs a same red or blue shifted photon from the other beam, $\omega = \omega_o + kv_z$. This chain of events is illustrated in Fig.8. This results in a broad "Doppler pedestal" which the narrow resonances are superimposed on.

In single-beam absorption spectroscopy, absorption profiles follow the Lambert-Beer Law

$$I = I_o \text{Exp}[-\Delta N \sigma \ell] \quad (3)$$

where I is the transmitted intensity, I_o is the incident intensity, ΔN is the difference in populations densities between the ground and excited state ($\Delta N = N_i - N_k$, for $|i\rangle \rightarrow |k\rangle$), σ is the absorption cross-section, and ℓ is absorption path length. This law is only valid when $N_i \gg N_k$. This is possible at low temperatures such that the Planckian distribution of atomic states yield the majority of atoms in the ground state. Even though the typical absorption profiles of Rubidium observed are well described by a Voigt line shape, this should not be true for saturation spectroscopy. Since the pump beam completely saturates the transition, N_k is actually much greater N_i and the Lambert-Beer law becomes invalid. Therefore, the probe beam absorption

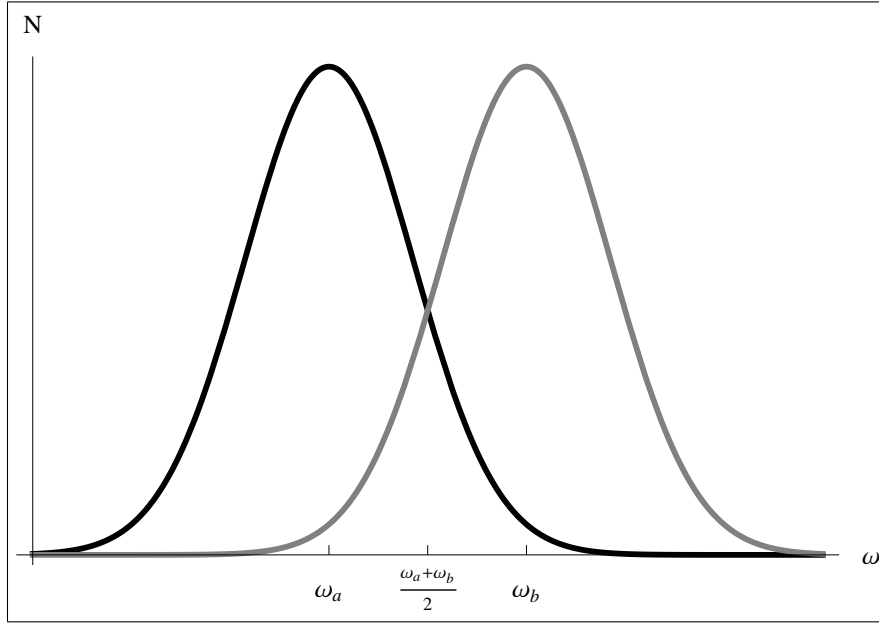


Figure 6. Overlapping Doppler profiles. The two profiles overlap halfway between the transitions ω_a and ω_b at $\frac{\omega_a + \omega_b}{2}$, where the cross-over resonance occurs.

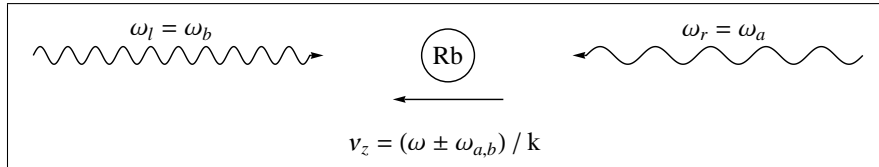


Figure 7. A Rubidium atom traveling at a velocity half-way between two transitions, ω_a and ω_b . It is blue shifted towards the photon from the left, ω_l , for the ω_a transition and is red shifted towards the photon from the right, ω_r , for the ω_b transition.

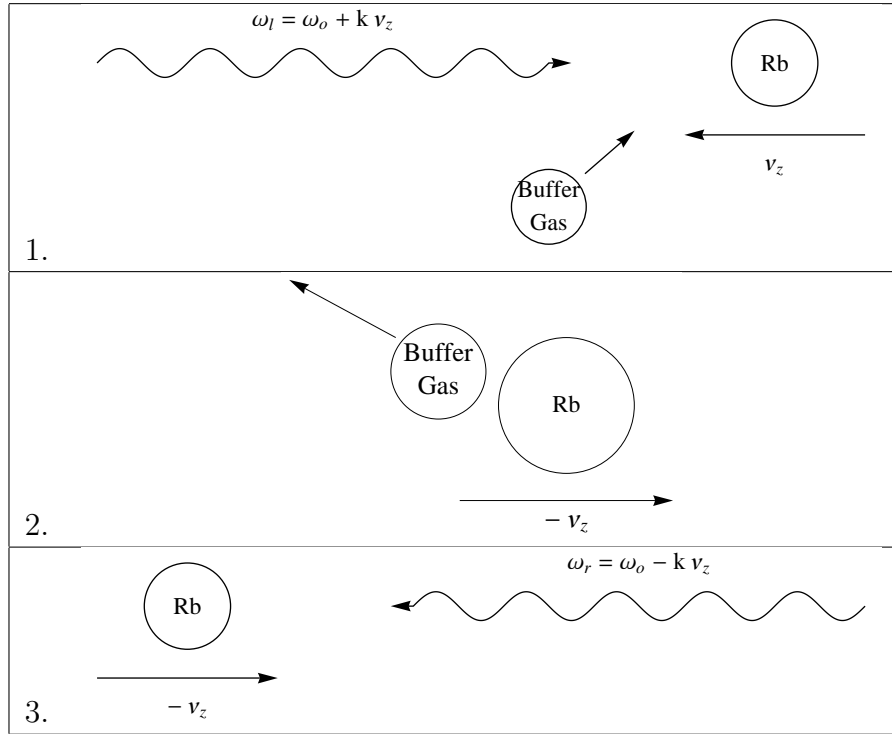


Figure 8. The chain of events for a detected velocity-changing collision. **1.** The Rubidium atom is shifted, red or blue, towards the photon from the left, ω_l . **2.** After absorption of ω_l photon, the atom suffers a velocity changing collision, $v_z \rightarrow -v_z$. **3.** The atom is shifted the same amount towards the photon from the right, ω_r .

line shape is expected to be much different than single-beam absorption.

Also, the observed signal in saturation spectroscopy is "up-right" rather than in single-beam absorption spectroscopy, the observed signal is "up side down". In single-beam absorption spectroscopy, the incident laser beam is amplitude modulated to remove background noise and the transmission of the beam through an atomic/molecular vapor is monitored at the chopping frequency with a lock-in amplifier. The lock-in amplifier acts as a band pass filter. The resulting signal is the difference between when the beam is blocked and unblocked. Since the blocked beam results in no signal and an unblocked beam results in a signal, the difference, or signal from the lock-in, is positive. Because the beam is being attenuated by the vapor while scanning over the investigated transition(s), the signal, or line shape, will appear "up side down", which is "corrected" by taking the negative natural log of I/I_o . In saturation spectroscopy, the probe beam transmission is being monitored at the pump beam chopping frequency with a lock-in amplifier. The observed signal from the lock-in will be the difference of the probe beam when the pump is blocked and unblocked. When the pump beam is blocked, the probe beam is attenuated by the vapor and when the pump beam is unblocked, the probe beam will be attenuated a lot less since the vapor will be made optically transparent to the probe beam by the pump beam. When the beams near a resonance and the pump beam is blocked, the probe beam will be attenuated a lot more than when the beams are far from a resonance. This makes the difference increase near resonances and means our signal's line shape will be up-right.

2.4 Previous Work

Saturation spectroscopy became popular in 1970's [36] as a way to observe the hyperfine structure in atoms. Linear spectroscopy is limited to about six or seven digits

of precision due to large Doppler profiles while non-linear (saturation spectroscopy) offers many more digits of precision, eight to ten digits of precision [21]. Through out the past decades, many studies have been accomplished to precisely locate atomic lines [13; 19; 20; 27; 28; 26; 44] and study atomic kinetics [2; 11; 9; 16; 24; 30; 37; 40].

The earliest known work in velocity-changing collisions using sub-Doppler spectroscopy was a study of the Helium-Neon collisions of the 6328 Å Neon laser line by Smith and Hänsch [43]. The "strong-collision", or also known as the "hard-sphere", model was used to develop theory in which the atoms are treated as billiard balls and the collision are elastic. A saturation spectroscopy experiment was done with Neon and varying pressures of Helium. Their theoretical model delivered the following line shape equation:

$$\mathcal{S} = A \left\{ \frac{\gamma^2}{\gamma^2 + 4\pi(\Delta\nu + \delta)^2} + C \text{Exp} \left[\left(\frac{\Delta\nu + \delta}{\Delta\nu_{\mathcal{D}}} \right)^2 \right] \right\} \text{Exp} \left[\left(\frac{\Delta\nu + \delta}{\Delta\nu_{\mathcal{D}}} \right)^2 \right] \quad (4)$$

where A is the relative amplitude of the line, γ is homogeneous width, C is weight of collisional background with respect to the homogeneous resonance, and δ is to adjust the line center for instabilities in the laser, $\Delta\nu$ is the laser frequency minus the transition frequency, and $\Delta\nu_{\mathcal{D}}$ is the Doppler line width times $4 \ln(2)$. Essentially, this is a Lorentzian profile plus a Doppler profile. It is noted that in Eq.(4), the exponentials are most likely missing a minus sign. The theoretical line shape was fitted to the data by adjusting A, C, γ , and δ . The theoretical model agreed well with the data, except for deviations in the wings of the data. The deviations were attributed to "weak" collisions which cause small velocity shifts which their theoretical model did not account for.

In a similar study of the neon - rare gas collisions was done some years later by Sasso et. al. [35]. The experiment used optogalvanic detection in saturation spectroscopy to give a quantitative evaluation of collisional parameters between neon

and rare gases. An equation similar to Eq.(4) was used for fits,

$$\mathcal{S} = A \left\{ \frac{\gamma^2/4}{\gamma^2/4 + (\Delta\nu - \nu_o)^2} + C \text{Exp} \left[- \left(\frac{\Delta\nu + \nu_o}{\Delta\nu_{\mathcal{D}}} \right)^2 \right] \right\} \text{Exp} \left[- \left(\frac{\Delta\nu + \nu_o}{\Delta\nu_{\mathcal{D}}} \right)^2 \right] \quad (5)$$

A definition of C was further derived,

$$C = 2\sqrt{\pi \ln(2)} \frac{\Gamma_{vcc}\gamma}{\gamma_a \Delta\nu_{\mathcal{D}}} \quad (6)$$

where γ is the Lorentzian line width, $\Delta\nu_{\mathcal{D}}$ is the Doppler line width, γ_a is the decay rate and Γ_{vcc} is the cross-relaxation rate, or the velocity changing collision rate. The decay rate γ_a was also given as

$$\gamma_a = \gamma_{coll} + \gamma_{diff} + \gamma_{disch} + \frac{1}{\tau_{nat}} + \frac{1}{\tau_{trans}} \quad (7)$$

where γ_{coll} is the decay rate due to collisions, γ_{diff} is the diffusive rate, γ_{disch} is the loss due to electronic collisions, τ_{nat} is the radiative lifetime of the ground state, and τ_{trans} is the transit time. The experiment used inter-modulated optogalvanic detection which is very similar to experimental set-up as described in Section 2.3, except that both beams are chopped at different frequencies and the current from the optogalvanic cell is monitored at the sum of the two chopping frequencies. The physics of the observed signal are the same as detecting the probe beam transmission with a few exceptions in the decay rate, or the time scale at which these collisions are allowed to occur. These exceptions are the diffusive rate γ_{diff} and the loss due to electronic collisions γ_{disch} can be ignored in this work. The collisional rate γ_{coll} can also be ignored because the quenching rate for ground state rubidium is very, very small. Another way to say it, it takes significant energy (very high temperatures) for

quenching of the rubidium ground state [45; 53]. An equation for the transit time is given

$$\tau_{trans} = \frac{\omega_o}{\bar{v}}(1 + \frac{\omega_o}{\lambda}) \quad (8)$$

where ω_o is the beam waist, λ is the mean free path of the neon atoms, and \bar{v} is the mean transverse velocity. A calculation for the velocity changing collision rate was not presented, however plots of homogeneous line widths, C , and $1/C$ vs rare gas pressure were shown. In a sub-Doppler study on molecular iodine, the spectra was observed to be dependent on chopping frequency [31]. To solve this, a study on methods minimizing the influence of velocity changing collisions in Doppler-free saturation spectroscopy [25] provides further insight. The experiment uses rf-modulation of a pump beam and optogalvanic detection to resolve the hyperfine structure in Gadolinium. The calculations use the previous Eq.(5), however the $1/\tau_{trans}$ term of the decay rate is substituted with the modulation frequency of the pump beam. This is understood that given a sufficient beam width, the transit time becomes significantly long and chopping shortens travel time of the atom through the beam. Therefore, under those conditions, the substitution is valid. One other study was carried out to characterize the transient time for collisions between krypton - krypton and krypton - helium using saturation spectroscopy [15]. In the study, the use the "hard sphere" chemical kinetic model to get a value of the collisional rate to calculate the time at which these collisions take place. This could have been done because of the fact that the transient nature of the collisions is not well understood and can only be roughly estimated. This shows that these types of experiments can be done to calculate either the collisional rate or transient time at which these collisions take place. In a preliminary set of data collected by Dr. Grady Phillips at a constant buffer gas pressure and varied chopping frequency, the velocity-changing collision rate, Γ_{vcc} , was still varied with chopping frequency. The problem that arises is with the decay rate,

γ_a , which is essentially the time scale at which these collisions occur and chopping frequency isn't the only term in the decay rate. However, all the above studies show the relationship between C and γ versus the concentration of collisional partner, or calculated a velocity-changing collision rate or decay rate to plot the decay rate or velocity-changing collisions versus buffer gas concentration. Since this work is focused on calculating a velocity-changing collision rate, the decay rate must be known. To better estimate the transient nature of the collision, data can be collected with varying chopping frequencies and varying buffer gas pressure to interpolate the time at which these collisions take place to reach an improved calculation of the collisional rate.

2.5 Expectations

Even though the Doppler profile is removed in saturation spectroscopy, homogeneous line widths are multiple times greater than the natural line width in the experiment caused by power broadening and beam alignment. Due to closely spaced hyperfine and cross-over resonances in ^{85}Rb and the $F'' = 1$ state of ^{87}Rb , the individual hyperfine and cross-over lines are not well resolved, but the $F'' = 2$ state of ^{87}Rb is well resolved. Therefore, since the best resolution is needed in this experiment, especially since by adding the buffer gas, the narrow resonances will be much smaller than Doppler pedestal, only the $F'' = 2$ state of ^{87}Rb is investigated. Also, because each of the three hyperfine Doppler profiles in $F'' = 2$ state of ^{87}Rb overlap, three cross-over resonances will be observed along with the three hyperfine transitions. Since correct pump and probe powers must be used, an empirical study will be ran prior to data collection.

Intuitively, the more buffer gas concentration there is in the cell, the more collisions will occur and the faster the pump beam is chopped, the less time there is for

collisions to occur, therefore, less collisions are observed. For that reason, the collisional fit parameter should be proportional to buffer gas concentration and inversely proportional to pump beam chopping frequency. Furthermore, data will be taken at various buffer gas concentrations and at various pump beam chopping frequencies of $F'' = 2$ state of ^{87}Rb with argon.

III. Experiment

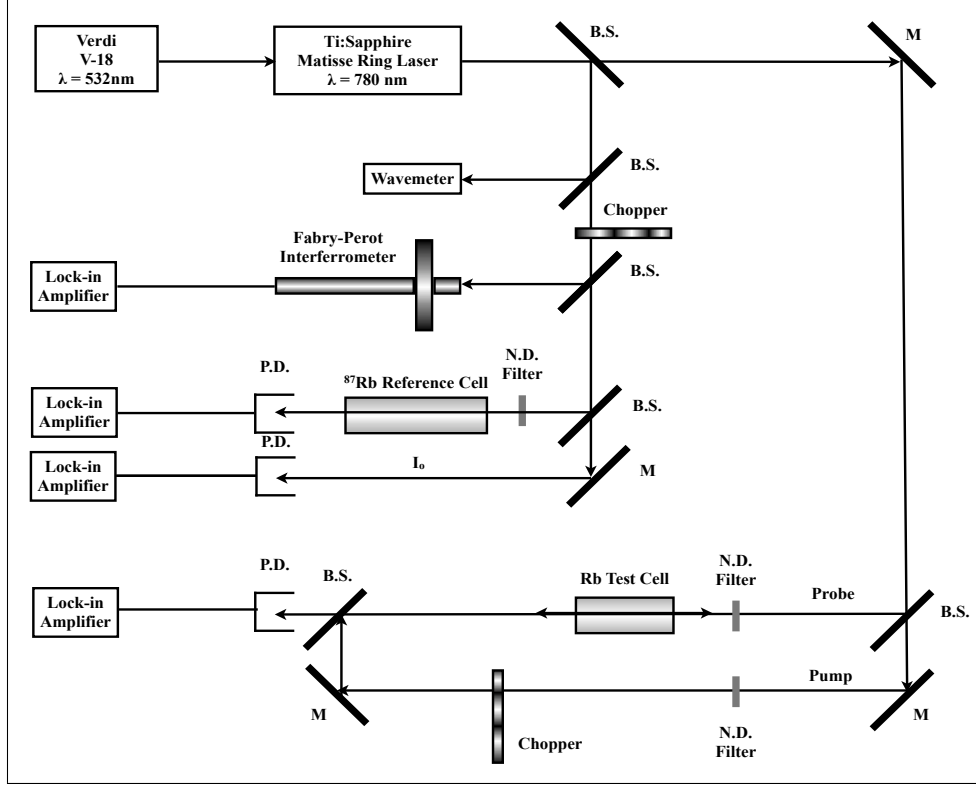


Figure 9. Experimental apparatus for sub-Doppler spectroscopy, where M are mirrors, B.S. are beam samplers, P.D. are photodiodes, and N.D. Filter are neutral density filters.

A diagram of the experiment apparatus can be seen in Fig.9. The Verdi is an 18 watt, frequency doubled Nd:YAG cw laser which pumps a Ti:Sapphire crystal at 10 watts in the Matisse ring laser. The output from the ring laser cavity is fed into the Matisse external reference cavity, which controls the frequency stabilization of the beam. The ring laser outputs about 1.5 watts of laser power with beam diameter of about 1-2 millimeters, measured from laser burn sheets with calipers. The line width of the beam was measured directed outside the cavity to be between 40 - 60 kHz with an *EagleEye*, which is an instrument that measures laser bandwidth. However, after passing through some beam splitters and mirrors, the beam's bandwidth was

re-measured to be a few hundred kHz, which is still greater than magnitude less than the natural line width of rubidium, ≈ 6 MHz. The ring laser is scanned over the D_2 transition of rubidium at a rate of about 10 - 11 MHz/sec, calculated from the frequency axis calibration. Immediately outside the laser cavity, a fraction of the beam is sampled and sent into a wave meter for an approximate real-time wavelength measurement. The sampled beam is sampled again, chopped at 1100 Hz, and sent into a Fabry-Perot interferometer, a rubidium reference cell of only isotope 87, and photodiode for a relative incident intensity measurement. The Fabry-Perot interferometer has free-spectral range (ν_{FSR}) of 300 MHz and a finesse of greater than 200. The signal from the interferometer is sent a lock-in amplifier. The rubidium reference cell is left at room temperature (26° C). The incident beam intensity for the reference cell is attenuated to about 10 μW for best signal to noise ratio. The transmitted beam power is measured with a photodiode behind the reference cell and the signal is sent to a lock-in amplifier. After the laser beam out of the Matisse has been sampled, the beam is split into two beams, pump and probe beam, and attenuated with neutral density filters. The probe beam is reflected directly through the rubidium test cell, through a beam sampler, into a photodiode which is connected to a lock-in amplifier. The pump beam is chopped and steered around the test cell to be anti-aligned with the probe beam to remove as much of the residual Doppler width as possible. In an empirical study, the crossing angle of the two beams has been calculated to be about 1.67°, which is comparable to a previous, similar experiment [1]. Also from the empirical study, the pump beam power was determined to be 50 μW and the probe beam power determined to be 2 μW . Measured saturation intensity of rubidium from [34] is around 5 $\frac{mW}{cm^2}$. Using a beam diameter of one millimeter, this gives a pump beam intensity of 6.4 $\frac{mW}{cm^2}$ and a pump beam intensity of 0.25 $\frac{mW}{cm^2}$. Since laser feedback can cause laser instabilities, it is to be noted that no laser instabilities were observed.

The rubidium test cell contains both isotopes in their natural abundance and is left at room temperature for all the tests to remove issues of the Rubidium vapor condensing and plating on the cell windows. However, the cell had to be heated with a heat gun and then cooled to ambient temperature prior to tests in order to acquire a signal. The test cell is connected to a vacuum pump system and argon gas cylinder. The residual pressure or zero point of the pressure meter is about 6 mTorr. All lock-in amplifiers monitor their signal at their chopping frequency, given by an output square wave by the chopper controller. The real and imaginary parts of the signal from the lock-in amplifiers are connected to a National Instruments data acquisition board. The data acquisition board is connected to a computer and National Instruments Lab View software collects and saves the data. Data was collected by only changing the chopping frequency of the pump beam, avoiding multiples of 30 Hz to eliminate interference from electricity, and varying the concentration of Argon in the rubidium test cell.

IV. Analysis

4.1 Frequency Axis Calibration

The data were analyzed using the software package Igor Pro. The raw data contains 9 different signals: the real and imaginary components of the probe beam transmission, Fabry-Perot transmission, reference cell transmission, relative laser intensity, and one signal for the time. The real and imaginary parts of each signal is investigated to ensure quality of data and phase jumps of the laser beam. Then the magnitude of each is calculated and divided by the relative laser beam intensity to eliminate any power fluctuations. The natural log of the magnitude of the reference cell transmission is taken to get an absorbance. This consolidates our signals to four. Since only the $F'' = 2 \rightarrow F' = 1, 2, 3$ transitions of ^{87}Rb are fitted and to reduce the size of the data fits, the data is first partitioned so that seven Fabry-Perot transmission peaks coincide with the $F'' = 2$ state of ^{87}Rb . Seven peaks are chosen because one falls within the hyperfine peaks and then three peaks on either side of the hyperfine lines to allow ample space for a baseline calculation in the fits. This first partition does include some of the ^{85}Rb $F'' = 3$ lines. All data is normalized to one and their minimums set to zero for convenience. Since the data is taken with respect to time, a calibrated frequency axis is needed. To calibrate the frequency axis, an algorithm is ran to find the peaks of the Fabry-Perot signal in time. After the peaks are found, a Lorentzian line shape, similar to Eq.24, is fit to each peak in time to increase precision of peak location, as seen in Fig.10. Next, the hyperfine and cross-over resonance peaks are visually selected in time. If one or more of the hyperfine peaks are not resolved or discerned, then three Voigt line shapes are fitted to the absorbance of the reference cell, using an algorithm for the Voigt described in Appendix A. The Doppler width, Eq.23, is calculated for room temperature and is held constant for the

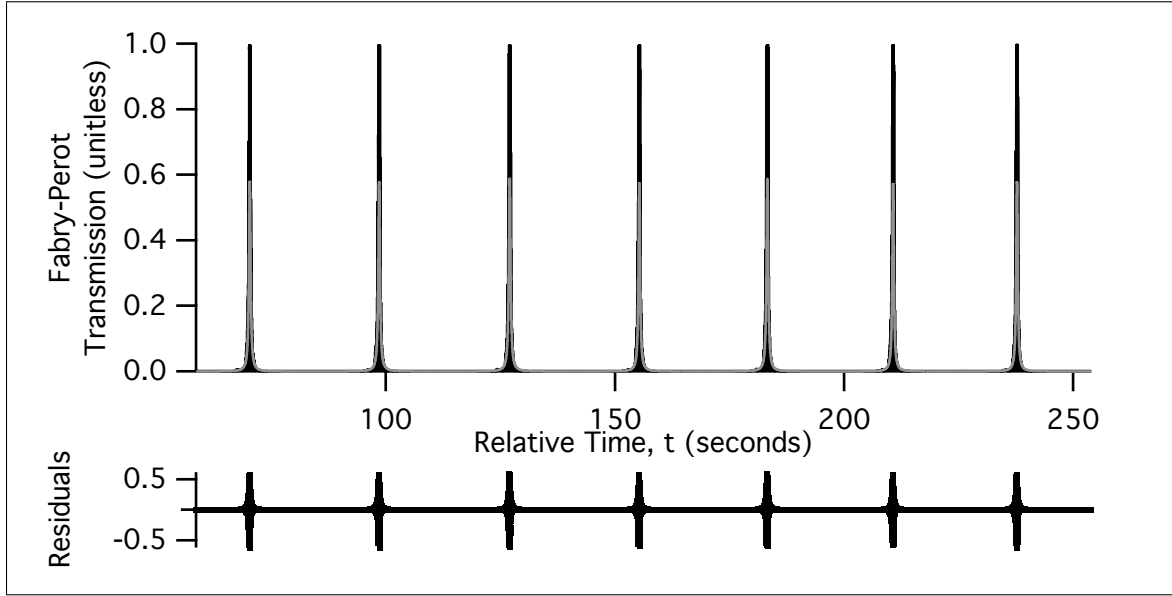


Figure 10. Fabry-Perot transmission fit, where the signal is (—) and the fit is (---).

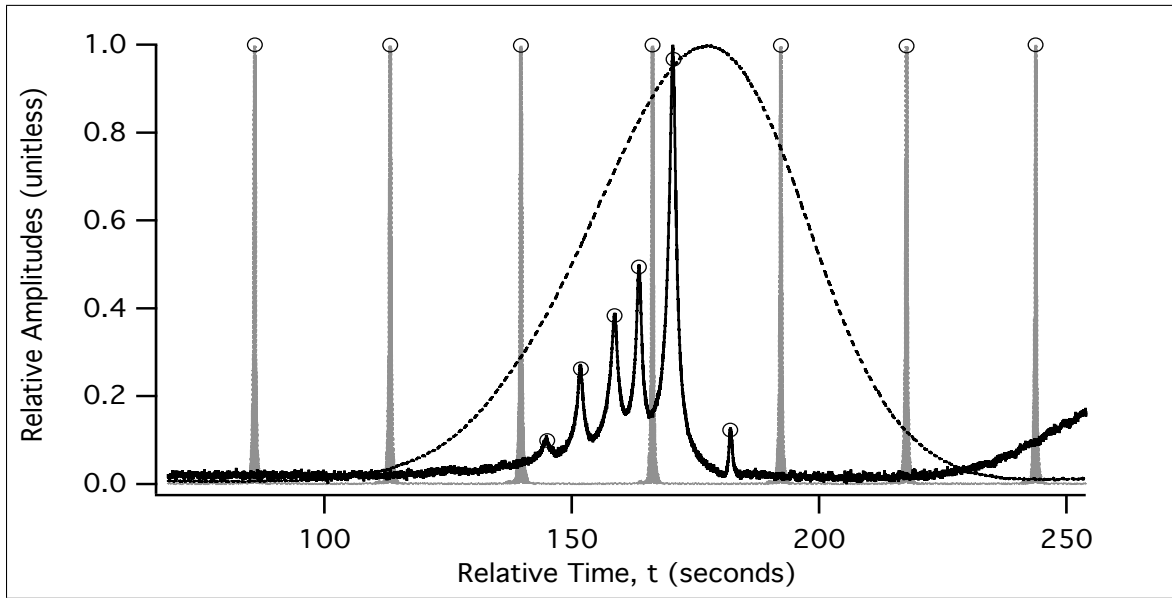


Figure 11. A sample data set, where the probe beam transmission is (—), the reference cell absorbance, $\ln(I/I_o)$, is (---), the Fabry-Perot transmission is (···), and the peak locations of the Fabry-Perot and probe beam signals are (o). The rising right baseline of the probe beam transmission is from the rubidium 85 isotope. The probe beam transmission is divided by the incident intensity signal and the frequency axis, ν , is relative, ν_r , to the ^{87}Rb D_2 transition.

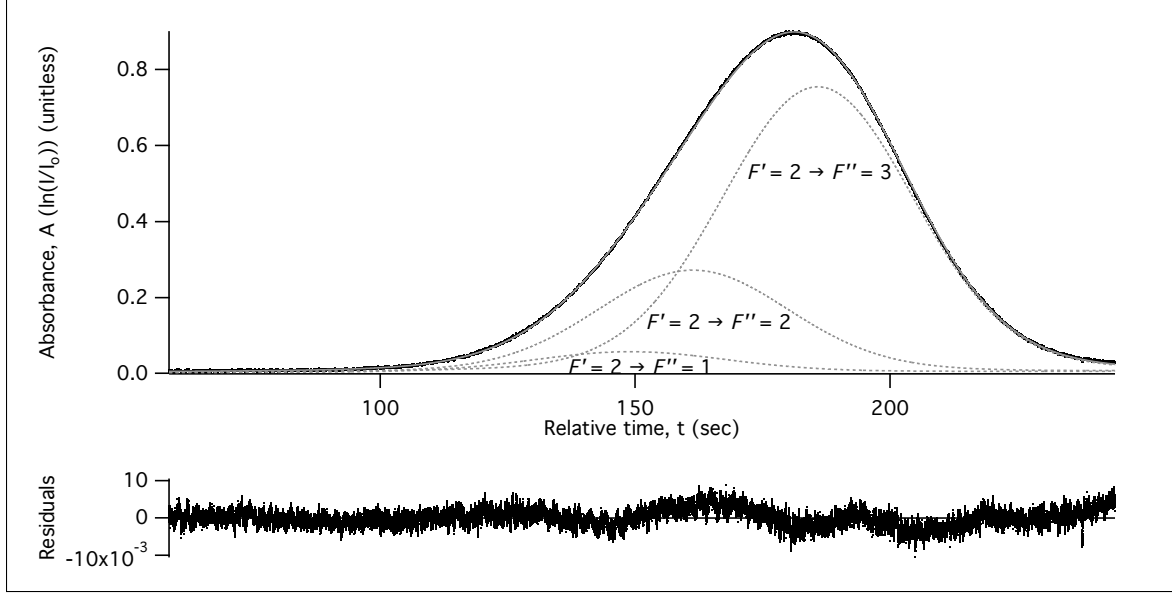


Figure 12. Fit of the ^{87}Rb reference cell absorbance, where the data is (—) and the fit is (---). Since the residuals are on the order of 10^{-3} , the fit line masks the data.

fit. Also, the relative amplitudes of each line is fixed based on the ratio given by their line strengths, Appendix A. The hyperfine peaks that were selected are allowed to move \pm a second, corresponding to ± 10 MHz based on the laser scan rate. A rough estimate based on the known locations in time of the resolved hyperfine is used to estimate the location of the unknown hyperfine peak for initial guess of the fit. The remaining variables are the homogenous width, overall amplitude, and a linear baseline. The residuals are on the order of one part in a thousand. A plot of the reference cell absorbance and fit with residuals can be viewed in Fig.12. A sample data set can be seen in Fig.11 with all the peaks located. After the fit, any unknown cross-over resonance location in time is estimated by the knowing the fact that they are halfway between two hyperfine lines and assuming that the laser scans linearly. Next, the Fabry-Perot peaks must be translated into frequency. Taking the Fabry-Perot peak that is closest to a hyperfine or cross-over line, the peak frequency is calibrated using the equation

$$\nu_{FP'} = \nu_i - (t_i - t_{FP'}) \frac{\nu_i - \nu_j}{t_i - t_j}, \quad (9)$$

where $t_{FP'}$ is the location in time and $\nu_{FP'}$ is the frequency of the Fabry-Perot peak that's closest to a hyperfine or cross-over resonance, t_i is the location in time and ν_i is the frequency of the hyperfine or cross-over resonance closest to a Fabry-Perot peak, and t_j is the location in time and ν_j is the frequency of the next closest hyperfine or cross-over resonance. All other Fabry-Perot peaks are 300 MHz apart, given by the free spectral range of the Fabry-Perot interferometer, and assigned a frequency relative to the frequency calibrated in Eq.9. Once all the Fabry-Perot peaks, hyperfine peaks, and cross-over peaks are estimated in time and frequency, a line is fitted to a plot of frequency versus time. Below is a plot of the frequency versus time fit. The frequency is relative to the ^{87}Rb D_2 line. The calibration near the hyperfine frequencies are \pm a few MHz while the wings are on the order of ± 10 MHz. The wings of the spectrum have a larger residuals because the wings are based on the locations Fabry-Perot peaks in frequency, which is dependent on the accuracy of the free spectral range of the Fabry-Perot interferometer. This is expected since the free spectral range of the Fabry-Perot interferometer is not calibrated. The degree of precision of this frequency axis is sufficient since fits do not show a dependence of the frequency axis. To remove any spectra from the ^{85}Rb $F'' = 3$ lines and to reduce fitting computations, the data is sectioned again from -3300 MHz to -2000 MHz. Coincidentally, this also increases the certainty of the frequency axis since this section occurs where the residuals are the smallest. In Fig.14, the probe beam transmission, reference cell absorbance, and theoretical Lorentzian spectrum is plotted along with transition labels to orientate the reader to the ensuing observed spectra fits being discussed.

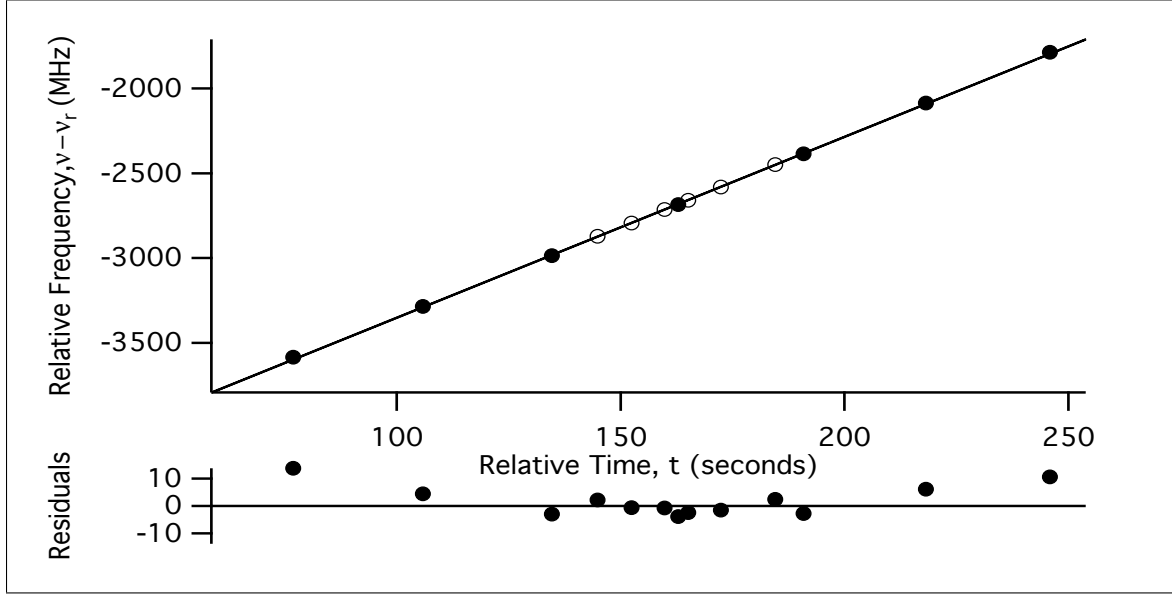


Figure 13. Frequency axis calibration by plotting peaks of the hyperfine and cross-over resonances (o) and Fabry-Perot peak locations (●) in frequency versus time. The line is the conversion equation from time to frequency. The frequency axis is a relative frequency, ν_r , from the ^{87}Rb D_2 line.

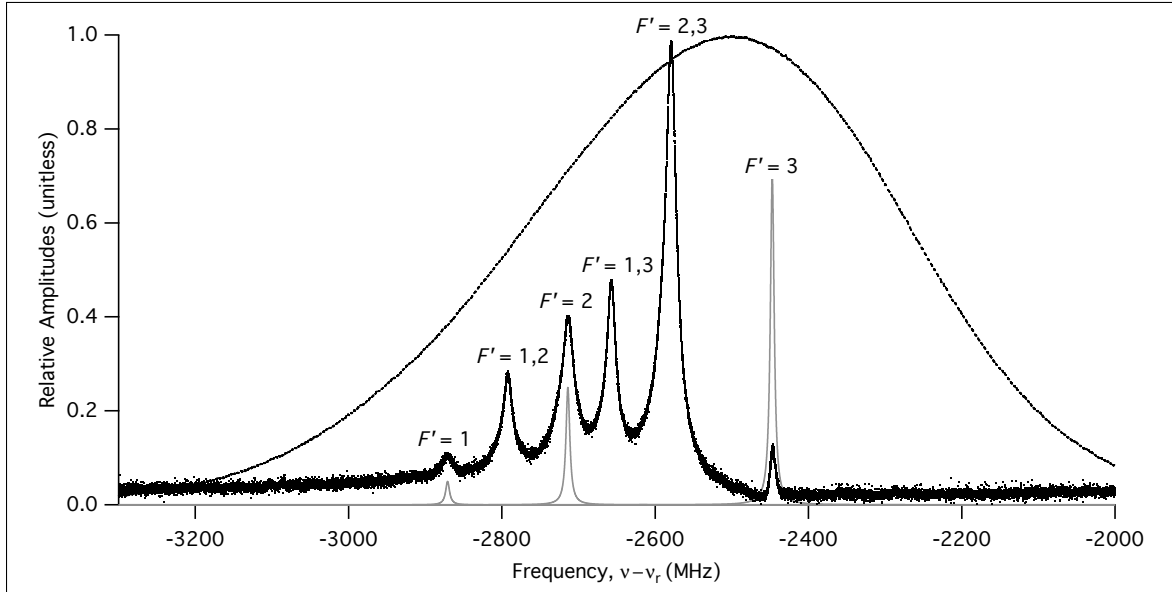


Figure 14. A sample data set, where the probe beam transmission is (●), the reference cell absorbance, $\ln(I/I_0)$, is (---), and the theoretical Lorentzian spectrum of the hyperfine transitions is (—). The F' numbers, total angular momentum of orbital, electron and nuclear spin, are given of the excited state, where the cross-over resonances are given by the F' states they are between. The theoretical Lorentzian profile is a unit amplitude Lorentzian with their respective line strengths. The probe beam transmission is relative to the incident beam intensity and the horizontal axis is the laser beam frequency (ν) relative to the ^{87}Rb D_2 transition (ν_r).

4.2 Empirical Study

To understand how pump and probe intensity effect the collected signal, an empirical study was carried out prior to the experiment. In this study, data was collected at zero argon concentration and a pump beam chopping frequency of 1100 Hz while varying the pump beam power at a constant probe beam power and vice versa. Fig.15 shows spectra at a probe beam power of $2 \mu W$ while varying the pump beam power. It is apparent that increasing pump power gives a stronger signal, however when the signal amplitudes are normalized in the bottom plot of Fig.15, the pump also significantly broadens the narrow resonances due to power broadening. Therefore, a pump power of $50 \mu W$, or pump intensity of $6.4 \frac{mW}{cm^2}$, was chosen for best resolution while still being above the saturation intensity ($I_{sat} \sim 5 \frac{mW}{cm^2}$). Furthermore, the data was fitted using a similar equation to Eq.(5), which will be described later. The resulting line widths are plotted versus pump power in Fig.16. The plot was fitted using the equation from a similar experiment done by Akulshin et. al. [1],

$$\gamma = \gamma_n(1 + \sqrt{1 + I/I_{sat}})/2 + \Delta\nu_{rd}, \quad (10)$$

where γ is the fitted line width, γ_n is the natural line width of rubidium, I is the pump beam intensity, I_{sat} is the saturation intensity, and $\Delta\nu_{rd}$ is the residual Doppler width. In the fit, γ_n is held constant to the rubidium natural line width ($\sim 6 MHz$) and I_{sat} and $\Delta\nu_{rd}$ are varied. The fit resulted in a I_{sat} of $1.99 \pm 0.02 \frac{mW}{cm^2}$ and a $\Delta\nu_{rd}$ of $15.17 \pm 0.06 MHz$. Since $\Delta\nu_{rd} = \theta\Delta\nu_D$, where θ is crossing angle of pump and probe beam and $\Delta\nu_D$ is the Doppler width, calculated to be about 508 MHz, then the crossing angle of the pump and probe beam is 1.71° . Also from Fig.16, there might be a trade-off between the Lorentzian line width and the collisional fit parameter, C .

Alternatively, the pump beam power was held constant at $50 \mu W$ and data was

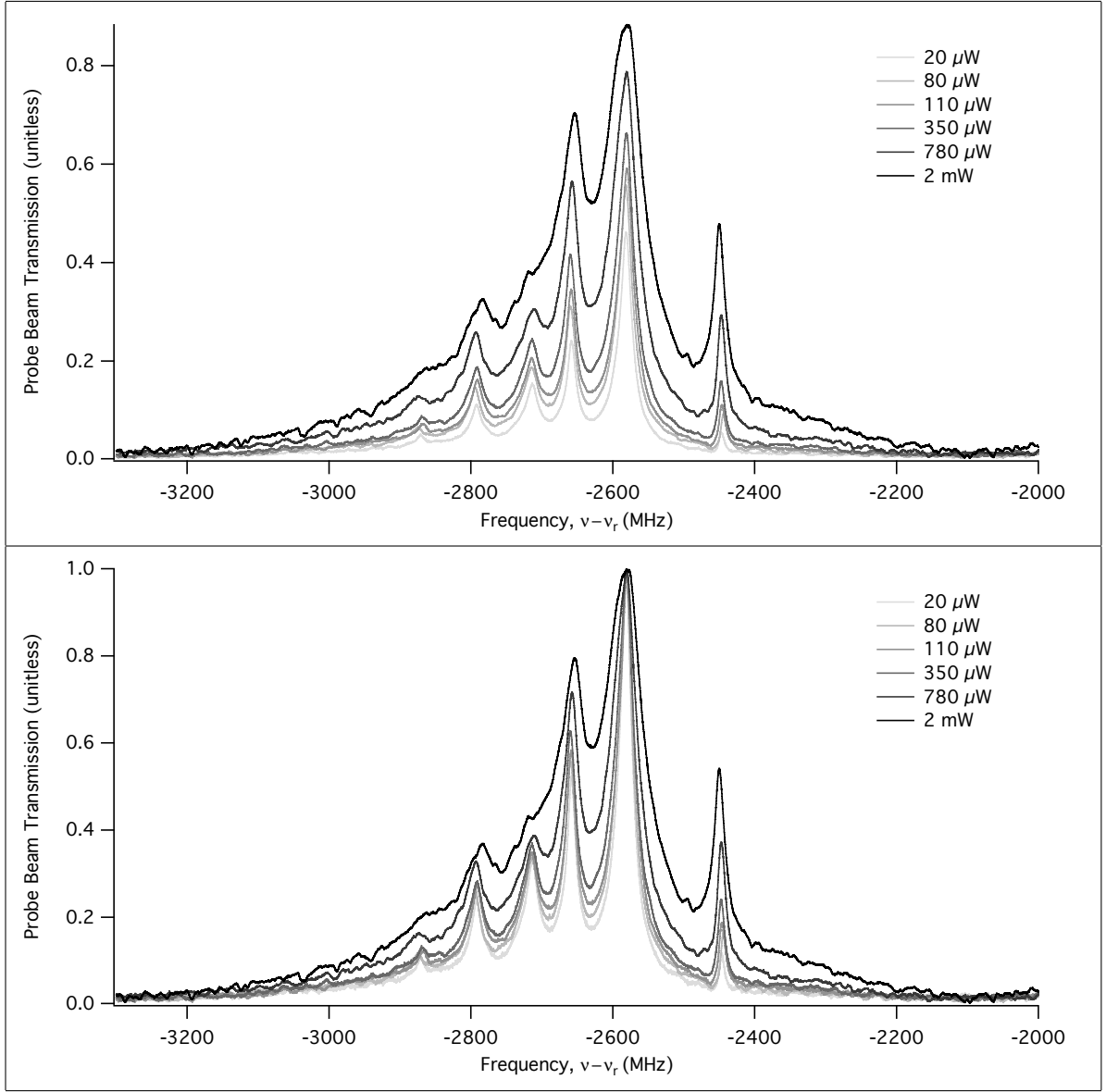


Figure 15. Empirical study data at 0 mTorr of Argon, 1100 Hz chopping frequency, $2 \mu\text{W}$ probe power, and varying pump power where the top plot is the raw data and bottom plot is amplitude normalized. The probe beam transmission is relative to the incident beam intensity and the horizontal axis is the laser beam frequency (ν) relative to the $^{87}\text{Rb } D_2$ transition (ν_r).

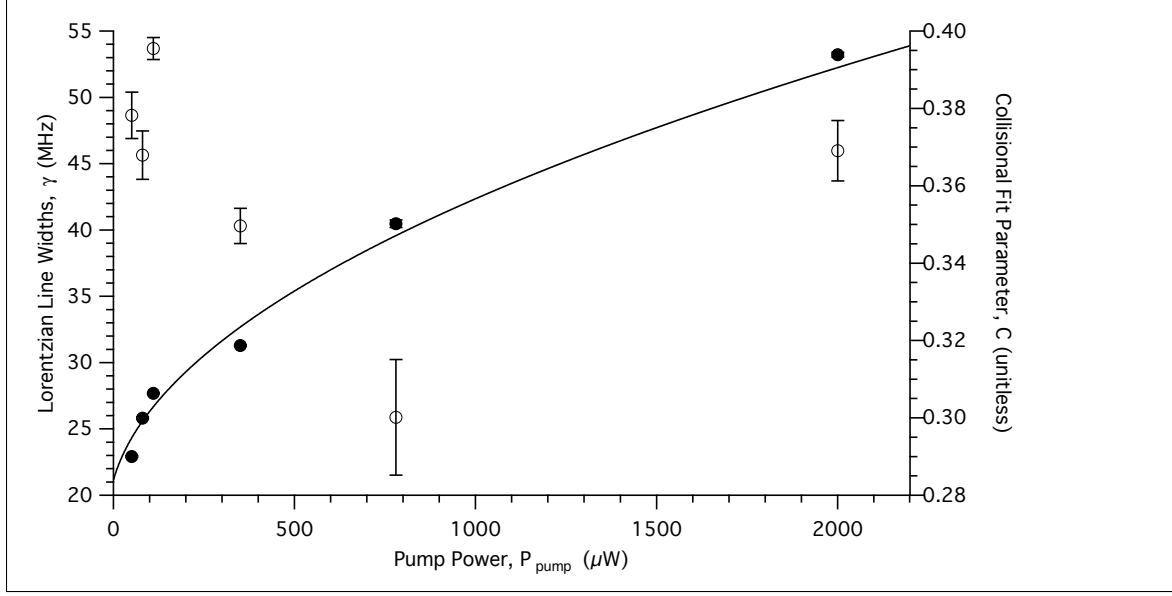


Figure 16. Lorentzian line width (●) and fit parameter, C , (○) versus pump power. A line is fitted to the Lorentzian line width to find the power broadening.

collected at varying probe beam powers. In Fig.17, the data shows that a decrease in probe power increases the signal. This can be explained by how the lock-in amplifier outputs the collected signal. The lock-in produces the differential signal of the probe beam between when the pump beam is blocked and unblocked. When the pump beam is blocked, increasing the probe beam increases the amount of light that is transmitted through the vapor. However, the amount of the probe beam that is transmitted when the pump beam is blocked isn't as affected by the incident probe beam intensity. Therefore, a smaller difference is observed when the probe beam power is increased. When the data is normalized in the bottom plot Fig.17, it is very apparent that the probe beam causes no power broadening. Therefore, the lower probe beam power that could be accurately measured, $2 \mu\text{W}$, or $0.25 \frac{\text{mW}}{\text{cm}^2}$, was decided to be used. It is acknowledged that this might not as weak of probe beam that should be used [39], but a weaker probe beam than this (on the order of 100's of nW) results in the inability to measure it accurately. The data was fitted and the Lorentzian line widths and collisional fit parameter, C , is plotted versus probe beam power in

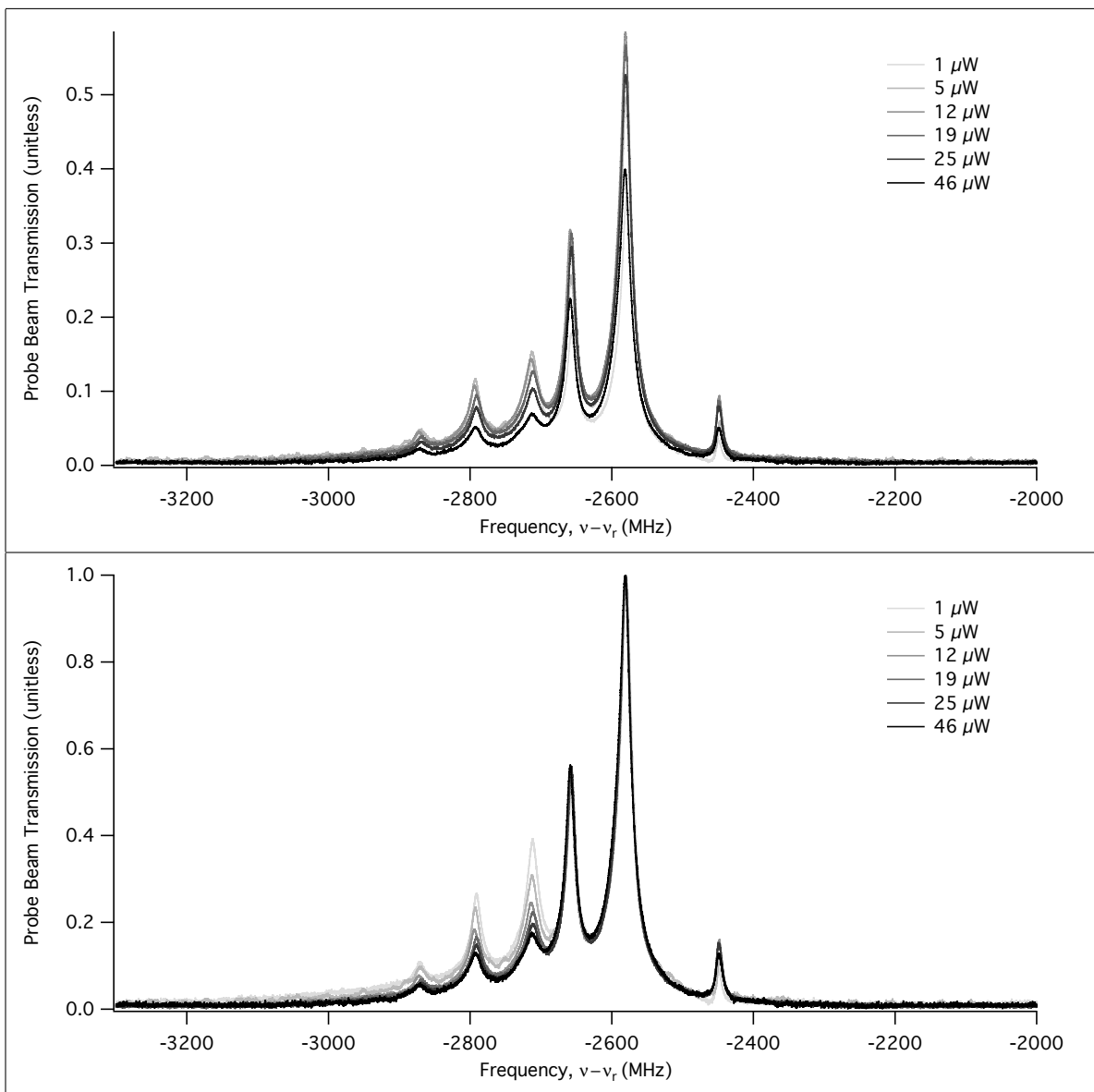


Figure 17. Empirical study data at 0 mTorr of Argon, 1100 Hz chopping frequency, $2 \mu W$ probe power, and varying probe power where the top plot is the raw data and bottom plot is amplitude normalized. The probe beam transmission is relative to the incident beam intensity and the horizontal axis is the laser beam frequency (ν) relative to the $^{87}\text{Rb } D_2$ transition (ν_r).

Fig.18. Again, the plot shows a possible trade-off between the Lorentzian line width and collisional fit parameter. This is accounted for and will be explained in the next section.

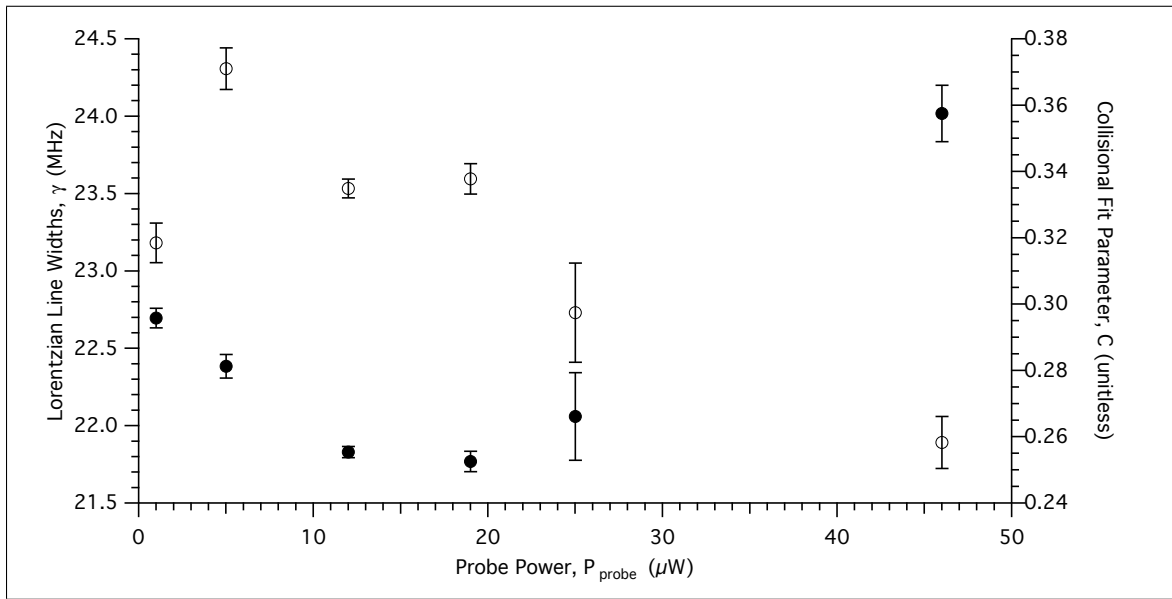


Figure 18. Lorentzian line width (●) and fit parameter, C , (○) versus probe power.

4.3 Initial Fits

First of all without fits, the data show the relationships as expected in Fig.19. An increase in argon concentration increases the Doppler pedestal and an increase in pump beam chopping frequency removes some of the Doppler pedestal. Next, the probe beam transmission is fitted using the following equation for each hyperfine and cross-over line,

$$\mathcal{S}(\nu, \nu_o) = A(\mathcal{L}(\nu, \nu_o) + C\sqrt{2}\mathcal{D}(\nu, \nu_o))\mathcal{D}(\nu, \nu_o), \quad (11)$$

where $\mathcal{L}(\nu, \nu_o)$ is the Lorentzian, as described by Eq.(24), $\mathcal{D}(\nu, \nu_o)$ is the Doppler profile, as described by Eq.(22), A is the amplitude of the hyperfine or cross-over line and C is the collisional fit parameter. This is the same form as Eq.(4, 5), except the Lorentzian and Doppler profiles are unit area normalized inside the parenthesis and the Doppler profile outside the parenthesis is unit amplitude normalized. A $\sqrt{2}$ is multiplied by C to normalize the Doppler squared term. All the fits allowed the hyperfine and cross-over line frequencies to move ± 5 MHz. The Doppler width was calculated using Eq.23 to be 508 MHz at 26° C and was held constant. The data at zero argon pressure allowed the Lorentzian line width to vary. The subsequent spectra with some argon concentration had a fixed Lorentzian line width, calculated to be the average Lorentzian line width of the zero pressure fits, ~ 22 MHz; which is about four times the natural line width, ≈ 6 MHz. This was done to negate any Lorentzian line width and collisional fit parameter trade-off. When the fits were performed without this precaution, Lorentzian line widths from the fits were as large as 35 MHz at 110 mTorr of argon. Typical pressure broadening rates are about 20 MHz/Torr [34; 33]. Therefore broadening of the Lorentzian line width over 0.1 Torr isn't conceivable and the precaution must be done. Also, a baseline was added to remove any residual spectra from the wings of $^{85}\text{Rb } F'' = 3$. A probe beam transmission fit is shown

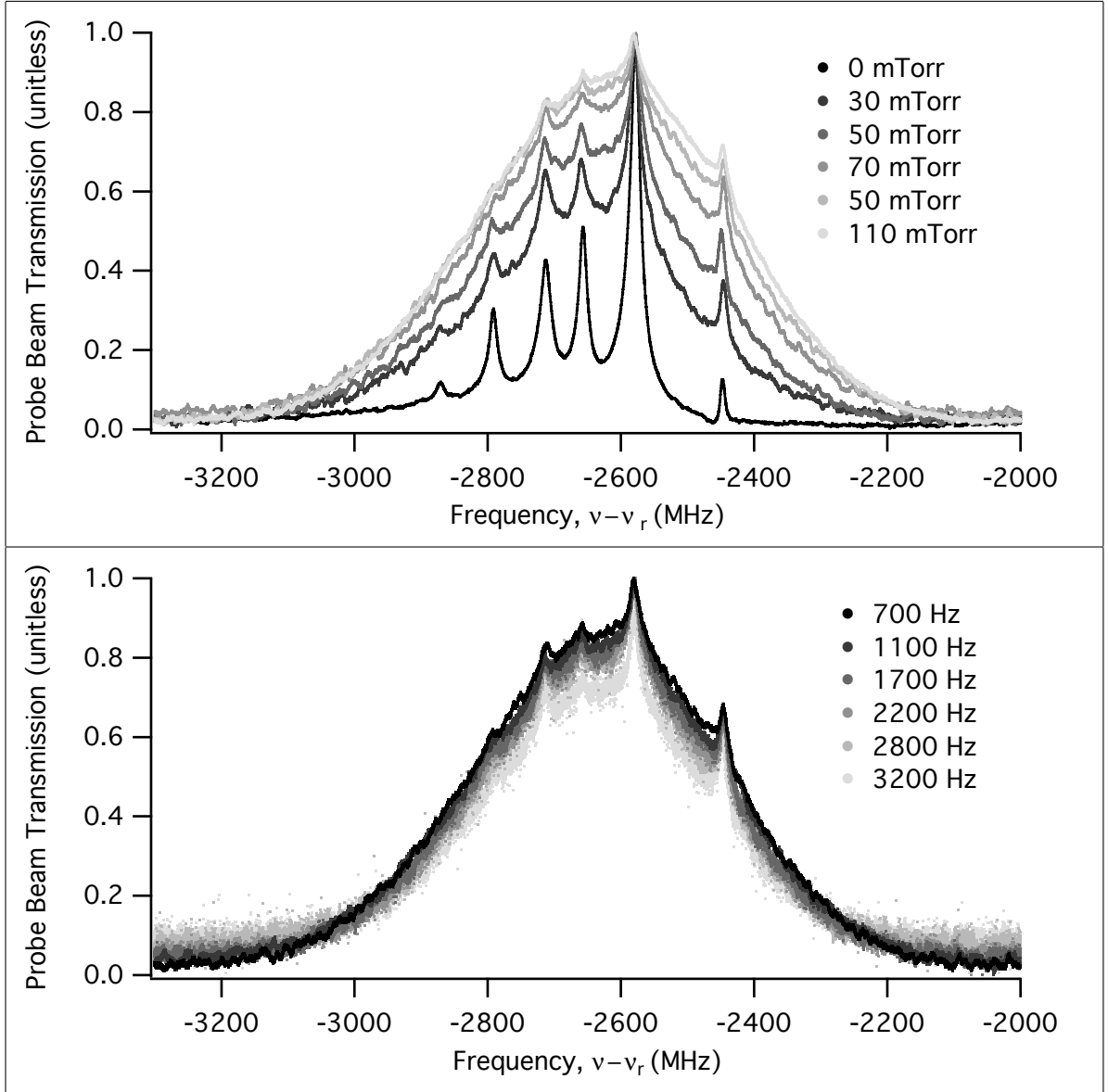


Figure 19. Data plot at a chopping frequency of 700 Hz with varying argon concentration (Top) and an argon pressure of 90 mTorr with varying pump beam chopping frequency (Bottom). Both are amplitude normalized. The vertical axis is the probe beam transmission relative to the incident beam intensity and the horizontal axis is the laser beam frequency (ν) relative to the ^{87}Rb D_2 transition (ν_r).

below in Fig.20 at zero argon concentration. The rest of the probe beam transmission fits and fit parameter results can be seen in Appendix B.

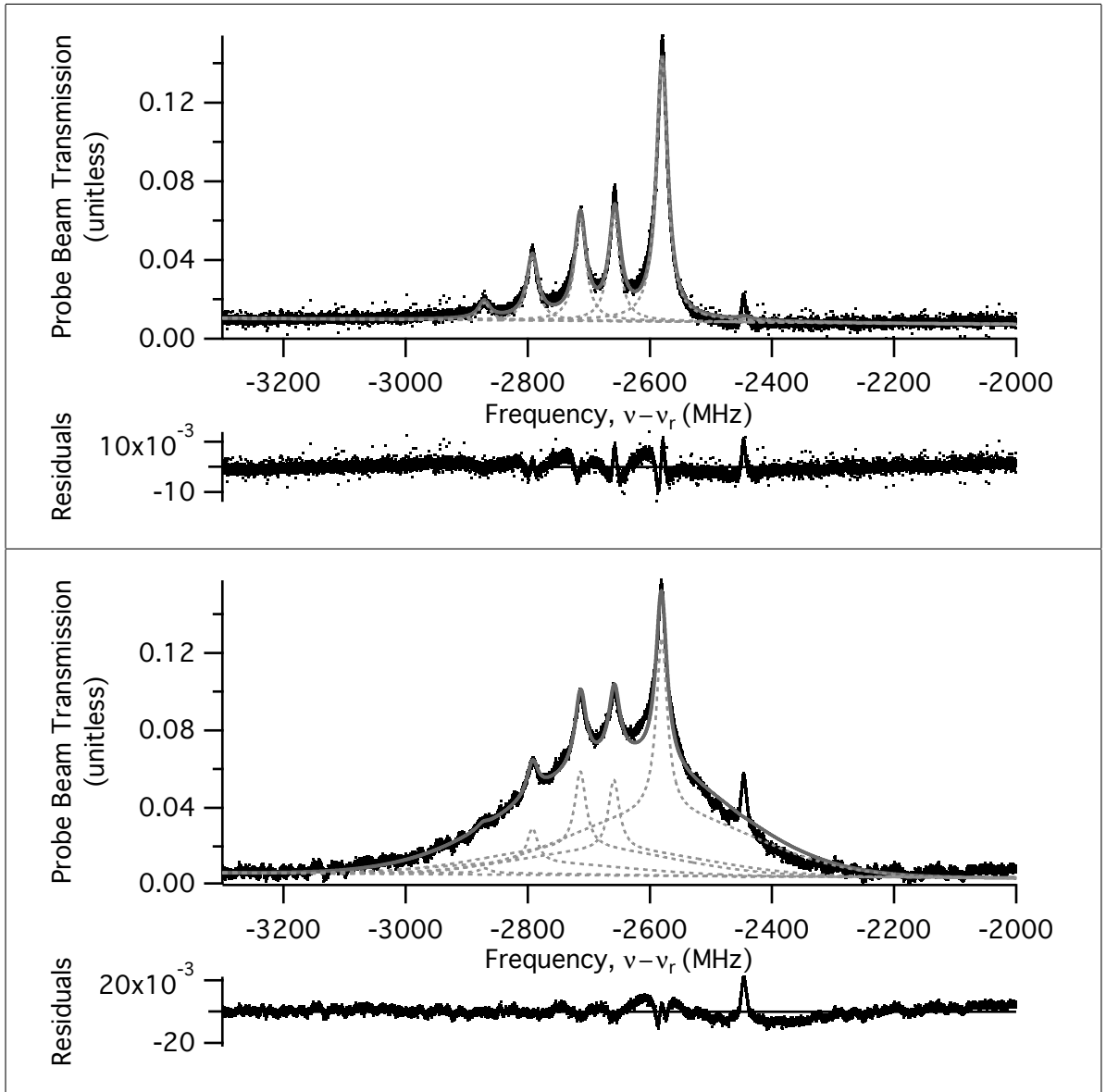


Figure 20. A probe beam transmission fit at 0 mTorr of argon and 2800 Hz pump beam chopping frequency (Top) and at 30 mTorr of argon and 1700 Hz pump beam chopping frequency (Top) and, where the data is (\bullet), the fit is ($-$), and the individual line fits are ($- -$). The probe beam transmission is relative to the incident beam intensity and the horizontal axis is the laser beam frequency (ν) relative to the $^{87}\text{Rb } D_2$ transition (ν_r).

As can be seen in the fits, there is structure in the residuals and the right most peak, $F' = 3$, is always neglected. The structure in the residuals exemplify the fact that the line shape is only an approximate line shape. Excluding the right peak for a fit in Fig.21 shows that residual structure is still apparent when the right most peak is absent. This is not a surprise since the fits are problematic. The initial fit coefficients must be near the final fit coefficients for the fits to converge. Also, different initial fit coefficients can yield slightly different final fit coefficients. Because of these difficulties, more insight is needed to resolve these issues.

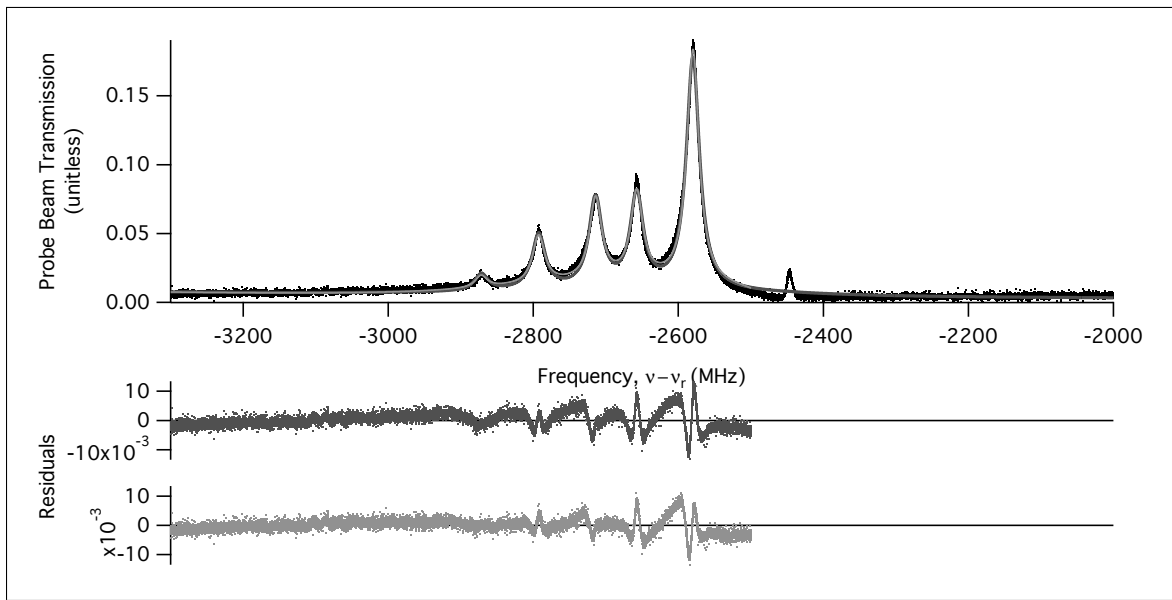


Figure 21. A probe beam transmission fit at 0 mTorr of argon, where the data is (\bullet), the full data fit is in (\bullet) and the partial fit from -3300 MHz to -2500 MHz in (\bullet). The probe beam transmission is relative to the incident beam intensity and the horizontal axis is the laser beam frequency (ν) relative to the ^{87}Rb D_2 transition (ν_r).

4.4 Line Shape Problem

Going back to Fig. 14, the right most peak is the strongest transition. Naively, we would expect the sub-Doppler hyperfine peaks to be proportional to their line strengths and the cross-overs to the sum or average of the two hyperfine peaks in between. This is true for all the peaks except for the right most peak. Further insight in the study by Akulshin et. al. [1], shows similar results in their study. The reason for this is because that peak is a "cycling" transition. For the other two hyperfine transitions, $F'' = 2 \rightarrow F' = 1, 2$, they can relax to either of the ground state hyperfine levels, $F'' = 1 \text{ or } 2$. However, for the $F'' = 2 \rightarrow F' = 3$ transition, the optical transition rule, $\Delta F = \pm 1$, only allows the $F' = 3$ hyperfine state to relax to the $F' = 2$ hyperfine state. In Fig. 22 illustrates the excitation and relaxation paths of the hyperfine transitions. This problem is often referred to as hyperfine pumping, where the individual hyperfine transitions must be considered [42]. This means that the far right transition has a much higher saturation intensity than the other hyperfine transitions. The observed data shows that in the experiment, the far right transition wasn't completely saturated. Furthermore, this means that each hyperfine transition, and cross-over resonance, has a different saturation intensity and therefore power broaden differently. In the fits, each line has the same Lorentzian line width. The fits were tried with a different Lorentzian line width for each transition, however the fits never converged or converged with much less eye-pleasing results.

Some theoretical saturation line shape papers [1; 8; 10; 23; 50] show that the Lorentzian profile in the fits is actually the sum of the two Lorentzians, one Lorentzian from the absorbed probe beam photon and one power broaden Lorentzian from the pump beam photon. Although, no experimental work has been done to prove this quantitatively. This line shape was attempted and all attempts failed to converge. The title of this section is actually borrowed from a section in *Introduction to Nonlin-*

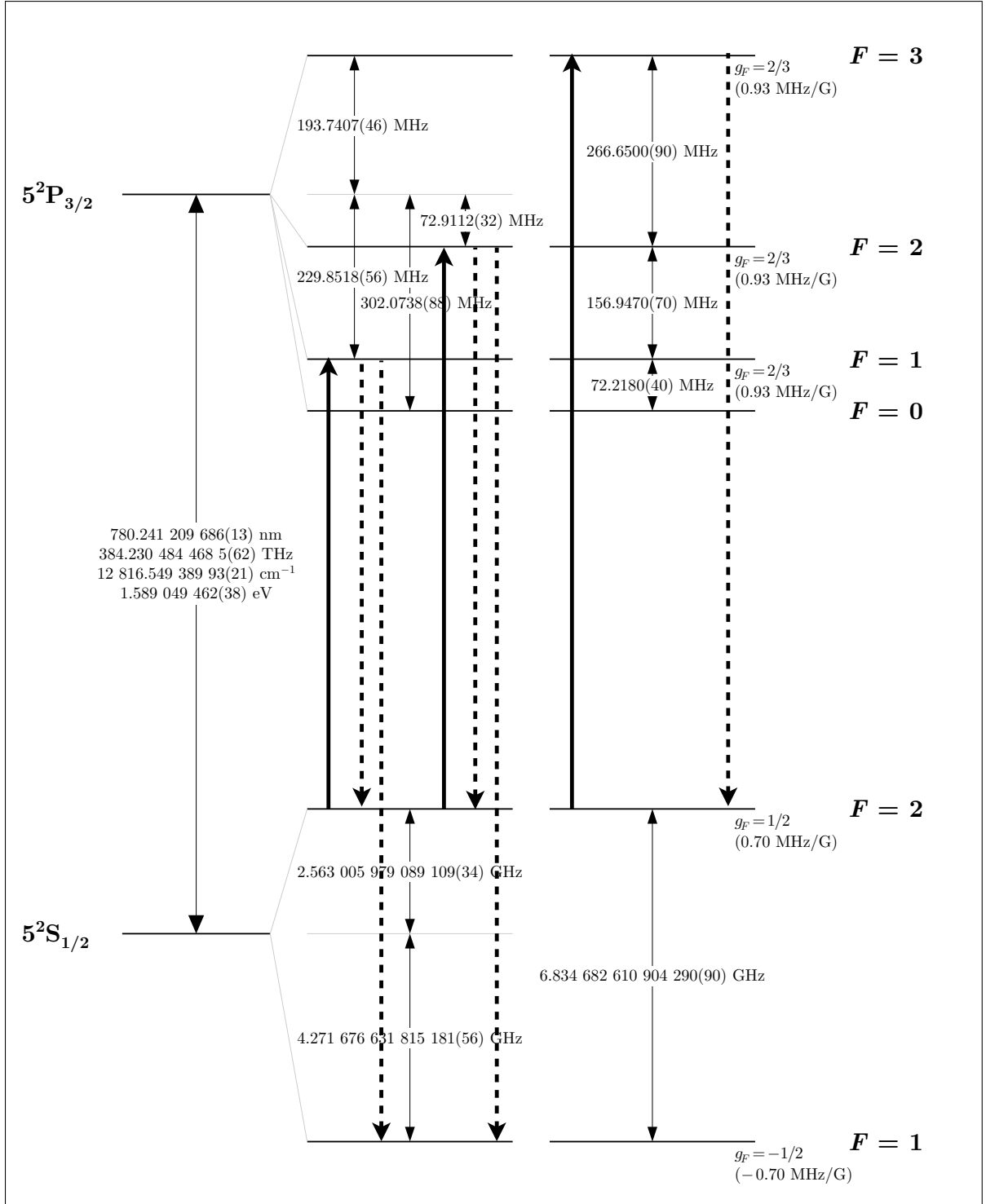


Figure 22. The hyperfine spacing of ^{87}Rb D_2 transition. The absorption hyperfine transitions are solid arrows and the relaxation transitions are the dashed arrows.

ear Laser Spectroscopy [29]. In the section, the text book discusses the complexities that a good approximate line shape for saturation spectroscopy would have result from relativity and complex quantum mechanics. With what is currently known, only rough approximate line shapes for saturation spectroscopy are available. Regardless of the line shape, the line shape fit is merely measuring the amount of collisions. As long as the fits are able to extract the collision information, the fits are accomplishing the purpose of this work. To prove this, a second, simple line shape is fitted to the all data.

4.5 A Second Fit

Looking at the physical shape of the collected probe beam transmission signals, the signal appears to have a crude line shape of a single Gaussian with six Lorentzians on top. Therefore, the second, simple line shape that is fitted to the data is

$$\mathcal{S}(\nu) = A_{\mathcal{D}}\mathcal{D}(\nu, \nu_{\mathcal{D}}) + \sum_i A_i \mathcal{L}(\nu, \nu_i), \quad (12)$$

where $A_{\mathcal{D}}$ is the amplitude and $\nu_{\mathcal{D}}$ is the line center of the Doppler profile ($\mathcal{D}(\nu)$), as described by Eq.(22), and A_i is the amplitude and ν_i is the center line position for each resonance of the Lorentzian Profile, $\mathcal{L}(\nu, \nu_i)$, as described by Eq.(24) except that it is unit amplitude. The Lorentzians are treated the same as before: floating line positions ± 5 MHz, floating amplitudes, and the spectra with some argon concentration have a constant Lorentzian line width of the average Lorentzian line width of the zero pressure spectra fits. Also, a linear baseline is added just as before. In Fig.23 and 24, data at two different argon concentrations with a comparison of both fits are shown. The rest of the second fits along with the second fit parameters results can be viewed in Appendix B. The residuals display similar structure, showing that this line shape is suffers similar deficiencies as the first. The individual resonance lines of the second fit epitomizes the idea of the "Doppler pedestal". The fits are somewhat better than the first and fit the right most peak better. However, this only because this line shape has more degrees of freedom than the other. Since the collisional fit parameter, C , in the Eq.(11) is, in essence, the ratio of the Doppler profile area to the Lorentzian profile area, the same can be calculated for the second fit. The area of Doppler profile is

$$A_{\mathcal{D}} = \frac{A_{\mathcal{D}}\Delta\nu_{\mathcal{D}}}{2} \sqrt{\frac{\pi}{\ln(2)}}, \quad (13)$$

where $A_{\mathcal{D}}$ is the Doppler profile amplitude and $\Delta\nu_{\mathcal{D}}$ is the Doppler line width of the second fit. The area of a amplitude normalized Lorentzian is

$$A_{\mathcal{L}} = \Gamma \frac{\pi}{2} \sum_i A_i, \quad (14)$$

where A_i is the amplitude of each resonance and γ is the Lorentzian line width. Therefore, the collisional fit parameter for the second fit is

$$C = A_{\mathcal{D}}/A_{\mathcal{L}}. \quad (15)$$

4.6 Initial Hard Collision Rate Calculation

To have an estimate of the velocity-changing collision rate, a theoretical rate is calculated from *Chemical Kinetics and Dynamics* [48]. The chemical kinetic "hard sphere" model is used in

$$\Gamma_{vcc} = \sigma_{vcc}[Ar], \quad (16)$$

where Γ_{vcc} is the collision rate (sec^{-1}), $[Ar]$ is the concentration of the argon, and σ_{vcc} is the collision cross-section given by

$$\sigma_{vcc} = \sqrt{\frac{8\pi k_B T}{\mu}} d^2, \quad (17)$$

where k_B is the Boltzmann constant, T is temperature, μ is the reduced mass of the colliding atoms, and d^2 is the distance between the nuclei of the colliding atoms which is the sum of the two atomic radii. The atomic radii used can be found in *Molecular Theory of Gases and Liquids* [22]. In this work, the collisional rate is wanted in per concentration, so a factor of $k_B T$ is used to divide k_{vcc} . Also, since this experiment only observes collisions that go from the zero-velocity group into all other velocity groups, a factor of the Lorentzian line width, (γ) , to Doppler line width, $(\Delta\nu_D)$, is needed. Therefore, the average Lorentzian line width from the first fits (Eq.(11)) is used and it is 21.86 ± 0.34 MHz and a Doppler line width of 508 MHz is used. To include all of this, the theoretical velocity-changing collision rate, k_{vcc} ($\text{sec}^{-1} \text{mTorr}^{-1}$), is defined as

$$k_{vcc} = \frac{\gamma}{\Delta\nu_D} \sqrt{\frac{8\pi}{\mu k_B T}} d^2, \quad (18)$$

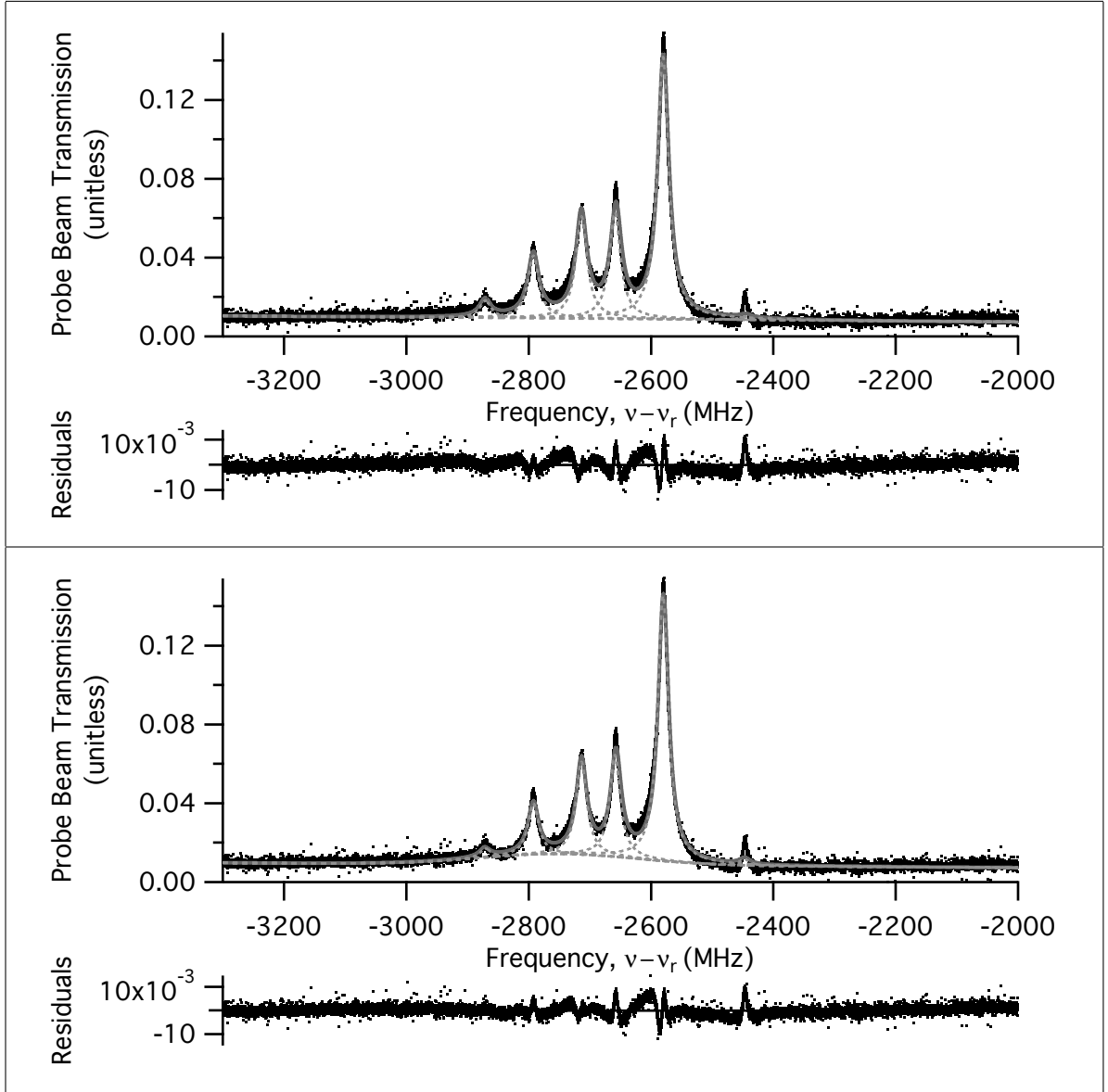


Figure 23. The data has zero argon concentration and a pump beam chopping frequency of 1700 Hz. The top fit use Eq.(11) and the bottom fit use Eq.(12). The data is (\bullet), the fit is (—), and the individual line fits are (---). The probe beam transmission is relative to the incident beam intensity and the horizontal axis is the laser beam frequency (ν) relative to the $^{87}\text{Rb } D_2$ transition (ν_r).

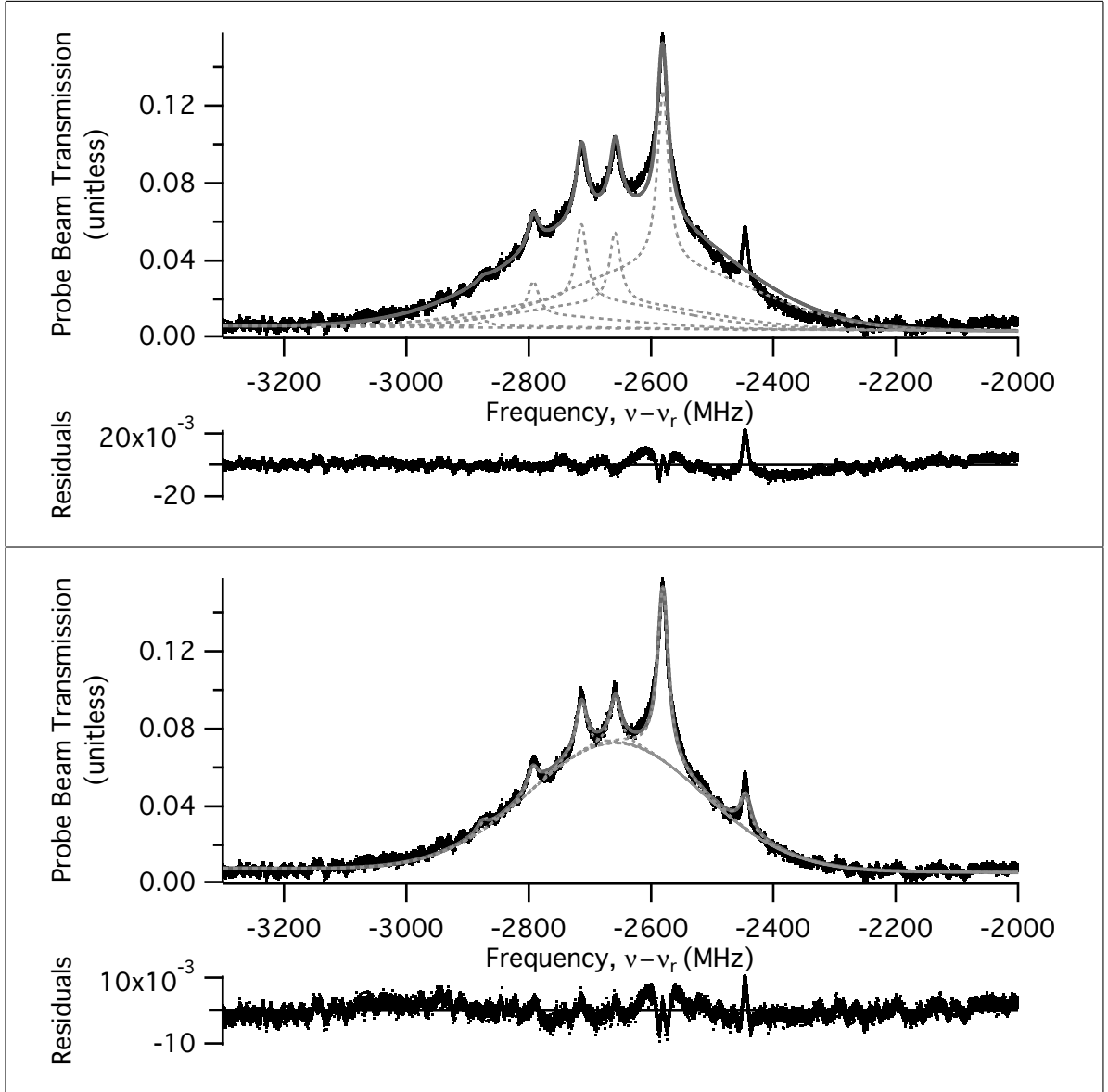


Figure 24. The data has an argon pressure of 30 mTorr and at a pump beam chopping frequency of 1700 Hz. The top fit use Eq.(11) and the bottom fit use Eq.(12). The data is (\bullet), the fit is ($-$), and the individual line fits are ($- - -$). The probe beam transmission is relative to the incident beam intensity and the horizontal axis is the laser beam frequency (ν) relative to the $^{87}\text{Rb } D_2$ transition (ν_r).

which is $872.78 \pm 13.73 s^{-1} mTorr^{-1}$. To calculate the collisional rate for this work, the following equation is used

$$\Gamma_{vcc} = C f_{chop}, \quad (19)$$

where f_{chop} is the pump beam chopping frequency and C is the collisional fit parameter. This is the same formulation as Eq.(6), where the other constants and parameters are to adjust C so that it is the ratio of the Doppler area to the Lorentzian area. The first fit equation, Eq.(11), is refined so that C is the ratio of the Doppler profile to the Lorentzian profile. For the second fit, Eq.(12), C is already calculated to be the ratio in Eq.(15). The values of Γ_{vcc} of each data set for each fit can be seen in Table 1. Plotting Γ_{vcc} versus argon pressure, Fig.25, gives similar results for both line shape fits, which is reassuring that the line shapes are extracting the collisional information. The error bars are greater in the second fit data points because there is more error in collisional fit parameter calculations. Also, the error bars increase with argon concentration, which is attributed to transitions line shapes overlapping so the fitting becomes more vague for each transition at higher pressures. However, both data sets yields velocity-changing collision rates that are much less than the theoretical rate: $k_{vcc} = 416.61 \pm 22.80 s^{-1} mTorr^{-1}$ for the first line shape fit and $k_{vcc} = 402.16 \pm 18.70 s^{-1} mTorr^{-1}$ for the second line shape fit. This is more than half the theoretical rate. Regardless, it is troubling that data points at the same argon pressure yield different Γ_{vcc} . Further insight shows that the data at the same argon pressure are still inversely proportional to pump beam chopping frequency. This means that there is still some limiting time parameter that hasn't been included in the calculations.

Table 1. Initial rate plot data points from Fig.25, where p_{Ar} is the argon pressure in mTorr, f_{chop} is the pump beam chopping frequency in Hz, and Γ_{vcc} is the velocity-changing collision rate (sec^{-1}) calculated from Eq.(19) for each fit.

p_{Ar} (mTorr)	f_{chop} (Hz)	Γ_{vcc} (sec^{-1}) First Fit	Γ_{vcc} (sec^{-1}) Second Fit
0	700	265.45 ± 1.4439	343.55 ± 3.8784
0	1100	340.56 ± 25.023	475.1 ± 93.945
0	1700	368.59 ± 34.078	563.89 ± 123.17
0	2200	293.67 ± 2.4059	531.95 ± 8.3807
0	2800	185.09 ± 3.8902	559.77 ± 13.321
0	3200	147.32 ± 4.4164	564.89 ± 14.877
30	700	3743.1 ± 98.074	3920.7 ± 454.53
30	1100	5330.5 ± 116.77	5410.2 ± 295.16
30	1700	6749.3 ± 87.136	6920 ± 415.78
30	2200	7578.1 ± 81.548	7821.2 ± 397.09
30	2800	9104.8 ± 182.55	9293 ± 908.51
30	3200	9559.6 ± 67.681	9492.2 ± 308.97
50	700	7992.5 ± 131.81	7703.1 ± 629.14
50	1100	11324 ± 246.49	11314 ± 1100.1
50	1700	14845 ± 190.89	13932 ± 765.8
50	2200	17239 ± 255.82	16358 ± 1064.1
50	2800	19370 ± 614.5	18141 ± 2691.5
50	3200	19960 ± 77.591	18026 ± 292.66
70	700	14706 ± 978.5	14686 ± 4252.2
70	1100	19853 ± 600.81	19766 ± 2553.9
70	1700	28652 ± 1726.6	28845 ± 3137.8
70	2200	30728 ± 1404.7	28760 ± 5721.1
70	2800	34970 ± 160.68	33698 ± 622.46
70	3200	37295 ± 1476.3	32442 ± 5465.7
90	700	19851 ± 1759.7	22165 ± 4992.1
90	1100	26953 ± 2241	28790 ± 6059.6
90	1700	38992 ± 2622.2	35447 ± 5403.4
90	2200	42737 ± 1743.9	39027 ± 3620.5
90	2800	50339 ± 1943	47679 ± 4469
90	3200	53978 ± 2253.4	46851 ± 4491.8
110	700	27635 ± 3107.1	30373 ± 8713.5
110	1100	36247 ± 3265.2	40850 ± 9630
110	1700	48000 ± 3749.8	49138 ± 9370
110	2200	55690 ± 3394.5	52586 ± 7434.9
110	2800	64753 ± 4480.5	59738 ± 9562
110	3200	66323 ± 3092.5	61316 ± 6721.2

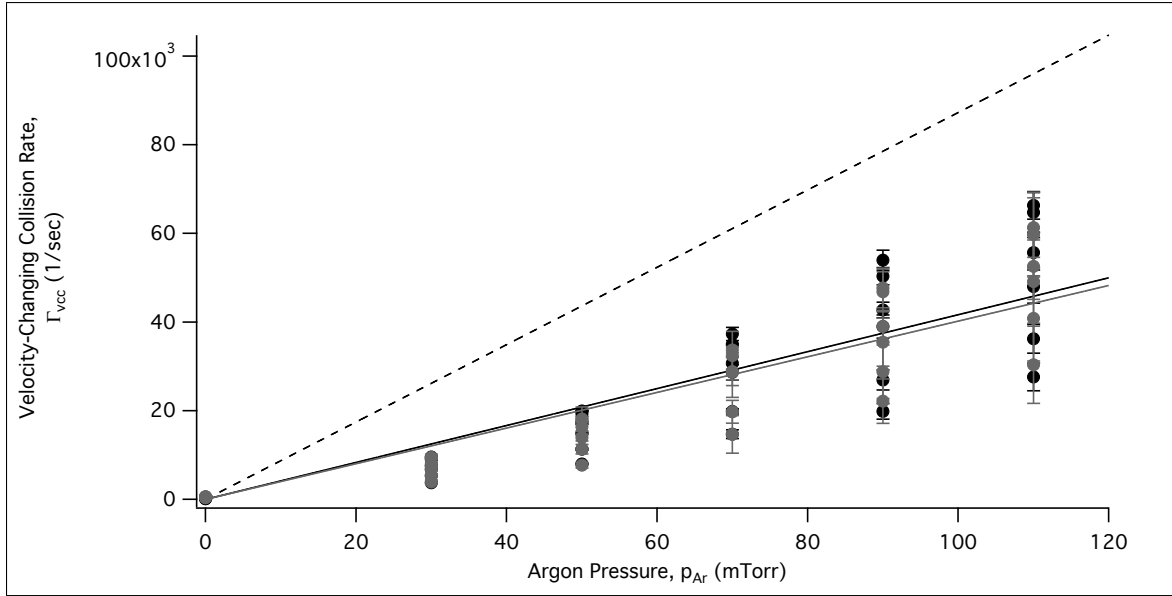


Figure 25. Initial collisional rate Γ_{vcc} versus argon pressure. The first fit, Eq.(11), data points, (\bullet), yields a $k_{vcc} = 416.61 \pm 22.80 s^{-1} mTorr^{-1}$ and the second fit, Eq. (12), data points, (\bullet), yields a $k_{vcc} = 402.16 \pm 18.70 s^{-1} mTorr^{-1}$. The theoretical rate (- - -) is calculated from chemical kinetic "hard sphere" model, which is $872.78 \pm 13.73 s^{-1} mTorr^{-1}$, and the linear fit of the first fits (-) and linear fit of the second fits (-) is fitted without weights and has a y-intercept of zero.

4.7 The Time Scale of Collisions

As stated in Ch.II, the collisional rate will be dependent of chopping frequency, which has been shown, because the chopping frequency shortens the time that is allowed for these collisions to happen. However, we cannot assume that the chopping frequency is the only limiting factor because of the variance in the data at each pressure and previous works have multiple limiting time factors. Even though there is no knowledge or understanding of what other processes would shorten the time scale at which these collision events can happen, we can estimate what the total time these other processes since data was taken at different chopping frequency for a single pressure of argon.

To do this, a term is added to the chopping frequency, so that Eq.(19) now looks like

$$\Gamma_{vcc} = C(f_{chop} + 1/\tau), \quad (20)$$

where τ will be the other processes the shorten the collisional time, which will be also be called the time scaling parameter. Since the collisional fit parameter, C , is inversely related to the chopping frequency, $1/C$ can be plotted versus chopping frequency with a linear fit for each argon pressure. The time scale parameter would be when the pump beam isn't chopped, or when $1/C$ is zero. Another to view this is if the pump beam isn't chopped, then an infinity amount of collisions would be observed and $1/C$ would be zero. Therefore, setting $1/C$, or y , to zero for the linear fit equation $y = ax + b$, the $\tau = a/b$. Similar analysis of $1/C$ vs a limiting time factor has been done before in inter-modulated opto-galvanic saturation spectroscopy experiments [19; 35]. In their case, $1/C$ vs discharge current was plotted to characterize the collision time limiting electron collisions. Below in Fig.26 and 27 , are the plots at a single pressure of $1/C$ versus chopping frequency, f_{chop} .

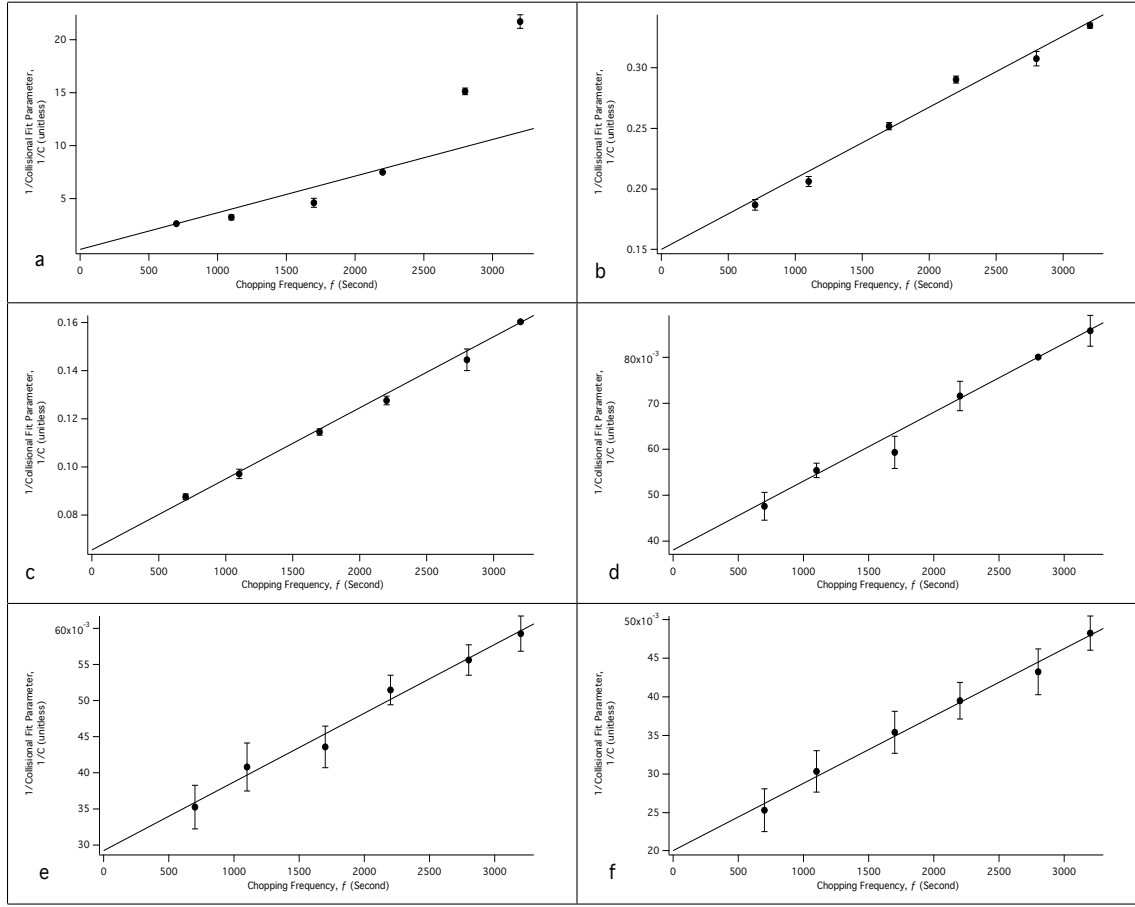


Figure 26. Inverse of the collisional fit parameter, C , versus chopping frequency at different pressures. Argon pressures are follows: a, 0 mTorr; b, 30 mTorr; c, 50 mTorr; d, 70 mTorr; e, 90 mTorr; f, 110 mTorr.

Table 2. The adjustment parameter τ for each fit in Fig.26 and 27, which is the slope of the linear fit divided by the y-intercept.

Argon Pressure (mTorr)	τ (msec) First Fit	τ (msec) Second Fit
0	16.1631 ± 2.1510	1.3516 ± 0.0689
30	0.3895 ± 0.0195	0.4670 ± 0.0943
50	0.4512 ± 0.0153	0.5895 ± 0.1053
70	0.3934 ± 0.0418	0.5421 ± 0.2325
90	0.3255 ± 0.0755	0.5832 ± 0.3066
110	0.4337 ± 0.1156	0.8060 ± 0.5450

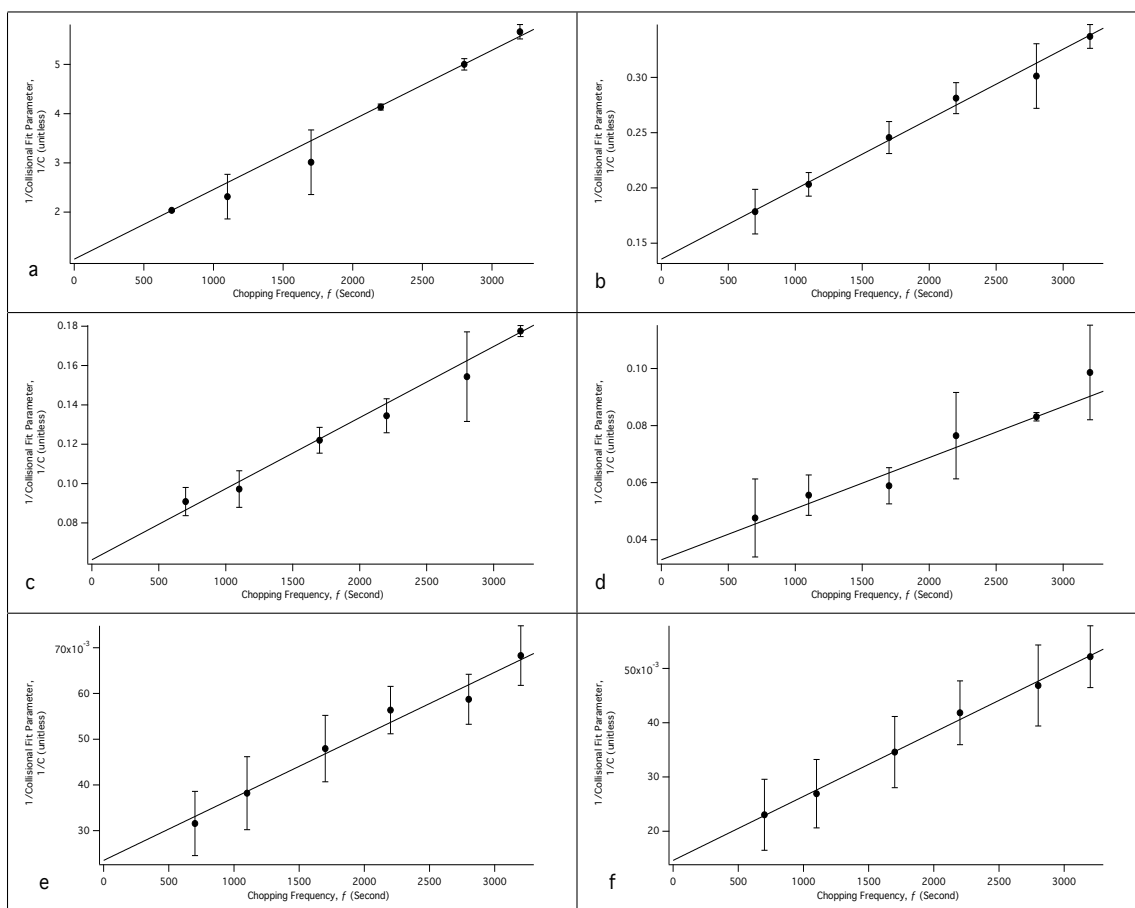


Figure 27. Inverse of the collisional fit parameter, C , versus chopping frequency at different pressures. Argon pressures are follows: a ,0 mTorr; b, 30 mTorr; c, 50 mTorr; d, 70 mTorr; e, 90 mTorr; f, 110 mTorr.

The fits are weighted by the inverse of the standard deviation of the data point. Plot a in Fig.26 points have curvature, which might be attributed to the fact that maybe the chopping frequency at some point between 700 - 3200 Hz be the only limiting time factor. Nevertheless, all C at zero argon pressure are so small that this curvature can be neglected and doesn't effect the rate caculation. Table 2 has the time scaling parameters. It is excepted that τ would decrease as argon concentration increases because mean-free path would decrease as argon concentration increases. In Table 2, that relationship isn't clear. This is most likely due to the deficiencies of the fits, although the zero pressure τ is clearly must longer than the subsequent pressures.

4.8 Final Hard Collision Rate Calculation

In Fig.28, Eq.(20) is used to plot Γ_{vcc} vs argon pressure. The individual data points can be seen in Table 3. The error bars in Fig.28 become larger because of the added uncertainty with the time scale parameter, τ . A linear fit is done for both data sets which is an unweighted fit with a y-intercept set to zero. This is done because the error bars systematically increase with argon pressure, so a weighted fit would strongly favor the points at the lower pressures and effectively lower the calculated rate. The results of the linear fits for the velocity-changing collision rate, k_{vcc} is as follows: $k_{vcc} = 1020.7 \pm 26.3 s^{-1} mTorr^{-1}$ for the first fit using Eq. (11) and $k_{vcc} = 758.81 \pm 13.90 s^{-1} mTorr^{-1}$ for the second fit using Eq. (12). This corresponds to a percent difference with the theoretical $872.78 \pm 13.73 s^{-1} mTorr^{-1}$ of 17% for the first fit and 13% for the second fit. This may be an inadequate method for comparison because some curvature appears in Fig.28. One of the assumptions in this experiment is that a single collision takes an atom from v_z to $-v_z$. However, if it takes multiple collisions for an atom to go from v_z to $-v_z$, then Γ_{vcc} would non-linearly increase with pressure. Therefore, to have a velocity-changing collision rate that is higher than theory would be rational, which is the case for the first fits using the developed line shape in Eq.(11).

Table 3. Final rate plot data points from Fig.28, where p_{Ar} is the argon pressure in mTorr, f_{chop} is the pump beam chopping frequency in Hz, and Γ_{vcc} is the velocity-changing collision rate (sec^{-1}) calculated using Eq. (20) for each fit.

p_{Ar} (mTorr)	f_{chop} (Hz)	Γ_{vcc} (sec^{-1}) First Fit	Γ_{vcc} (sec^{-1}) Second Fit
0	2200	301.93 ± 3.5651	710.85 ± 20.153
0	2800	189.18 ± 4.5176	707.68 ± 24.273
0	3200	150.16 ± 4.8791	695.49 ± 24.89
0	1700	382.01 ± 37.088	809.3 ± 189
0	1100	359.71 ± 28.945	794.66 ± 172.84
0	700	288.91 ± 4.6268	706.67 ± 25.445
30	700	17471 ± 1104.1	15913 ± 4232.6
30	1100	17772 ± 987.93	15941 ± 2977.4
30	1700	16942 ± 715.72	15636 ± 2689.4
30	2200	16422 ± 610.28	15433 ± 2314
30	2800	17453 ± 760.85	16399 ± 3033.4
30	3200	17229 ± 500.18	15843 ± 1794.5
50	700	33298 ± 1337.8	26371 ± 5435.1
50	1100	34139 ± 1477.9	28761 ± 5881.6
50	1700	34198 ± 1075.4	27834 ± 3997
50	2200	34606 ± 1088.6	28971 ± 4126.3
50	2800	34702 ± 1611.6	29131 ± 6277.5
50	3200	33785 ± 593.03	27582 ± 2148.8
70	700	68102 ± 10058	53384 ± 31938
70	1100	65727 ± 6784.5	52912 ± 20987
70	1700	71491 ± 8813.9	60143 ± 19925
70	2200	66228 ± 6770.9	52874 ± 20835
70	2800	66713 ± 3660	55897 ± 10535
70	3200	66918 ± 5780.9	51142 ± 16622
90	700	$1.0697e+05 \pm 29426$	76457 ± 45601
90	1100	$1.0222e+05 \pm 25810$	73666 ± 39011
90	1700	$1.0945e+05 \pm 23610$	71199 ± 29603
90	2200	$1.0241e+05 \pm 17957$	69443 ± 22402
90	2800	$1.0557e+05 \pm 16837$	76875 ± 22531
90	3200	$1.058e+05 \pm 16395$	71955 ± 20078
110	1700	$1.131e+05 \pm 26118$	84996 ± 40408
110	2200	$1.1405e+05 \pm 22462$	82239 ± 31647
110	700	$1.1866e+05 \pm 37353$	84200 ± 60392
110	1100	$1.1222e+05 \pm 30230$	86920 ± 51552
110	2800	$1.1807e+05 \pm 22350$	86205 ± 31673
110	3200	$1.1411e+05 \pm 18033$	85087 ± 25382

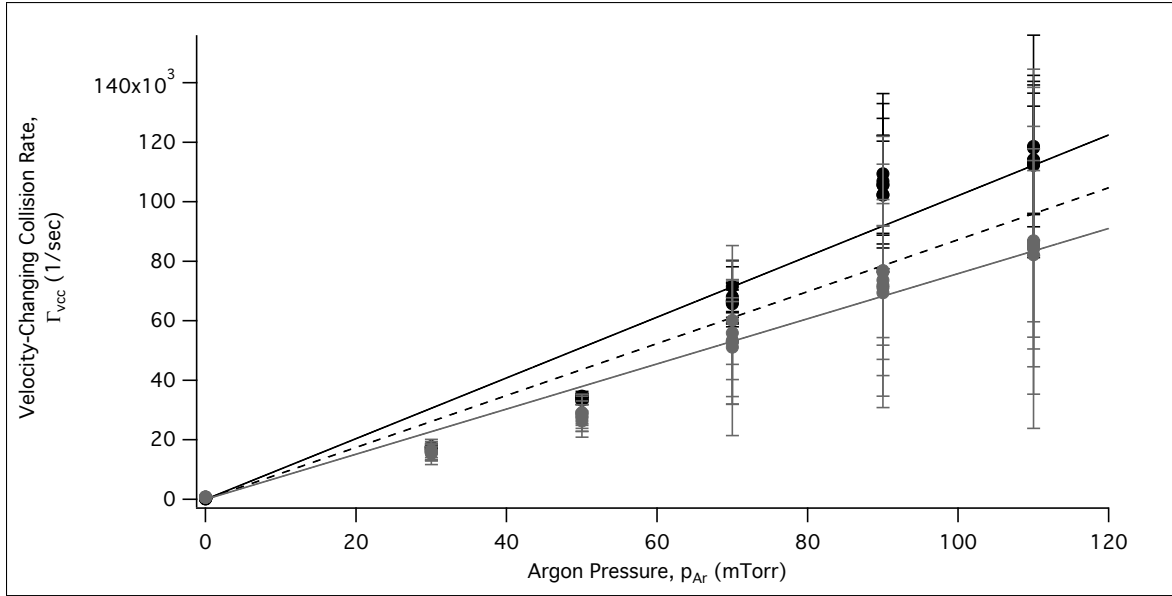


Figure 28. Initial collisional rate Γ_{vcc} versus argon pressure. The first fit, Eq. (11), data points, (\bullet), yields a $k_{vcc} = 1020.7 \pm 26.3 s^{-1} mTorr^{-1}$ and the second fit, Eq. (12), data points, (\bullet), yields a $k_{vcc} = 758.81 \pm 13.90 s^{-1} mTorr^{-1}$. The theoretical rate (- - -) is calculated from chemical kinetic "hard sphere" model, which is $872.78 \pm 13.73 s^{-1} mTorr^{-1}$, and the linear fit of the first fits (-) and linear fit of the second fits (-) is fitted without weights and has a y-intercept of zero.

V. Conclusion

5.1 Discussion of Findings

Previous works have studied hard collisions of atomic vapors using sub-Doppler spectroscopy, but only the ratio of the areas of Lorentzian to Doppler profiles of the sub-Doppler spectra or the time scale at which these hard collisions occur have been presented. An empirical study is ran prior to data collection which yielded insight on the best laser intensities to be used in the saturation spectroscopy experiment. In the experiment, spectra was collected at varying pump beam chopping frequencies and argon concentrations. The spectra illustrate the experimental expectations very well. Because of the uncertainty in the validity of the line shape, the data was fitted using two different line shapes; one line shape developed by using a "hard-sphere" model and another line shape based of the physical shape of the data. From both fits, the collisional information is extracted and the time scale at which these collisions occur is interpolated. Then Γ_{vcc} versus argon pressure is plotted. Both fits yield similar results. The first fit using the developed line shape yields a velocity-changing collision rate per argon concentration, $k_{vcc} = 1020.7 \pm 26.3 s^{-1} mTorr^{-1}$, which is 17% greater than the theoretical rate. The second fit yields a $k_{vcc} = 758.81 \pm 13.90 s^{-1} mTorr^{-1}$, which is 13% less than the theoretical rate. This method doesn't give better precision for the rate, but both fits show some curvature which maybe attributed to multi-collision events being observed at higher argon concentrations.

5.2 Recommendations for Future Work

First off, the collected spectra display periodic "wiggles". This could be attributed to etalon effects within the rubidium test cell or serial correlations due to over sampling of data. Therefore, both need to be investigated to improve the spectra. Next, a

different inert gas should be investigated to verify this method of calculating velocity-changing collisions. To investigate the proper line shape, the cesium D_1 line could be investigated because cesium has only one stable isotope and the hyperfine splitting is large enough so that no cross-over resonances would be observed. Therefore, the line shape of the transitions wouldn't overlap to convolute the fitting. Then to investigate the validity of the line shape for cross-over resonances, the cesium D_2 could be investigated which has two sets of hyperfine transitions that would give rise to cross-over resonances. Last, linear absorption experiment, just like the method of the reference cell absorbance, could be ran at low buffer gas pressure (10's Torr) to collect data and fit a Galatry profile. The Galatry profile has a collisional narrowing term that could be extracted to develop a velocity-changing collision rate. That would round up everything that could be done in saturation spectroscopy to observe velocity-changing collisions.

Appendix A. Rubidium Constants

1.1 Rubidium Hyperfine Structure

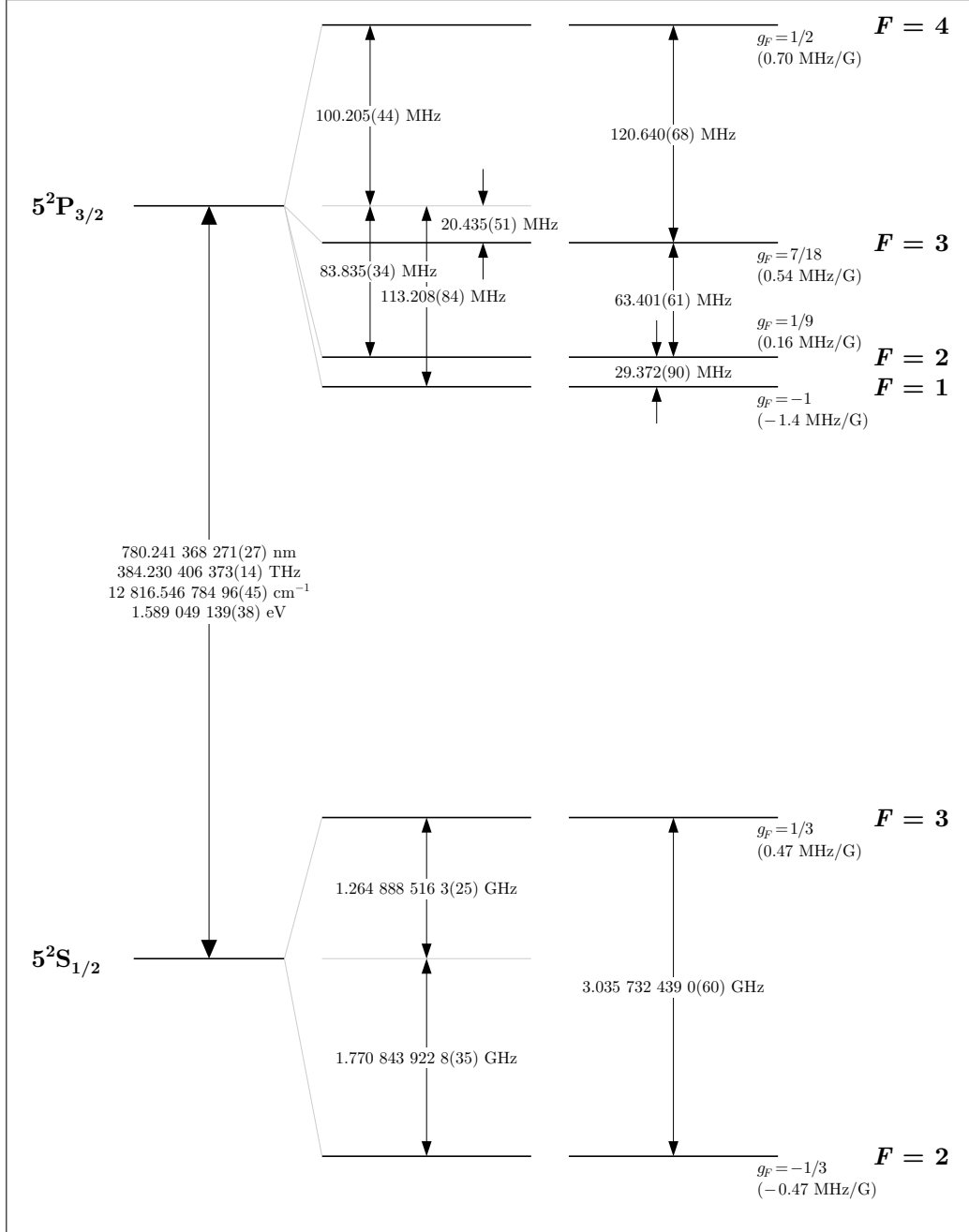


Figure 29. ^{85}Rb Hyperfine Structure of the D_2 Line from Steck [46]

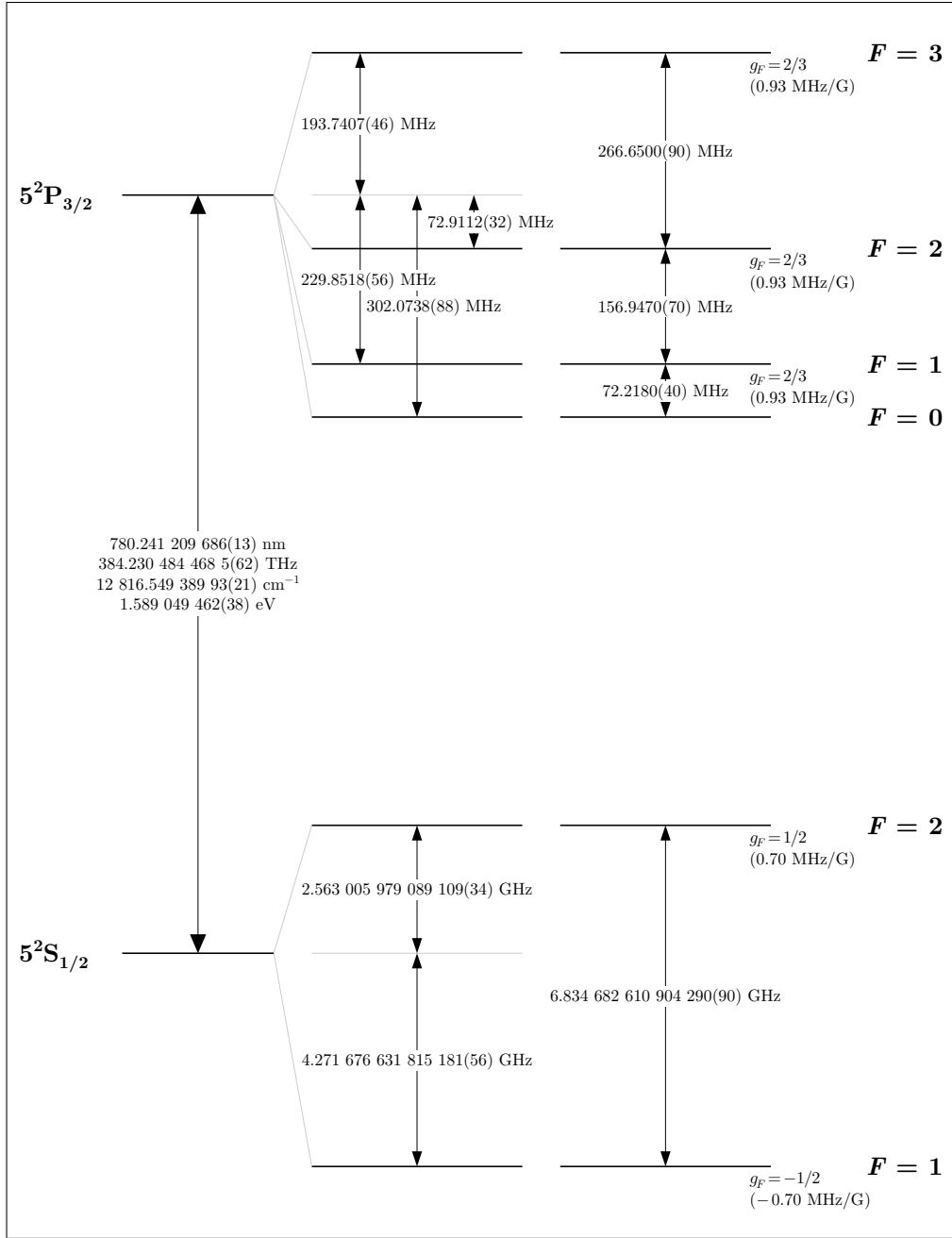


Figure 30. ^{87}Rb Hyperfine Structure of the D_2 Line from Steck [47]

1.2 Rubidium Spectroscopic Constants

Table 4. Rubidium D_2 Optical Properties from Steck [46; 47]

Frequency	ν_o	384.230406373(14) THz [52; 5]
Isotope Shift	$\nu_o(^{87}\text{Rb}) - \nu_o(^{85}\text{Rb})$	78.095(12) MHz [5]
Lifetime	τ_R	26.2348(77) ns [51; 41; 14]

Table 5. Rubidium 85 D Transition Hyperfine Structure Constants from Steck [46]

Magnetic Dipole Constant, $5^2S_{1/2}$	$A_{5^2S_{1/2}}$	$h \cdot 1.0119108130(20)$ GHz [3]
Magnetic Dipole Constant, $5^2P_{1/2}$	$A_{5^2P_{1/2}}$	$h \cdot 120.527(56)$ MHz[5; 4]
Magnetic Dipole Constant, $5^2P_{3/2}$	$A_{5^2P_{3/2}}$	$h \cdot 25.0020(99)$ MHz[4; 3]
Electric Quadrupole Constant, $5^2P_{3/2}$	$B_{5^2P_{3/2}}$	$h \cdot 25.790(93)$ MHz[4; 3]

Table 6. Rubidium 87 D Transition Hyperfine Structure Constants from Steck [47]

Magnetic Dipole Constant, $5^2S_{1/2}$	$A_{5^2S_{1/2}}$	$h \cdot 3.417341305452145(45)$ GHz [12]
Magnetic Dipole Constant, $5^2P_{1/2}$	$A_{5^2P_{1/2}}$	$h \cdot 407.24(77)$ MHz[3; 5; 4]
Magnetic Dipole Constant, $5^2P_{3/2}$	$A_{5^2P_{3/2}}$	$h \cdot 84.7185(20)$ MHz [52]
Electric Quadrupole Constant, $5^2P_{3/2}$	$B_{5^2P_{3/2}}$	$h \cdot 12.4965(37)$ MHz[52]

Table 7. ^{85}Rb D_2 Line Strengths from Steck [46]

$F'' = 3 \leftrightarrow F' = 2$	5/63
$F'' = 3 \leftrightarrow F' = 3$	5/18
$F'' = 3 \leftrightarrow F' = 4$	9/14
$F'' = 2 \leftrightarrow F' = 1$	3/10
$F'' = 2 \leftrightarrow F' = 2$	7/18
$F'' = 2 \leftrightarrow F' = 3$	14/45

Table 8. $^{87}\text{Rb } D_2$ Line Strengths from Steck [47]

$F'' = 2 \leftrightarrow F' = 1$	1/20
$F'' = 2 \leftrightarrow F' = 2$	1/4
$F'' = 2 \leftrightarrow F' = 3$	7/10
$F'' = 1 \leftrightarrow F' = 0$	1/6
$F'' = 1 \leftrightarrow F' = 1$	5/12
$F'' = 1 \leftrightarrow F' = 2$	5/12

1.3 Line Shapes

The rubidium relative amplitudes calculated in Fig.4, were taken from Pitz [32], using the following equation

$$\sum_{F'', iso} \left(\frac{g_{J'}}{g_{J''}} \right) \left(\frac{\lambda^2}{8\pi} \right) A_{21} S_{F'F''} f_{F''} f_{iso} g(\nu, \nu_{F'' \rightarrow F'}) \quad (21)$$

where

$g_J = 2J + 1 =$ degeneracy of the fine structure component

$\nu_{F'' \rightarrow F'} =$ line center of the $F'' \rightarrow F'$ component

$\lambda = \frac{c}{\nu}$

$c =$ speed of light

$\nu =$ optical frequency

$A_{21} = \frac{1}{\tau_R} =$ spontaneous emission rate or the Einstein A coefficient

$\tau_R =$ radiative lifetime

$S_{F'F''} =$ hyperfine line strength for the $F'' \rightarrow F'$ component

$f_{iso} =$ relative natural abundance

$f_{F''} =$ statistical distribution of population among F'' states

$$= \frac{(2F''+1)e^{-\frac{E(F'')}{k_B T}}}{\sum_{F''} (2F''+1)e^{-\frac{E(F'')}{k_B T}}}$$

$g(\nu, \nu_{F'' \rightarrow F'}) =$ line shape centered at $\nu_{F'' \rightarrow F'}$

The three most common line shapes in spectroscopy are the Doppler profile,

Lorentzian, and Voigt profile, as described by the following equations. All are area normalized. The Doppler profile is characterized by

$$D(\nu, \nu_o) = \frac{2\sqrt{\ln(2)/\pi}}{\Delta\nu_D(\nu_o)} \text{Exp} \left[-4\ln(2) \left(\frac{\nu - \nu_o}{\Delta\nu_D(\nu_o)} \right)^2 \right] \quad (22)$$

$$\Delta\nu_D(\nu_o) = 2\frac{\nu_o}{c} \left(\frac{2\ln(2)k_B T}{m} \right)^{1/2} \quad (23)$$

where ν_o is the line center, $\Delta\nu_o$ is the Doppler profile full width at half the maximum amplitude, m is the mass of the atom or molecule, k_B is Boltzmann constant, and T is the temperature in Kelvin. The Lorentzian profile is characterized by

$$L(\nu, \nu_o) = \frac{\gamma}{2\pi} \frac{1}{(\nu - \nu_o)^2 + \gamma^2/4} \quad (24)$$

$$\gamma = \frac{A_{21}}{2\pi} = \frac{1}{2\pi\tau_R} \quad (25)$$

where γ is the homogenous full line width at half the maximum amplitude. The Voigt profile is the convolution of the Lorentzian profile with the Doppler profile. An exact solution is very cumbersome, however there are many numerical approximations, as described in [38; 49]. The algorithm used from the papers is described below in Igor Pro code.

```

// Returns the Voigt profile (a convolution between a Gaussian and a Lorentzian).
// Y is the shape parameter. When Y is zero, the Voigt function is 100% Gaussian
// and transitions to 100% Lorentzian as Y approaches infinity. When Y is one the
// mix is 50/50. Its relative accuracy is better than
// 0.0001 and most of the time is much better.

Function Voigt(X,Y)
variable X,Y
Y= abs(Y)
X= abs(X)
variable/C W,U,T= cmplx(Y,-X)
variable S= X+Y

if( S >= 15 ) // Region I
W= T*0.5641896/(0.5+T*T)
else
if( S >= 5.5 ) // Region II
U= T*T
W= T*(1.410474+U*0.5641896)/(0.75+U*(3+U))
else
if( Y >= (0.195*X-0.176) ) // Region III
W= (16.4955+T*(20.20933+T*(11.96482+T*(3.778987+T*0.5642236))))
W /= (16.4955+T*(38.82363+T*(39.27121+T*(21.69274+T*(6.699398+T))))))
else // Region IV
U= T*T
W= T*(36183.31-U*(3321.9905-U*(1540.787-U*(219.0313-U*(35.76683-U*(1.320522-U*0.56419))))))
W /= (32066.6-U*(24322.84-U*(9022.228-U*(2186.181-U*(364.2191-U*(61.57037-U*(1.841439-U))))))
W= cmplx(exp(real(U))*cos(imag(U)),0)-W
endif
endif
endif
return real(W)
end

// A fitting function utilizing the Voigt profile (a convolution between a
// Gaussian and a Lorentzian). Can handle a number of peaks depending on the
// number of points in the coefficient wave w. If w contains 5 points then one
// peak will be generated as follows:
// w[0]+w[1]*Voigt(w[2]*(x-w[3]),w[4])
// Parameter w[0] sets the DC offset, w[1] sets the amplitude, w[2] affects the
// width, w[3] sets the location of the peak and w[4] adjusts the shape (but also
// affects the amplitude).
// After the fit, you can use the returned coefficients to calculate the area (a)
// along with the half width at half max for the Gaussian (wg), Lorentzian (wl)
// and the Voigt (wv). Assuming the coefficient wave is named coef:
// a= coef[1]*sqrt(pi)/coef[2]
// wg= sqrt(ln(2))/coef[2]
// wl= coef[4]/coef[2]
// wv= wl/2 + sqrt( wl^2/4 + wg^2)

```

Appendix B. Data Plots

2.1 Data at Single Argon Pressure

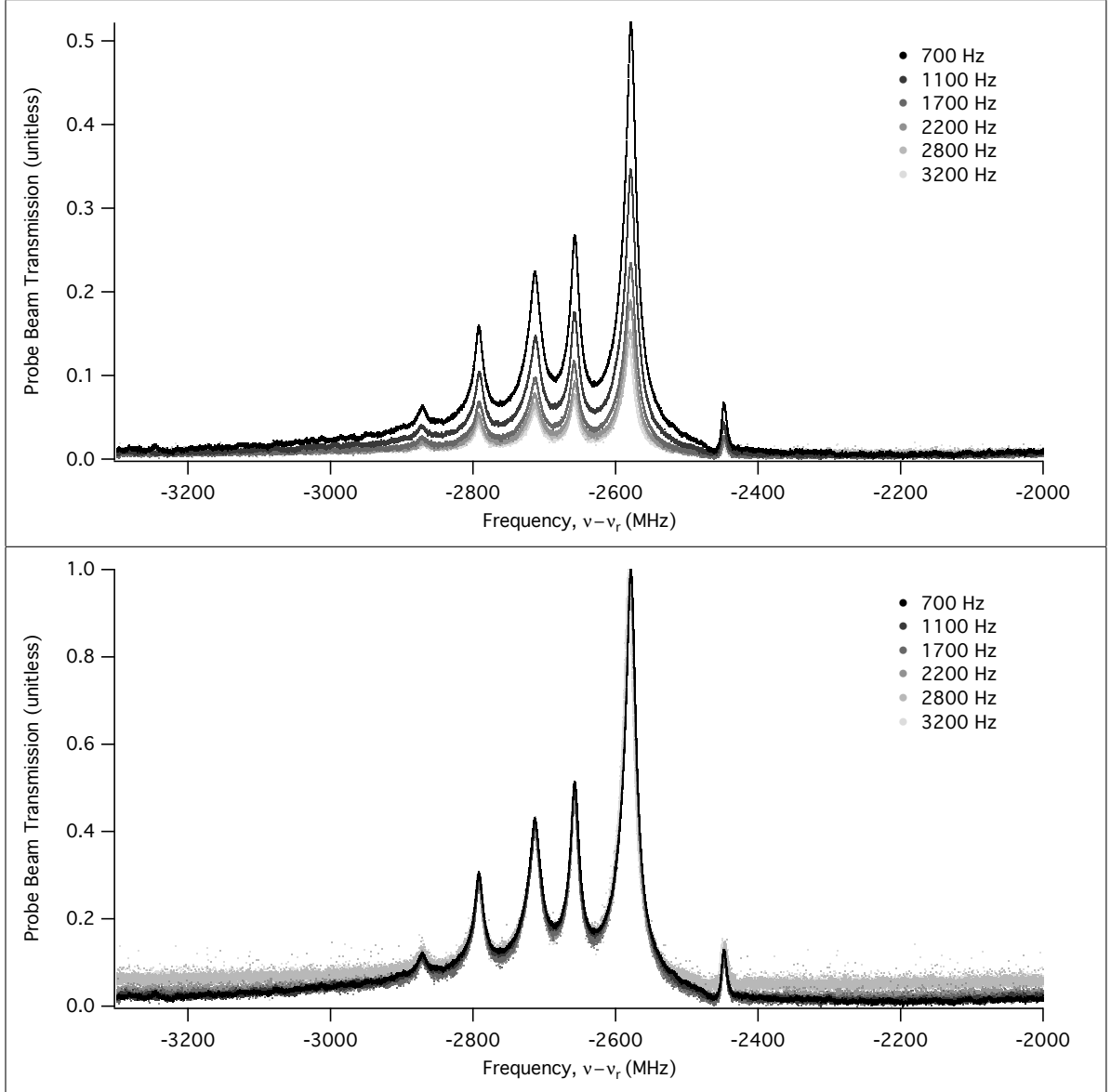


Figure 31. Data with no argon pressure and varying chopping frequency. The top plot is the raw data and the bottom plot is amplitude normalized. The vertical axis is the probe beam transmission relative to the incident beam intensity and the horizontal axis is the laser beam frequency (ν) relative to the ^{87}Rb D_2 line (ν_r).

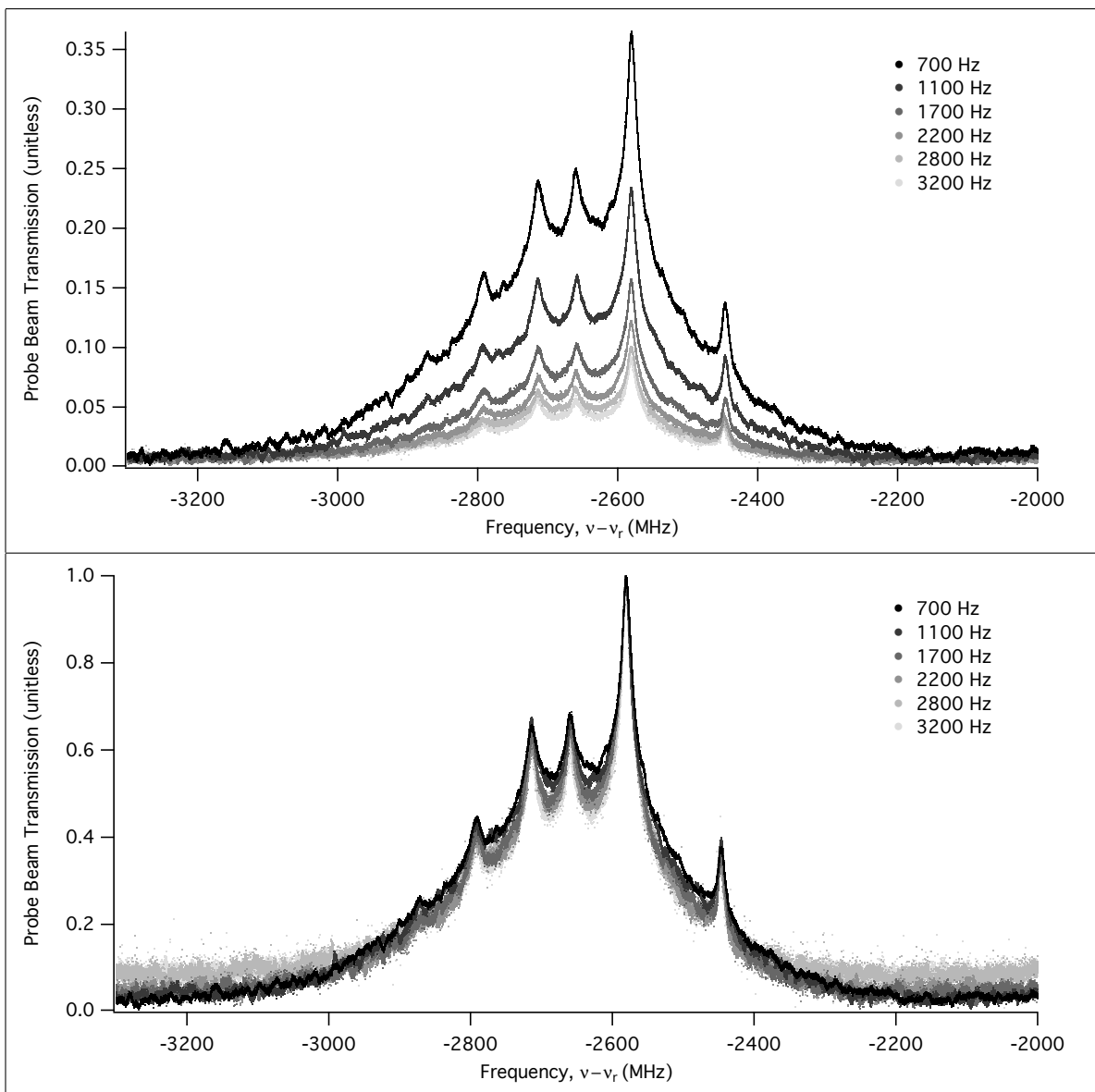


Figure 32. Data at 30 mTorr of argon and varying chopping frequency. The top plot is the raw data and the bottom plot is amplitude normalized. The vertical axis is the probe beam transmission relative to the incident beam intensity and the horizontal axis is the laser beam frequency (ν) relative to the ^{87}Rb D_2 line (ν_r).

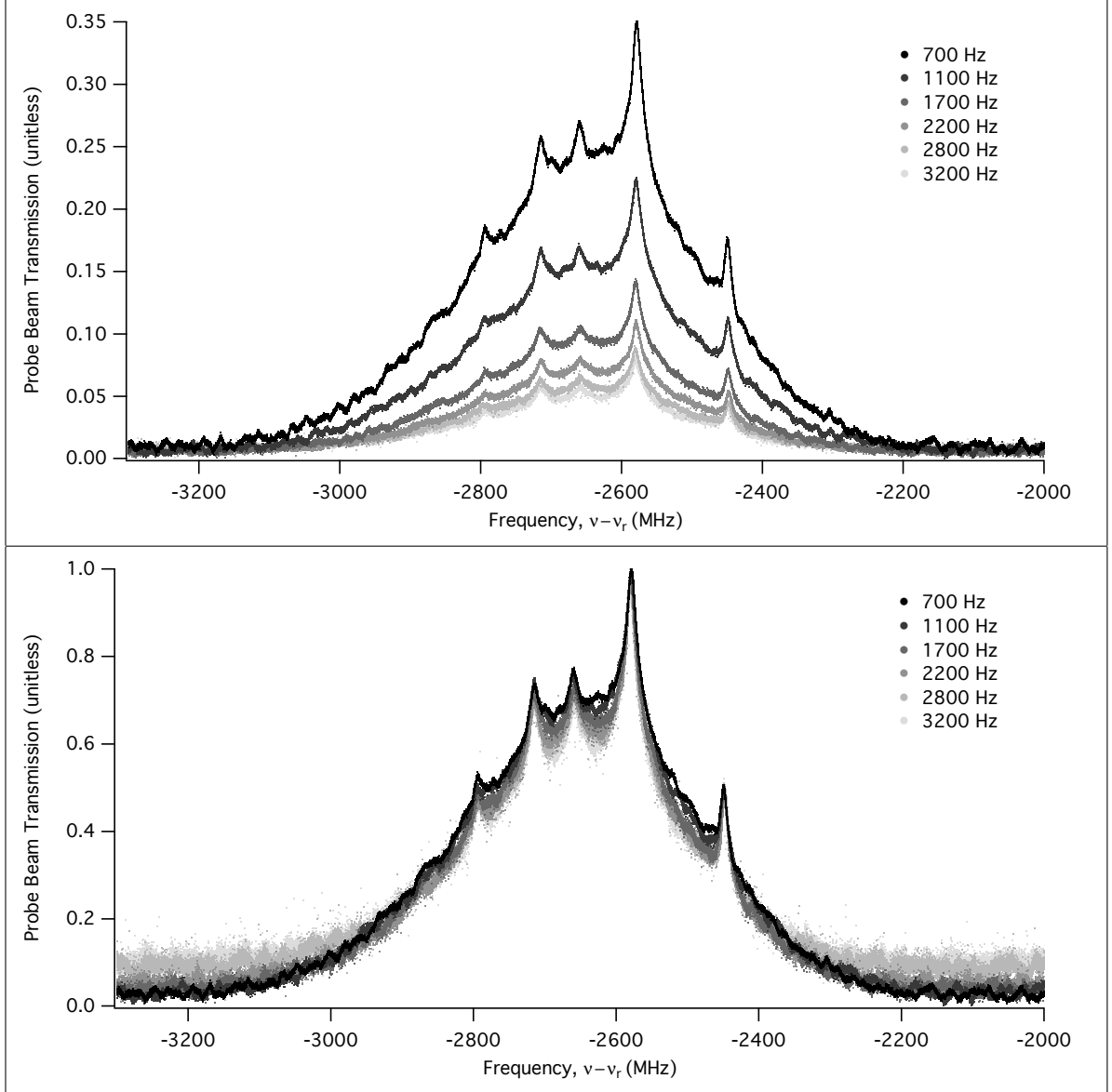


Figure 33. Data at 50 mTorr of argon and varying chopping frequency. The top plot is the raw data and the bottom plot is amplitude normalized. The vertical axis is the probe beam transmission relative to the incident beam intensity and the horizontal axis is the laser beam frequency (ν) relative to the ^{87}Rb D_2 line (ν_r).

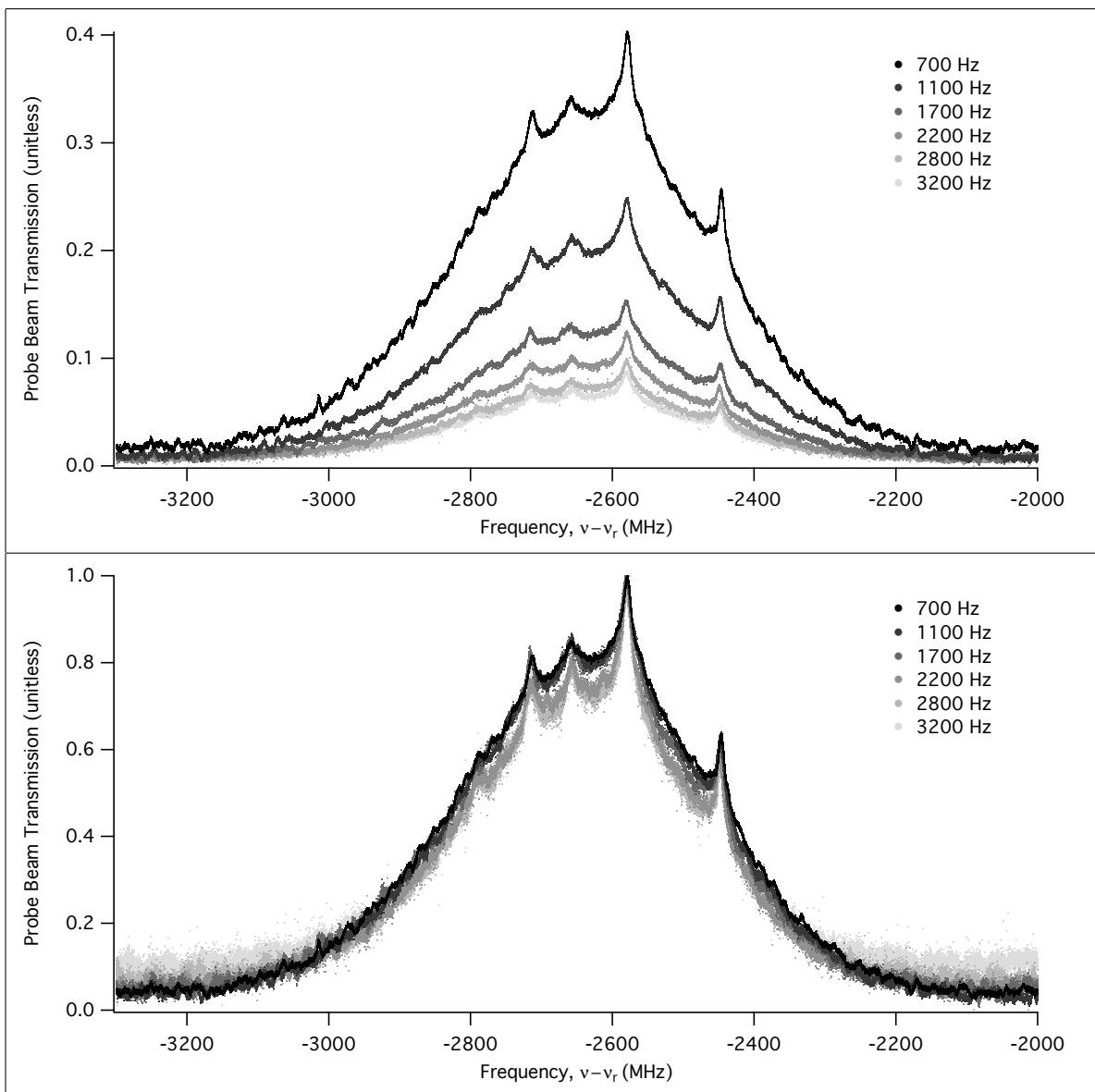


Figure 34. Data at 70 mTorr of argon and varying chopping frequency. The top plot is the raw data and the bottom plot is amplitude normalized. The vertical axis is the probe beam transmission relative to the incident beam intensity and the horizontal axis is the laser beam frequency (ν) relative to the ^{87}Rb D_2 line (ν_r).

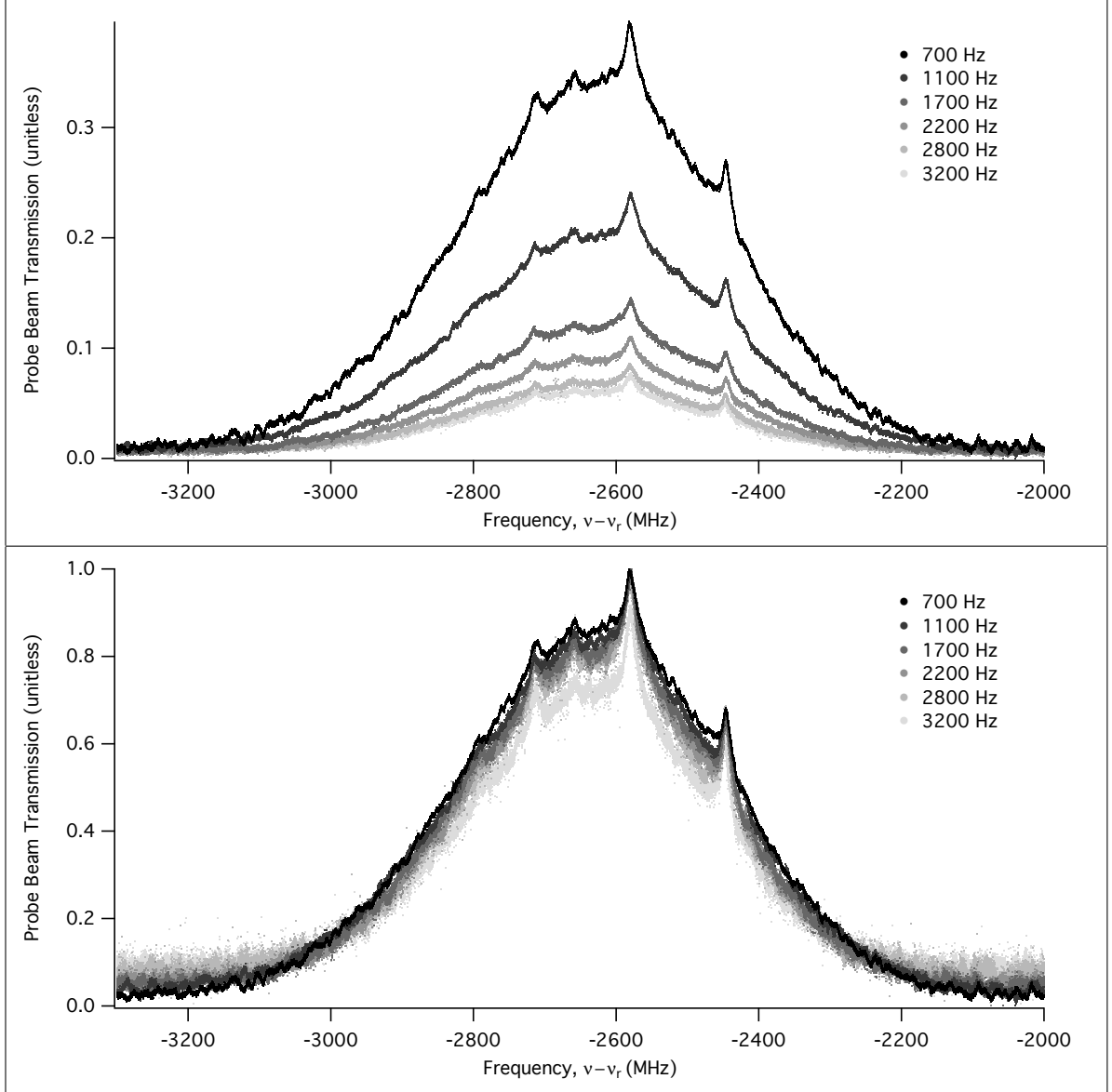


Figure 35. Data at 90 mTorr of argon and varying chopping frequency. The top plot is the raw data and the bottom plot is amplitude normalized. The vertical axis is the probe beam transmission relative to the incident beam intensity and the horizontal axis is the laser beam frequency (ν) relative to the ^{87}Rb D_2 line (ν_r).

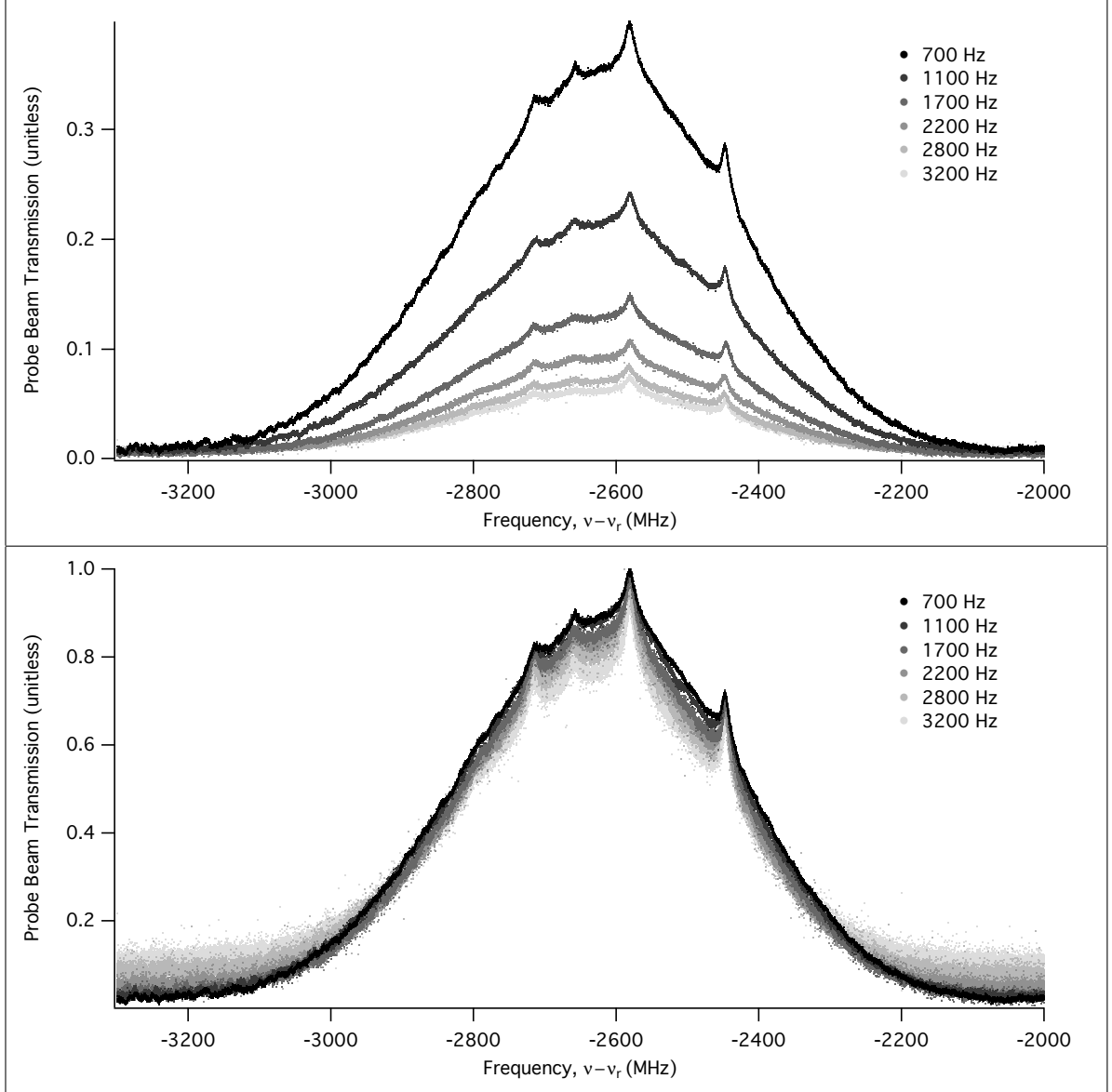


Figure 36. Data at 110 mTorr of argon and varying chopping frequency. The top plot is the raw data and the bottom plot is amplitude normalized. The vertical axis is the probe beam transmission relative to the incident beam intensity and the horizontal axis is the laser beam frequency (ν) relative to the ^{87}Rb D_2 line (ν_r).

2.2 Data at Single Chopping Frequency

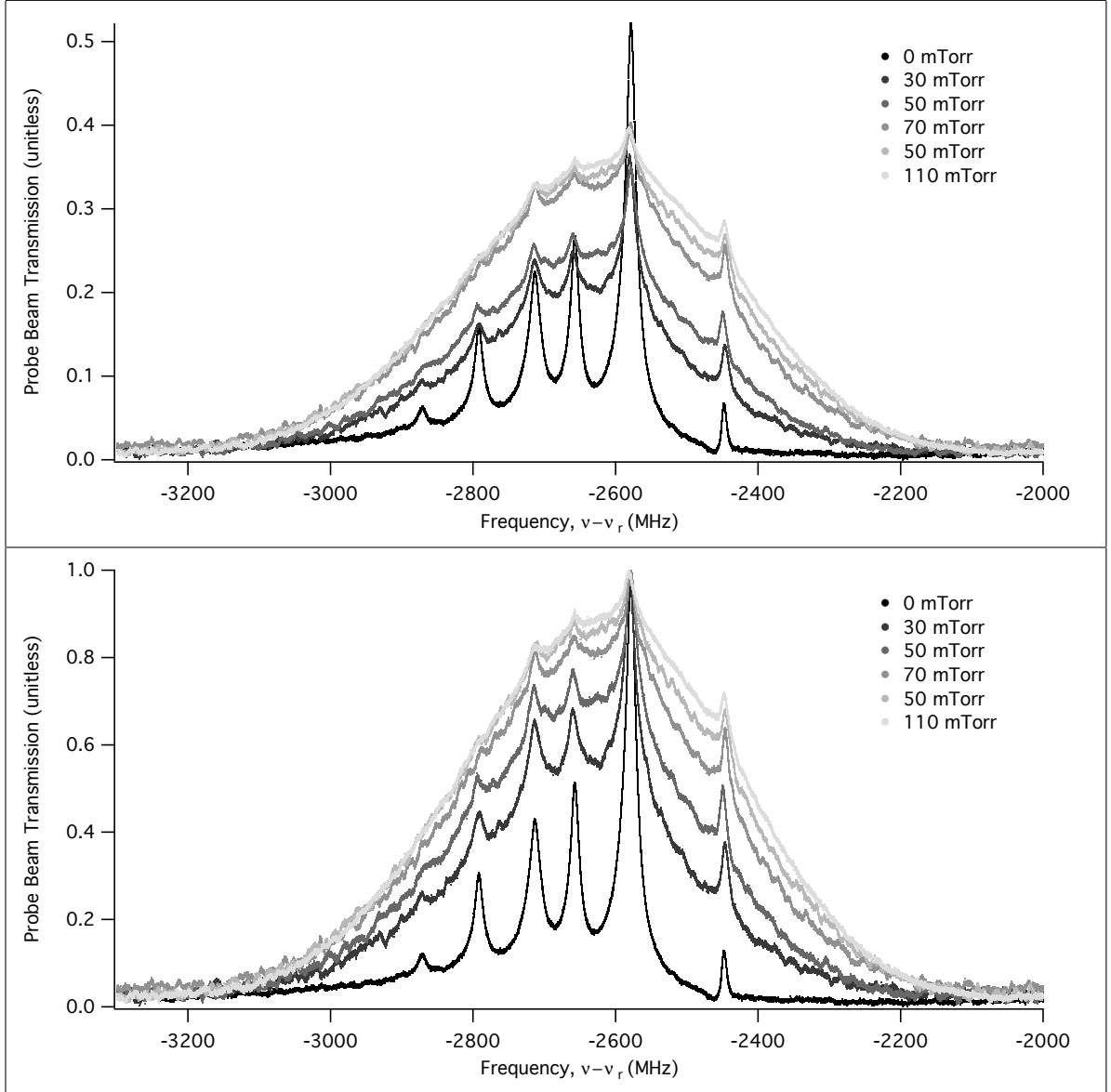


Figure 37. Data at a pump beam chopping frequency of 700 Hz and varying argon concentration. The top plot is the raw data and the bottom plot is amplitude normalized. The vertical axis is the probe beam transmission relative to the incident beam intensity and the horizontal axis is the laser beam frequency (ν) relative to the ^{87}Rb D_2 line (ν_r).

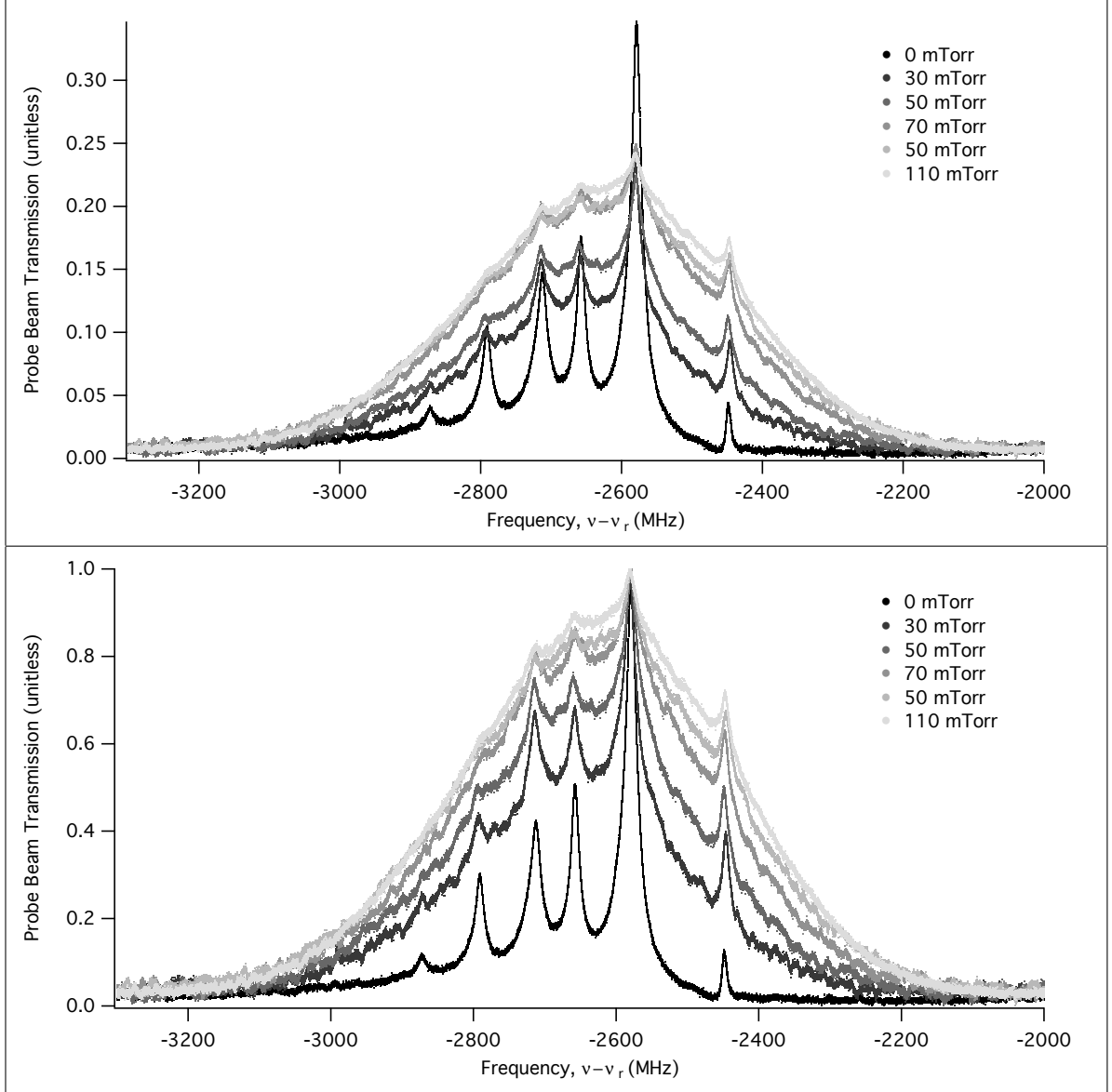


Figure 38. Data at a pump beam chopping frequency of 1100 Hz and varying argon concentration. The top plot is the raw data and the bottom plot is amplitude normalized. The vertical axis is the probe beam transmission relative to the incident beam intensity and the horizontal axis is the laser beam frequency (ν) relative to the ^{87}Rb D_2 line (ν_r).

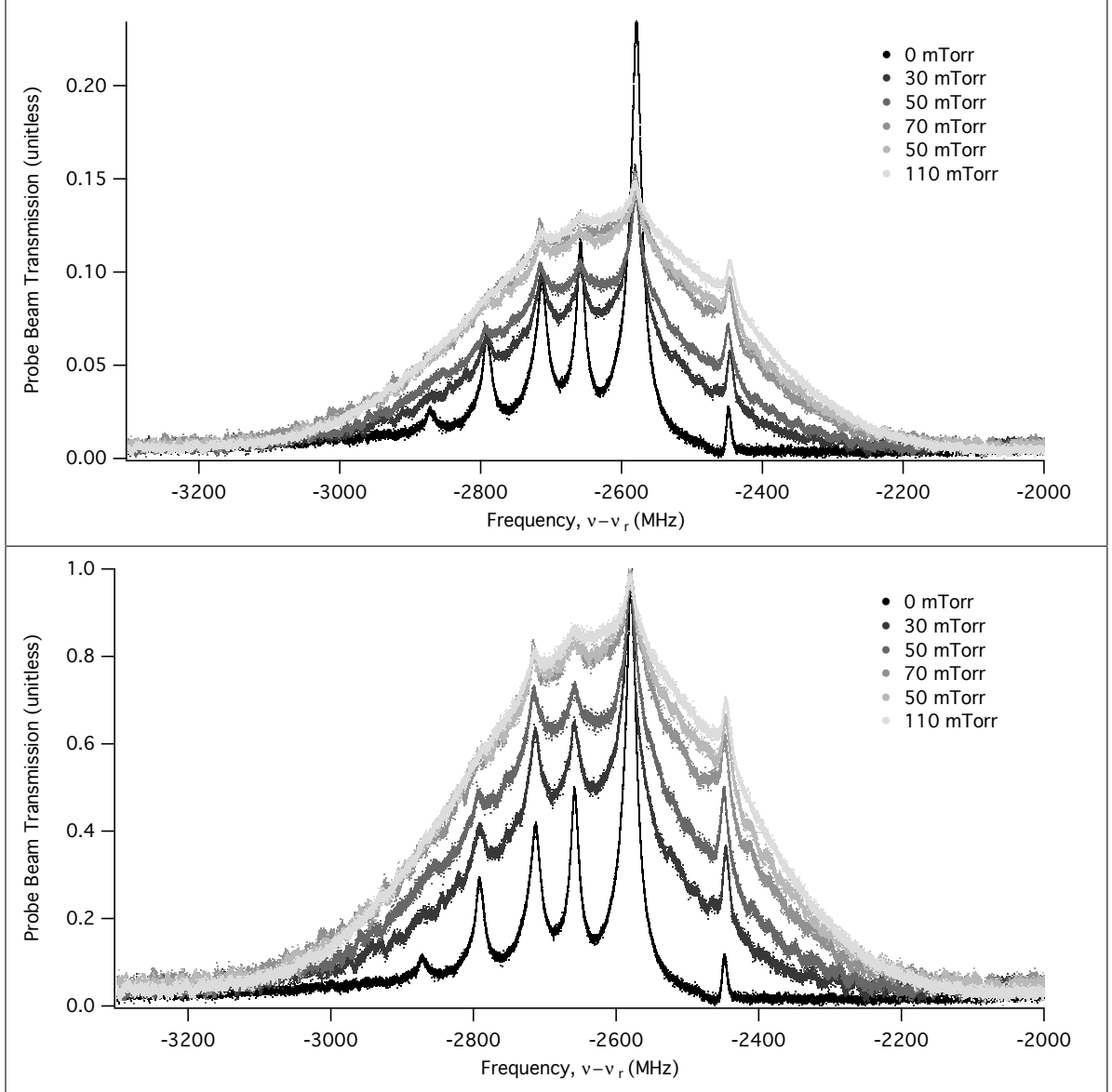


Figure 39. Data at a pump beam chopping frequency of 1700 Hz and varying argon concentration. The top plot is the raw data and the bottom plot is amplitude normalized. The vertical axis is the probe beam transmission relative to the incident beam intensity and the horizontal axis is the laser beam frequency (ν) relative to the ^{87}Rb D_2 line (ν_r).

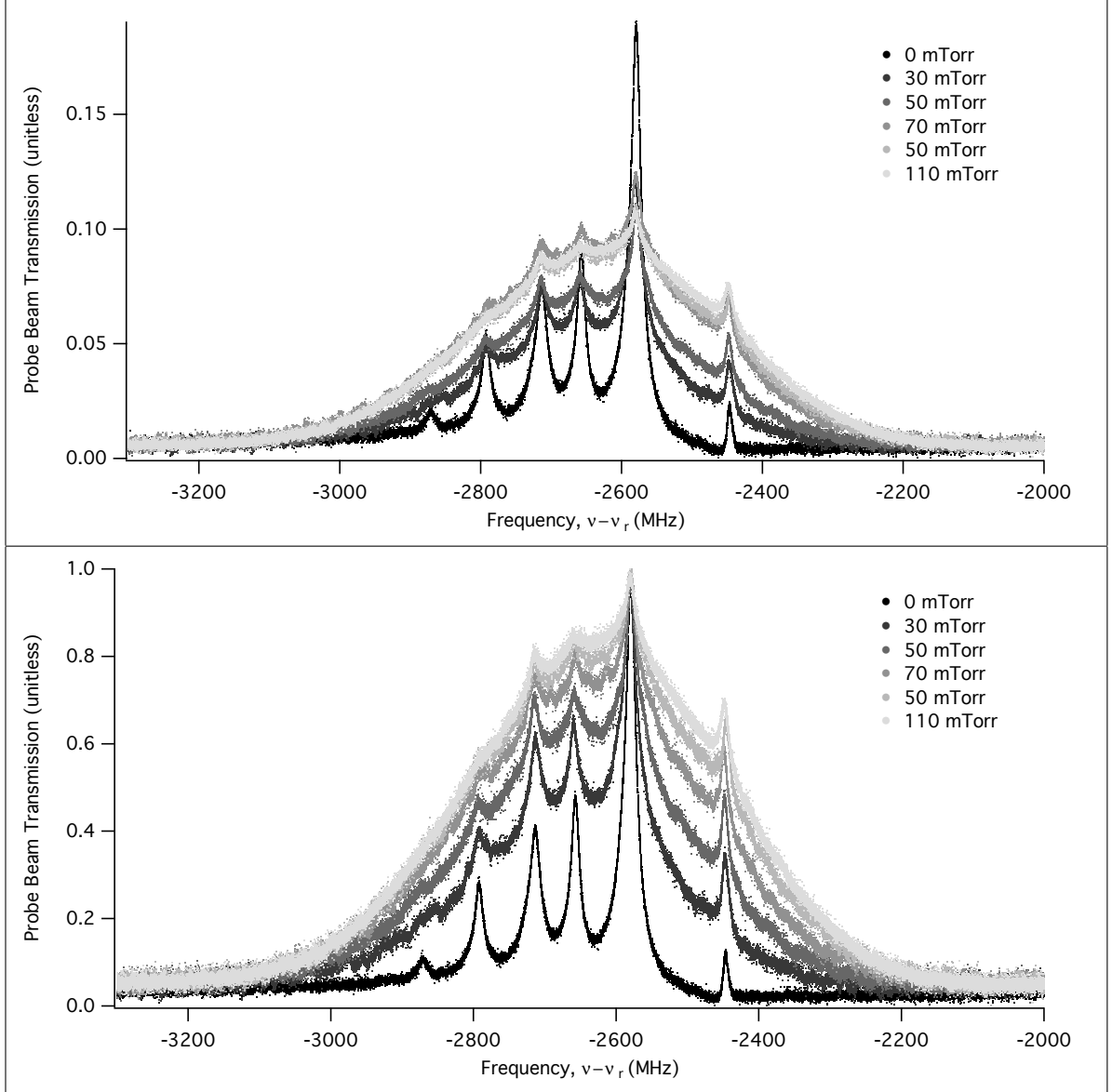


Figure 40. Data at a pump beam chopping frequency of 2200 Hz and varying argon concentration. The top plot is the raw data and the bottom plot is amplitude normalized. The vertical axis is the probe beam transmission relative to the incident beam intensity and the horizontal axis is the laser beam frequency (ν) relative to the ^{87}Rb D_2 line (ν_r).

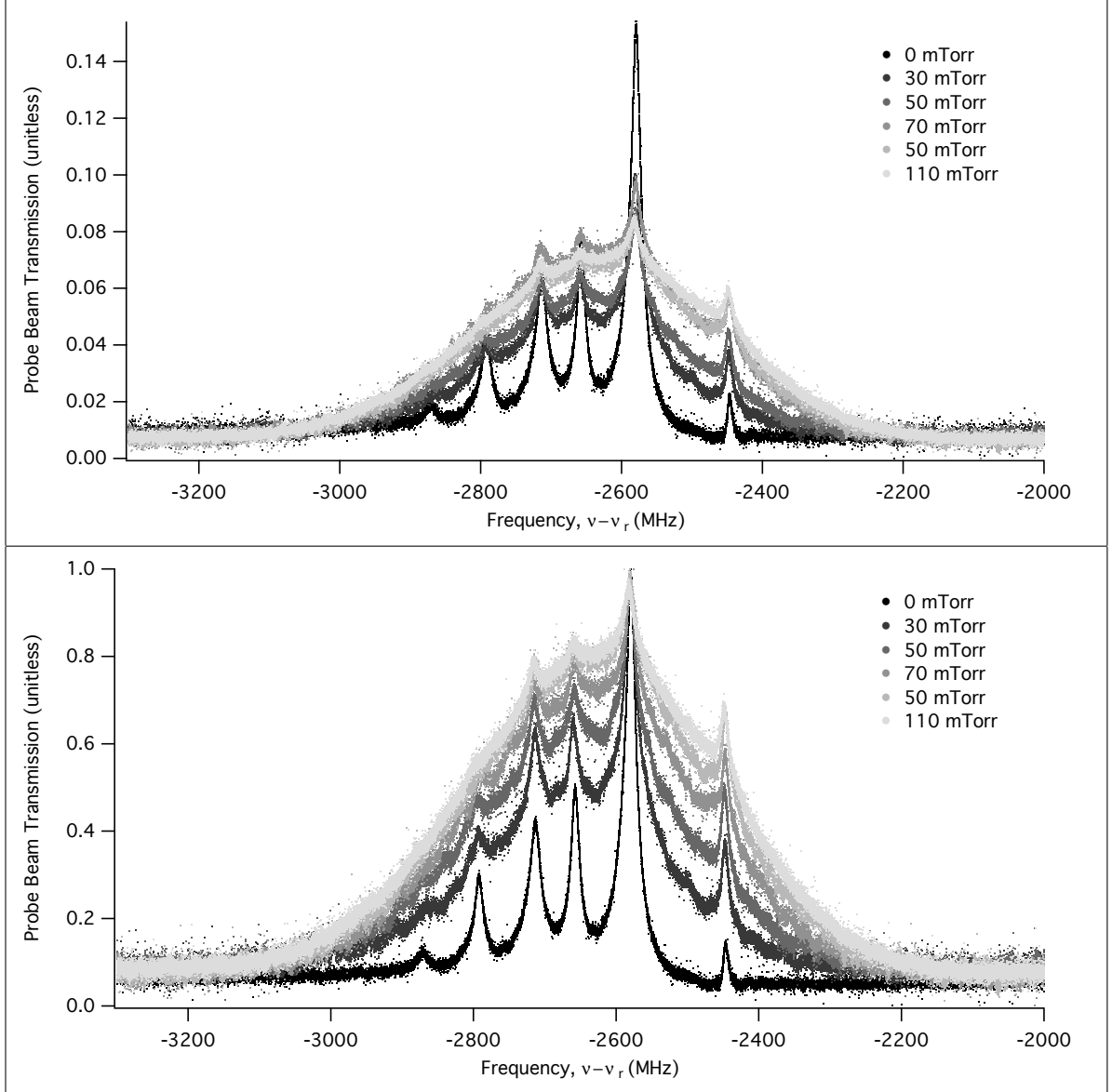


Figure 41. Data at a pump beam chopping frequency of 2800 Hz and varying argon concentration. The top plot is the raw data and the bottom plot is amplitude normalized. The vertical axis is the probe beam transmission relative to the incident beam intensity and the horizontal axis is the laser beam frequency (ν) relative to the ^{87}Rb D_2 line (ν_r).

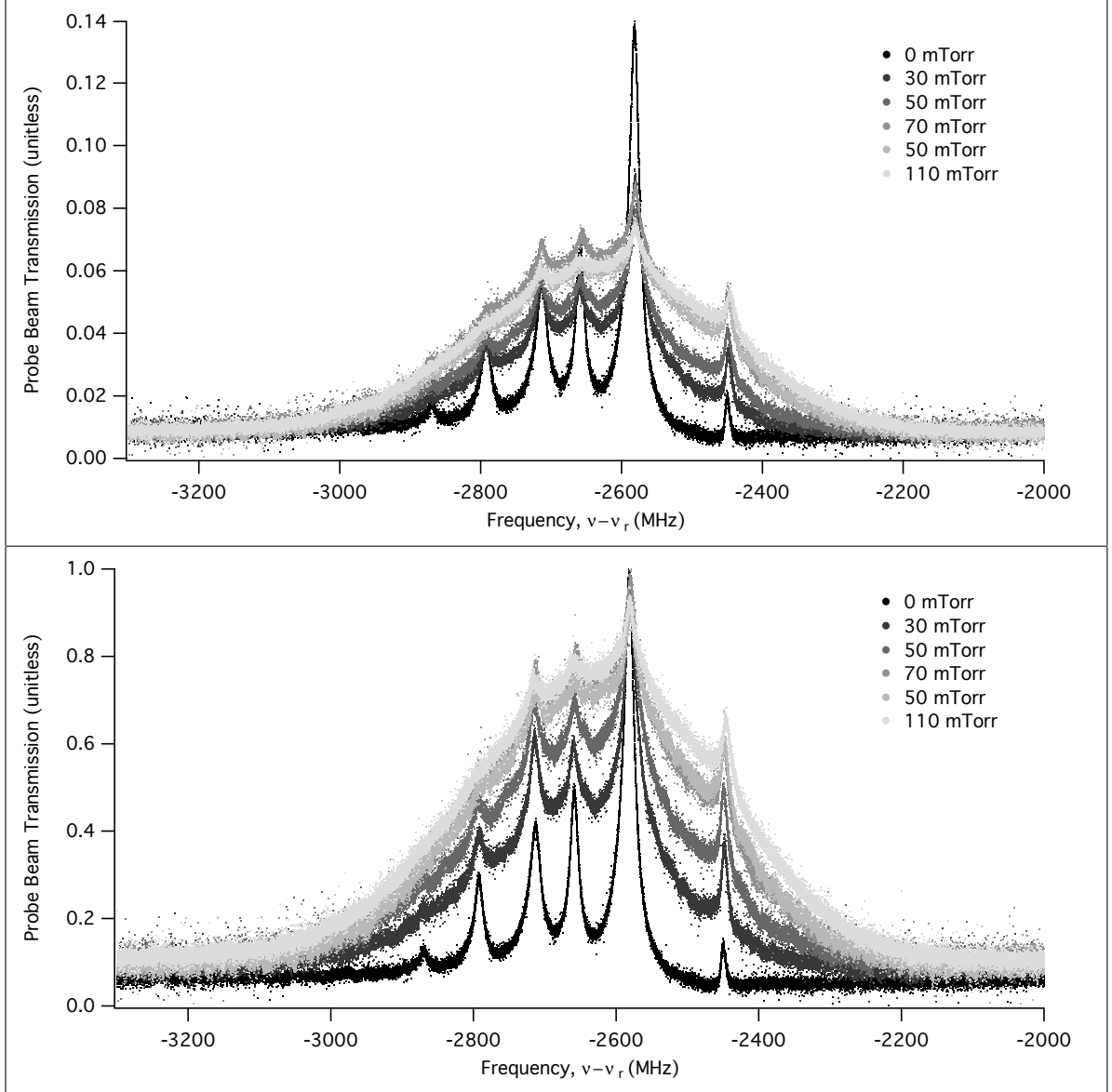


Figure 42. Data at a pump beam chopping frequency of 3300 Hz and varying argon concentration. The top plot is the raw data and the bottom plot is amplitude normalized. The vertical axis is the probe beam transmission relative to the incident beam intensity and the horizontal axis is the laser beam frequency (ν) relative to the ^{87}Rb D_2 line (ν_r).

2.3 All Data Fits

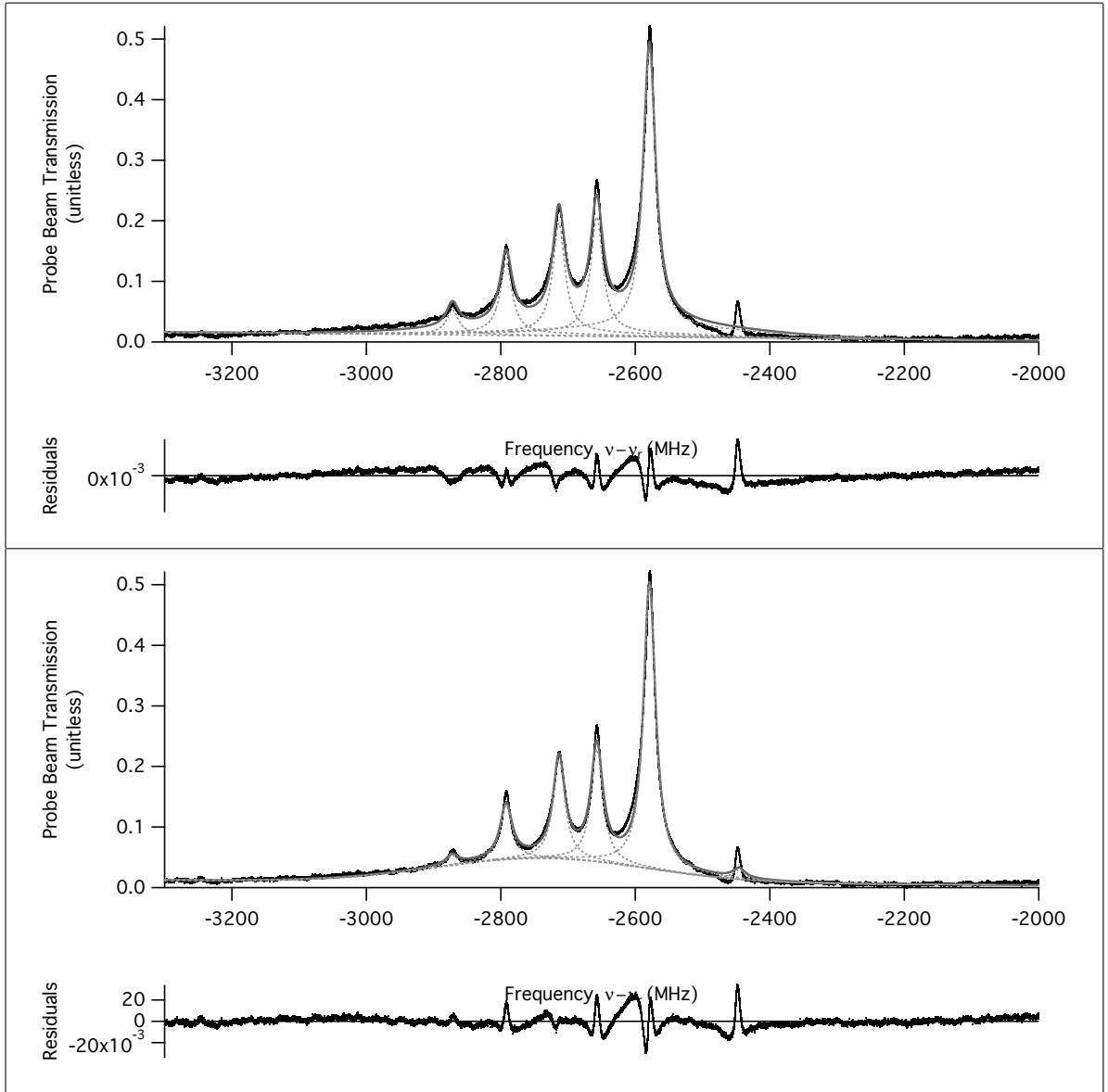


Figure 43. Data fits of both line shapes at 0 mTorr of Argon and 700 Hz chopping frequency. The top plot is a fit using the first line shape, Eq.(11), and the bottom plot is the fit using the second line shape, Eq.(12). The vertical axis is the probe beam transmission relative to the incident beam intensity and the horizontal axis is the laser beam frequency (ν) relative to the $^{87}\text{Rb } D_2$ line (ν_r). The data is in (\bullet), the fit is in ($-$), and the individual hyperfine or cross-over line fit is ($- -$).

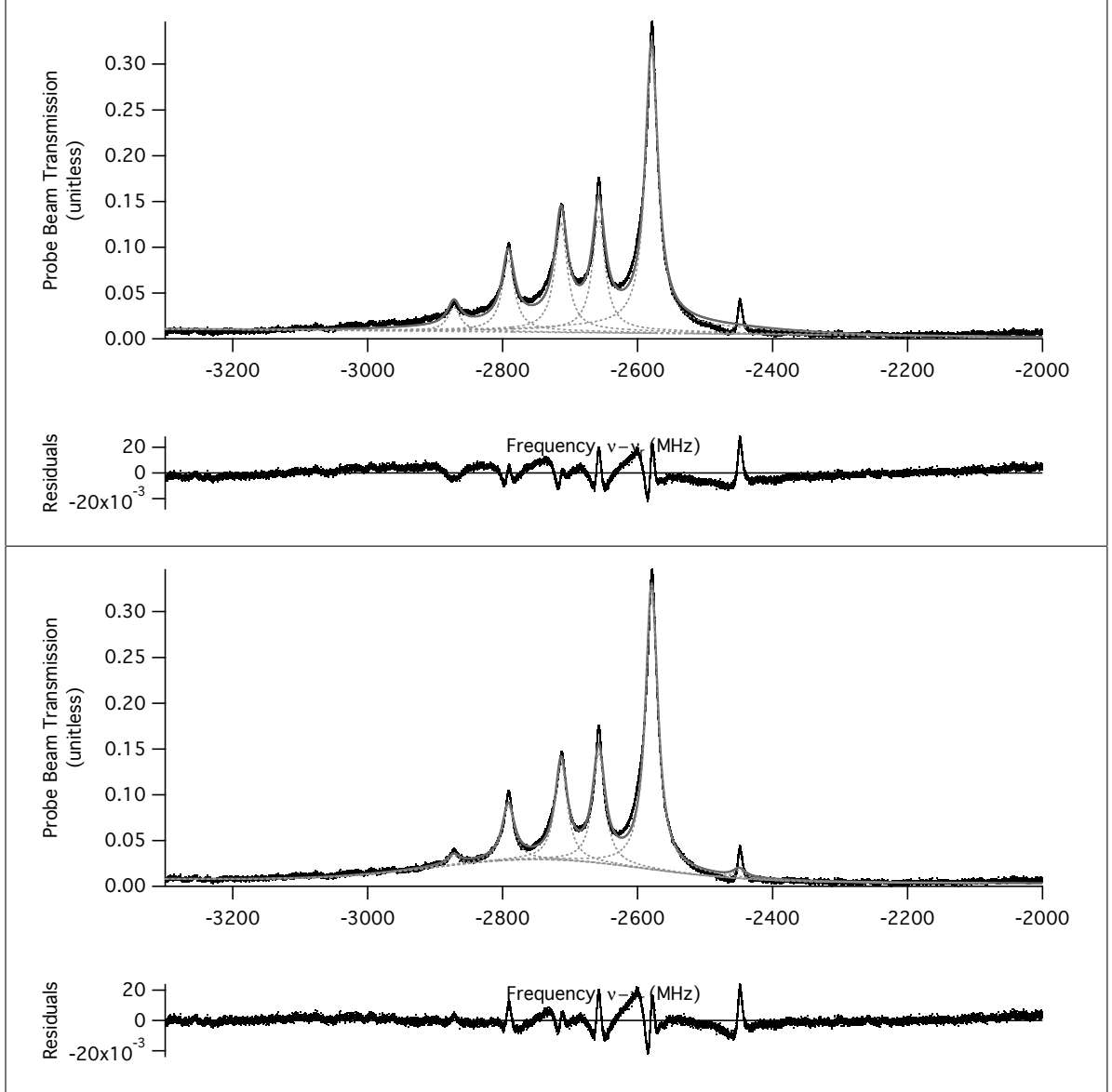


Figure 44. Data fits of both line shapes at 0 mTorr of Argon and 1100 Hz chopping frequency. The top plot is a fit using the first line shape, Eq.(11), and the bottom plot is the fit using the second line shape, Eq.(12). The vertical axis is the probe beam transmission relative to the incident beam intensity and the horizontal axis is the laser beam frequency (ν) relative to the ^{87}Rb D_2 line (ν_r). The data is in (\bullet), the fit is in (-), and the individual hyperfine or cross-over line fit is (- - -).

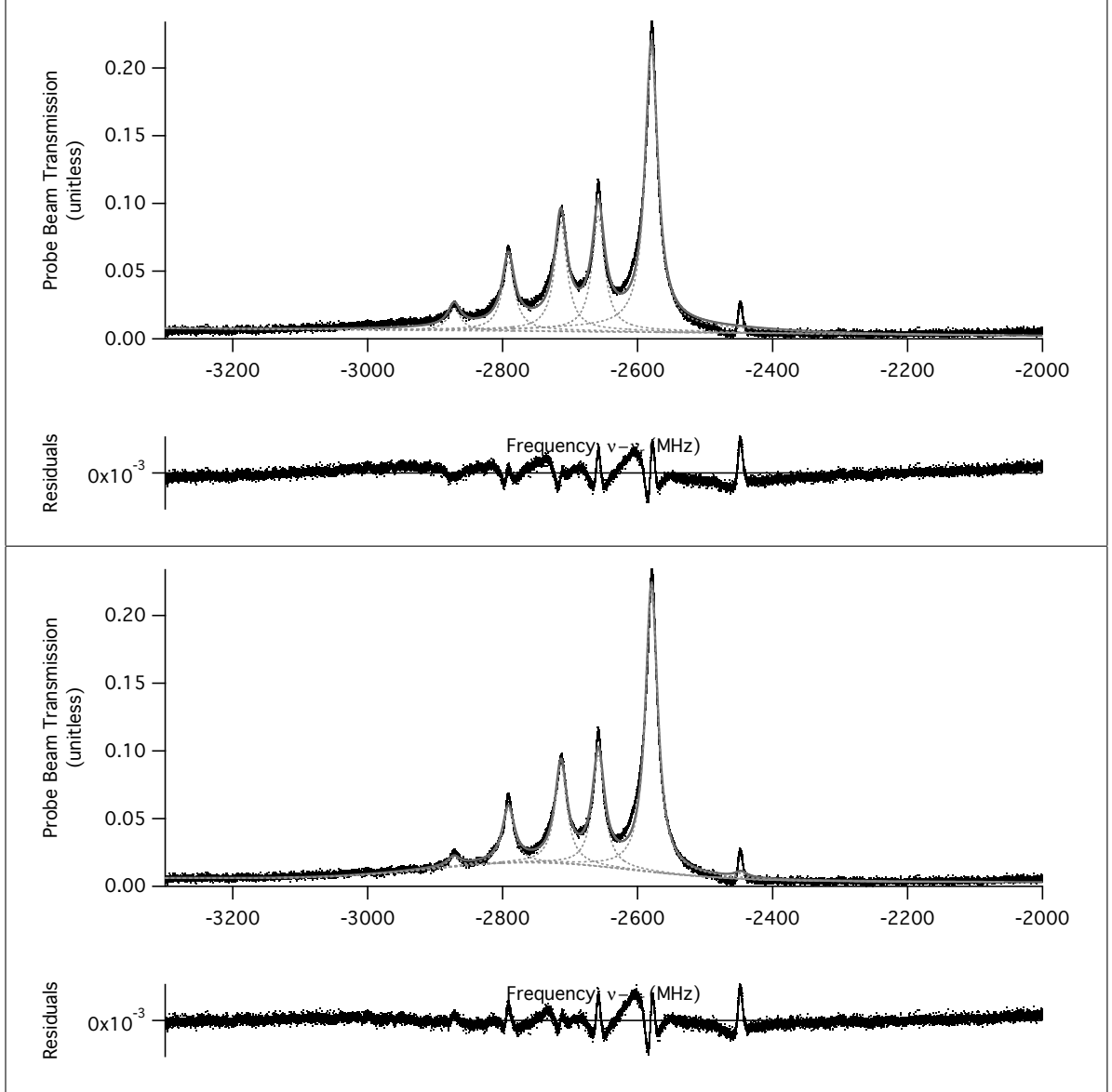


Figure 45. Data fits of both line shapes at 0 mTorr of Argon and 1700 Hz chopping frequency. The top plot is a fit using the first line shape, Eq.(11), and the bottom plot is the fit using the second line shape, Eq.(12). The vertical axis is the probe beam transmission relative to the incident beam intensity and the horizontal axis is the laser beam frequency (ν) relative to the ^{87}Rb D_2 line (ν_r). The data is in (●), the fit is in (-), and the individual hyperfine or cross-over line fit is (- - -).

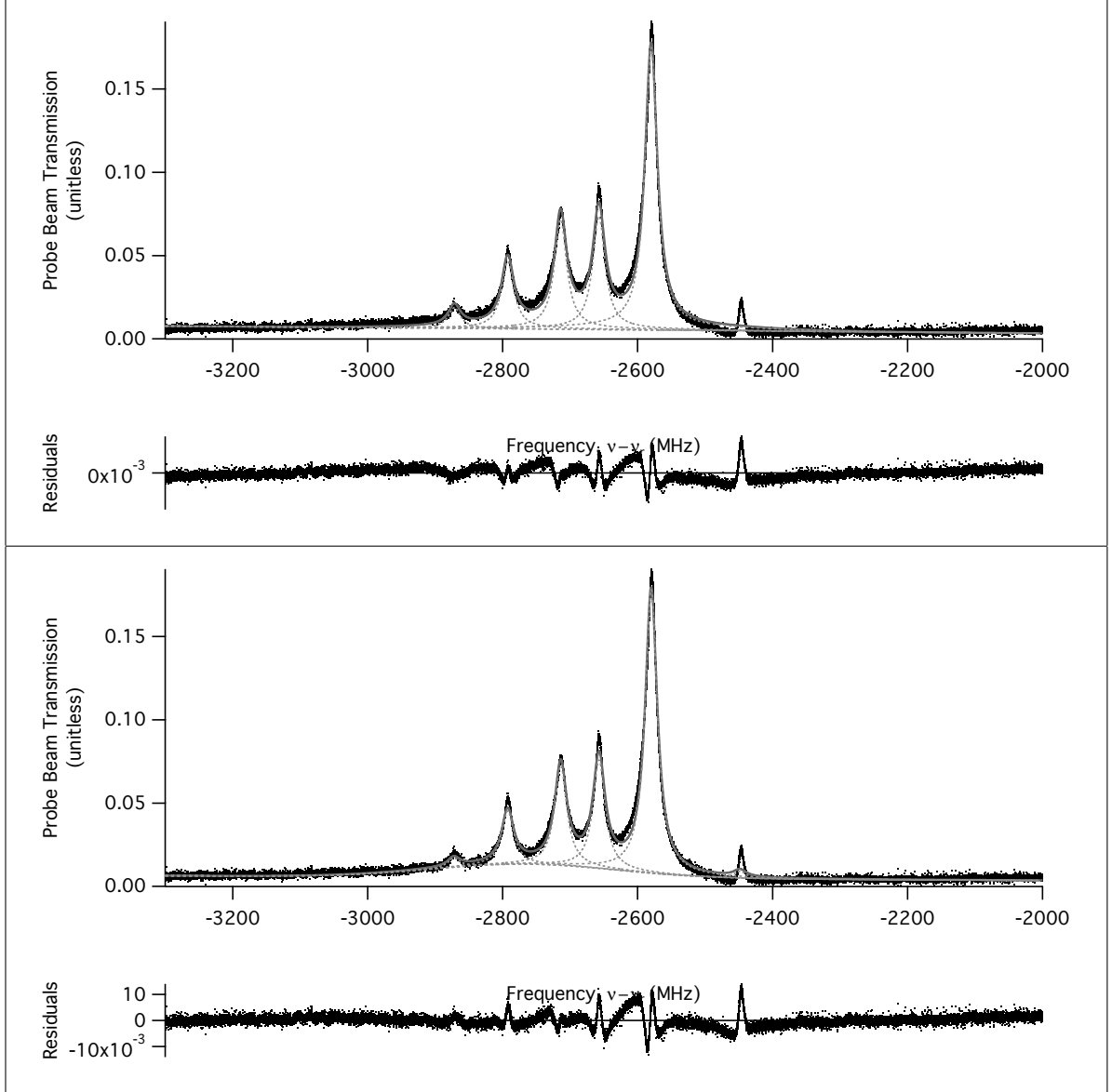


Figure 46. Data fits of both line shapes at 0 mTorr of Argon and 2200 Hz chopping frequency. The top plot is a fit using the first line shape, Eq.(11), and the bottom plot is the fit using the second line shape, Eq.(12). The vertical axis is the probe beam transmission relative to the incident beam intensity and the horizontal axis is the laser beam frequency (ν) relative to the ^{87}Rb D_2 line (ν_r). The data is in (\bullet), the fit is in (—), and the individual hyperfine or cross-over line fit is (---).

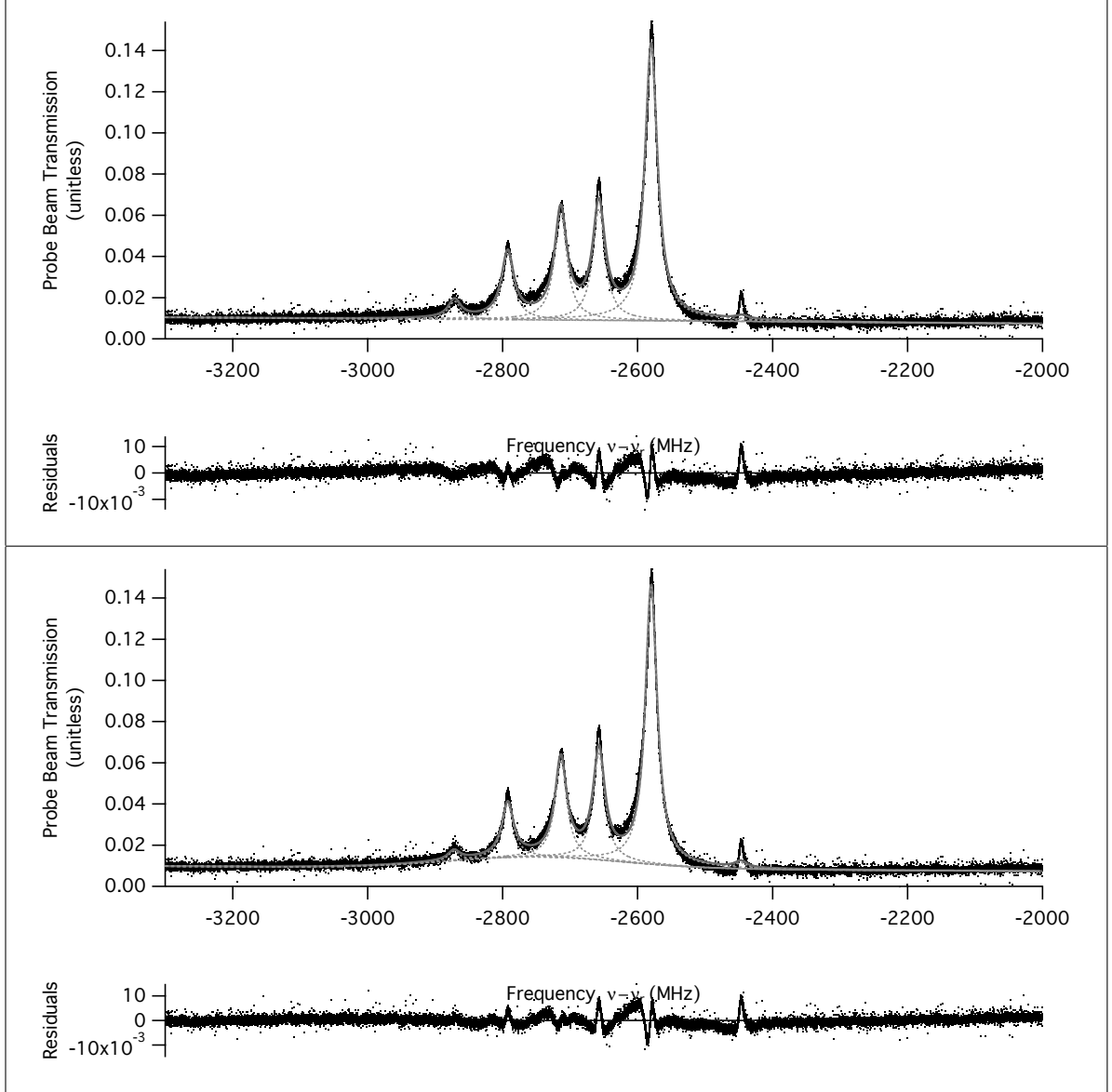


Figure 47. Data fits of both line shapes at 0 mTorr of Argon and 2800 Hz chopping frequency. The top plot is a fit using the first line shape, Eq.(11), and the bottom plot is the fit using the second line shape, Eq.(12). The vertical axis is the probe beam transmission relative to the incident beam intensity and the horizontal axis is the laser beam frequency (ν) relative to the $^{87}\text{Rb } D_2$ line (ν_r). The data is in (\bullet), the fit is in (-), and the individual hyperfine or cross-over line fit is (- - -).

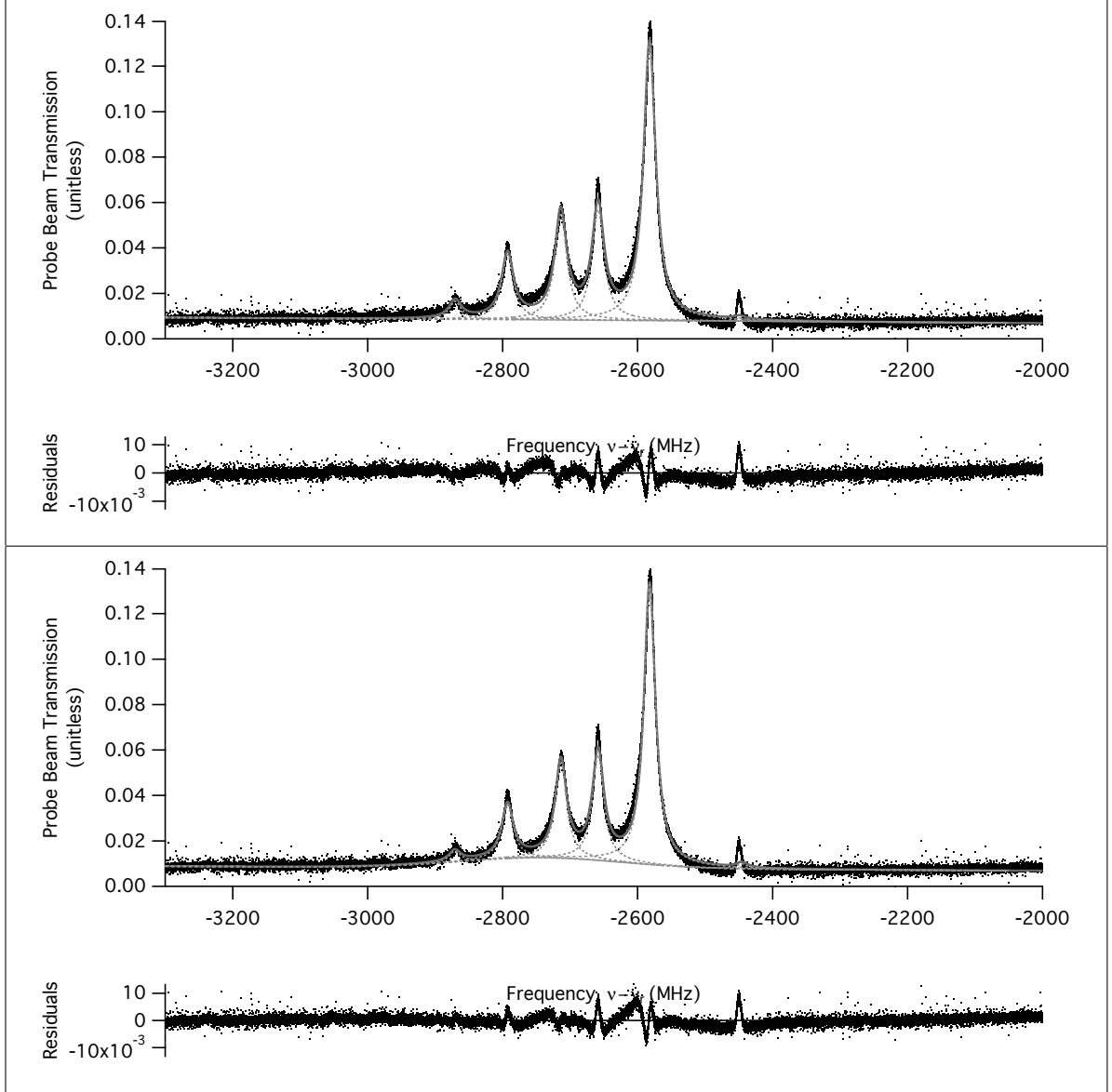


Figure 48. Data fits of both line shapes at 0 mTorr of Argon and 3200 Hz chopping frequency. The top plot is a fit using the first line shape, Eq.(11), and the bottom plot is the fit using the second line shape, Eq.(12). The vertical axis is the probe beam transmission relative to the incident beam intensity and the horizontal axis is the laser beam frequency (ν) relative to the $^{87}\text{Rb } D_2$ line (ν_r). The data is in (\bullet), the fit is in (-), and the individual hyperfine or cross-over line fit is (- - -).

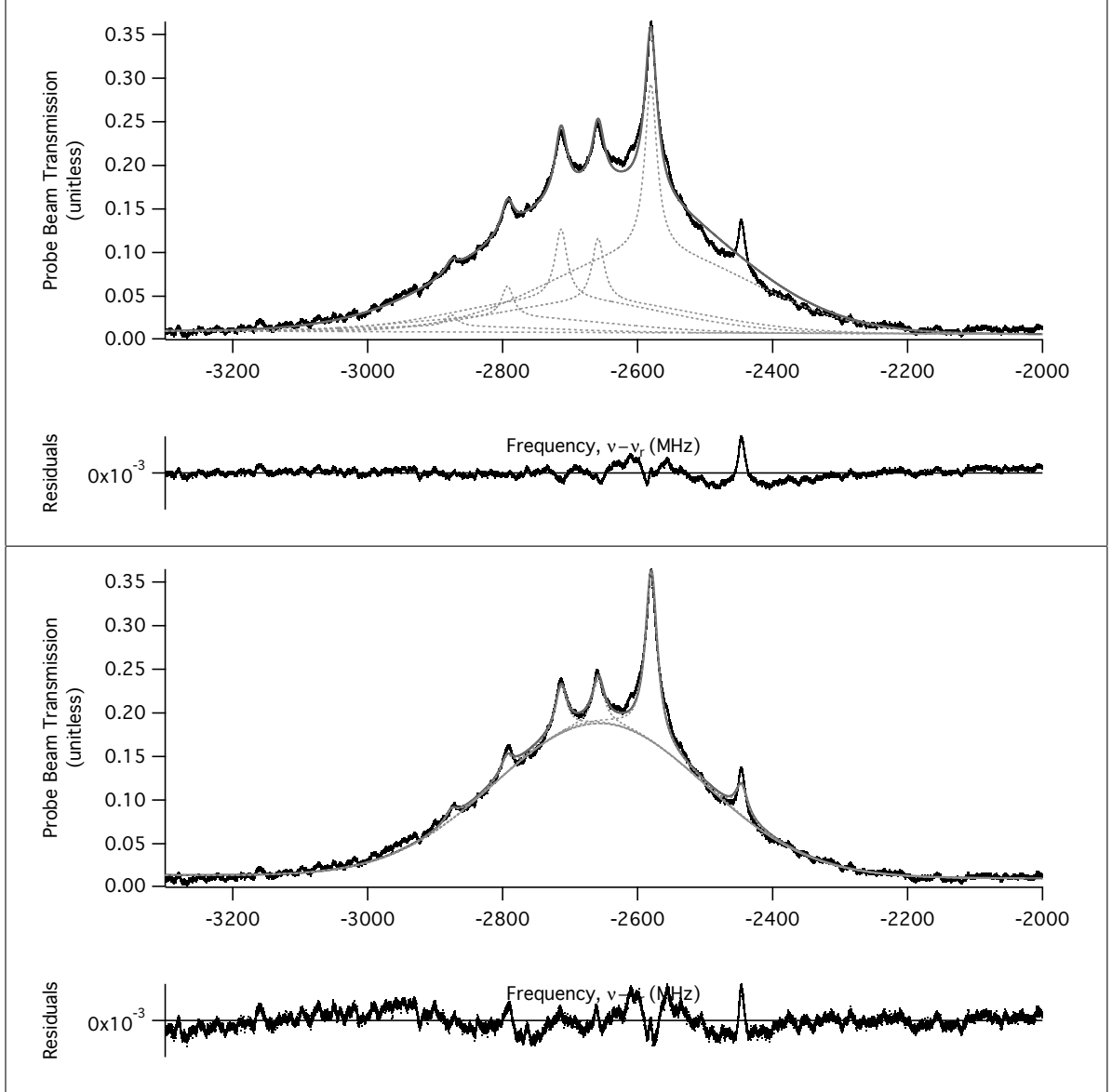


Figure 49. Data fits of both line shapes at 30 mTorr of Argon and 700 Hz chopping frequency. The top plot is a fit using the first line shape, Eq.(11), and the bottom plot is the fit using the second line shape, Eq.(12). The vertical axis is the probe beam transmission relative to the incident beam intensity and the horizontal axis is the laser beam frequency (ν) relative to the $^{87}\text{Rb } D_2$ line (ν_r). The data is in (\bullet), the fit is in ($-$), and the individual hyperfine or cross-over line fit is ($- -$).

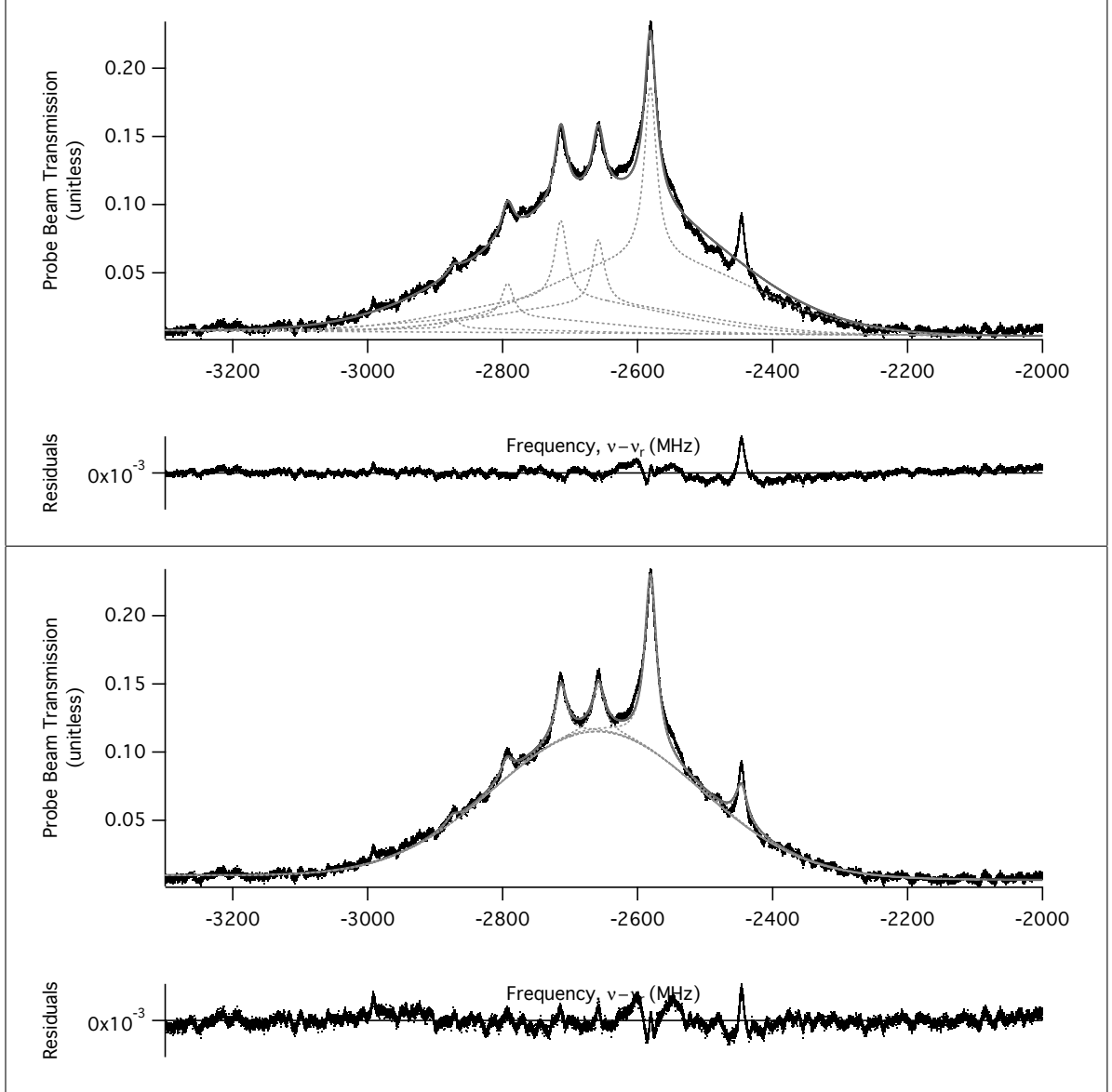


Figure 50. Data fits of both line shapes at 30 mTorr of Argon and 1100 Hz chopping frequency. The top plot is a fit using the first line shape, Eq.(11), and the bottom plot is the fit using the second line shape, Eq.(12). The vertical axis is the probe beam transmission relative to the incident beam intensity and the horizontal axis is the laser beam frequency (ν) relative to the ^{87}Rb D_2 line (ν_r). The data is in (\bullet), the fit is in ($-$), and the individual hyperfine or cross-over line fit is ($- -$).

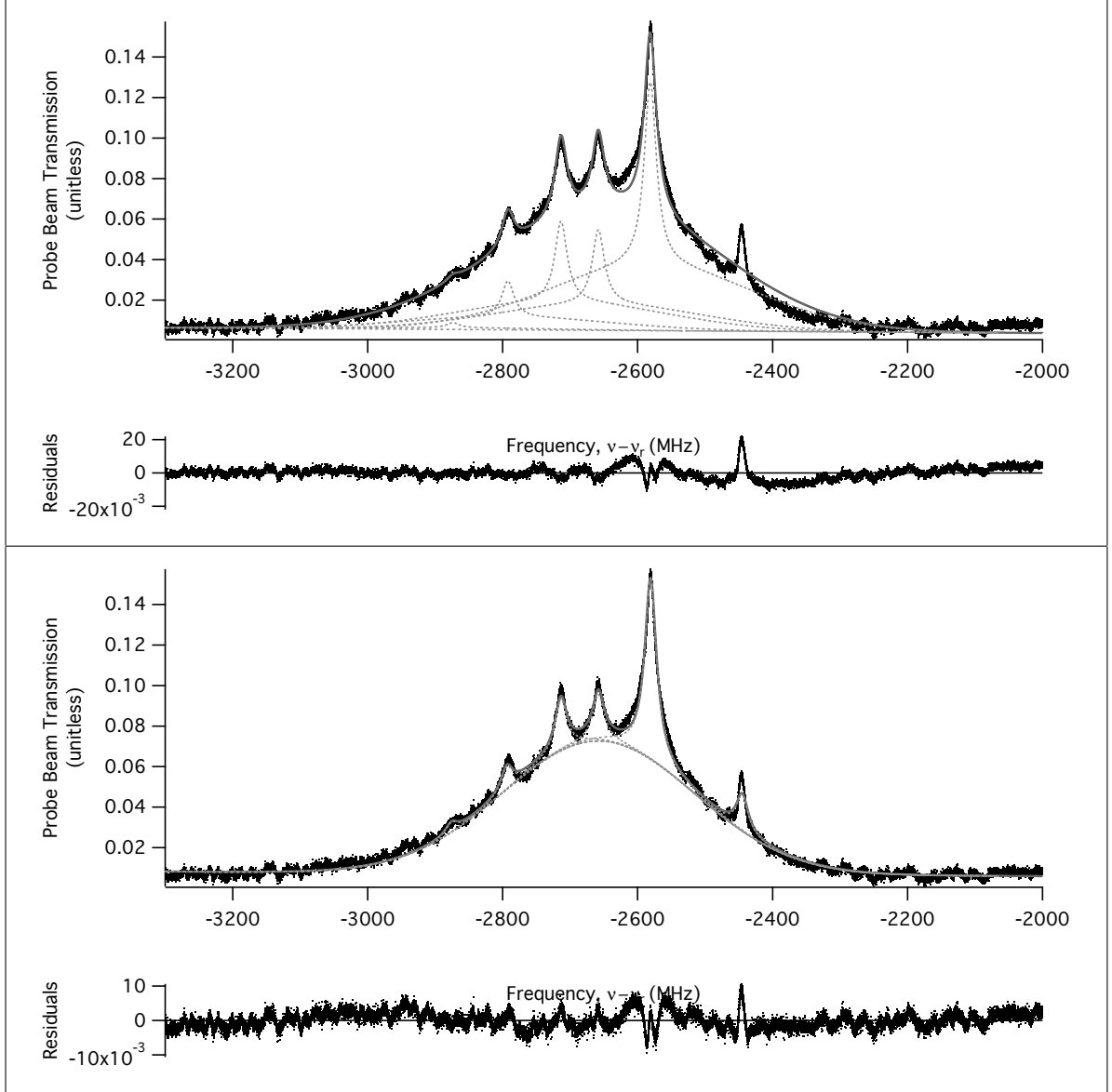


Figure 51. Data fits of both line shapes at 30 mTorr of Argon and 1700 Hz chopping frequency. The top plot is a fit using the first line shape, Eq.(11), and the bottom plot is the fit using the second line shape, Eq.(12). The vertical axis is the probe beam transmission relative to the incident beam intensity and the horizontal axis is the laser beam frequency (ν) relative to the $^{87}\text{Rb } D_2$ line (ν_r). The data is in (\bullet), the fit is in ($-$), and the individual hyperfine or cross-over line fit is ($- -$).

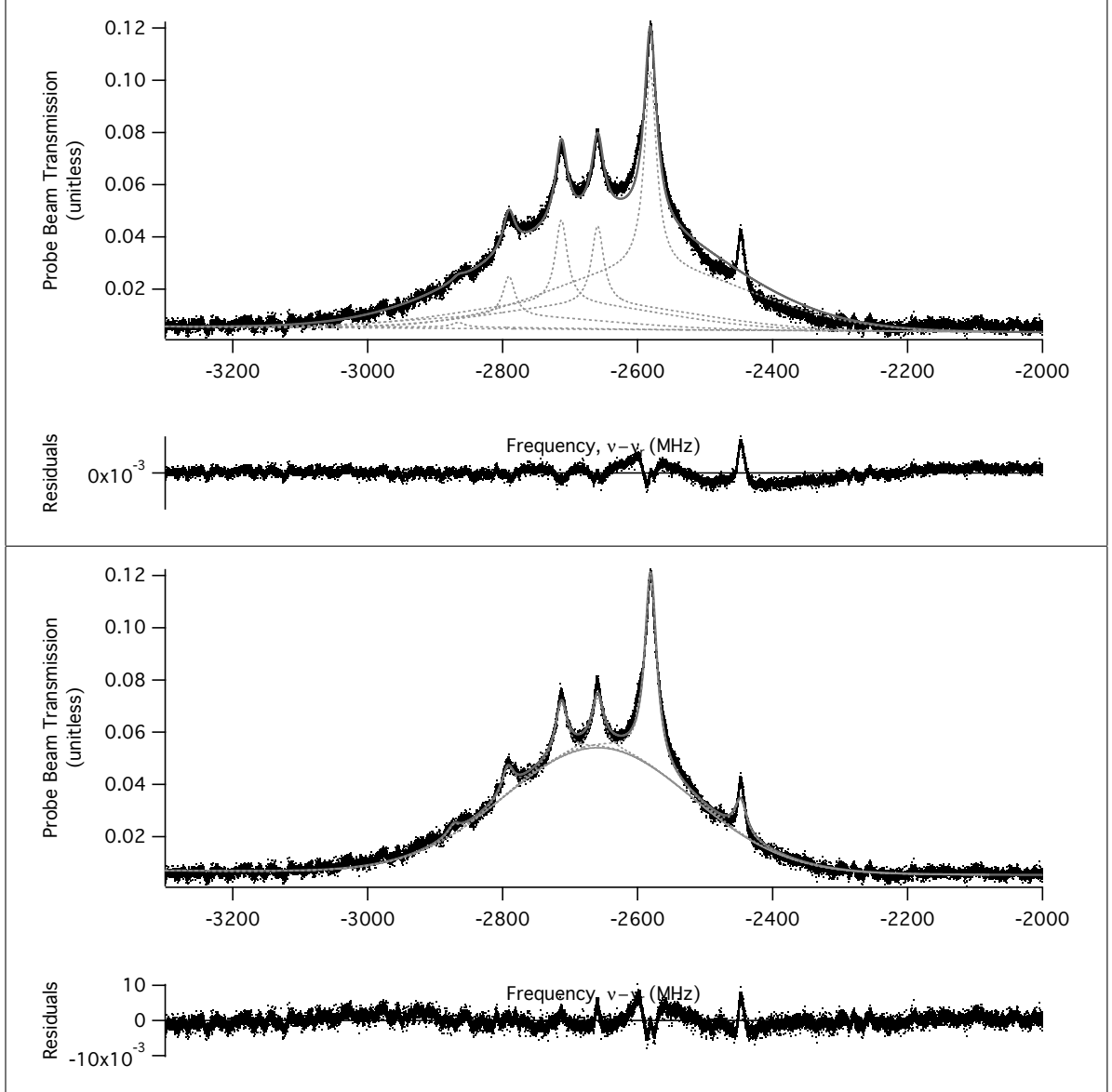


Figure 52. Data fits of both line shapes at 30 mTorr of Argon and 2200 Hz chopping frequency. The top plot is a fit using the first line shape, Eq.(11), and the bottom plot is the fit using the second line shape, Eq.(12). The vertical axis is the probe beam transmission relative to the incident beam intensity and the horizontal axis is the laser beam frequency (ν) relative to the $^{87}\text{Rb } D_2$ line (ν_r). The data is in (\bullet), the fit is in ($-$), and the individual hyperfine or cross-over line fit is ($- -$).

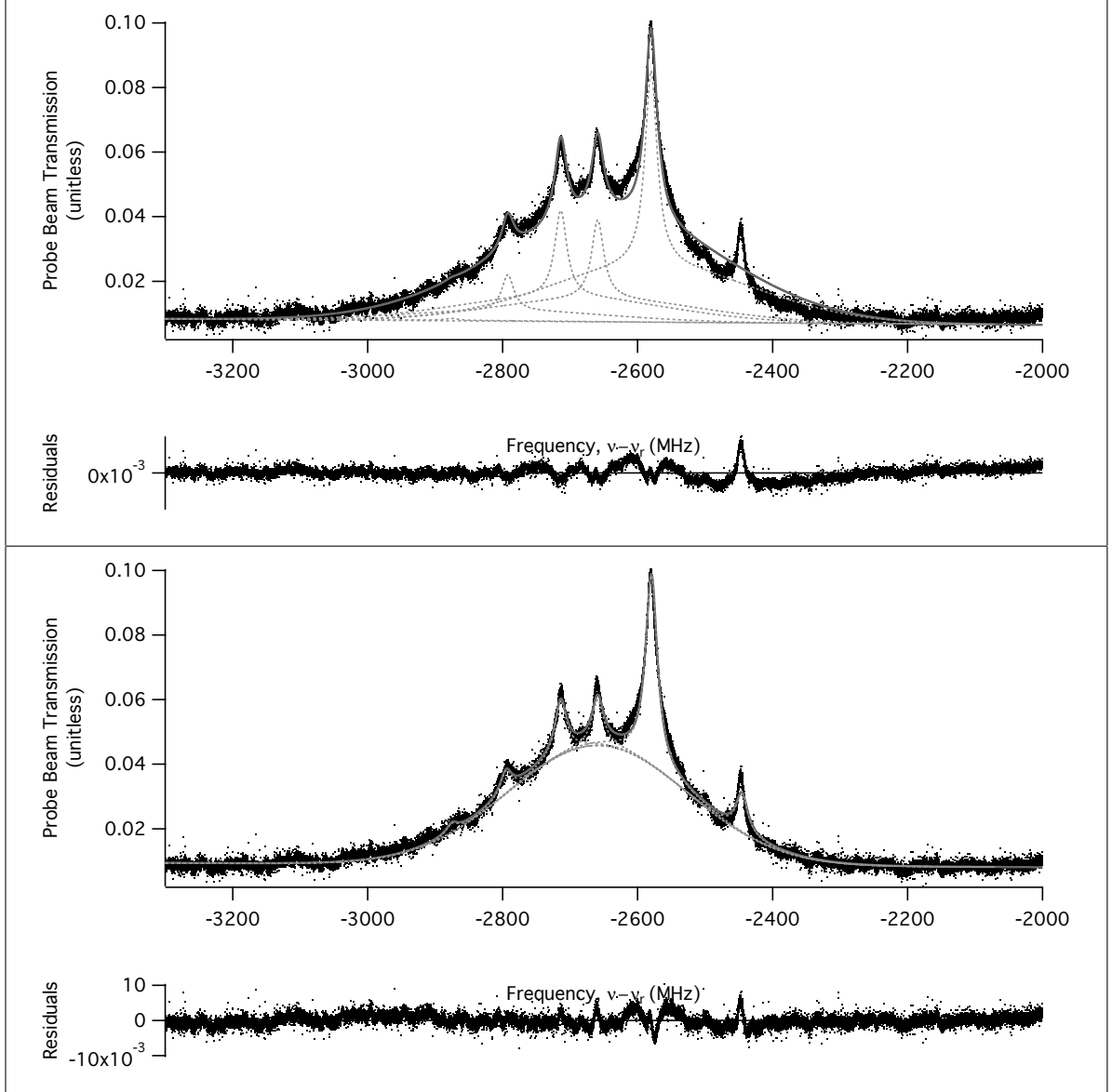


Figure 53. Data fits of both line shapes at 30 mTorr of Argon and 2800 Hz chopping frequency. The top plot is a fit using the first line shape, Eq.(11), and the bottom plot is the fit using the second line shape, Eq.(12). The vertical axis is the probe beam transmission relative to the incident beam intensity and the horizontal axis is the laser beam frequency (ν) relative to the $^{87}\text{Rb } D_2$ line (ν_r). The data is in (\bullet), the fit is in ($-$), and the individual hyperfine or cross-over line fit is ($- -$).

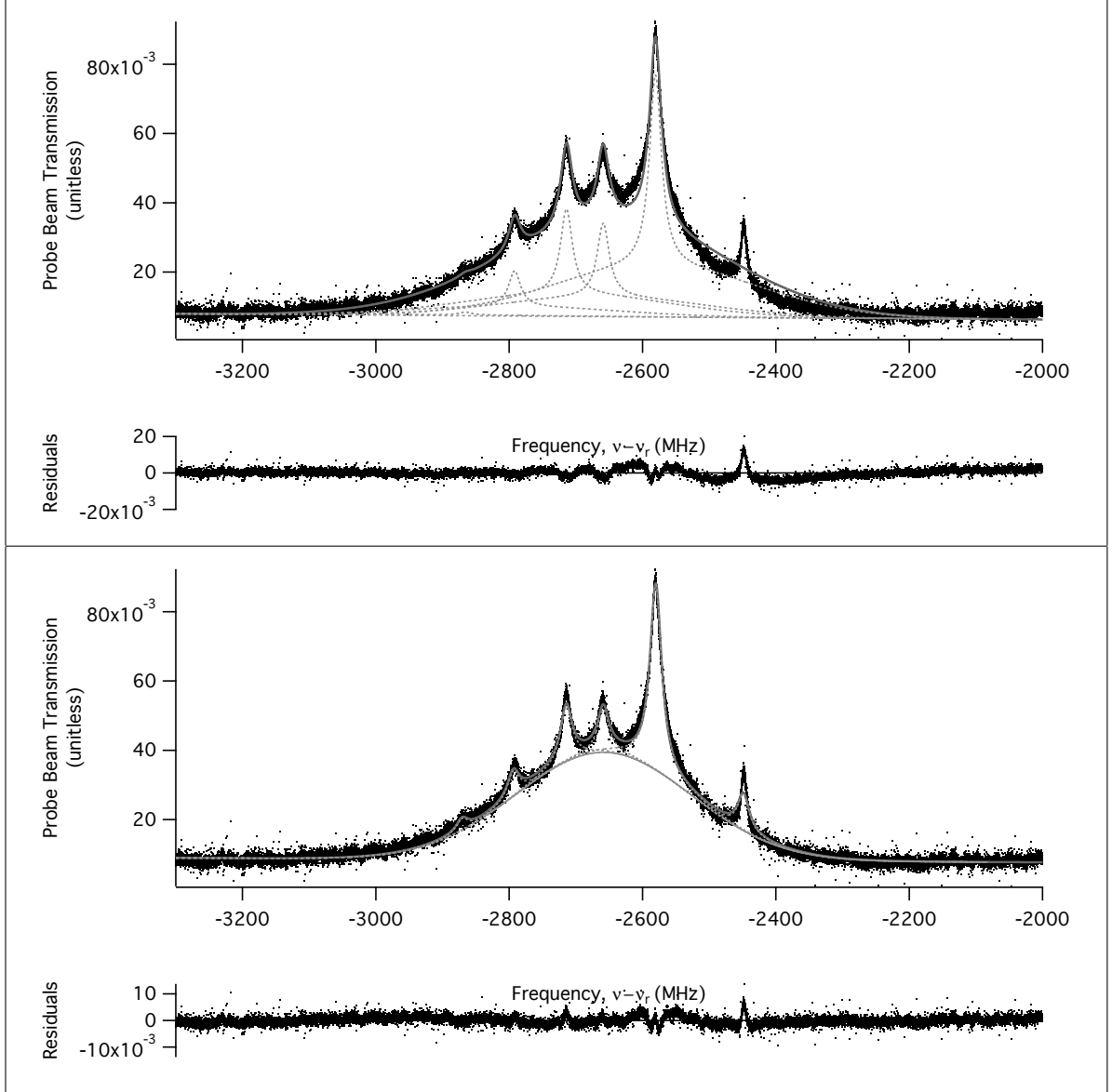


Figure 54. Data fits of both line shapes at 30 mTorr of Argon and 3200 Hz chopping frequency. The top plot is a fit using the first line shape, Eq.(11), and the bottom plot is the fit using the second line shape, Eq.(12). The vertical axis is the probe beam transmission relative to the incident beam intensity and the horizontal axis is the laser beam frequency (ν) relative to the $^{87}\text{Rb } D_2$ line (ν_r). The data is in (\bullet), the fit is in ($-$), and the individual hyperfine or cross-over line fit is ($- -$).

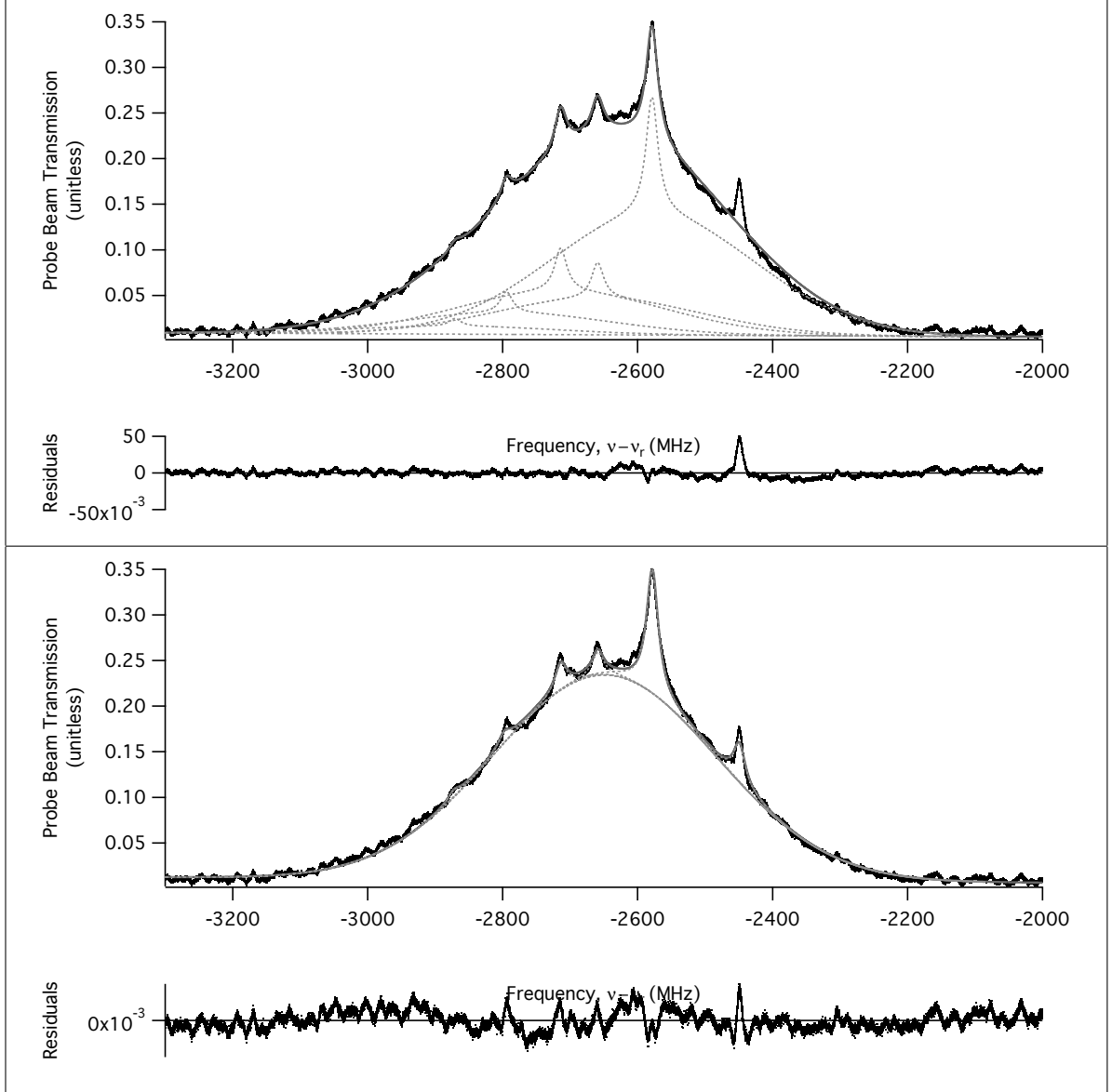


Figure 55. Data fits of both line shapes at 50 mTorr of Argon and 700 Hz chopping frequency. The top plot is a fit using the first line shape, Eq.(11), and the bottom plot is the fit using the second line shape, Eq.(12). The vertical axis is the probe beam transmission relative to the incident beam intensity and the horizontal axis is the laser beam frequency (ν) relative to the ^{87}Rb D_2 line (ν_r). The data is in (\bullet), the fit is in ($-$), and the individual hyperfine or cross-over line fit is ($- -$).

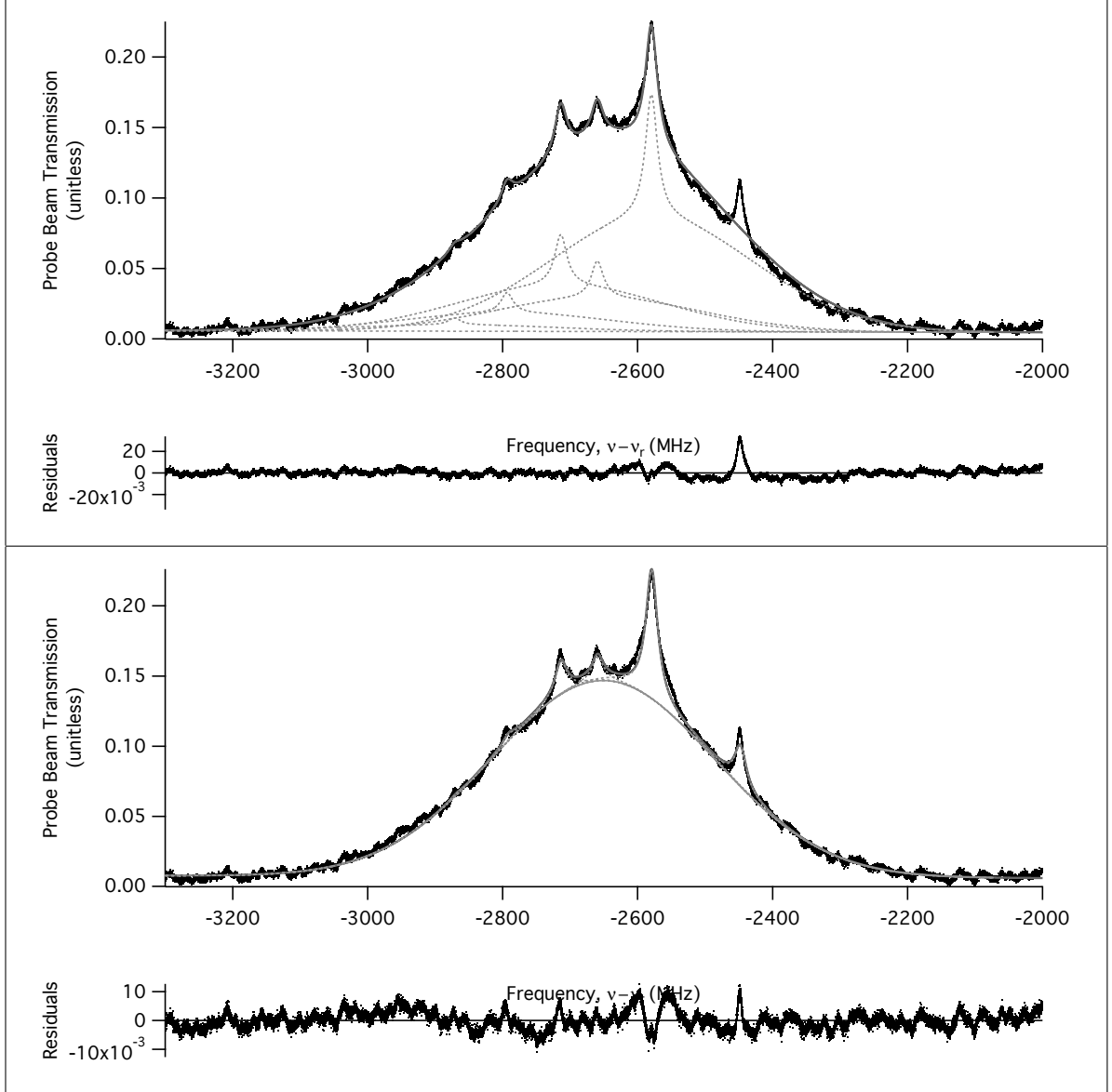


Figure 56. Data fits of both line shapes at 50 mTorr of Argon and 1100 Hz chopping frequency. The top plot is a fit using the first line shape, Eq.(11), and the bottom plot is the fit using the second line shape, Eq.(12). The vertical axis is the probe beam transmission relative to the incident beam intensity and the horizontal axis is the laser beam frequency (ν) relative to the ^{87}Rb D_2 line (ν_r). The data is in (\bullet), the fit is in ($-$), and the individual hyperfine or cross-over line fit is ($- -$).

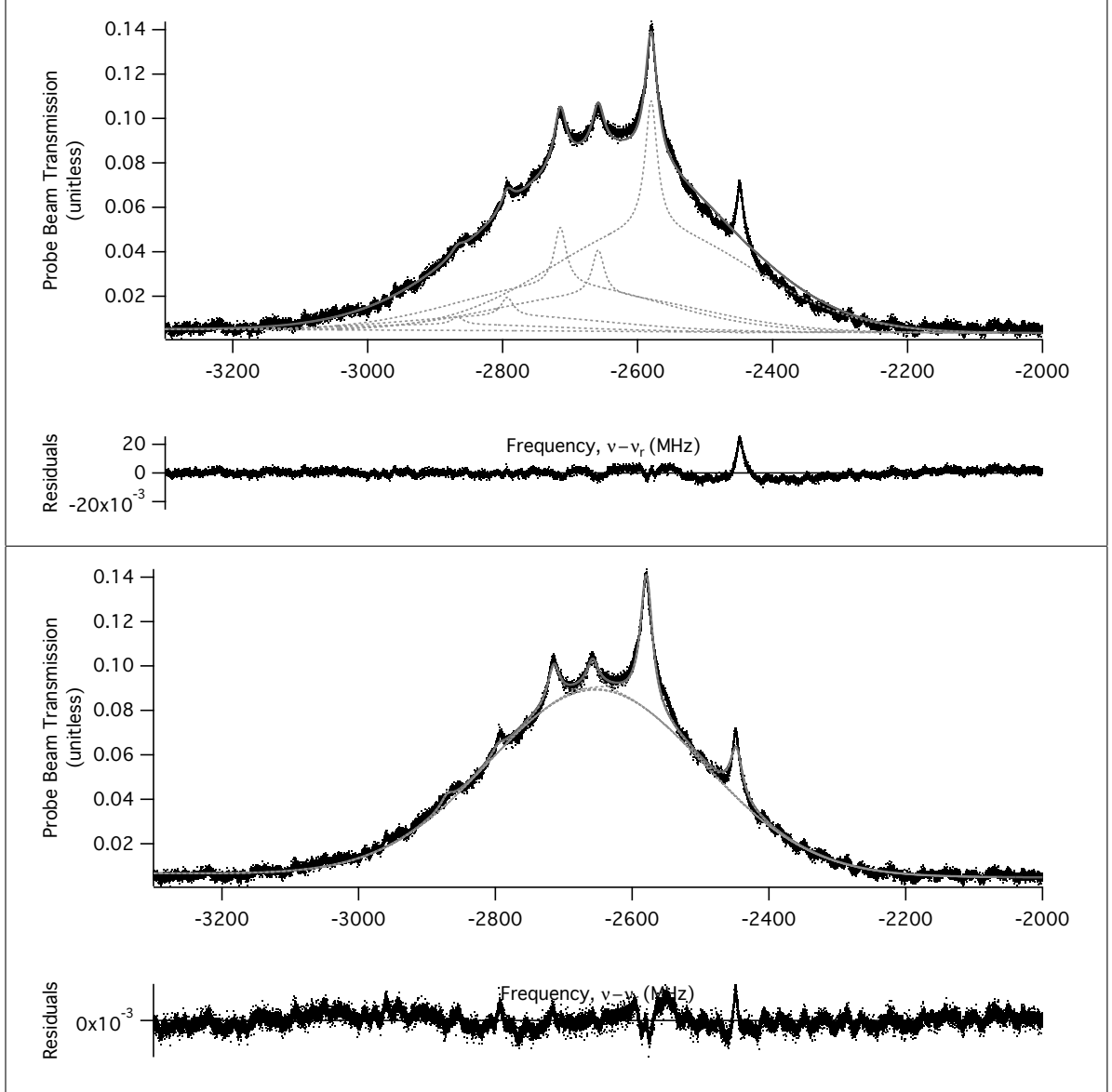


Figure 57. Data fits of both line shapes at 50 mTorr of Argon and 1700 Hz chopping frequency. The top plot is a fit using the first line shape, Eq.(11), and the bottom plot is the fit using the second line shape, Eq.(12). The vertical axis is the probe beam transmission relative to the incident beam intensity and the horizontal axis is the laser beam frequency (ν) relative to the ^{87}Rb D_2 line (ν_r). The data is in (\bullet), the fit is in ($-$), and the individual hyperfine or cross-over line fit is ($- -$).

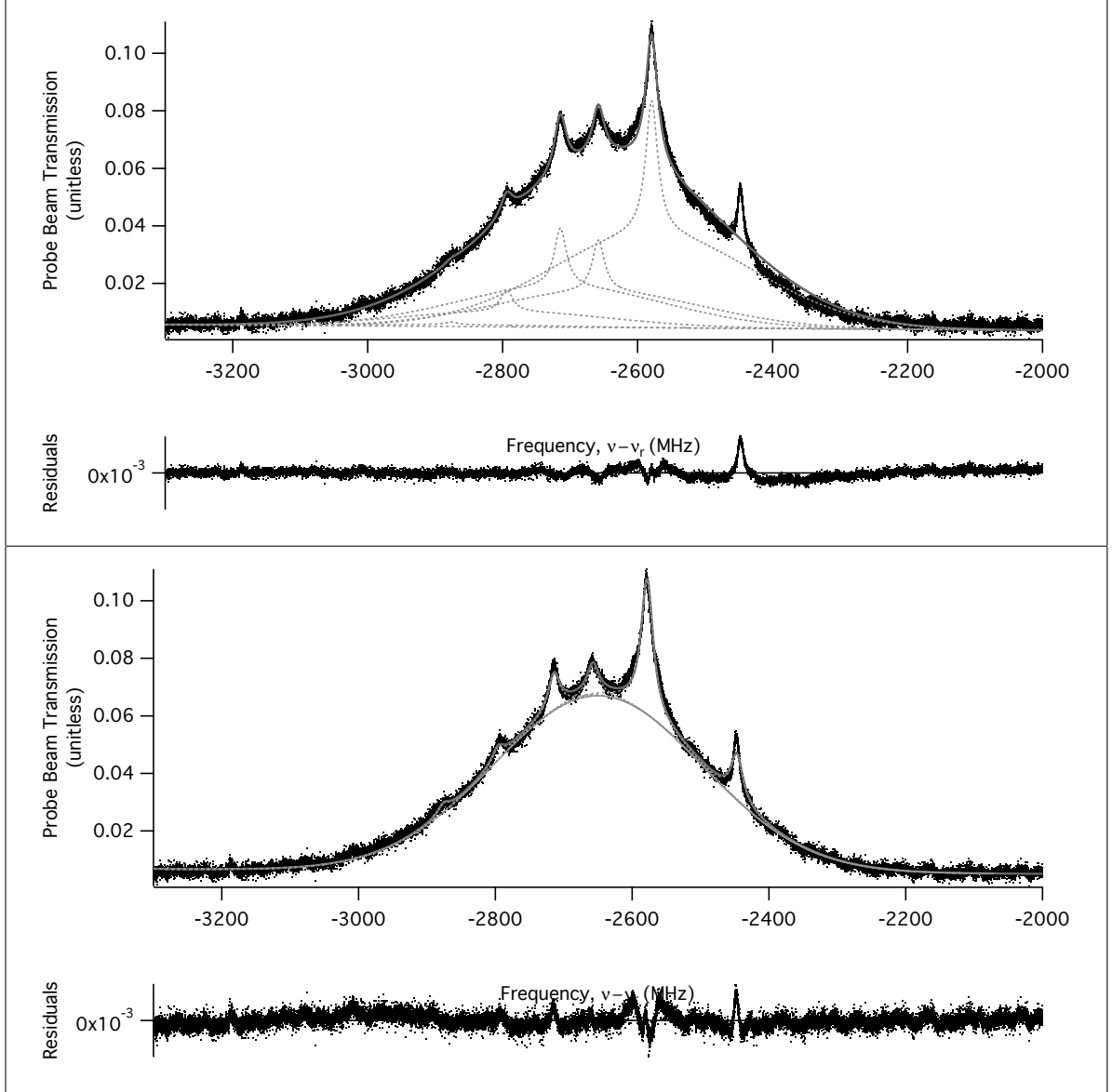


Figure 58. Data fits of both line shapes at 50 mTorr of Argon and 2200 Hz chopping frequency. The top plot is a fit using the first line shape, Eq.(11), and the bottom plot is the fit using the second line shape, Eq.(12). The vertical axis is the probe beam transmission relative to the incident beam intensity and the horizontal axis is the laser beam frequency (ν) relative to the $^{87}\text{Rb } D_2$ line (ν_r). The data is in (\bullet), the fit is in ($-$), and the individual hyperfine or cross-over line fit is ($- -$).

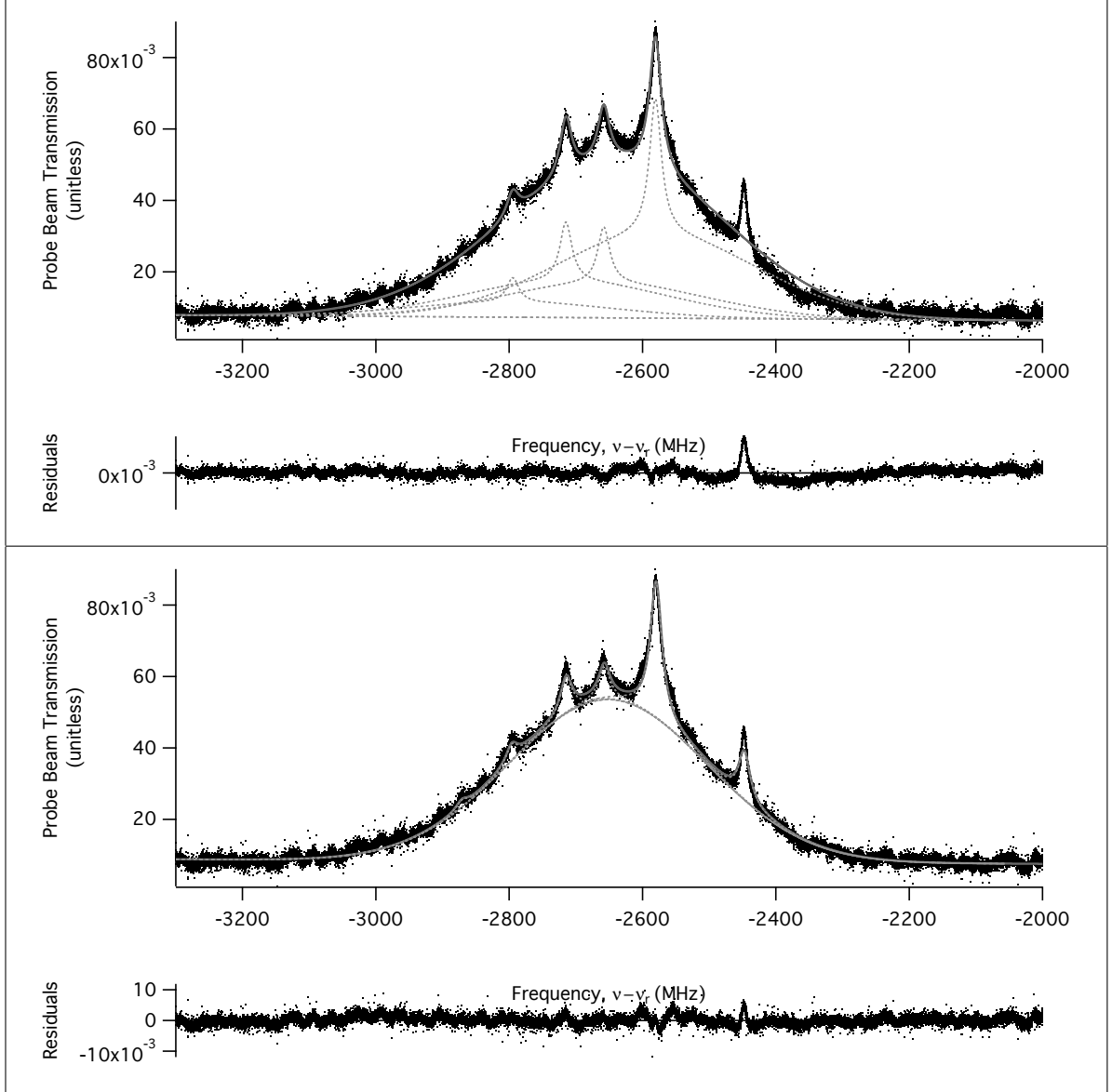


Figure 59. Data fits of both line shapes at 50 mTorr of Argon and 2800 Hz chopping frequency. The top plot is a fit using the first line shape, Eq.(11), and the bottom plot is the fit using the second line shape, Eq.(12). The vertical axis is the probe beam transmission relative to the incident beam intensity and the horizontal axis is the laser beam frequency (ν) relative to the $^{87}\text{Rb } D_2$ line (ν_r). The data is in (\bullet), the fit is in ($-$), and the individual hyperfine or cross-over line fit is ($- -$).

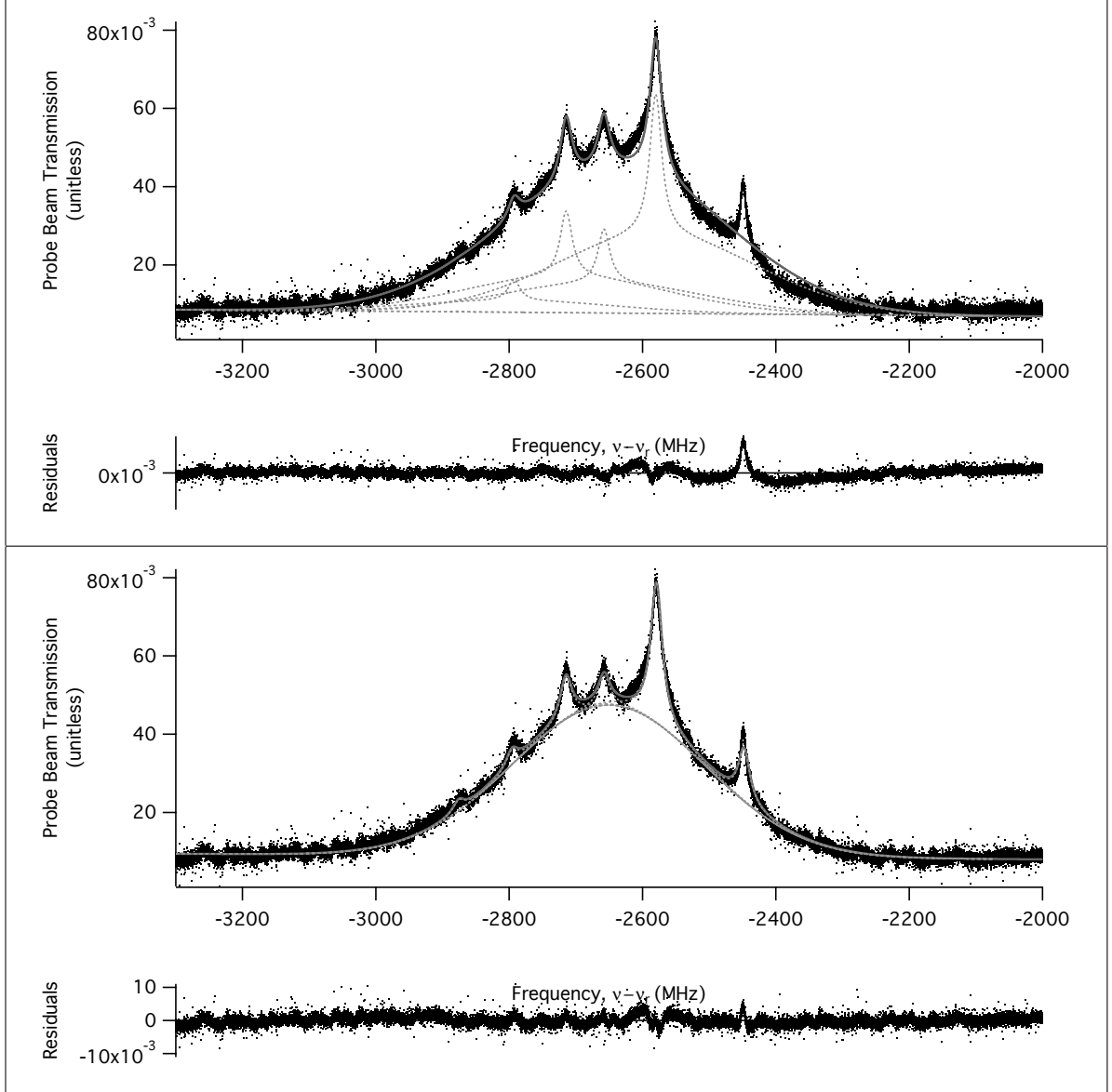


Figure 60. Data fits of both line shapes at 50 mTorr of Argon and 3200 Hz chopping frequency. The top plot is a fit using the first line shape, Eq.(11), and the bottom plot is the fit using the second line shape, Eq.(12). The vertical axis is the probe beam transmission relative to the incident beam intensity and the horizontal axis is the laser beam frequency (ν) relative to the $^{87}\text{Rb } D_2$ line (ν_r). The data is in (\bullet), the fit is in ($-$), and the individual hyperfine or cross-over line fit is ($- -$).

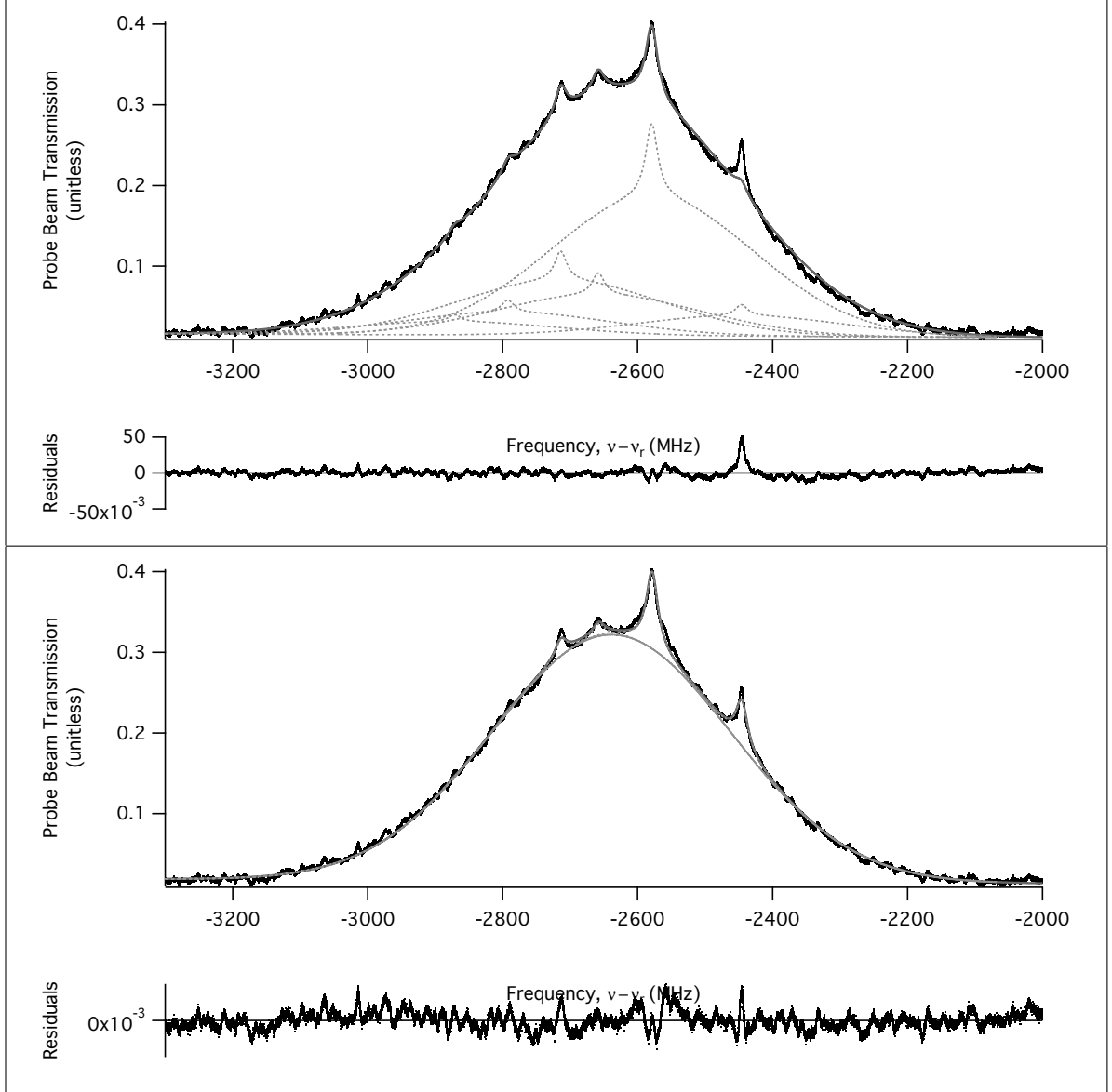


Figure 61. Data fits of both line shapes at 70 mTorr of Argon and 700 Hz chopping frequency. The top plot is a fit using the first line shape, Eq.(11), and the bottom plot is the fit using the second line shape, Eq.(12). The vertical axis is the probe beam transmission relative to the incident beam intensity and the horizontal axis is the laser beam frequency (ν) relative to the $^{87}\text{Rb } D_2$ line (ν_r). The data is in (\bullet), the fit is in ($-$), and the individual hyperfine or cross-over line fit is ($- -$).

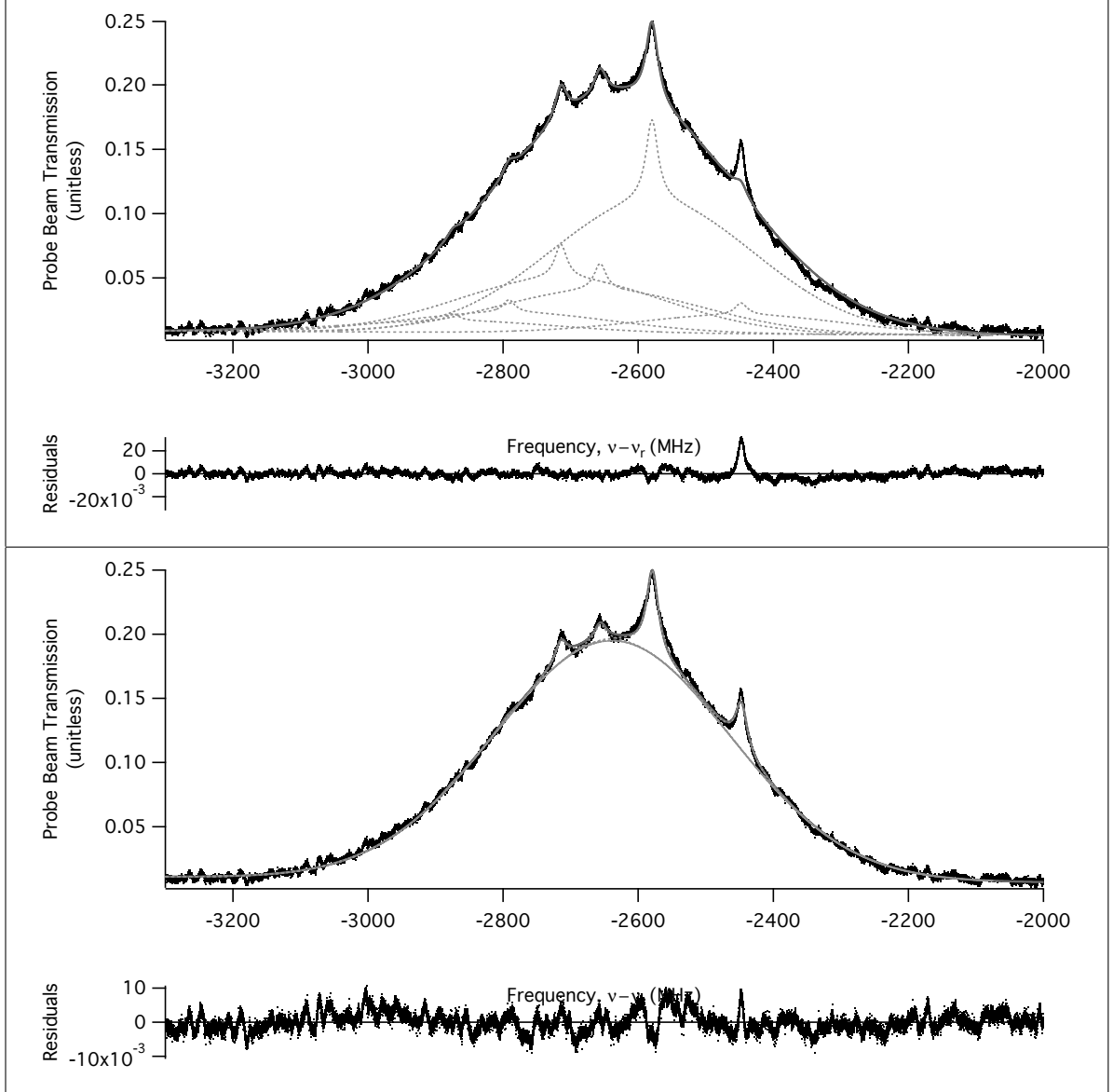


Figure 62. Data fits of both line shapes at 70 mTorr of Argon and 1100 Hz chopping frequency. The top plot is a fit using the first line shape, Eq.(11), and the bottom plot is the fit using the second line shape, Eq.(12). The vertical axis is the probe beam transmission relative to the incident beam intensity and the horizontal axis is the laser beam frequency (ν) relative to the $^{87}\text{Rb } D_2$ line (ν_r). The data is in (\bullet), the fit is in (—), and the individual hyperfine or cross-over line fit is (---).

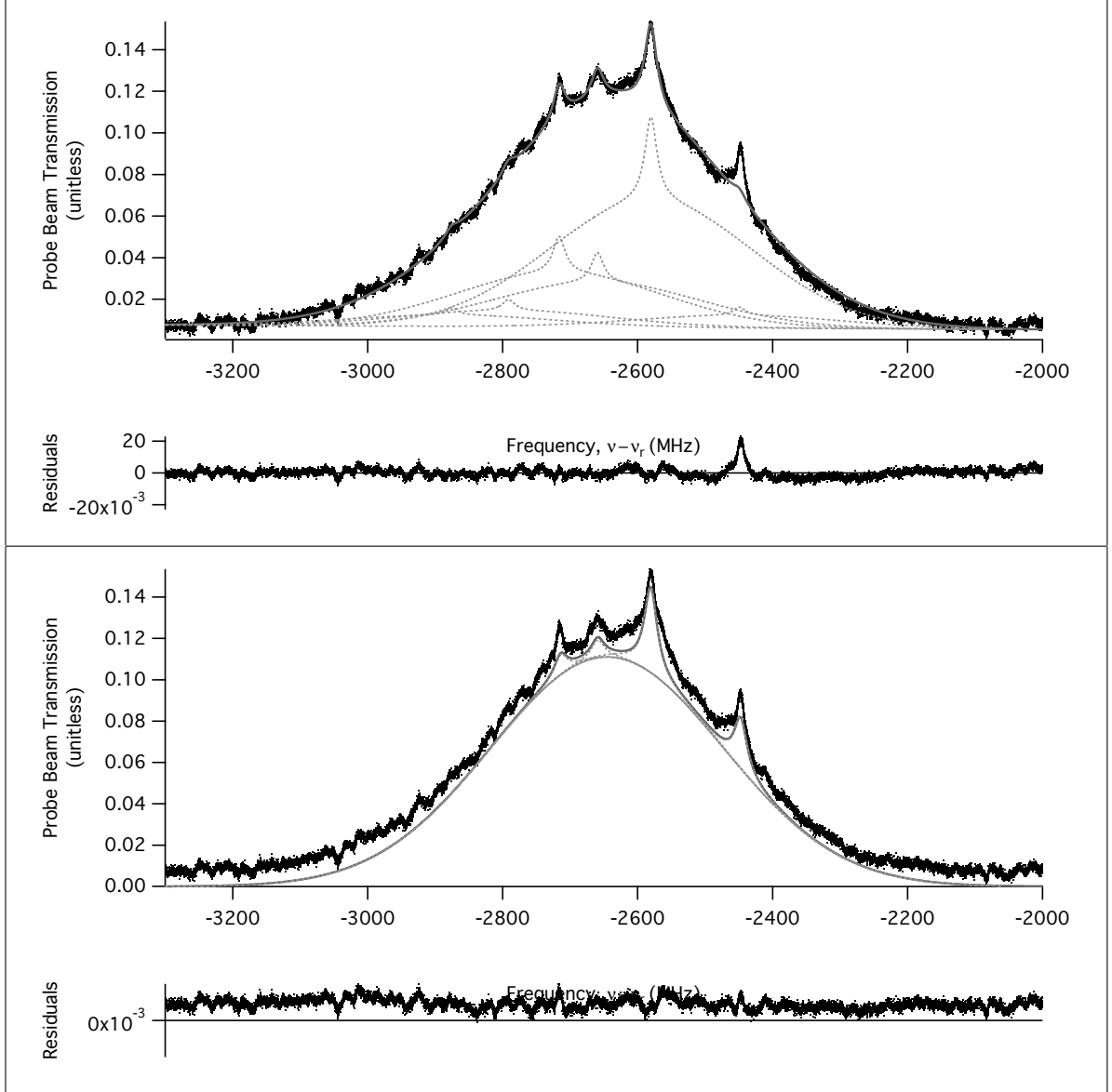


Figure 63. Data fits of both line shapes at 70 mTorr of Argon and 1700 Hz chopping frequency. The top plot is a fit using the first line shape, Eq.(11), and the bottom plot is the fit using the second line shape, Eq.(12). The vertical axis is the probe beam transmission relative to the incident beam intensity and the horizontal axis is the laser beam frequency (ν) relative to the ^{87}Rb D_2 line (ν_r). The data is in (\bullet), the fit is in ($-$), and the individual hyperfine or cross-over line fit is ($- -$).

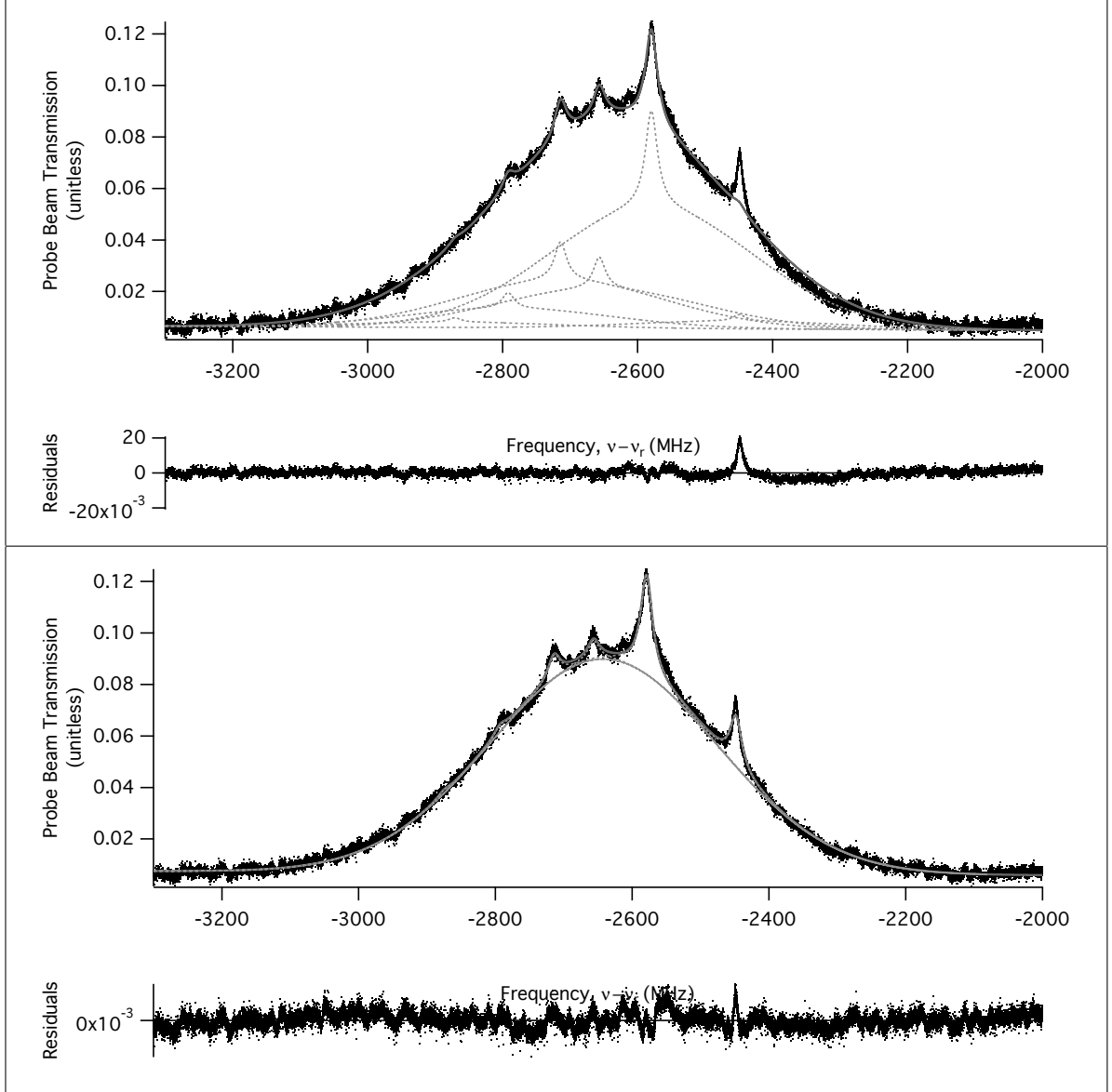


Figure 64. Data fits of both line shapes at 70 mTorr of Argon and 2200 Hz chopping frequency. The top plot is a fit using the first line shape, Eq.(11), and the bottom plot is the fit using the second line shape, Eq.(12). The vertical axis is the probe beam transmission relative to the incident beam intensity and the horizontal axis is the laser beam frequency (ν) relative to the $^{87}\text{Rb } D_2$ line (ν_r). The data is in (\bullet), the fit is in ($-$), and the individual hyperfine or cross-over line fit is ($- -$).

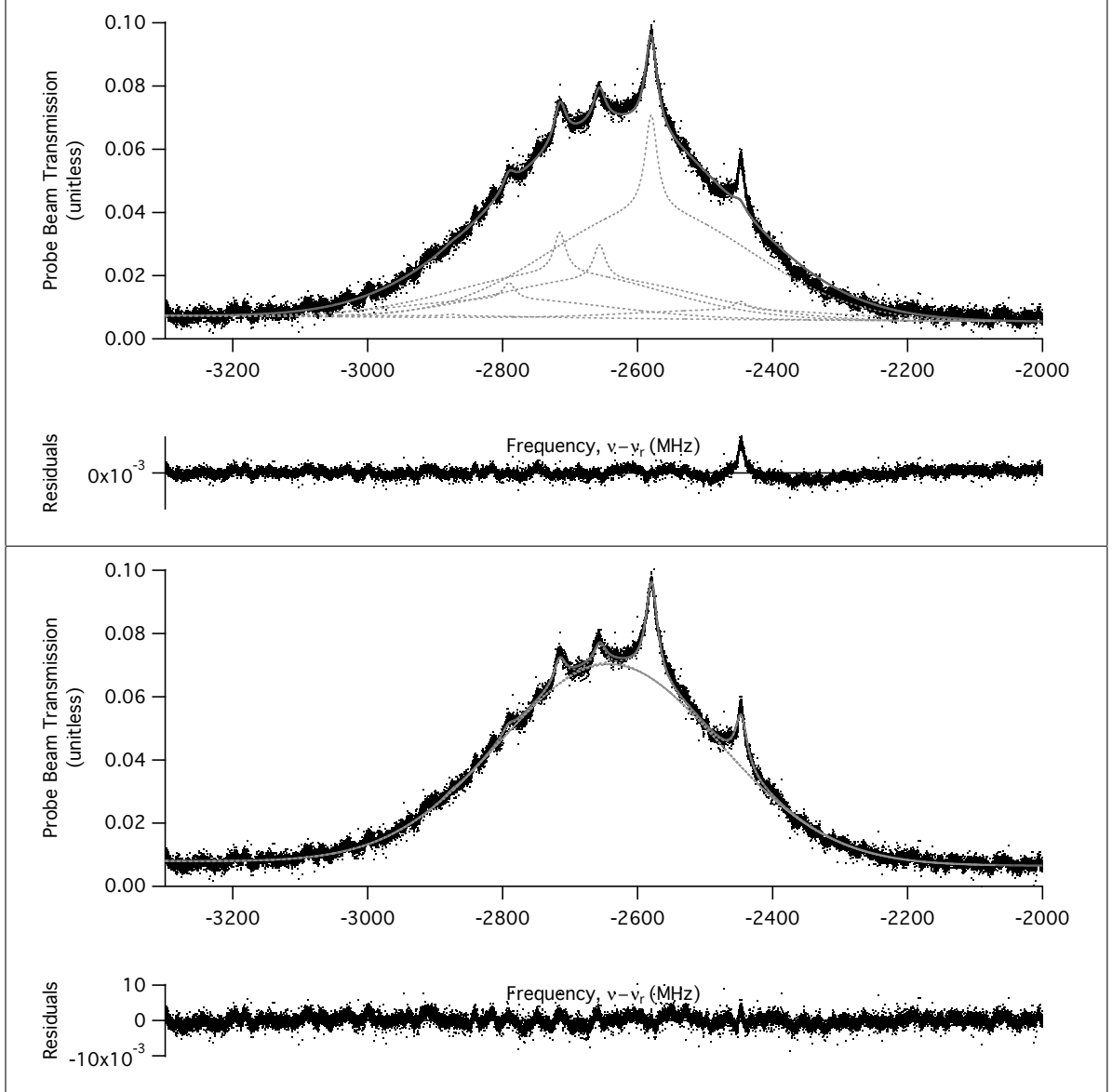


Figure 65. Data fits of both line shapes at 70 mTorr of Argon and 2800 Hz chopping frequency. The top plot is a fit using the first line shape, Eq.(11), and the bottom plot is the fit using the second line shape, Eq.(12). The vertical axis is the probe beam transmission relative to the incident beam intensity and the horizontal axis is the laser beam frequency (ν) relative to the $^{87}\text{Rb } D_2$ line (ν_r). The data is in (\bullet), the fit is in ($-$), and the individual hyperfine or cross-over line fit is ($- -$).

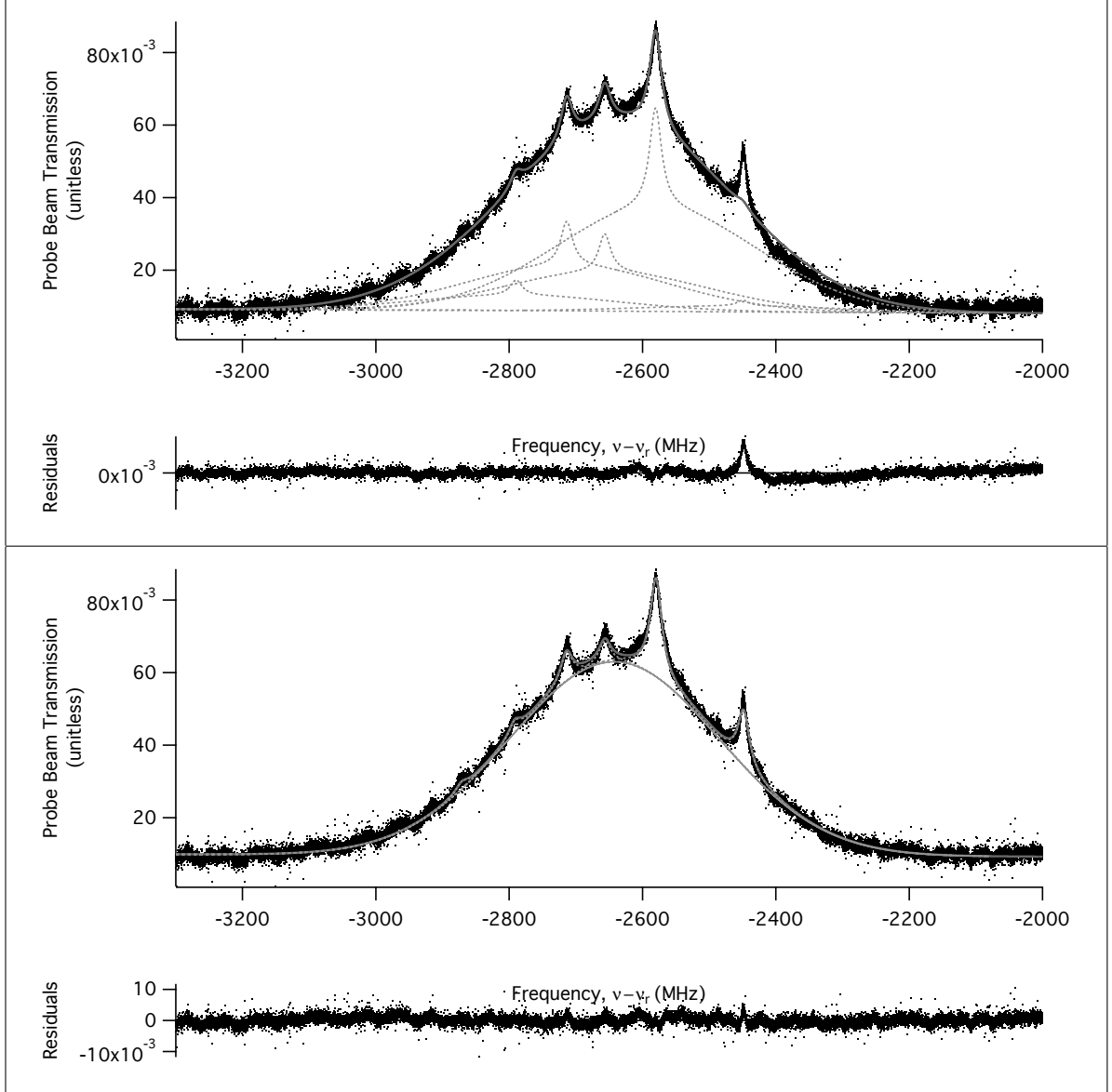


Figure 66. Data fits of both line shapes at 70 mTorr of Argon and 3200 Hz chopping frequency. The top plot is a fit using the first line shape, Eq.(11), and the bottom plot is the fit using the second line shape, Eq.(12). The vertical axis is the probe beam transmission relative to the incident beam intensity and the horizontal axis is the laser beam frequency (ν) relative to the $^{87}\text{Rb } D_2$ line (ν_r). The data is in (\bullet), the fit is in ($-$), and the individual hyperfine or cross-over line fit is ($- -$).

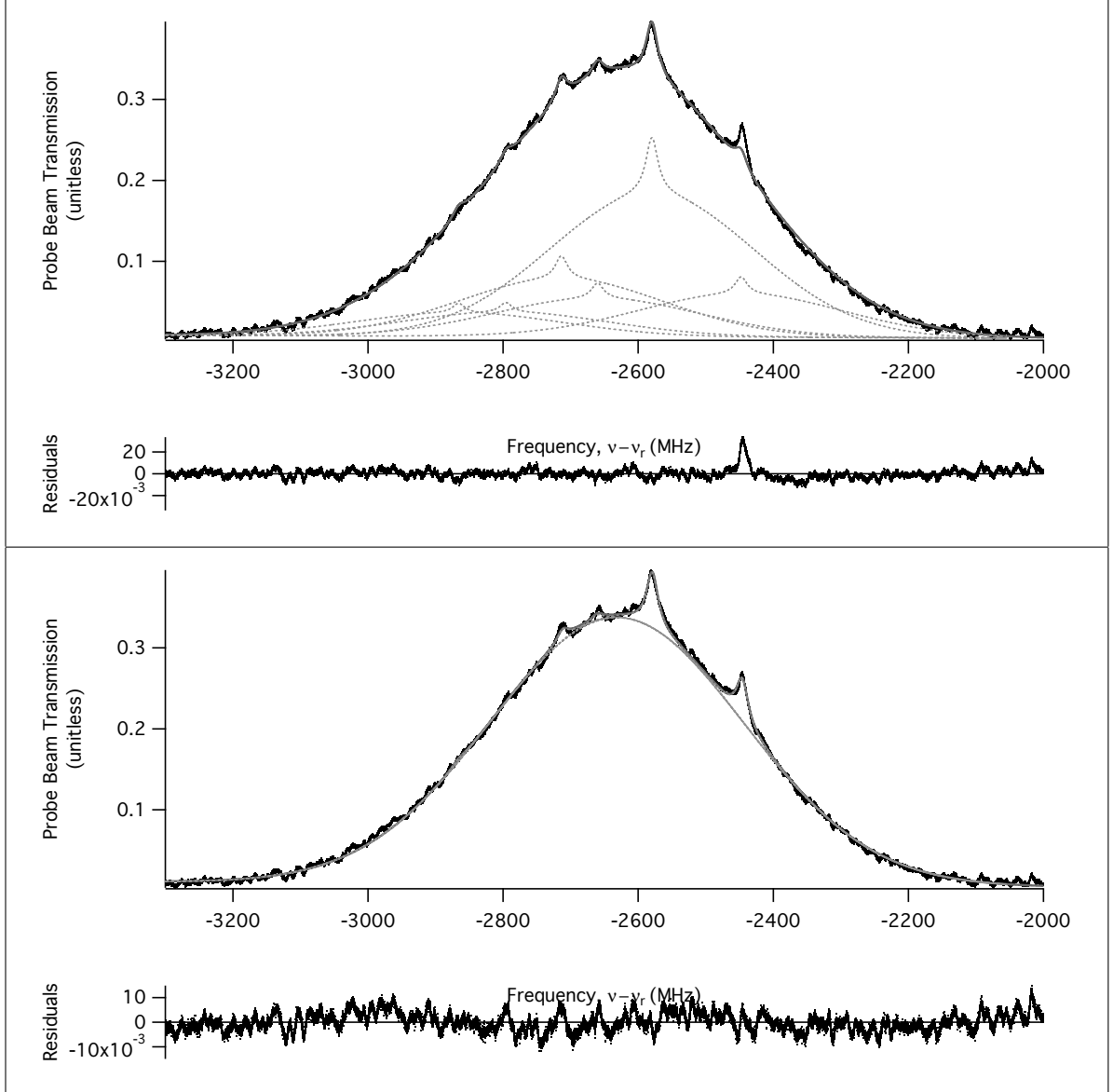


Figure 67. Data fits of both line shapes at 90 mTorr of Argon and 700 Hz chopping frequency. The top plot is a fit using the first line shape, Eq.(11), and the bottom plot is the fit using the second line shape, Eq.(12). The vertical axis is the probe beam transmission relative to the incident beam intensity and the horizontal axis is the laser beam frequency (ν) relative to the ^{87}Rb D_2 line (ν_r). The data is in (\bullet), the fit is in ($-$), and the individual hyperfine or cross-over line fit is ($- -$).

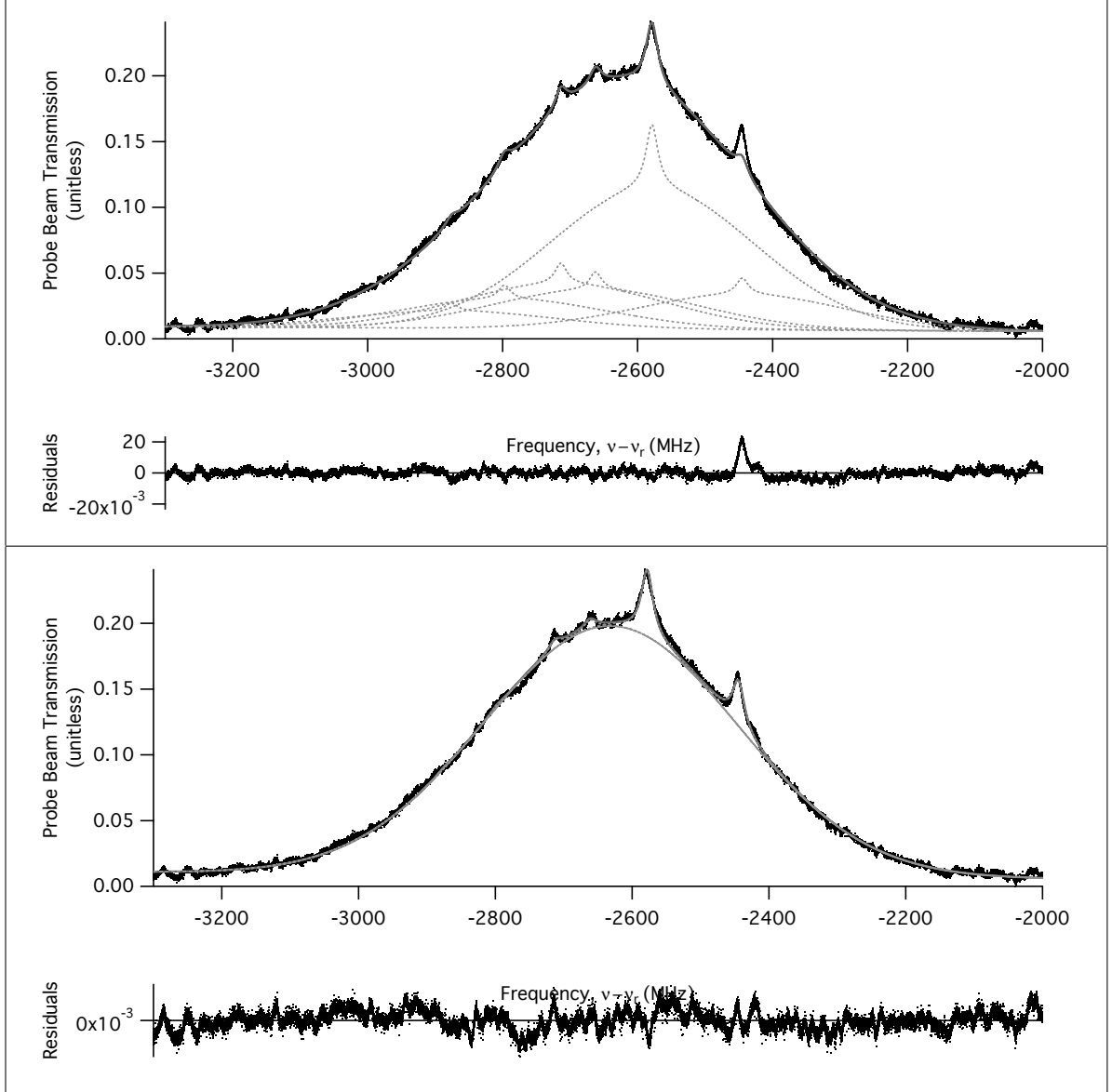


Figure 68. Data fits of both line shapes at 90 mTorr of Argon and 1100 Hz chopping frequency. The top plot is a fit using the first line shape, Eq.(11), and the bottom plot is the fit using the second line shape, Eq.(12). The vertical axis is the probe beam transmission relative to the incident beam intensity and the horizontal axis is the laser beam frequency (ν) relative to the ^{87}Rb D_2 line (ν_r). The data is in (\bullet), the fit is in ($-$), and the individual hyperfine or cross-over line fit is ($- -$).

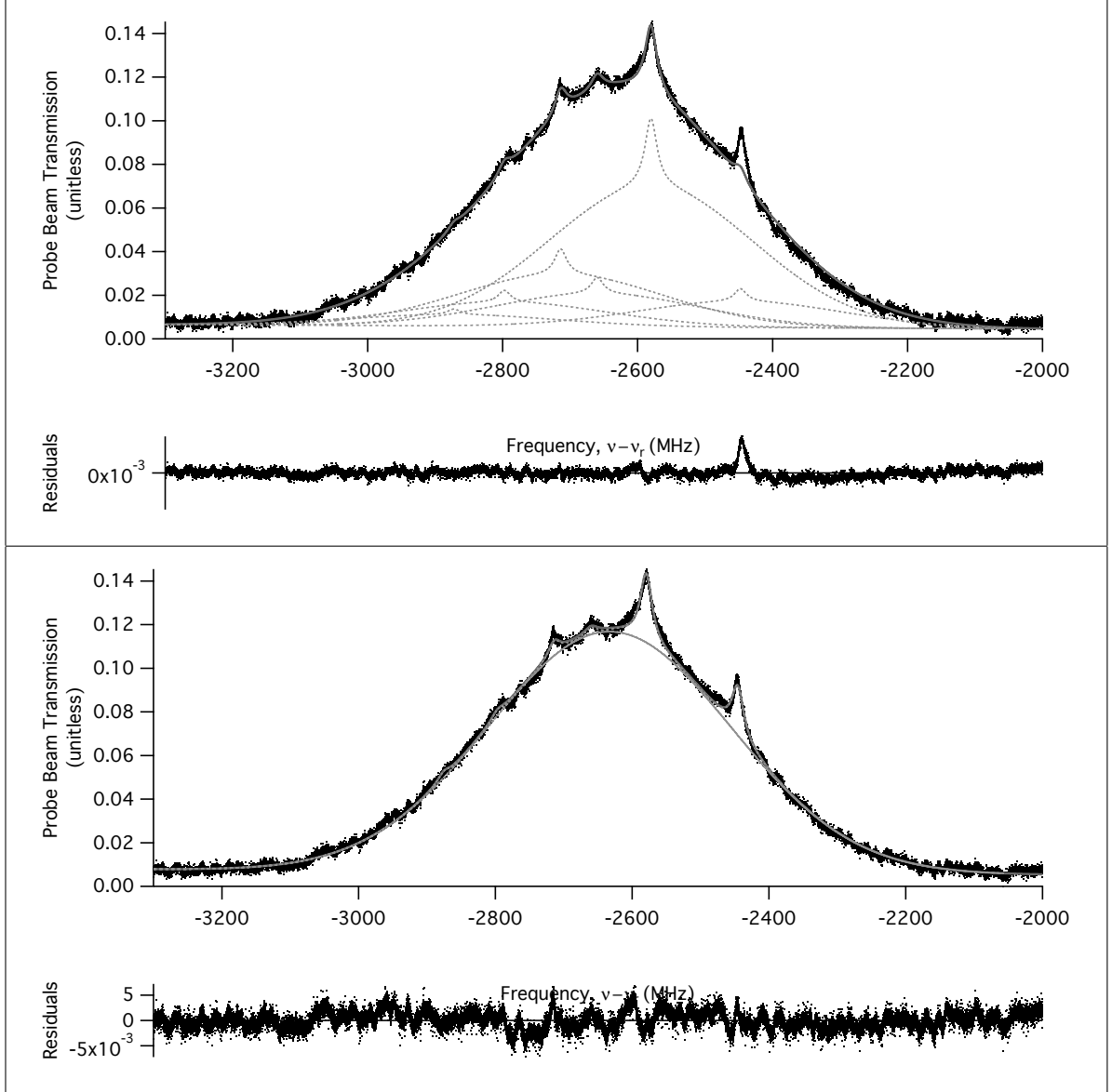


Figure 69. Data fits of both line shapes at 90 mTorr of Argon and 1700 Hz chopping frequency. The top plot is a fit using the first line shape, Eq.(11), and the bottom plot is the fit using the second line shape, Eq.(12). The vertical axis is the probe beam transmission relative to the incident beam intensity and the horizontal axis is the laser beam frequency (ν) relative to the ^{87}Rb D_2 line (ν_r). The data is in (\bullet), the fit is in ($-$), and the individual hyperfine or cross-over line fit is ($- -$).

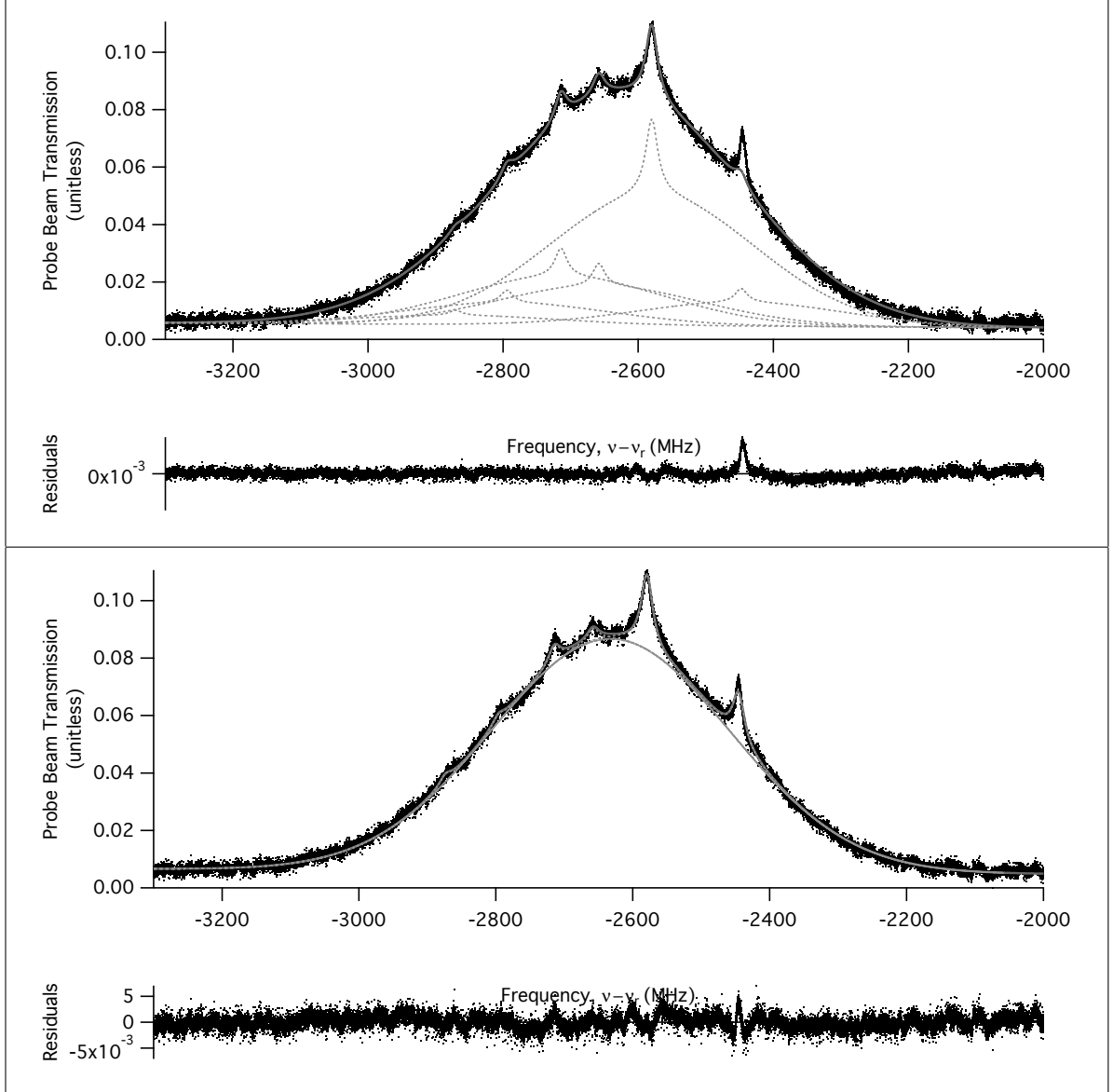


Figure 70. Data fits of both line shapes at 90 mTorr of Argon and 2200 Hz chopping frequency. The top plot is a fit using the first line shape, Eq.(11), and the bottom plot is the fit using the second line shape, Eq.(12). The vertical axis is the probe beam transmission relative to the incident beam intensity and the horizontal axis is the laser beam frequency (ν) relative to the $^{87}\text{Rb } D_2$ line (ν_r). The data is in (\bullet), the fit is in ($-$), and the individual hyperfine or cross-over line fit is ($- -$).

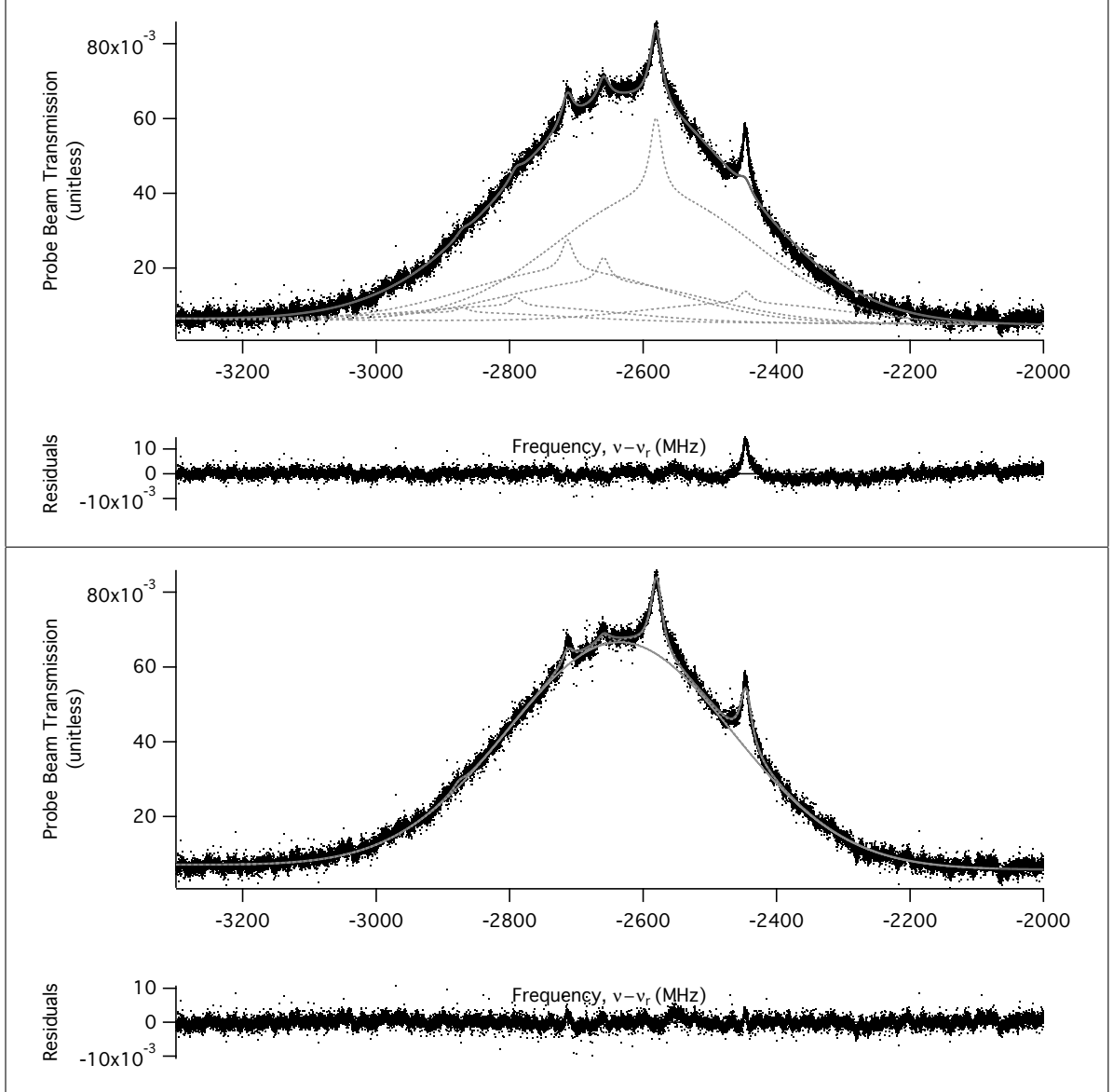


Figure 71. Data fits of both line shapes at 90 mTorr of Argon and 2800 Hz chopping frequency. The top plot is a fit using the first line shape, Eq.(11), and the bottom plot is the fit using the second line shape, Eq.(12). The vertical axis is the probe beam transmission relative to the incident beam intensity and the horizontal axis is the laser beam frequency (ν) relative to the ^{87}Rb D_2 line (ν_r). The data is in (\bullet), the fit is in ($-$), and the individual hyperfine or cross-over line fit is ($- -$).

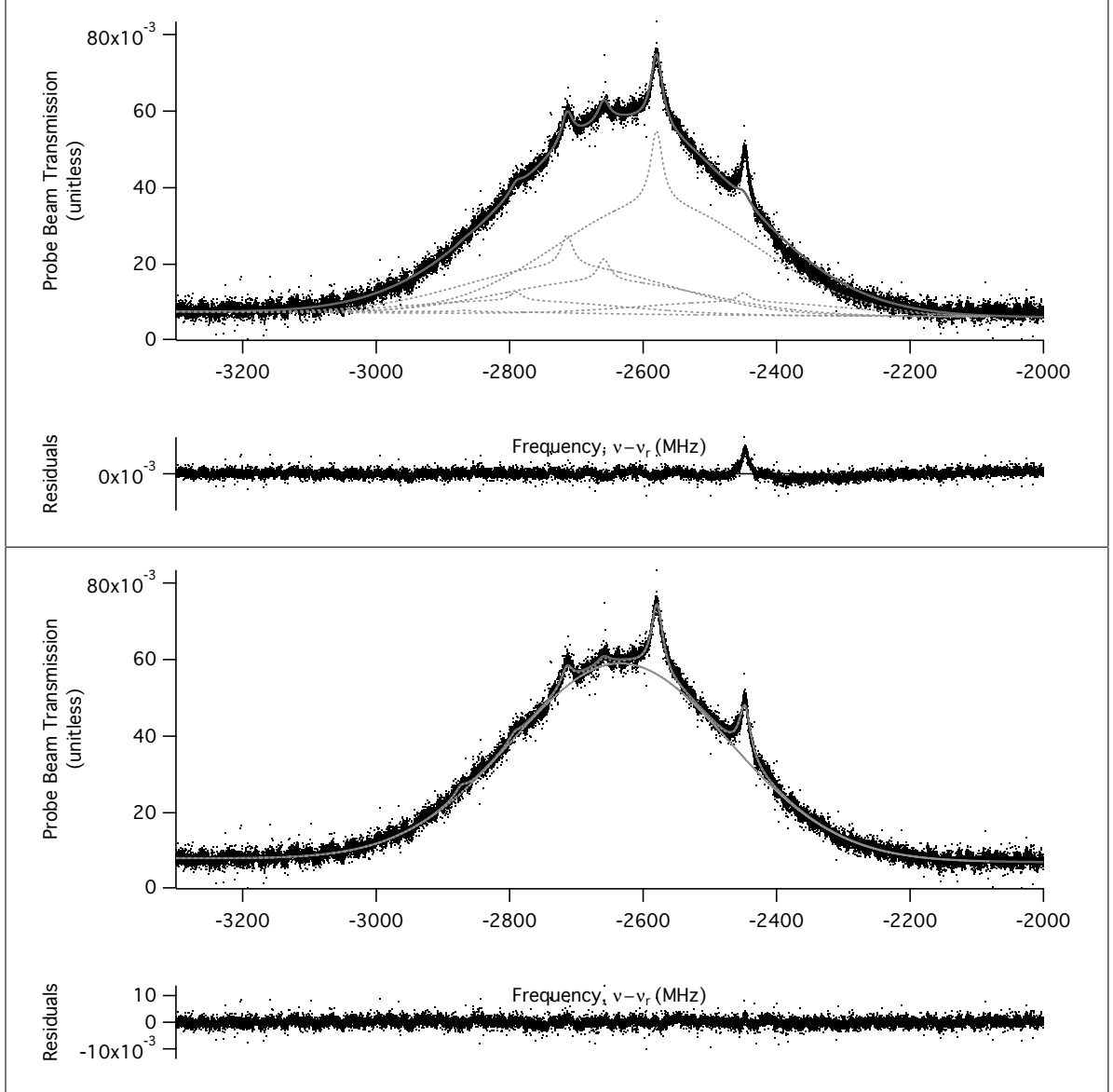


Figure 72. Data fits of both line shapes at 90 mTorr of Argon and 3200 Hz chopping frequency. The top plot is a fit using the first line shape, Eq.(11), and the bottom plot is the fit using the second line shape, Eq.(12). The vertical axis is the probe beam transmission relative to the incident beam intensity and the horizontal axis is the laser beam frequency (ν) relative to the ^{87}Rb D_2 line (ν_r). The data is in (\bullet), the fit is in ($-$), and the individual hyperfine or cross-over line fit is ($- -$).

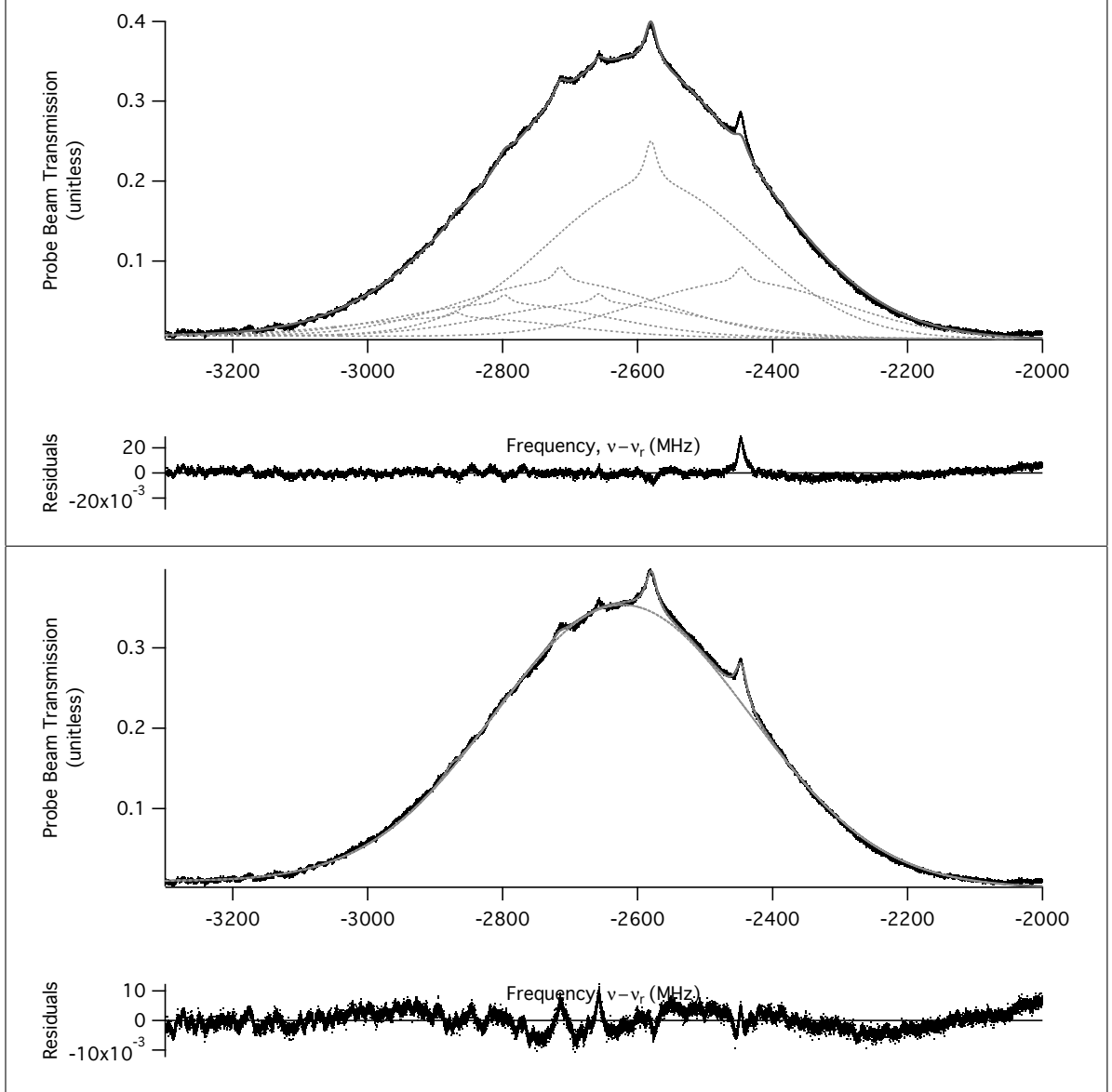


Figure 73. Data fits of both line shapes at 110 mTorr of Argon and 700 Hz chopping frequency. The top plot is a fit using the first line shape, Eq.(11), and the bottom plot is the fit using the second line shape, Eq.(12). The vertical axis is the probe beam transmission relative to the incident beam intensity and the horizontal axis is the laser beam frequency (ν) relative to the ^{87}Rb D_2 line (ν_r). The data is in (\bullet), the fit is in ($-$), and the individual hyperfine or cross-over line fit is ($- -$).

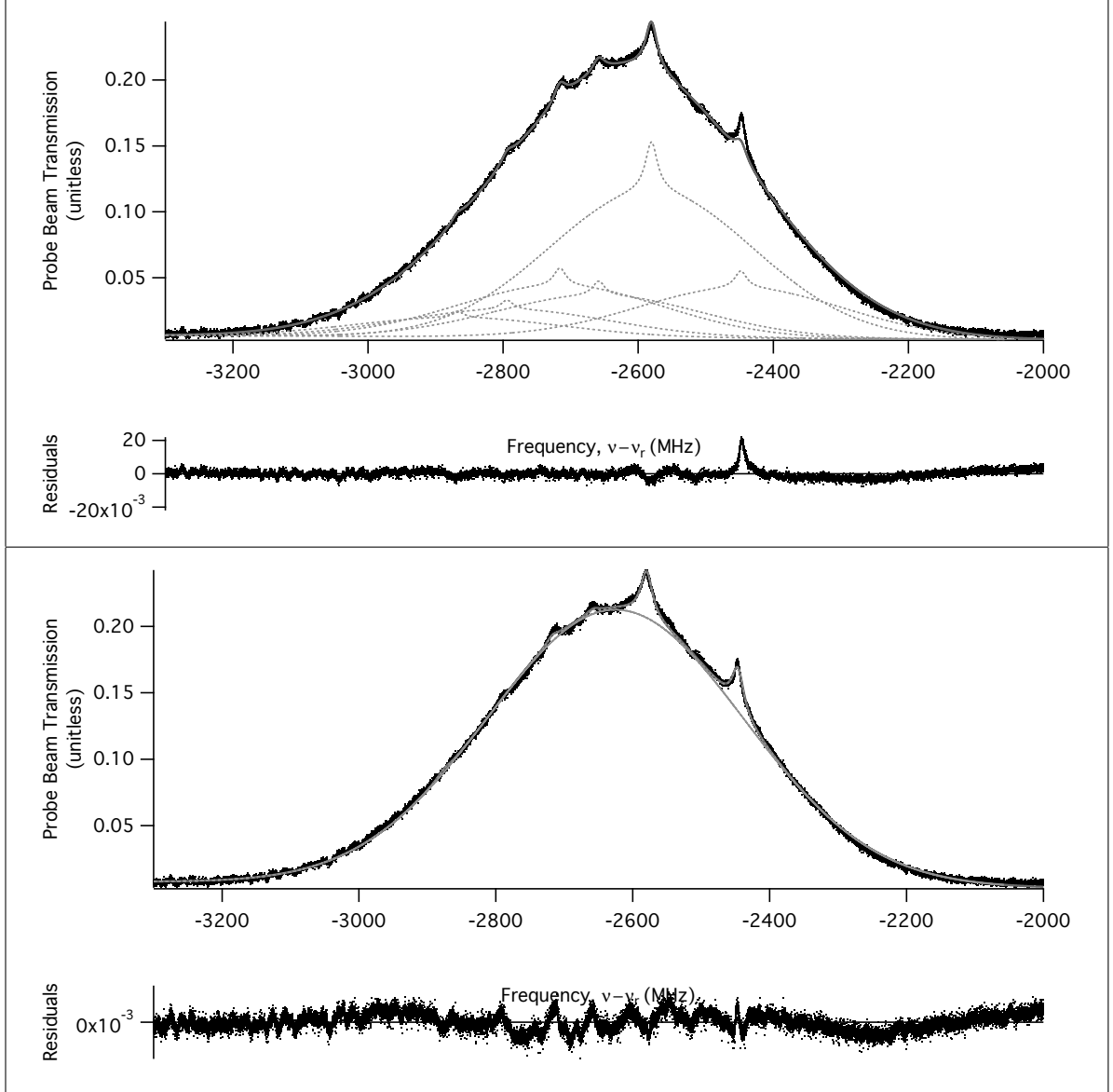


Figure 74. Data fits of both line shapes at 110 mTorr of Argon and 1100 Hz chopping frequency. The top plot is a fit using the first line shape, Eq.(11), and the bottom plot is the fit using the second line shape, Eq.(12). The vertical axis is the probe beam transmission relative to the incident beam intensity and the horizontal axis is the laser beam frequency (ν) relative to the ^{87}Rb D_2 line (ν_r). The data is in (\bullet), the fit is in ($-$), and the individual hyperfine or cross-over line fit is ($- -$).

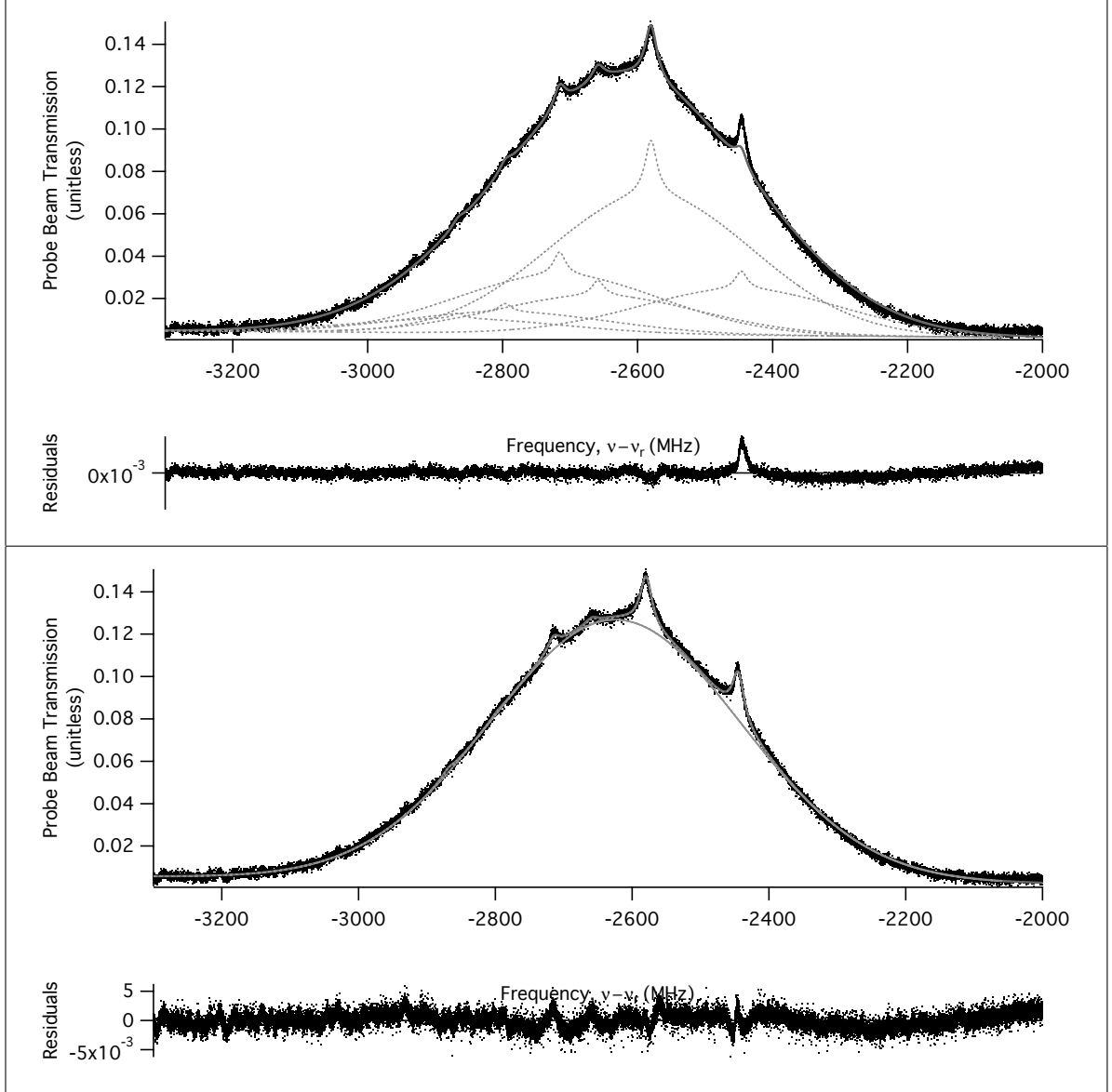


Figure 75. Data fits of both line shapes at 110 mTorr of Argon and 1700 Hz chopping frequency. The top plot is a fit using the first line shape, Eq.(11), and the bottom plot is the fit using the second line shape, Eq.(12). The vertical axis is the probe beam transmission relative to the incident beam intensity and the horizontal axis is the laser beam frequency (ν) relative to the ^{87}Rb D_2 line (ν_r). The data is in (\bullet), the fit is in ($-$), and the individual hyperfine or cross-over line fit is ($- -$).

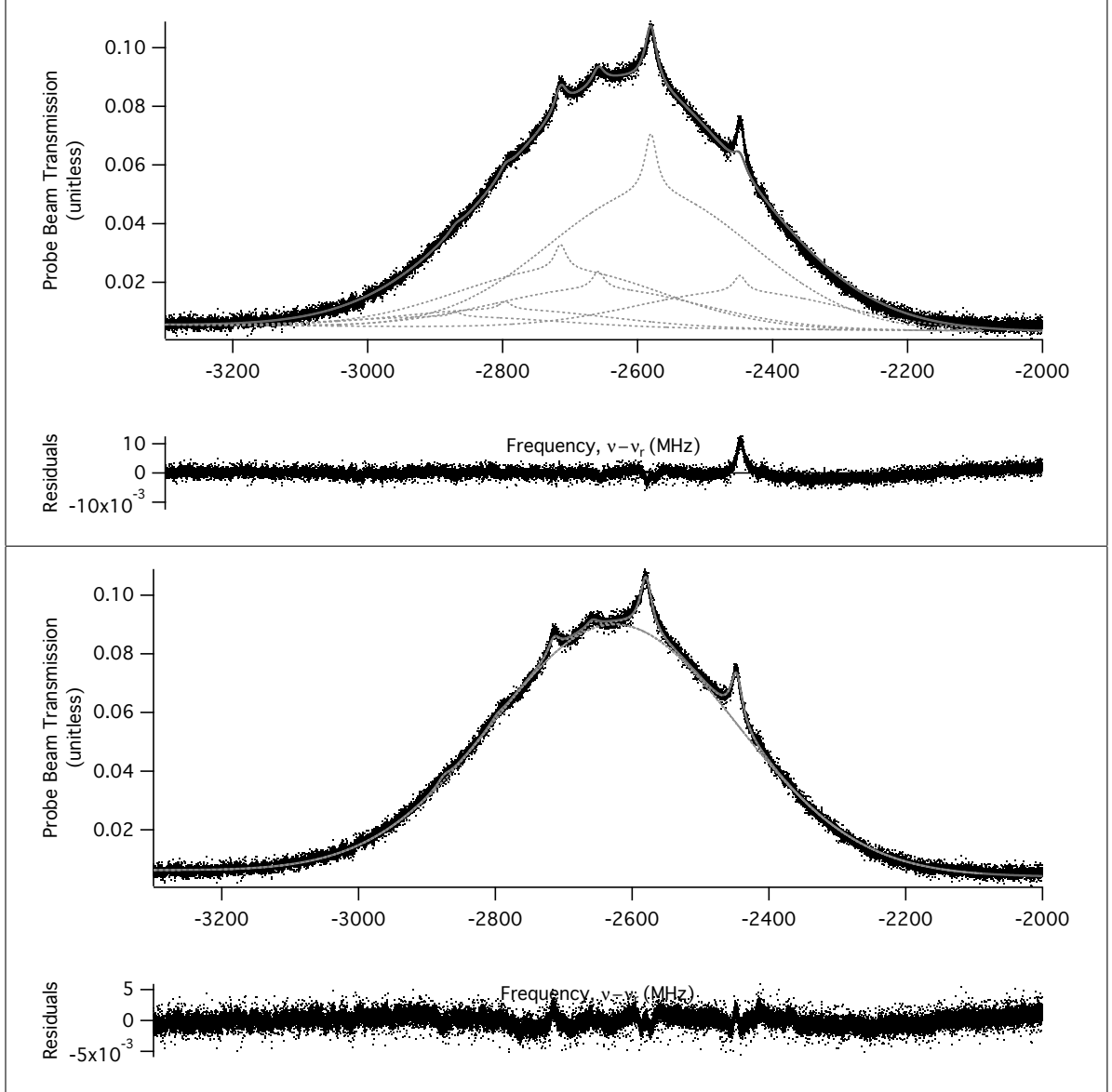


Figure 76. Data fits of both line shapes at 110 mTorr of Argon and 2200 Hz chopping frequency. The top plot is a fit using the first line shape, Eq.(11), and the bottom plot is the fit using the second line shape, Eq.(12). The vertical axis is the probe beam transmission relative to the incident beam intensity and the horizontal axis is the laser beam frequency (ν) relative to the $^{87}\text{Rb } D_2$ line (ν_r). The data is in (\bullet), the fit is in ($-$), and the individual hyperfine or cross-over line fit is ($- -$).

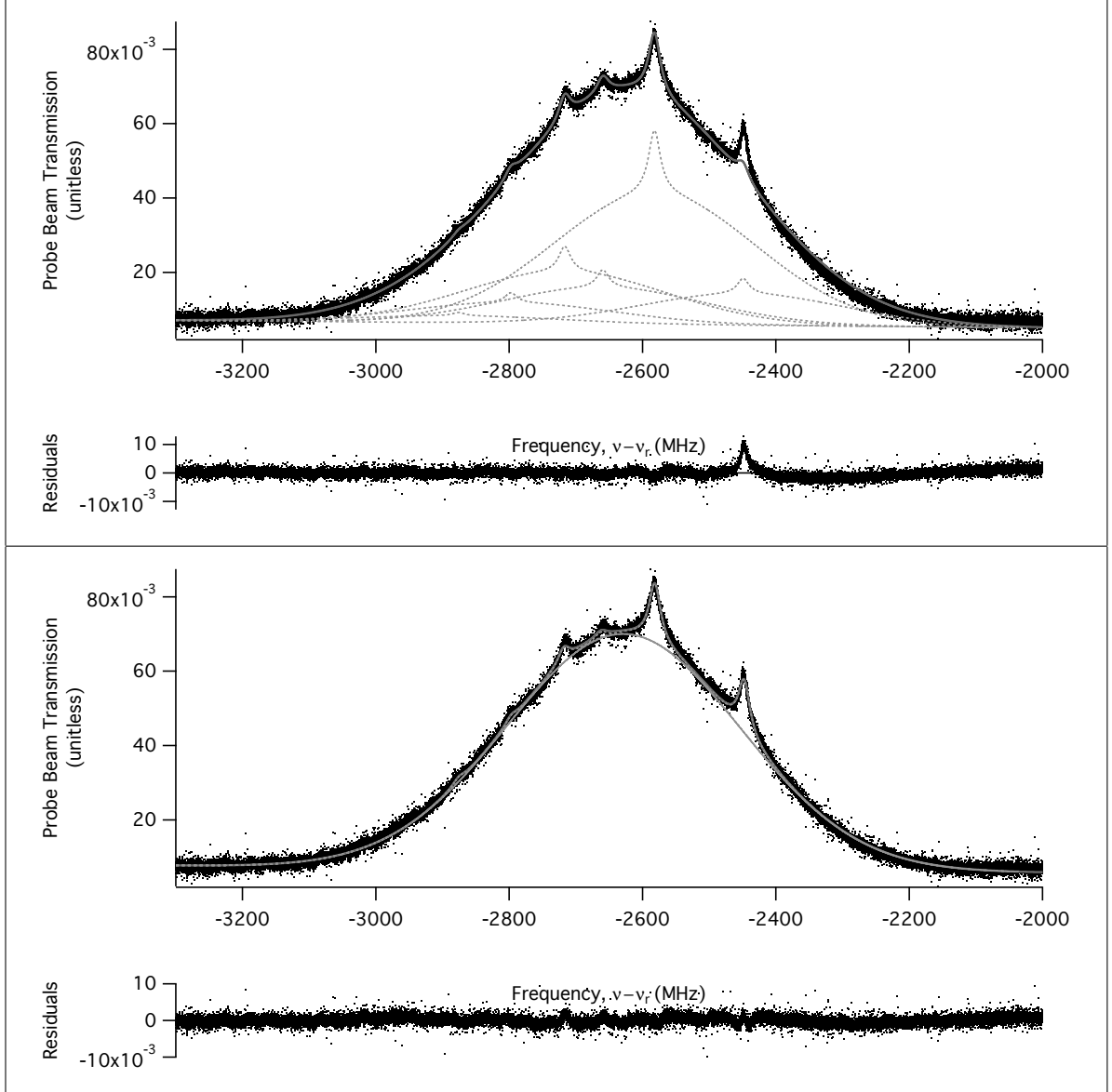


Figure 77. Data fits of both line shapes at 110 mTorr of Argon and 2800 Hz chopping frequency. The top plot is a fit using the first line shape, Eq.(11), and the bottom plot is the fit using the second line shape, Eq.(12). The vertical axis is the probe beam transmission relative to the incident beam intensity and the horizontal axis is the laser beam frequency (ν) relative to the $^{87}\text{Rb } D_2$ line (ν_r). The data is in (\bullet), the fit is in ($-$), and the individual hyperfine or cross-over line fit is ($- -$).

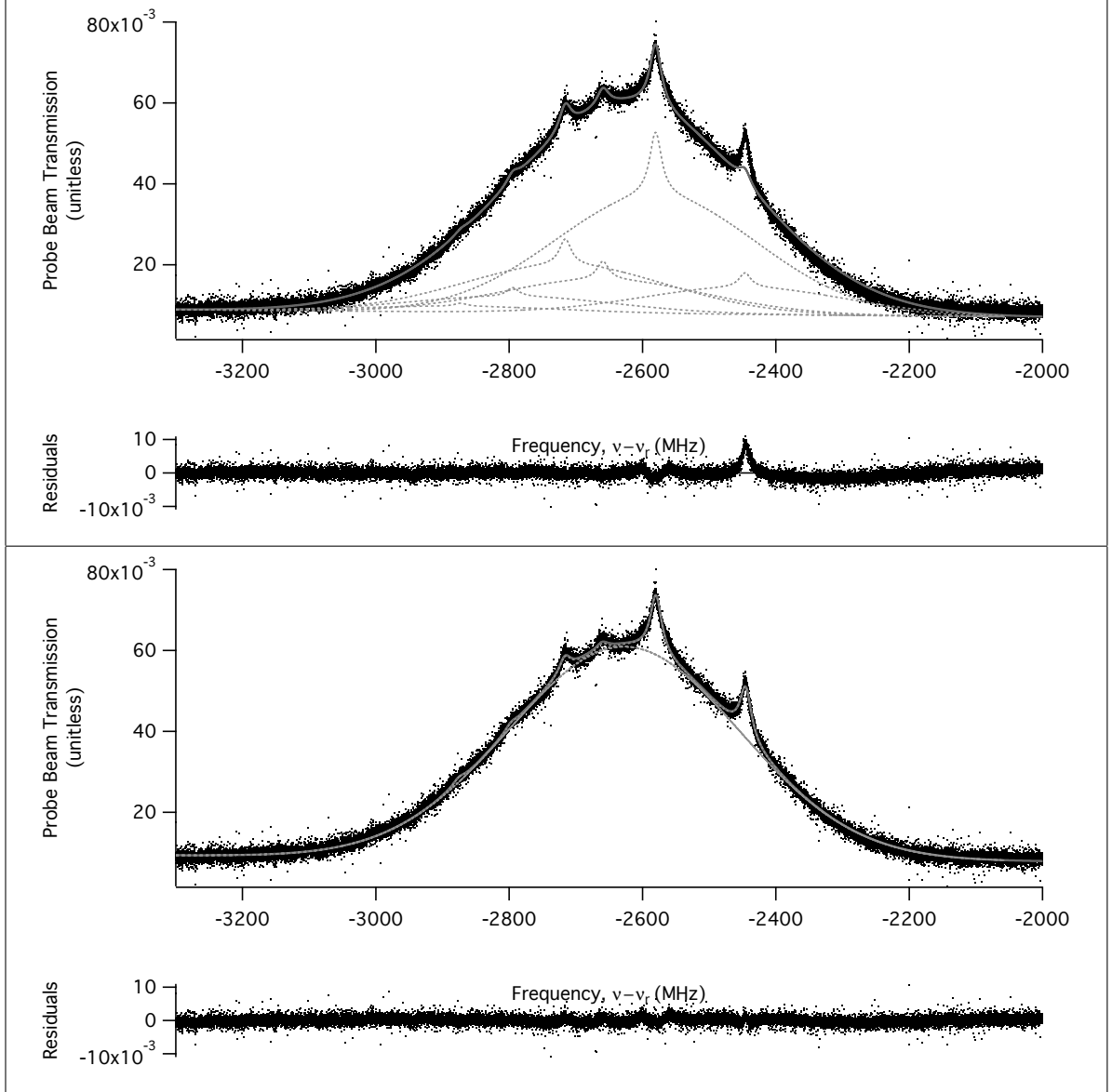


Figure 78. Data fits of both line shapes at 110 mTorr of Argon and 3200 Hz chopping frequency. The top plot is the fit using the first line shape, Eq.(11), and the bottom plot is the fit using the second line shape, Eq.(12). The vertical axis is the probe beam transmission relative to the incident beam intensity and the horizontal axis is the laser beam frequency (ν) relative to the $^{87}\text{Rb } D_2$ line (ν_r). The data is in (\bullet), the fit is in ($-$), and the individual hyperfine or cross-over line fit is ($- -$).

2.4 Fit Parameter Results

Table 9. First line shape (Eq.(11)) fit results of the collisional fit parameter, C , Lorentzian line width, γ , and Doppler line width, $\Delta\nu_D$. f_{chop} is the pump beam chopping frequency in Hz and p_{Ar} is the argon pressure in mTorr.

f_{chop}	p_{Ar}	C	γ (MHz)	$\Delta\nu_D$ (MHz)
0	700	0.37921 ± 0.00097921	21.855 ± 0.010636	508 ± 0
0	1100	0.3096 ± 0.022186	22.354 ± 0.24168	508 ± 0
0	1700	0.21682 ± 0.019791	22.168 ± 0.22413	508 ± 0
0	2200	0.13349 ± 0.00097222	22.061 ± 0.011867	508 ± 0
0	2800	0.066105 ± 0.0013421	22.175 ± 0.016647	508 ± 0
0	3200	0.046036 ± 0.0013514	21.537 ± 0.016355	508 ± 0
30	700	5.3473 ± 0.12483	21.856 ± 0	508 ± 0
30	1100	4.8459 ± 0.097342	21.856 ± 0	508 ± 0
30	1700	3.9702 ± 0.046586	21.856 ± 0	508 ± 0
30	2200	3.4446 ± 0.033936	21.858 ± 0	508 ± 0
30	2800	3.2517 ± 0.062875	21.858 ± 0	508 ± 0
30	3200	2.9874 ± 0.019283	21.856 ± 0	508 ± 0
50	700	11.418 ± 0.15568	21.856 ± 0	508 ± 0
50	1100	10.294 ± 0.20536	21.856 ± 0	508 ± 0
50	1700	8.7322 ± 0.10201	21.856 ± 0	508 ± 0
50	2200	7.8358 ± 0.10916	21.856 ± 0	508 ± 0
50	2800	6.9178 ± 0.21452	21.856 ± 0	508 ± 0
50	3200	6.2375 ± 0.020349	21.856 ± 0	508 ± 0
70	700	21.008 ± 1.3378	21.856 ± 0	508 ± 0
70	1100	18.048 ± 0.51338	21.856 ± 0	508 ± 0
70	1700	16.854 ± 0.99583	21.856 ± 0	508 ± 0
70	2200	13.967 ± 0.62578	21.856 ± 0	508 ± 0
70	2800	12.489 ± 0.048464	21.856 ± 0	508 ± 0
70	3200	11.655 ± 0.45405	21.856 ± 0	508 ± 0
90	700	28.359 ± 2.4328	21.856 ± 0	508 ± 0
90	1100	24.503 ± 1.9927	21.856 ± 0	508 ± 0
90	1700	22.937 ± 1.5155	21.856 ± 0	508 ± 0
90	2200	19.426 ± 0.77502	21.856 ± 0	508 ± 0
90	2800	17.978 ± 0.6811	21.856 ± 0	508 ± 0
90	3200	16.868 ± 0.69364	21.856 ± 0	508 ± 0
110	700	39.479 ± 4.3259	21.856 ± 0	508 ± 0
110	1100	32.952 ± 2.9085	21.856 ± 0	508 ± 0
110	1700	28.235 ± 2.1725	21.856 ± 0	508 ± 0
110	2200	25.313 ± 1.5199	21.856 ± 0	508 ± 0
110	2800	23.126 ± 1.5837	21.856 ± 0	508 ± 0
110	3200	20.726 ± 0.95346	21.856 ± 0	508 ± 0

Table 10. First line shape (Eq.(11)) fit results of the hyperfine transition amplitudes: A_1 is the $F'' = 2 \rightarrow F' = 1$ transition amplitude, A_2 is the $F'' = 2 \rightarrow F' = 2$ transition amplitude, and A_3 is the $F'' = 2 \rightarrow F' = 3$ transition amplitude. f_{chop} is the pump beam chopping frequency in Hz and p_{Ar} is the argon pressure in mTorr.

f_{chop}	p_{Ar}	A_1	A_2	A_3
0	700	1.3605 ± 0.0036689	6.1726 ± 0.0048212	$-0.0010724 \pm 0.00076947$
0	1100	0.90481 ± 0.05376	4.0793 ± 0.072713	0.0060174 ± 0.054874
0	1700	0.57069 ± 0.034364	2.7529 ± 0.046068	0.0020394 ± 0.035069
0	2200	0.42516 ± 0.0015189	2.2513 ± 0.001981	0.0046678 ± 0.00062794
0	2800	0.30456 ± 0.001652	1.7972 ± 0.0022079	0.0591 ± 0.0016851
0	3200	0.26835 ± 0.0014975	1.5623 ± 0.0019724	0.046715 ± 0.0015264
30	700	0.45135 ± 0.056756	2.7442 ± 0.084289	-0.00049107 ± 0.060306
30	1100	0.20716 ± 0.033243	1.9668 ± 0.048028	0.00086476 ± 0.033878
30	1700	0.084842 ± 0.013679	1.3594 ± 0.019206	0.0018788 ± 0.014255
30	2200	0.060548 ± 0.0094534	1.0915 ± 0.012786	$-6.655e-07 \pm 0.0097885$
30	2800	0.020186 ± 0.014252	0.91093 ± 0.019499	$8.7172e-06 \pm 0.015481$
30	3200	0.028876 ± 0.0043187	0.83757 ± 0.0057278	$-4.1372e-05 \pm 0.0046097$
50	700	0.29088 ± 0.026118	1.6069 ± 0.039114	0.0014584 ± 0.0032087
50	1100	0.16921 ± 0.021121	1.2233 ± 0.03467	$9.3483e-05 \pm 0.019421$
50	1700	0.11615 ± 0.0087049	0.89543 ± 0.013775	-0.010002 ± 0.0082278
50	2200	0.031564 ± 0.0079595	0.69301 ± 0.012924	$1.0116e-06 \pm 0.0083921$
50	2800	$8.2273e-06 \pm 0.015687$	0.56624 ± 0.023806	$-1.7916e-05 \pm 0.015293$
50	3200	0.0037526 ± 0.0012747	0.57089 ± 0.0022752	$2.1797e-06 \pm 0.0015685$
70	700	0.30054 ± 0.066474	1.2435 ± 0.1228	0.46575 ± 0.070852
70	1100	0.19072 ± 0.020583	0.90105 ± 0.038351	0.31392 ± 0.022859
70	1700	0.12451 ± 0.027179	0.59517 ± 0.051087	0.13757 ± 0.028658
70	2200	0.057702 ± 0.01941	0.50927 ± 0.034367	0.08469 ± 0.020056
70	2800	0.016825 ± 0.0013842	0.43936 ± 0.0024953	0.093562 ± 0.0015166
70	3200	0.0042601 ± 0.012606	0.41404 ± 0.022607	0.054119 ± 0.013444
90	700	0.39258 ± 0.07744	0.9637 ± 0.13176	0.72076 ± 0.09157
90	1100	0.20593 ± 0.047607	0.53509 ± 0.08527	0.42135 ± 0.056838
90	1700	0.087439 ± 0.023545	0.39883 ± 0.042327	0.19918 ± 0.026442
90	2200	0.06273 ± 0.012204	0.33453 ± 0.021908	0.16363 ± 0.013877
90	2800	0.046289 ± 0.0090093	0.28697 ± 0.016678	0.11042 ± 0.010116
90	3200	0.011335 ± 0.0089321	0.2821 ± 0.016372	0.079626 ± 0.0097588
110	700	0.22663 ± 0.071813	0.66199 ± 0.12714	0.66639 ± 0.096541
110	1100	0.16933 ± 0.040299	0.45531 ± 0.072823	0.44196 ± 0.053739
110	1700	0.091324 ± 0.024946	0.37435 ± 0.044127	0.29343 ± 0.032013
110	2200	0.052671 ± 0.014368	0.29724 ± 0.026577	0.19155 ± 0.018151
110	2800	0.031048 ± 0.013067	0.23169 ± 0.0247	0.14004 ± 0.016462
110	3200	0.026377 ± 0.0082906	0.21927 ± 0.015377	0.12334 ± 0.0102

Table 11. First line shape (Eq.(11)) fit results of the cross-over resonance amplitudes: $A_{1,2}$ is the $F'' = 2 \rightarrow F' = 1, 2$ cross-over resonance amplitude, $A_{1,3}$ is the $F'' = 2 \rightarrow F' = 1, 3$ cross-over resonance amplitude, and $A_{2,3}$ is the $F'' = 2 \rightarrow F' = 2, 3$ cross-over resonance amplitude. f_{chop} is the pump beam chopping frequency in Hz and p_{Ar} is the argon pressure in mTorr.

f_{chop}	p_{Ar}	$A_{1,2}$	$A_{1,3}$	$A_{2,3}$
0	700	3.9573 ± 0.0042526	6.5243 ± 0.004945	15.615 ± 0.0069913
0	1100	2.6745 ± 0.063959	4.3201 ± 0.074497	10.583 ± 0.10674
0	1700	1.7661 ± 0.040559	2.915 ± 0.0472	7.2026 ± 0.067664
0	2200	1.3832 ± 0.001747	2.3275 ± 0.0020095	5.8038 ± 0.0028611
0	2800	1.0984 ± 0.0019329	1.8712 ± 0.0022431	4.6074 ± 0.0032094
0	3200	0.96051 ± 0.0017387	1.6404 ± 0.0020027	4.1162 ± 0.0028739
30	700	1.2248 ± 0.071694	2.5002 ± 0.09188	6.6059 ± 0.093266
30	1100	0.85874 ± 0.041125	1.6337 ± 0.052199	4.3221 ± 0.052901
30	1700	0.60861 ± 0.016523	1.2535 ± 0.020778	3.1023 ± 0.021073
30	2200	0.52525 ± 0.011125	1.0342 ± 0.013761	2.5833 ± 0.013991
30	2800	0.38124 ± 0.016867	0.8364 ± 0.02098	2.0635 ± 0.021217
30	3200	0.35176 ± 0.0050036	0.72945 ± 0.0061514	1.8905 ± 0.006228
50	700	0.79689 ± 0.03536	1.3416 ± 0.043759	4.4169 ± 0.050631
50	1100	0.48958 ± 0.029112	0.89089 ± 0.039017	2.996 ± 0.040959
50	1700	0.28886 ± 0.011604	0.70081 ± 0.015478	1.9943 ± 0.015922
50	2200	0.25965 ± 0.010704	0.61208 ± 0.014428	1.5892 ± 0.014681
50	2800	0.23417 ± 0.020033	0.53772 ± 0.026501	1.2971 ± 0.027054
50	3200	0.18362 ± 0.0018537	0.47147 ± 0.0025126	1.2309 ± 0.002549
70	700	0.51868 ± 0.10299	0.92364 ± 0.14324	3.1239 ± 0.15529
70	1100	0.33364 ± 0.031971	0.70826 ± 0.044688	2.1723 ± 0.047732
70	1700	0.17867 ± 0.042371	0.49058 ± 0.059313	1.381 ± 0.062985
70	2200	0.20748 ± 0.028598	0.41962 ± 0.039692	1.2858 ± 0.041747
70	2800	0.18065 ± 0.0020652	0.37849 ± 0.0028595	1.0433 ± 0.002981
70	3200	0.14194 ± 0.018564	0.35748 ± 0.025804	0.94114 ± 0.026732
90	700	0.40426 ± 0.11393	0.63895 ± 0.15308	2.3792 ± 0.16904
90	1100	0.3528 ± 0.071538	0.46603 ± 0.098169	1.6673 ± 0.10917
90	1700	0.18457 ± 0.035628	0.25328 ± 0.04953	1.0726 ± 0.054591
90	2200	0.15065 ± 0.018464	0.2697 ± 0.025555	0.89821 ± 0.027749
90	2800	0.084691 ± 0.013876	0.22492 ± 0.019386	0.71653 ± 0.02102
90	3200	0.077632 ± 0.013611	0.19764 ± 0.019018	0.65432 ± 0.020359
110	700	0.3942 ± 0.11058	0.408 ± 0.14961	1.854 ± 0.16893
110	1100	0.24299 ± 0.062998	0.37117 ± 0.08554	1.2875 ± 0.09555
110	1700	0.13666 ± 0.038304	0.24581 ± 0.051778	0.88896 ± 0.057005
110	2200	0.092021 ± 0.022384	0.20178 ± 0.031232	0.69557 ± 0.034178
110	2800	0.091554 ± 0.020657	0.16245 ± 0.029004	0.5811 ± 0.031697
110	3200	0.07371 ± 0.012928	0.15395 ± 0.017969	0.53791 ± 0.019617

Table 12. First line shape (Eq.(11)) fit results of the hyperfine transition center line positions relative to the $^{87}\text{Rb } D_2$ line: ν_1 is the $F'' = 2 \rightarrow F' = 1$ transition, ν_2 is the $F'' = 2 \rightarrow F' = 2$ transition, and ν_3 is the $F'' = 2 \rightarrow F' = 3$ transition. f_{chop} is the pump beam chopping frequency in Hz and p_{Ar} is the argon pressure in mTorr.

f_{chop}	p_{Ar}	ν_1 (MHz)	ν_2 (MHz)	ν_3 (MHz)
0	700	-2872 ± 0.039378	-2713.8 ± 0.0087059	-2452.4 ± 49.972
0	1100	-2872.3 ± 0.86334	-2713.6 ± 0.19222	-2452.4 ± 129.87
0	1700	-2871.9 ± 0.8653	-2714 ± 0.18004	-2452.4 ± 242.24
0	2200	-2871.7 ± 0.051625	-2714.3 ± 0.0097792	-2446.7 ± 4.704
0	2800	-2871.5 ± 0.077613	-2714 ± 0.013195	-2445.3 ± 0.40012
0	3200	-2870.3 ± 0.077725	-2713.9 ± 0.013393	-2448.9 ± 0.44664
30	700	-2875.8 ± 2.6238	-2713.6 ± 0.43445	-2452.4 ± 2414.5
30	1100	-2872.1 ± 3.2538	-2713.9 ± 0.34477	-2442.4 ± 780.29
30	1700	-2873.7 ± 3.1643	-2713.7 ± 0.19853	-2442.4 ± 143.01
30	2200	-2866 ± 2.9404	-2713.2 ± 0.16395	$-2441.8 \pm 2.6715\text{e}+05$
30	2800	-2875.9 ± 13.38	-2714 ± 0.29791	-2453 ± 30999
30	3200	-2866 ± 2.7466	-2714.2 ± 0.095096	-2452.4 ± 1917.6
50	700	-2870.7 ± 2.2286	-2714.1 ± 0.40856	-2452.4 ± 440.65
50	1100	-2871.4 ± 3.0322	-2714 ± 0.42439	-2452.4 ± 5495
50	1700	-2867 ± 1.7202	-2714.8 ± 0.22529	-2442.4 ± 20.021
50	2200	-2875.9 ± 5.8449	-2714.6 ± 0.26851	$-2453.3 \pm 1.8235\text{e}+05$
50	2800	-2865.9 ± 41396	-2715 ± 0.60591	-2442.3 ± 19034
50	3200	-2875.9 ± 8.5681	-2714.6 ± 0.056738	-2452.8 ± 14775
70	700	-2871.3 ± 6.397	-2714.2 ± 1.5791	-2446.2 ± 4.1407
70	1100	-2874.2 ± 3.1027	-2714.6 ± 0.66884	-2447.8 ± 1.8905
70	1700	-2875.9 ± 6.2532	-2716.5 ± 1.3315	-2449.3 ± 5.6793
70	2200	-2870.9 ± 8.9542	-2714.4 ± 1.0295	-2449.5 ± 6.1205
70	2800	-2875.9 ± 2.2071	-2715.3 ± 0.085631	-2448.1 ± 0.3978
70	3200	-2874.1 ± 77.871	-2713.9 ± 0.81134	-2449.6 ± 6.1452
90	700	-2865.9 ± 5.4566	-2713.9 ± 2.2832	-2447.7 ± 2.9697
90	1100	-2875.9 ± 6.6862	-2713.8 ± 2.6379	-2445.1 ± 3.271
90	1700	-2872.3 ± 7.7446	-2714.2 ± 1.7367	-2447.7 ± 3.408
90	2200	-2870.6 ± 5.4909	-2714.5 ± 1.0499	-2447.7 ± 2.1096
90	2800	-2870.7 ± 5.5919	-2713.7 ± 0.91947	-2446.7 ± 2.3507
90	3200	-2867.1 ± 22.099	-2714.1 ± 0.904	-2449.6 ± 3.1546
110	700	-2868.4 ± 9.4934	-2714.8 ± 3.3597	-2446.2 ± 3.2164
110	1100	-2868.2 ± 7.1376	-2716 ± 2.7333	-2448.3 ± 2.7291
110	1700	-2865.9 ± 7.9121	-2715.8 ± 1.9805	-2446.6 ± 2.4584
110	2200	-2869.8 ± 8.1075	-2714.3 ± 1.4715	-2448.5 ± 2.2297
110	2800	-2875.9 ± 12.732	-2716.8 ± 1.7441	-2449.2 ± 2.8251
110	3200	-2872.8 ± 9.2712	-2716 ± 1.1384	-2446.5 ± 1.9849

Table 13. First line shape (Eq.(11)) fit results of the cross-over resonance center line positions relative to the $^{87}\text{Rb } D_2$ line: $\nu_{1,2}$ is the $F'' = 2 \rightarrow F' = 1, 2$ cross-over resonance, $\nu_{1,3}$ is the $F'' = 2 \rightarrow F' = 1, 3$ cross-over resonance, and $\nu_{2,3}$ is the $F'' = 2 \rightarrow F' = 2, 3$ cross-over resonance. f_{chop} is the pump beam chopping frequency in Hz and p_{Ar} is the argon pressure in mTorr.

f_{chop}	p_{Ar}	$\nu_{1,2}$ (MHz)	$\nu_{1,3}$ (MHz)	$\nu_{2,3}$ (MHz)
0	700	-2792.3 \pm 0.013545	-2657.4 \pm 0.0082359	-2579.1 \pm 0.0034298
0	1100	-2791.7 \pm 0.29224	-2657.7 \pm 0.18147	-2579.3 \pm 0.07379
0	1700	-2791.6 \pm 0.27974	-2658.3 \pm 0.16999	-2579.5 \pm 0.068537
0	2200	-2792.6 \pm 0.015876	-2657.5 \pm 0.0094579	-2580 \pm 0.0037809
0	2800	-2792.6 \pm 0.02153	-2657.5 \pm 0.01267	-2580 \pm 0.0051287
0	3200	-2792.8 \pm 0.021725	-2658.8 \pm 0.012753	-2582.3 \pm 0.0050658
30	700	-2793 \pm 0.97051	-2658.7 \pm 0.47746	-2580.5 \pm 0.17967
30	1100	-2792.9 \pm 0.78764	-2658.3 \pm 0.41551	-2581.2 \pm 0.15621
30	1700	-2792.3 \pm 0.4423	-2658.3 \pm 0.21553	-2581.3 \pm 0.086625
30	2200	-2790.9 \pm 0.3398	-2659.4 \pm 0.17325	-2581.2 \pm 0.068948
30	2800	-2792.5 \pm 0.70991	-2659.3 \pm 0.3248	-2580.2 \pm 0.13095
30	3200	-2792 \pm 0.22596	-2659.1 \pm 0.1093	-2580.7 \pm 0.041957
50	700	-2794.6 \pm 0.82045	-2659.4 \pm 0.49013	-2578.8 \pm 0.14699
50	1100	-2793.7 \pm 1.0566	-2659.9 \pm 0.58377	-2579.7 \pm 0.17218
50	1700	-2793.3 \pm 0.69654	-2658.6 \pm 0.28819	-2580 \pm 0.10066
50	2200	-2794.2 \pm 0.71479	-2658.3 \pm 0.30438	-2579.3 \pm 0.11657
50	2800	-2794.8 \pm 1.4624	-2658.2 \pm 0.63873	-2580.8 \pm 0.26334
50	3200	-2792.8 \pm 0.17575	-2658 \pm 0.068778	-2580.3 \pm 0.026206
70	700	-2792.4 \pm 3.7709	-2658.4 \pm 2.1296	-2579.3 \pm 0.62495
70	1100	-2791.5 \pm 1.8003	-2656.4 \pm 0.85181	-2579.7 \pm 0.27606
70	1700	-2791.4 \pm 4.4193	-2659.6 \pm 1.6172	-2580.5 \pm 0.57066
70	2200	-2792 \pm 2.5192	-2656.8 \pm 1.2508	-2579.8 \pm 0.40579
70	2800	-2790.8 \pm 0.20766	-2656.7 \pm 0.099471	-2580 \pm 0.035893
70	3200	-2789.6 \pm 2.3596	-2656.8 \pm 0.94058	-2580.6 \pm 0.3552
90	700	-2795.9 \pm 5.4185	-2660.3 \pm 3.4518	-2579.8 \pm 0.91889
90	1100	-2797.5 \pm 3.979	-2662.5 \pm 3.0381	-2578.9 \pm 0.84063
90	1700	-2797.5 \pm 3.7367	-2659.9 \pm 2.7414	-2580.4 \pm 0.64205
90	2200	-2794.5 \pm 2.3229	-2658.5 \pm 1.3046	-2580 \pm 0.38896
90	2800	-2790.7 \pm 3.1024	-2659.2 \pm 1.1752	-2580.8 \pm 0.36602
90	3200	-2790.2 \pm 3.2728	-2659 \pm 1.2922	-2579.9 \pm 0.38744
110	700	-2797.5 \pm 5.6228	-2657.7 \pm 5.4634	-2580.4 \pm 1.1928
110	1100	-2794.3 \pm 5.1033	-2658.6 \pm 3.3585	-2580.5 \pm 0.96106
110	1700	-2796.4 \pm 5.4068	-2658.8 \pm 3.021	-2580.3 \pm 0.82941
110	2200	-2796.2 \pm 4.7356	-2658.4 \pm 2.1718	-2580.5 \pm 0.62541
110	2800	-2797.5 \pm 4.3982	-2659.6 \pm 2.4916	-2582.2 \pm 0.69186
110	3200	-2794.8 \pm 3.374	-2659.5 \pm 1.6239	-2580.5 \pm 0.46151

Table 14. First line shape (Eq.(11)) fit results of the linear baseline noise, where a is y-intercept and b is the slope. f_{chop} is the pump beam chopping frequency in Hz and p_{Ar} is the argon pressure in mTorr.

f_{chop}	p_{Ar}	a	b
0	700	$-0.019552 \pm 8.5578\text{e-}05$	$-1.0935\text{e-}05 \pm 3.1757\text{e-}08$
0	1100	-0.011154 ± 0.0012125	$-6.7102\text{e-}06 \pm 4.4989\text{e-}07$
0	1700	$-0.0060746 \pm 0.00077392$	$-4.2556\text{e-}06 \pm 2.8699\text{e-}07$
0	2200	$-0.0031566 \pm 3.443\text{e-}05$	$-3.3412\text{e-}06 \pm 1.2755\text{e-}08$
0	2800	$0.0026997 \pm 3.6925\text{e-}05$	$-2.3677\text{e-}06 \pm 1.3669\text{e-}08$
0	3200	$0.0031983 \pm 3.3969\text{e-}05$	$-1.8872\text{e-}06 \pm 1.258\text{e-}08$
30	700	0.00088619 ± 0.0021084	$-2.851\text{e-}06 \pm 7.8672\text{e-}07$
30	1100	-0.0023441 ± 0.0011994	$-3.1006\text{e-}06 \pm 4.458\text{e-}07$
30	1700	$-0.0003396 \pm 0.00047153$	$-2.0584\text{e-}06 \pm 1.7538\text{e-}07$
30	2200	$0.00030276 \pm 0.00030994$	$-1.6321\text{e-}06 \pm 1.1507\text{e-}07$
30	2800	0.0036866 ± 0.00046672	$-1.425\text{e-}06 \pm 1.7408\text{e-}07$
30	3200	0.0037569 ± 0.00013581	$-1.2764\text{e-}06 \pm 5.0537\text{e-}08$
50	700	-0.001995 ± 0.0011497	$-3.3664\text{e-}06 \pm 4.3829\text{e-}07$
50	1100	0.0028945 ± 0.00095195	$-9.6989\text{e-}07 \pm 3.5557\text{e-}07$
50	1700	$0.00077078 \pm 0.00037158$	$-1.3551\text{e-}06 \pm 1.3765\text{e-}07$
50	2200	$0.00082782 \pm 0.00033752$	$-1.468\text{e-}06 \pm 1.259\text{e-}07$
50	2800	0.004009 ± 0.00062036	$-1.19\text{e-}06 \pm 2.2988\text{e-}07$
50	3200	$0.0042923 \pm 5.7587\text{e-}05$	$-1.3051\text{e-}06 \pm 2.139\text{e-}08$
70	700	0.0043922 ± 0.0038606	$-3.599\text{e-}06 \pm 1.4364\text{e-}06$
70	1100	$-0.00012328 \pm 0.0011709$	$-2.7564\text{e-}06 \pm 4.3633\text{e-}07$
70	1700	0.0019897 ± 0.0015316	$-1.7341\text{e-}06 \pm 5.7126\text{e-}07$
70	2200	0.0024291 ± 0.00099536	$-1.2539\text{e-}06 \pm 3.7018\text{e-}07$
70	2800	$0.0025252 \pm 7.0954\text{e-}05$	$-1.4692\text{e-}06 \pm 2.6434\text{e-}08$
70	3200	0.0063952 ± 0.00062872	$-8.6729\text{e-}07 \pm 2.341\text{e-}07$
90	700	$-0.00023722 \pm 0.0043905$	$-2.7791\text{e-}06 \pm 1.6339\text{e-}06$
90	1100	0.00036086 ± 0.0028102	$-2.6894\text{e-}06 \pm 1.0486\text{e-}06$
90	1700	0.0014575 ± 0.0013681	$-1.5505\text{e-}06 \pm 5.0975\text{e-}07$
90	2200	0.0013876 ± 0.00068396	$-1.3349\text{e-}06 \pm 2.5456\text{e-}07$
90	2800	0.0023622 ± 0.00051124	$-1.2441\text{e-}06 \pm 1.9015\text{e-}07$
90	3200	0.0039031 ± 0.00048906	$-1.1384\text{e-}06 \pm 1.8172\text{e-}07$
110	700	-0.0046592 ± 0.004554	$-3.604\text{e-}06 \pm 1.697\text{e-}06$
110	1100	-0.0017596 ± 0.0025113	$-2.4398\text{e-}06 \pm 9.3614\text{e-}07$
110	1700	-0.0033214 ± 0.0014801	$-2.4747\text{e-}06 \pm 5.5052\text{e-}07$
110	2200	$-8.6831\text{e-}05 \pm 0.00086663$	$-1.7023\text{e-}06 \pm 3.2295\text{e-}07$
110	2800	0.0020916 ± 0.0007977	$-1.5318\text{e-}06 \pm 2.9806\text{e-}07$
110	3200	0.004263 ± 0.00048909	$-1.4121\text{e-}06 \pm 1.8221\text{e-}07$

Table 15. Second line shape (Eq.(12)) fit results of the Doppler pedestal amplitude, A_D , Doppler pedestal center line position relative to the $^{87}\text{Rb } D_2$ line, ν_D , and Doppler pedestal line width, $\Delta\nu_D$. f_{chop} is the pump beam chopping frequency in Hz and p_{Ar} is the argon pressure in mTorr.

f_{chop}	p_{Ar}	A_D	ν_D (MHz)	$\Delta\nu_D$ (MHz)
0	700	0.039683 ± 0.00013068	-2737.4 ± 0.45295	364.62 ± 0.95166
0	1100	0.023306 ± 0.0018302	-2745.9 ± 11.281	365.73 ± 23.168
0	1700	0.012682 ± 0.0011486	-2756.4 ± 13.43	347.5 ± 26.224
0	2200	$0.008115 \pm 5.1051\text{e-}05$	-2767.2 ± 0.9779	320.26 ± 1.8098
0	2800	$0.0055089 \pm 5.7568\text{e-}05$	-2748.9 ± 1.4375	300.72 ± 2.607
0	3200	$0.0045643 \pm 5.4033\text{e-}05$	-2742.4 ± 1.5336	283.01 ± 2.7736
30	700	0.17571 ± 0.0022118	-2656.5 ± 1.9637	366.25 ± 4.9907
30	1100	0.10693 ± 0.00069047	-2659.7 ± 0.98269	360.32 ± 2.4985
30	1700	0.065568 ± 0.00052862	-2657.7 ± 1.1311	335.07 ± 2.8785
30	2200	0.04787 ± 0.00035691	-2658.6 ± 1.0228	327.42 ± 2.5815
30	2800	0.037019 ± 0.00055378	-2658.9 ± 1.9637	313.64 ± 4.9701
30	3200	0.031089 ± 0.00016393	-2658.3 ± 0.68718	309.5 ± 1.7227
50	700	0.22465 ± 0.0011512	-2649 ± 0.87486	388.69 ± 2.2025
50	1100	0.13977 ± 0.00092547	-2651 ± 1.1062	385.9 ± 2.7775
50	1700	0.083525 ± 0.00036755	-2653.3 ± 0.7036	368.96 ± 1.765
50	2200	0.061063 ± 0.000341	-2650 ± 0.86911	358.65 ± 2.19
50	2800	0.045333 ± 0.00064593	-2651.6 ± 2.1425	348.3 ± 5.3799
50	3200	$0.038693 \pm 6.4017\text{e-}05$	-2650.8 ± 0.24171	339.61 ± 0.60869
70	700	0.3056 ± 0.003303	-2638.4 ± 1.9987	415.59 ± 5.1225
70	1100	0.18631 ± 0.001024	-2638.5 ± 0.99877	409.83 ± 2.5481
70	1700	0.11098 ± 0.00057868	-2645.3 ± 0.56005	404.24 ± 1.4002
70	2200	0.083061 ± 0.00092031	-2642.4 ± 1.8909	388.73 ± 4.7716
70	2800	$0.063006 \pm 6.6543\text{e-}05$	-2641.7 ± 0.17786	383.64 ± 0.44751
70	3200	0.053386 ± 0.00060968	-2642.2 ± 1.8421	368.39 ± 4.5929
90	700	0.32926 ± 0.0019632	-2631.3 ± 1.1831	442.4 ± 3.0578
90	1100	0.18967 ± 0.0012439	-2631.9 ± 1.306	438.15 ± 3.3898
90	1700	0.11022 ± 0.00062685	-2632.6 ± 1.0703	416.38 ± 2.7315
90	2200	0.080936 ± 0.00032118	-2632.2 ± 0.73341	409.6 ± 1.8596
90	2800	0.060139 ± 0.0002485	-2634.9 ± 0.72323	395.46 ± 1.8209
90	3200	0.051355 ± 0.00024228	-2633.7 ± 0.81023	382.43 ± 2.0124
110	700	0.34789 ± 0.0019503	-2621.8 ± 1.146	447.03 ± 3.0015
110	1100	0.20702 ± 0.0010962	-2624.8 ± 1.0671	440.21 ± 2.7608
110	1700	0.12285 ± 0.00065751	-2624.1 ± 1.06	431.1 ± 2.7066
110	2200	0.084875 ± 0.00039363	-2625.1 ± 0.88307	417.15 ± 2.2444
110	2800	0.063209 ± 0.00036592	-2628.6 ± 1.0911	411.29 ± 2.7407
110	3200	0.052323 ± 0.0002266	-2627.5 ± 0.80749	406.74 ± 2.0303

Table 16. Second line shape (Eq.(12)) fit results of the hyperfine transition amplitudes: A_1 is the $F'' = 2 \rightarrow F' = 1$ transition, A_2 is the $F'' = 2 \rightarrow F' = 2$ transition, and A_3 is the $F'' = 2 \rightarrow F' = 3$ transition. f_{chop} is the pump beam chopping frequency in Hz and p_{Ar} is the argon pressure in mTorr.

f_{chop}	p_{Ar}	A_1	A_2	A_3
0	700	0.016245 ± 0.00022824	0.16293 ± 0.00024939	0.015986 ± 0.0002169
0	1100	0.010541 ± 0.0031957	0.10572 ± 0.0034868	0.0090314 ± 0.0030435
0	1700	0.0069662 ± 0.002065	0.072379 ± 0.0022384	0.0042034 ± 0.0019014
0	2200	$0.0055676 \pm 9.3616e-05$	0.059706 ± 0.00010112	$0.0040759 \pm 8.2211e-05$
0	2800	0.0045922 ± 0.00010219	0.047197 ± 0.00011101	$0.0031094 \pm 8.842e-05$
0	3200	$0.004799 \pm 9.6581e-05$	0.042029 ± 0.00010441	$0.0022205 \pm 8.1421e-05$
30	700	0.012552 ± 0.0051731	0.053328 ± 0.0054222	0.035952 ± 0.0050618
30	1100	0.0055394 ± 0.0015957	0.040103 ± 0.0016782	0.028261 ± 0.0015567
30	1700	0.0049419 ± 0.0011724	0.025522 ± 0.0012433	0.018124 ± 0.0011429
30	2200	0.0037221 ± 0.00078236	0.020381 ± 0.00082977	0.013326 ± 0.00076054
30	2800	0.0028637 ± 0.0011843	0.01649 ± 0.0012671	0.01208 ± 0.0011507
30	3200	0.0034679 ± 0.00034897	0.015926 ± 0.00037282	0.01055 ± 0.00033838
50	700	0.0078658 ± 0.0028091	0.02926 ± 0.0029123	0.042764 ± 0.0027508
50	1100	0.0013253 ± 0.0022268	0.023353 ± 0.0023143	0.028909 ± 0.0021765
50	1700	0.004486 ± 0.00087072	0.016882 ± 0.00090864	0.022277 ± 0.00085102
50	2200	0.0031929 ± 0.00079804	0.012609 ± 0.0008353	0.015927 ± 0.00078405
50	2800	0.0020233 ± 0.0014871	0.010026 ± 0.0015597	0.013627 ± 0.0014546
50	3200	0.0028718 ± 0.00014475	0.010822 ± 0.00015285	0.013477 ± 0.00014259
70	700	0.0017413 ± 0.008324	0.021028 ± 0.0085747	0.057174 ± 0.0081335
70	1100	0.0010747 ± 0.0025601	0.016663 ± 0.0026427	0.036954 ± 0.0025022
70	1700	$1.2051e-17 \pm 0.0013619$	0.0098511 ± 0.0014065	0.024518 ± 0.0013234
70	2200	0.0014023 ± 0.0022402	0.0090866 ± 0.0023244	0.019597 ± 0.0021956
70	2800	$0.00055504 \pm 0.00016097$	0.0078136 ± 0.00016727	0.016302 ± 0.00015784
70	3200	0.0019884 ± 0.001446	0.0080416 ± 0.0015067	0.015321 ± 0.001418
90	700	0.0037285 ± 0.0050481	0.014089 ± 0.0051571	0.052757 ± 0.0049093
90	1100	0.00094638 ± 0.0032324	0.0064761 ± 0.0033005	0.034557 ± 0.0031514
90	1700	0.0030296 ± 0.0015972	0.0067672 ± 0.0016385	0.022802 ± 0.0015591
90	2200	0.0028475 ± 0.00081204	0.0062553 ± 0.0008348	0.01712 ± 0.00079256
90	2800	0.001488 ± 0.00061095	0.0041458 ± 0.00063085	0.015966 ± 0.00059851
90	3200	0.0020263 ± 0.00059316	0.0050818 ± 0.00061317	0.013891 ± 0.0005816
110	700	0.0069073 ± 0.0050972	0.0066472 ± 0.005213	0.048192 ± 0.004958
110	1100	0.00269 ± 0.0028569	0.0044999 ± 0.0029191	0.032657 ± 0.0027782
110	1700	0.0021643 ± 0.0017068	0.0062337 ± 0.0017438	0.022523 ± 0.0016591
110	2200	0.0018669 ± 0.0010081	0.0055923 ± 0.0010332	0.017208 ± 0.00098311
110	2800	0.0012995 ± 0.00093454	0.0041046 ± 0.00095698	0.014269 ± 0.00091055
110	3200	0.0011849 ± 0.00057687	0.0040413 ± 0.00059181	0.012581 ± 0.00056325

Table 17. Second line shape (Eq.(12)) fit results of the cross-over resonance amplitudes: $A_{1,2}$ is the $F'' = 2 \rightarrow F' = 1, 2$ cross-over resonance, $A_{1,3}$ is the $F'' = 2 \rightarrow F' = 1, 3$ cross-over resonance, and $A_{2,3}$ is the $F'' = 2 \rightarrow F' = 2, 3$ cross-over resonance. f_{chop} is the pump beam chopping frequency in Hz and p_{Ar} is the argon pressure in mTorr.

f_{chop}	p_{Ar}	$A_{1,2}$	$A_{1,3}$	$A_{2,3}$
0	700	0.089351 ± 0.00024575	0.18529 ± 0.0002382	0.46868 ± 0.0002549
0	1100	0.059647 ± 0.003472	0.11996 ± 0.0033311	0.30964 ± 0.0035653
0	1700	0.040278 ± 0.0022501	0.081747 ± 0.0021525	0.212 ± 0.0023017
0	2200	0.031949 ± 0.00010211	$0.064962 \pm 9.9388e-05$	0.17 ± 0.00010327
0	2800	0.025869 ± 0.00010926	0.051695 ± 0.00010808	0.13458 ± 0.00011234
0	3200	0.023711 ± 0.00010144	0.046371 ± 0.00010177	0.12327 ± 0.00010532
30	700	0.019408 ± 0.0052939	0.049966 ± 0.0055072	0.19457 ± 0.0052806
30	1100	0.014081 ± 0.0016321	0.033399 ± 0.001702	0.128 ± 0.0016251
30	1700	0.011456 ± 0.0012152	0.022832 ± 0.0012694	0.088944 ± 0.0012015
30	2200	0.01023 ± 0.00081229	0.018858 ± 0.00084756	0.073835 ± 0.0008001
30	2800	0.0071108 ± 0.001246	0.014071 ± 0.0013006	0.058754 ± 0.0012187
30	3200	0.0074761 ± 0.00036707	0.012287 ± 0.00038278	0.053561 ± 0.00035825
50	700	0.012246 ± 0.0028589	0.025279 ± 0.0029571	0.13519 ± 0.0028728
50	1100	0.0048056 ± 0.0022669	0.016819 ± 0.0023508	0.091741 ± 0.0022734
50	1700	0.0036629 ± 0.00088854	0.012315 ± 0.00092302	0.060092 ± 0.00088741
50	2200	0.0047559 ± 0.00082193	0.010408 ± 0.00085193	0.046874 ± 0.00081862
50	2800	0.0046807 ± 0.0015317	0.0092802 ± 0.0015906	0.037949 ± 0.0015213
50	3200	0.0040243 ± 0.00015074	0.0074254 ± 0.00015649	0.035642 ± 0.00014923
70	700	0.0023511 ± 0.0084612	0.015383 ± 0.0087148	0.095043 ± 0.0085665
70	1100	0.0019445 ± 0.0026053	0.013382 ± 0.002688	0.065255 ± 0.0026367
70	1700	$-2.3141e-10 \pm 0.0013896$	0.0086546 ± 0.0014303	0.041152 ± 0.001408
70	2200	0.0027612 ± 0.0022911	0.0073128 ± 0.0023679	0.038468 ± 0.0023068
70	2800	0.0025639 ± 0.00016498	0.0063191 ± 0.00017066	0.030385 ± 0.00016582
70	3200	0.0034435 ± 0.0014875	0.0059068 ± 0.001537	0.027055 ± 0.0014899
90	700	$2.9631e-06 \pm 0.0051036$	0.0073248 ± 0.0052428	0.068544 ± 0.0052052
90	1100	0.0018134 ± 0.0032751	0.0069961 ± 0.0033494	0.050295 ± 0.0033288
90	1700	0.0027447 ± 0.0016267	0.0031649 ± 0.0016644	0.031558 ± 0.0016478
90	2200	0.0028002 ± 0.00082789	0.0044537 ± 0.00084855	0.026017 ± 0.00083769
90	2800	$5.8449e-05 \pm 0.00062656$	0.0024398 ± 0.00064375	0.020365 ± 0.00063278
90	3200	0.0015331 ± 0.00061094	0.0019926 ± 0.00062496	0.018181 ± 0.00061373
110	700	0.0016726 ± 0.0051632	0.00040038 ± 0.0052941	0.050284 ± 0.0052669
110	1100	$-7.1843e-10 \pm 0.0028958$	0.0033194 ± 0.0029661	0.034956 ± 0.002948
110	1700	0.00079567 ± 0.0017307	0.0026411 ± 0.0017694	0.023972 ± 0.0017607
110	2200	0.0011784 ± 0.0010295	0.0024971 ± 0.0010494	0.018813 ± 0.0010443
110	2800	0.0015237 ± 0.0009548	0.0017295 ± 0.00097306	0.015866 ± 0.00096512
110	3200	0.0011871 ± 0.00059088	0.0017278 ± 0.00060164	0.014636 ± 0.00059644

Table 18. Second line shape (Eq.(12)) fit results of the hyperfine transition center line positions relative to the $^{87}\text{Rb } D_2$ line: ν_1 is the $F'' = 2 \rightarrow F' = 1$ transition, ν_2 is the $F'' = 2 \rightarrow F' = 2$ transition, and ν_3 is the $F'' = 2 \rightarrow F' = 3$ transition. f_{chop} is the pump beam chopping frequency in Hz and p_{Ar} is the argon pressure in mTorr.

f_{chop}	p_{Ar}	ν_1 (MHz)	ν_2 (MHz)	ν_3 (MHz)
0	700	-2872.6 ± 0.17509	-2713.5 ± 0.017483	-2445.6 ± 0.1775
0	1100	-2872.9 ± 3.8473	-2713.3 ± 0.38435	-2449.5 ± 4.4781
0	1700	-2872.6 ± 3.7102	-2713.7 ± 0.35778	-2446.9 ± 6.132
0	2200	-2872.5 ± 0.20849	-2714 ± 0.01948	-2448.5 ± 0.28384
0	2800	-2872.2 ± 0.26592	-2713.8 ± 0.02593	-2447 ± 0.39168
0	3200	-2871 ± 0.23122	-2713.7 ± 0.026481	-2445.4 ± 0.49855
30	700	-2875.9 ± 5.0578	-2713.6 ± 1.1956	-2446 ± 1.766
30	1100	-2874.9 ± 3.5229	-2713.8 ± 0.48863	-2446.2 ± 0.69051
30	1700	-2875.9 ± 2.8867	-2713.8 ± 0.56179	-2445.1 ± 0.78709
30	2200	-2872.5 ± 2.545	-2713.2 ± 0.46743	-2447.3 ± 0.71077
30	2800	-2875.1 ± 5.0185	-2714.1 ± 0.8768	-2445.6 ± 1.1895
30	3200	-2870.6 ± 1.214	-2714.4 ± 0.26597	-2448.7 ± 0.39899
50	700	-2872.7 ± 4.4156	-2713.9 ± 1.1918	-2449.3 ± 0.81245
50	1100	-2868.9 ± 20.717	-2713.8 ± 1.1805	-2447.8 ± 0.94993
50	1700	-2870.8 ± 2.3791	-2714.8 ± 0.63457	-2447.8 ± 0.47911
50	2200	-2875.9 ± 3.0667	-2714.3 ± 0.77995	-2447 ± 0.61495
50	2800	-2871.1 ± 8.9558	-2714.5 ± 1.8153	-2447.4 ± 1.3299
50	3200	-2875.9 ± 0.61646	-2714.9 ± 0.16437	-2447.8 ± 0.13138
70	700	-2875.9 ± 59.695	-2713.8 ± 4.9611	-2445.7 ± 1.8195
70	1100	-2875.9 ± 29.692	-2714.5 ± 1.9212	-2447.3 ± 0.86425
70	1700	-2870.9 ± 0	-2714 ± 0	-2447.4 ± 0
70	2200	-2875.9 ± 19.788	-2714.4 ± 3.0648	-2448.3 ± 1.4171
70	2800	-2875.9 ± 3.5873	-2715.6 ± 0.25571	-2446.7 ± 0.12222
70	3200	-2871.3 ± 8.9386	-2714.2 ± 2.2191	-2448.5 ± 1.1608
90	700	-2866.4 ± 17.01	-2711.9 ± 4.5235	-2446 ± 1.2031
90	1100	-2875.9 ± 42.947	-2713.1 ± 6.3077	-2444.7 ± 1.1772
90	1700	-2875.9 ± 6.5889	-2714.1 ± 2.9623	-2445.8 ± 0.87622
90	2200	-2874 ± 3.5548	-2714.7 ± 1.6241	-2445.6 ± 0.59178
90	2800	-2876 ± 5.1056	-2713.3 ± 1.8407	-2446 ± 0.47627
90	3200	-2873.3 ± 3.6237	-2714.3 ± 1.4514	-2447.5 ± 0.52911
110	700	-2875.9 ± 9.2966	-2716.4 ± 9.6826	-2446.5 ± 1.334
110	1100	-2875.6 ± 13.346	-2717.2 ± 8.0001	-2446.6 ± 1.1006
110	1700	-2869 ± 9.8834	-2715.3 ± 3.4426	-2445.1 ± 0.95051
110	2200	-2875.4 ± 6.7554	-2714.5 ± 2.2637	-2447.5 ± 0.73377
110	2800	-2875.9 ± 8.9665	-2718.3 ± 2.8498	-2447.6 ± 0.81752
110	3200	-2875.9 ± 6.0712	-2716.6 ± 1.7871	-2445.4 ± 0.57242

Table 19. Second line shape (Eq.(12)) fit results of the cross-over resonance center line positions relative to the $^{87}\text{Rb } D_2$ line: $\nu_{1,2}$ is the $F'' = 2 \rightarrow F' = 1, 2$ cross-over resonance, $\nu_{1,3}$ is the $F'' = 2 \rightarrow F' = 1, 3$ cross-over resonance, and $\nu_{2,3}$ is the $F'' = 2 \rightarrow F' = 2, 3$ cross-over resonance. f_{chop} is the pump beam chopping frequency in Hz and p_{Ar} is the argon pressure in mTorr.

f_{chop}	p_{Ar}	$\nu_{1,2}$ (MHz)	$\nu_{1,3}$ (MHz)	$\nu_{2,3}$ (MHz)
0	700	-2792.2 ± 0.031828	-2657.3 ± 0.015371	-2579 ± 0.0060617
0	1100	-2791.7 ± 0.6794	-2657.6 ± 0.33863	-2579.2 ± 0.13073
0	1700	-2791.6 ± 0.64111	-2658.2 ± 0.31672	-2579.5 ± 0.12158
0	2200	-2792.6 ± 0.036312	-2657.3 ± 0.017893	-2580 ± 0.0068007
0	2800	-2792.6 ± 0.047272	-2657.4 ± 0.023681	-2579.9 ± 0.0090492
0	3200	-2792.9 ± 0.046947	-2658.7 ± 0.024014	-2582.3 ± 0.0089847
30	700	-2793.9 ± 3.2787	-2658.4 ± 1.2754	-2579.8 ± 0.32727
30	1100	-2794.1 ± 1.3894	-2657.9 ± 0.58639	-2580.7 ± 0.15296
30	1700	-2793.9 ± 1.2489	-2658.1 ± 0.62738	-2580.8 ± 0.1611
30	2200	-2792.7 ± 0.9288	-2659.3 ± 0.50472	-2580.7 ± 0.12892
30	2800	-2795.1 ± 2.0273	-2659.2 ± 1.0261	-2579.7 ± 0.24599
30	3200	-2793.8 ± 0.56488	-2658.9 ± 0.34421	-2580.2 ± 0.079067
50	700	-2797.3 ± 2.8411	-2659 ± 1.379	-2578.3 ± 0.25744
50	1100	-2791.2 ± 5.7241	-2659.3 ± 1.6385	-2579.2 ± 0.29994
50	1700	-2796.1 ± 2.9198	-2658 ± 0.86943	-2579.4 ± 0.17808
50	2200	-2796.3 ± 2.0634	-2657.5 ± 0.94419	-2578.3 ± 0.20957
50	2800	-2796.2 ± 3.8804	-2657.3 ± 1.9595	-2579.7 ± 0.47918
50	3200	-2795.7 ± 0.44098	-2657.5 ± 0.23931	-2579.2 ± 0.049871
70	700	-2795 ± 44.278	-2657.7 ± 6.78	-2578.6 ± 1.0954
70	1100	-2794.4 ± 16.436	-2656.1 ± 2.3915	-2579 ± 0.48981
70	1700	-2792.5 ± 0	-2659.2 ± 0	-2580.7 ± 0
70	2200	-2793.3 ± 10.068	-2656.5 ± 3.8065	-2579.1 ± 0.7229
70	2800	-2791.9 ± 0.77807	-2656.1 ± 0.316	-2579.3 ± 0.065681
70	3200	-2791.8 ± 5.172	-2656.6 ± 3.0193	-2579.8 ± 0.65872
90	700	-2787.5 ± 21430	-2660.6 ± 8.7009	-2579.3 ± 0.92609
90	1100	-2797.5 ± 22.44	-2661.7 ± 5.8391	-2578.2 ± 0.80896
90	1700	-2797.5 ± 7.2823	-2660 ± 6.3329	-2579.7 ± 0.63342
90	2200	-2796.4 ± 3.6198	-2658.2 ± 2.2805	-2579.5 ± 0.38965
90	2800	-2787.5 ± 130.21	-2658.9 ± 3.1268	-2580.1 ± 0.37375
90	3200	-2792.9 ± 4.7972	-2659.2 ± 3.7002	-2579.1 ± 0.40475
110	700	-2797.5 ± 38.435	-2654.1 ± 160.72	-2579.9 ± 1.2783
110	1100	$-2797.5 \pm 2.4688\text{e}+07$	-2657.6 ± 10.844	-2580 ± 1.0282
110	1700	-2797.5 ± 26.913	-2659 ± 8.1244	-2579.8 ± 0.89305
110	2200	-2797.5 ± 10.716	-2658.6 ± 5.0687	-2580 ± 0.67123
110	2800	-2797.5 ± 7.6571	-2662.2 ± 6.7619	-2581.7 ± 0.73546
110	3200	-2797.5 ± 6.0677	-2660.6 ± 4.179	-2579.9 ± 0.49226

Table 20. Second line shape (Eq.(12)) fit results of the Lorentzian line width, γ , and linear baseline noise, where a is y-intercept and b is the slope. f_{chop} is the pump beam chopping frequency in Hz and p_{Ar} is the argon pressure in mTorr.

f_{chop}	p_{Ar}	γ (MHz)	a	b
0	700	21.288 ± 0.021318	$-0.0086517 \pm 0.00016996$	$-6.4211\text{e-}06 \pm 6.6591\text{e-}08$
0	1100	21.762 ± 0.46454	-0.0041898 ± 0.0024141	$-3.7273\text{e-}06 \pm 9.514\text{e-}07$
0	1700	21.562 ± 0.43793	-0.0020559 ± 0.0015308	$-2.517\text{e-}06 \pm 6.0225\text{e-}07$
0	2200	21.661 ± 0.025423	$-0.00074846 \pm 6.7453\text{e-}05$	$-2.2141\text{e-}06 \pm 2.6402\text{e-}08$
0	2800	21.029 ± 0.033661	$0.0035644 \pm 7.0309\text{e-}05$	$-1.8938\text{e-}06 \pm 2.7118\text{e-}08$
0	3200	20.457 ± 0.033439	$0.0037268 \pm 6.4016\text{e-}05$	$-1.5613\text{e-}06 \pm 2.4516\text{e-}08$
30	700	21.287 ± 0	0.0042979 ± 0.0037558	$-2.9766\text{e-}06 \pm 1.3911\text{e-}06$
30	1100	21.287 ± 0	0.0007303 ± 0.0011467	$-2.7914\text{e-}06 \pm 4.2585\text{e-}07$
30	1700	21.287 ± 0	0.0024402 ± 0.00082377	$-1.7468\text{e-}06 \pm 3.0577\text{e-}07$
30	2200	21.287 ± 0	0.0027205 ± 0.00054408	$-1.2953\text{e-}06 \pm 2.0211\text{e-}07$
30	2800	21.287 ± 0	0.0059772 ± 0.00081878	$-1.0552\text{e-}06 \pm 3.043\text{e-}07$
30	3200	21.287 ± 0	0.0056621 ± 0.00023937	$-9.9537\text{e-}07 \pm 8.8946\text{e-}08$
50	700	21.287 ± 0	-0.0031645 ± 0.0021108	$-4.7801\text{e-}06 \pm 7.7616\text{e-}07$
50	1100	21.287 ± 0	0.0032928 ± 0.0016616	$-1.3951\text{e-}06 \pm 6.1216\text{e-}07$
50	1700	21.287 ± 0	0.0020036 ± 0.00063418	$-1.4307\text{e-}06 \pm 2.3436\text{e-}07$
50	2200	21.287 ± 0	0.0024145 ± 0.00057805	$-1.3278\text{e-}06 \pm 2.1322\text{e-}07$
50	2800	21.287 ± 0	0.0055692 ± 0.0010596	$-9.928\text{e-}07 \pm 3.9162\text{e-}07$
50	3200	21.287 ± 0	0.0058213 ± 0.00010294	$-1.1091\text{e-}06 \pm 3.8039\text{e-}08$
70	700	21.287 ± 0	0.0043816 ± 0.0065889	$-4.4518\text{e-}06 \pm 2.3914\text{e-}06$
70	1100	21.287 ± 0	-0.00015331 ± 0.002008	$-3.3582\text{e-}06 \pm 7.2955\text{e-}07$
70	1700	21.287 ± 0	0.0002439 ± 0.0010923	$-6.4567\text{e-}06 \pm 3.9688\text{e-}07$
70	2200	21.287 ± 0	0.0033646 ± 0.0016971	$-1.28\text{e-}06 \pm 6.2053\text{e-}07$
70	2800	21.287 ± 0	0.0041913 ± 0.00012121	$-1.1616\text{e-}06 \pm 4.4323\text{e-}08$
70	3200	21.287 ± 0	0.0082732 ± 0.0010652	$-4.9498\text{e-}07 \pm 3.9043\text{e-}07$
90	700	21.287 ± 0	-0.0044165 ± 0.0042217	$-4.7539\text{e-}06 \pm 1.5133\text{e-}06$
90	1100	21.287 ± 0	-0.0019732 ± 0.0026828	$-3.8904\text{e-}06 \pm 9.6306\text{e-}07$
90	1700	21.287 ± 0	0.0015366 ± 0.0012762	$-1.8996\text{e-}06 \pm 4.606\text{e-}07$
90	2200	21.287 ± 0	0.002056 ± 0.00064177	$-1.39\text{e-}06 \pm 2.3187\text{e-}07$
90	2800	21.287 ± 0	0.003791 ± 0.00047216	$-1.0108\text{e-}06 \pm 1.7138\text{e-}07$
90	3200	21.287 ± 0	0.0054831 ± 0.0004502	$-8.0355\text{e-}07 \pm 1.6365\text{e-}07$
110	700	21.287 ± 0	-0.011212 ± 0.0043719	$-6.3719\text{e-}06 \pm 1.5495\text{e-}06$
110	1100	21.287 ± 0	-0.0037756 ± 0.0024052	$-3.5167\text{e-}06 \pm 8.5686\text{e-}07$
110	1700	21.287 ± 0	-0.0028081 ± 0.0014142	$-2.5655\text{e-}06 \pm 5.0481\text{e-}07$
110	2200	21.287 ± 0	0.0007384 ± 0.00081588	$-1.6722\text{e-}06 \pm 2.9244\text{e-}07$
110	2800	21.287 ± 0	0.0029645 ± 0.0007443	$-1.4503\text{e-}06 \pm 2.68\text{e-}07$
110	3200	21.287 ± 0	0.0055704 ± 0.00045742	$-1.1452\text{e-}06 \pm 1.6468\text{e-}07$

Bibliography

- [1] Akulshin, A. M., V. A. Sautenkov, V. L. Velichansky, A. S. Zibrov, and M. V. Zverkov. “Power Broadening of Saturation Absorption Resonance on the D_2 Line of Rubidium”. *Opt. Commun.*, 77(4):295–298, July 1990.
- [2] Aminoff, C. G., J. Javanainen, and M. Kaivola. “Collision effects in velocity-selective optical pumping of sodium”. *Phys. Rev. A*, 28(2):722 – 737, Aug 1983.
- [3] Arimondo, E., M. Inguscio, and P. Violino. “Experimental determinations of the hyperfine structure in the alkali atoms”. *Rev. Mod. Phys.*, 49:31, 1977.
- [4] Banerjee, A., D. Das, and V. Natarajan. “Absolute frequency measurements of the D1 lines in 39 K, 85 Rb, and Absolute frequency measurements of the D1 lines in 39 K, 85 Rb, and Absolute frequency measurements of the D_1 lines in ^{39}K , ^{85}Rb , and ^{87}Rb with 0.1 ppb uncertainty”. *Europhys. Lett.*, 172, 200465.
- [5] Barwood, G. P., P. Gill, and W. R. C. Rowley. “Frequency Measurements on Optically Narrowed Rb-Stabilized Laser Diodes at 780 nm and 795 nm”. *App. Phys. B*, 53:142, 1991.
- [6] Beach, Raymond J., William F. Kupke, V. Keith Kanz, Stephen A. Payne, Mark A. Dubinskii, and Larry D. Merkle. “End-pumped continuous-wave alkali vapor lasers: experiment, model, and power scaling”. *J. Opt. Soc. Am. B*, 21(12):2151–2163, Dec 2004.
- [7] Bennett, W. R. “Hole Burning Effects in a He-Ne Optical Maser”. *Phys. Rev.*, 126(2):580 – 593, Apr 1962.
- [8] Berman, Paul R. “Theory of collision effects in Doppler-free spectroscopy”. *Phys. Rev. A*, 13(6):2191–2211, June 1976.
- [9] Berman, Paul R., J. M. Levy, and Richard G. Brewer. “Coherent optical transient study of molecular collisions: Theory and observations”. *Phys. Rev. A*, 11(5):1668 – 1688, May 1975.
- [10] Biraben, F., M. Bassini, and B. Cagnac. “Line-shapes in Doppler-free two-photon spectroscopy. The effect of finite transit time”. *Le Journal de Physique*, 40(5):445 – 455, May 1979.
- [11] Bischel, William K. and Charles K. Rhodes. “Study of momentum-transfer distributions in rotationally inelastic collisions of CO_2 with foreign gas perturbers”. *Phys. Rev. A*, 14(1):176–188, July 1976.
- [12] Bize, S., Y. Sortais, M. S. Santos, C. Mandache, A. Clairon, and C. Salomon. “High-accuracy measurement of the ^{87}Rb ground-state hyperfine splitting in an atomic fountain”. *Europhys. Lett.*, 45:558, 1999.

- [13] Bloomfield, L. A., B. Couillaud, P. Dabkiewicz, H. Gerhardt, and T. W. Hänsch. “Hyperfine structure of the $2^3S \rightarrow 5^3P$ transition in ^3He by high-resolution uv-laser spectroscopy”. *Phys. Rev. A*, 26(1):713 – 716, July 1982.
- [14] Boesten, H. M. J. M., C. C. Tsai, J. R. Gardner, D. J. Heinzen, and B. J. Verhaar. “Observation of a shape resonance in the collision of two cold ^{87}Rb atoms”. *Phys. Rev. A*, 55:636, 1997.
- [15] Bréchnignac, C., R. Vetter, and P. R. Berman. “Study of velocity-changing collisions in excited Kr using saturation spectroscopy”. *Phys. Rev. A*, 17(5):1609–1613, May 1978.
- [16] Brewer, Richard G., R. L. Shoemaker, and S. Stenholm. “Collision-Induced Optical Double Resonance”. *Phys. Rev. Lett.*, 33(2):63–66, July 1974.
- [17] Demtröder, W. *Laser Spectroscopy, 3rd Ed.* Springer - Verlag, 2003.
- [18] Dicke, R. H. “The Effect of Collisions upon the Doppler Width of Spectral Lines”. *Phys. Rev.*, 89(2):472–473, Jan 1953.
- [19] Gough, D. S. and P. Hannaford. “Very High Resolution Laser Saturation Spectroscopy in Hollow-Cathode and Glow Discharges”. *Opt. Commun.*, 55(2):91 – 96, Aug 1985.
- [20] Hänsch, T. W., I. S. Shahin, and A. L. Shawlow. “High-Resolution Saturation Spectroscopy of the Sodium D lines with a Pulsed Tunable Dye Laser”. *Phys. Rev. Lett.*, 27(11):707 – 710, Sep 1971.
- [21] Hänsch, Theo W. “Nobel Lecture: Passion for precision”. *Rev. Mod. Phys.*, 78(4):1297 – 1309, Oct - Dec 2006.
- [22] Hirschfelder, J.O., Charles F. Curtiss, and R. Byron Bird. *Molecular Theory of Gases and Liquids*. John Wiley and Sons, Inc., 1954.
- [23] Holt, Helen K. “Theory of Laser Saturation Spectroscopy”. *Phys. Rev. Lett.*, 29(17):1138 – 1140, Oct 1972.
- [24] Kan, Tehmau and George J. Wolga. “Influence of Collisions on Radiative Saturation and Lamb Dip Formation in CO_2 Molecular Lasers”. *IEEE J. Quantum Electron.*, 7(4):141 – 150, Apr 1971.
- [25] Kronfeldt, H. D., G. Klemz, and D. Ashkenasi. “Experimental study on methods minimizing the influence of velocity-changing collisions in Doppler-free saturation spectroscopy”. *Opt. Commun.*, 110:594–554, 1994.
- [26] Kronfeldt, H. D., G. Klemz, S. Kröger, and J. F. Wyart. “Experimental and theoretical study of the hyperfine structure in the $4f^7 5d 6s 6p$ configuration of Gd I”. *Phys. Rev. A*, 48(6):4500 – 4514, Dec 1993.

- [27] Kronfeldt, H. D. and D. J. Weber. “Doppler-free two-photon spectroscopy in Eu: Fine Structure, hyperfine structures, and isotope shifts of odd levels between 34400 and 36700 cm^{-1} ”. *Phys. Rev. A*, 43(9):4837–4844, May 1991.
- [28] Kronfeldt, H. D., D. J. Weber, J. Dembczyński, and E. Stachowska. “J off-diagonal effects in the hyperfine-structure splitting in the Eu I term $e\ ^6D$ of the $4f^76s6d$ ”. *Phys. Rev. A*, 44(9):5737 – 5743, Nov 1991.
- [29] Levenson, M. D. and S. S. Kano. *Introduction to Nonlinear Laser Spectroscopy*. Academic Press, Inc., revised edition, 1988.
- [30] Meyer, Thomas W. and Charles K. Rhodes. “Observation of Momentum Transfer in Rotationally Inelastic Molecular Collisions of CO_2 with H_2 , He, CO_2 , and Kr”. *Phys. Rev. Lett.*, 32(12):637 – 640, Mar 1974.
- [31] Phillips, Grady T. *Spatially-Resolved Temperature Diagnostic for Supersonic Flow using Cross-Beam Doppler-Limited Laser Saturation Spectroscopy*. Ph.D. thesis, Air Force Institute of Technology, 2950 Hobson Way, WPAFB, OH, Mar 2006.
- [32] Pitz, Greg A., Matthew A. Lange, and Glen P. Perram. “Pressure Broadening of the D_1 and D_2 lines in Diode Pumped Alkali Lasers”. *SPIE*, 2008.
- [33] Rotondaro, M. D. and G. P. Perram. “Collisional broadening and shift of the Rubidium D_1 and D_2 lines ($5^2S_{1/2} \rightarrow 5^2P_{1/2}, 5^2P_{3/2}$) by rare gases, H_2 , D_2 , N_2 , CH_4 , and CF_4 ”. *J. Quant. Spectrosc. Radiat. Transfer*, 57(4):497–507, Apr 1997.
- [34] Rotondaro, Matthew Don. *Collisional Dynamics of the Rubidium 5^2P Levels*. Ph.D. thesis, Air Force Institute of Technology, 2950 Hobson Way, WPAFB, OH, Aug 1995.
- [35] Sasso, A., G. M. Tino, M. Inguscio, N. Beverini, and M. Francesconi. “Investigation of Collisional Lineshapes of Neon Transitions in Noble Gases’ Mixtures”. *Il Nuovo Cimento*, 10(8):941 – 957, Aug 1988.
- [36] Schawlow, Arthur L. “Spectroscopy in a new light”. *Rev. Mod. Phys.*, 54(3):697 – 707, July 1982.
- [37] Schmidt, J., Paul R. Berman, and Richard G. Brewer. “Coherent Transient Study of Velocity-Changing Collisions”. *Phys. Rev. Lett.*, 31(18):1103–1106, Oct 1973.
- [38] Schreier, F. “The Voigt and Complex Error Function: A Comparison of Computational Methods”. *J. Quant. Spectrosc. Radiat. Transfer*, 48(5/6):743–762, Mar 1992.
- [39] Sherlock, Ben E. and Ifan G. Hughes. “How weak is a weak probe in laser spectroscopy?” *Am. J. Phys.*, 77(2):111 – 115, Feb 2009.

- [40] Shoemaker, R. L., S. Stenholm, and Richard G. Brewer. “Collision-Induced Optical Double Resonance”. *Phys. Rev. A*, 10(4):2037–2050, Dec 1974.
- [41] Simsarian, J. E., L. A. Orozco, G. D. Sprouse, and W. Z. Zhao. “Lifetime measurements of the 7p levels of atomic francium”. *Phys. Rev. A*, 57:2448, 1998.
- [42] Smith, David A. and Ifan G. Hughes. “The role of hyperfine pumping in multi-level systems exhibiting saturated absorption”. *Am. J. Phys.*, 72(5):631 – 637, May 2004.
- [43] Smith, P. W. and T. W. Hänsch. “Cross-Relaxation Effects in the Saturation of the 6328-Å Neon-Laser Line”. *Phys. Rev. Lett.*, 26(12):740 – 743, Mar 1971.
- [44] Sorem, M. S. and A. L. Shawlow. “Saturation Spectroscopy in molecular iodine by intermodulated fluorescence”. *Opt. Commun.*, 5(3):148 –151, June 1972.
- [45] Speller, E., B. Staudenmayer, and V. Kempter. “Quenching Cross Sections for Alkali-Inert Gas Collisions”. *Z. Phys. A*, 311–318, Apr 1979.
- [46] Steck, Daniel Adam. “Rubidium 85 D Line Data”. URL <http://steck.us/alkalidata/rubidium85numbers.pdf>.
- [47] Steck, Daniel Adam. “Rubidium 87 D Line Data”. URL <http://steck.us/alkalidata/rubidium87numbers.pdf>.
- [48] Steinfeld, J. I., J. S. Francisco, and W. L. Hase. *Chemical Kinetics and Dynamics*. Prentice-Hall, Inc., 2nd edition, 1999.
- [49] Thompson, William J. “Numerous Neat Algorithms for the Voigt Profile Function”. *Computers in Physics*, 7(6):627–631, Nov/Dec 1993.
- [50] Vasilenko, L.S., V.P. Chebotaev, and A.V. Shishaev. “Line shape of two-photon absorption in a standing-wave field in a gas”. *JTEP Lett.*, 12(3):113–116, Aug 1970.
- [51] Volz, U. and H. Schmoranz. “Precision Lifetime Measurements on Alkali Atoms and on Helium by Beam-Gas-Laser Spectroscopy”. *Phys. Scr.*, T65:48, 1996.
- [52] Ye, Jun, Steve Swartz, Peter Junger, and John L. Hall. “Hyperfine structure and absolute frequency of the $^{87}\text{Rb}5P_{3/2}$ state”. *Opt. Lett.*, 21:1280, 1996.
- [53] Zameroski, Nathan D., Wolfgang Rudolph, David A. Hostutler, and Gordon D. Hager. “A study of collisional quenching and radiation trapping kinetics for Rb(5P) in the presence of Methane and Ethane using time resolved fluorescence”, June 2009.

Vita

My name is Douglas Edward Thornton. I grew up in Columbus, OH and Indianapolis, IN, where I graduated from high school. After high school, I attended Rose-Hulman Institute of Technology where I joined Air Force ROTC. I graduated with a Bachelors of Science degree in Electrical Engineering with a German technical translation minor and commissioned as Second Lieutenant in the United States Air Force. Upon graduation and commissioning, I was assigned to the Air Force Institute of Technology to pursue a Masters degree in Electro-Optics. - Future -

REPORT DOCUMENTATION PAGE

Form Approved
OMB No. 0704-0188

The public reporting burden for this collection of information is estimated to average 1 hour per response, including the time for reviewing instructions, searching existing data sources, gathering and maintaining the data needed, and completing and reviewing the collection of information. Send comments regarding this burden estimate or any other aspect of this collection of information, including suggestions for reducing this burden to Department of Defense, Washington Headquarters Services, Directorate for Information Operations and Reports (0704-0188), 1215 Jefferson Davis Highway, Suite 1204, Arlington, VA 22202-4302. Respondents should be aware that notwithstanding any other provision of law, no person shall be subject to any penalty for failing to comply with a collection of information if it does not display a currently valid OMB control number. **PLEASE DO NOT RETURN YOUR FORM TO THE ABOVE ADDRESS.**

1. REPORT DATE (DD-MM-YYYY) 25-03-2010		2. REPORT TYPE Master's Thesis		3. DATES COVERED (From — To) Aug 2008 — Mar 2010	
4. TITLE AND SUBTITLE Hard Collisions in Rubidium using Sub-Doppler Spectroscopy				5a. CONTRACT NUMBER	
				5b. GRANT NUMBER	
				5c. PROGRAM ELEMENT NUMBER	
6. AUTHOR(S) Thornton, Douglas E. , 2dLt, USAF				5d. PROJECT NUMBER	
				5e. TASK NUMBER	
				5f. WORK UNIT NUMBER	
7. PERFORMING ORGANIZATION NAME(S) AND ADDRESS(ES) Air Force Institute of Technology Graduate School of Engineering and Management (AFIT/EN) 2950 Hobson Way WPAFB OH 45433-7765				8. PERFORMING ORGANIZATION REPORT NUMBER AFIT/GEO/ENP/10-M02	
9. SPONSORING / MONITORING AGENCY NAME(S) AND ADDRESS(ES) HEL-JTO (Dr. Harro Ackermann) 901 University Blvd. SE, Suite 100 Albuquerque, NM 87106 (505) 248-8208, harro.ackermann@JTO.HPC.MIL				10. SPONSOR/MONITOR'S ACRONYM(S) HEL-JTO	
				11. SPONSOR/MONITOR'S REPORT NUMBER(S)	
12. DISTRIBUTION / AVAILABILITY STATEMENT APPROVED FOR PUBLIC RELEASE; DISTRIBUTION UNLIMITED.					
13. SUPPLEMENTARY NOTES					
14. ABSTRACT To better understand the laser kinetics of an alkali gain medium, hard collisions, or velocity-changing collisions, has been studied and a velocity-changing collisional rate has been calculated. Previous works have studied these collisions, but no rate has been calculated. Using the precise tool of sub-Doppler spectroscopy, atomic hard collisions can be observed. The collected spectra are fitted with two different line shapes to demonstrate the accuracy of this method. From the fits, the number of hard collisions can be extracted. The time scale of the hard collisions in rubidium is interpolated by varying the chopping frequency of the pump beam, or how long the collisions are being observed. Using the time scale and the collisional information from the fits, the velocity-changing collision rate was determined to be $1020.7 \pm 26.3 s^{-1} mTorr^{-1}$ for the first line shape and $758.81 \pm 13.90 s^{-1} mTorr^{-1}$ for the second line shape, which is a 17% and 13% difference, respectively, of the chemical kinetic "hard sphere" collisional model rate, $872.78 \pm 13.73 s^{-1} mTorr^{-1}$.					
15. SUBJECT TERMS Sub-Doppler, Saturation Spectroscopy, Hard Collisions, Velocity-Changing Collision Rate, Rubidium, DPAL					
16. SECURITY CLASSIFICATION OF:			17. LIMITATION OF ABSTRACT	18. NUMBER OF PAGES	19a. NAME OF RESPONSIBLE PERSON
a. REPORT	b. ABSTRACT	c. THIS PAGE			Dr. Glen P. Perram
U	U	U	UU	146	19b. TELEPHONE NUMBER (include area code) (937) 255-3636, x4501; glen.perram@afit.edu